ENSC- 2015 n° 597

THESE DE DOCTORAT
DE L'ECOLE NORMALE SUPERIEURE DE CACHAN

Présentée par
**Yang SI**

Pour obtenir le grade de
**DOCTEUR DE L'ECOLE NORMALE SUPERIEURE DE CACHAN**

Domaine :
**CHIMIE**

Sujet de la thése :

# Fluorescent Nanomaterials for Bioimaging and Biosensing: Application on *E.coli* Bacteria

Thèse présentée et soutenue à Cachan le 16 Septembre 2015 devant le jury composé de :

| | | |
|---|---|---|
| **Niko HILDEBRANDT** | **Professeur, Université Paris-Sud 11** | **Rapporteur** |
| **Marie ERARD** | **Enseignant-chercheur, Université Paris-Sud 11** | **Rapporteur** |
| **Romain BRIANDET** | **Directeur de Recherche, INRA** | **Président** |
| **Rachel MEALLET-RENAULT** | **Professeur, Université Paris-Sud 11** | **Directrice** |
| **Bianca SCLAVI** | **Chargée de Recherche, ENS-Cachan** | **Co-encadrant** |
| **Gilles CLAVIER** | **Chargé de recherche, ENS-Cachan** | **Examinateur** |

Laboratoire de photophysique et photochimie supra et macromoléculaire (PPSM, CNRS UMR8531)/
Laboratoire de biologie et de pharmacologie appliquée (LBPA, CNRS UMR8113)

ENS-Cachan, 61, avenue du Président Wilson, 94235 CACHAN Cedex France

# Table of Contents

**Abbreviations** ..... **V**

**Chapter 1 Introduction: bibliographical background** ..... **1**

1.1 What are bacteria? Why to study them? ..... 1

1.2 What is fluorescence? ..... 3

1.3 Fluorescent probes and labels for bioimaging and biosensing ..... 7

1.3.1 Organic dyes ..... 8

1.3.2 Fluorescent proteins ..... 14

1.3.3 Fluorescent nanomaterials ..... 16

1.4 Novel fluorescent nanomaterials for bioimaging and biosensing: application on *E.coli* bacteria ..... 32

**Chapter 2 Fluorescent nanoparticles (FNPs) for internal bioimaging of *E.coli* bacteria** ..... **37**

2.1 Synthesis of fluorescent nanoparticles (FNPs) ..... 37

2.2 Characterizations of fluorescent nanoparticles (FNPs) ..... 38

2.3 Toxicity assessments of FNPs on *E.coli* ..... 41

2.4 FNPs for internal bioimaging of *E.coli* ..... 41

2.4.1 Chemical treatments of *E.coli* with FNPs ..... 41

2.4.2 Electroporation of *E.coli* bacteria with FNPs ..... 43

2.4.3 Emission quenching of $FNP^-$ with Methylene Blue (MB) ..... 48

2.4.4 Fluorescence bioimaging of *E.coli* with $FNP^-$ after quenching with MB ..... 51

2.4.5 SEM images of *E.coli* interacting with $FNP^-$ ..... 53

2.5 Conclusion ..... 57

2.6 Additional images ..... 59

**Chapter 3 Fluorescent nanoparticles (FNPs) for external bioimaging of *E.coli* bacteria** ..... **65**

3.1 Design of “Sandwich” for targeting bacterial surface ..... 65

3.1.1 Conjugation of biotin on FNPs ..... 65

3.1.2 Target *E.coli*’s outer membrane with “sandwich system” ..... 66

3.2 Characterizations of the “Sandwich” ..... 67

3.2.1 Spectroscopy analysis ..... 67

3.2.2 Surface Plasmon Resonance ..... 69

3.2.3 Secondary fluorescent antibody ..... 72

3.2.4 Fluorescence bioimaging of “sandwich” labelling bacterial surface ..... 74

3.2.5 SEM images of “sandwich” labelling bacterial surface ..... 74

3.2.6 Sandwich complex in a microfluidic device ..... 75
3.3 Design of "Nanoparticle-Antibody" for targeting bacterial surface ..... 79
3.4 Conclusion ..... 83
3.5 Additional images ..... 85
**Chapter 4 Fluorescent polymer chains (FPCs) for bioimaging of *E.coli* bacteria ..... 89**
4.1 Synthesis of fluorescent polymer chains (FPCs) ..... 89
4.2 Characterizations of Green fluorescent polymer chains (GFPCs) ..... 91
4.3 Toxicity assessments of GFPCs on *E.coli* ..... 96
4.4 GFPCs for internal bioimaging application of *E.coli* bacteria ..... 97
4.4.1 Bioimaging of *E.coli* interacting with GFPCs ..... 97
4.4.2 Emission quenching of $GFPC^-$ with Methylene Blue (MB) ..... 100
4.4.3 Multi-color imaging application of $GFPC^-$ ..... 103
4.5 Characterizations of Red fluorescent polymer chains (RFPCs) ..... 108
4.6 Toxicity assessments of RFPCs on *E.coli* ..... 111
4.7 RFPCs for external bioimaging application of *E.coli* bacteria ..... 112
4.7.1 Bioimaging of RFPCs labelling the membrane of *E.coli* ..... 112
4.7.2 Multi-color Imaging application of $GFPC^-$ and $RFPC^+$ ..... 114
4.7.3 Comparison of PKH26 and RFPCs ..... 115
4.8 Conclusion ..... 116
4.9 Additional images ..... 119
**Chapter 5 Fluorescent pH-sensitive nanoparticles (FANPs) for rapid detection of *E.coli* growth ...125**
5.1 Synthesis of fluorescent pH-sensitive nanoparticles (FANPs) ..... 125
5.1.1 Synthesis of polystyrene nanoparticles (PSNPs) ..... 125
5.1.2 Grafting pH sensitive fluorophores on the PSNPs ..... 127
5.2 Characterization of FANPs ..... 128
5.2.1 Spectroscopic properties of the FANPs ..... 128
5.2.1 Photostability and reversibility assessments of FANPs ..... 130
5.3 Toxicity assessments of FANPs on *E.coli* ..... 132
5.4 Detection of *E.coli* growth with FANPs ..... 132
5.4.1 Real-time detection of *E.coli* growth ..... 132
5.4.2 Sensitivity assessments ..... 134
5.5 High-throughput screening applications ..... 137
5.5.1 Screening of cell growth in a 96 well plate ..... 137
5.5.2 High-throughput screening of bacterial growth inhibition by antibiotics ..... 139

5.6 Imaging of *E.coli* growth ..... 141
5.7 Conclusion ..... 143
**Chapter 6 General conclusion and perspectives ..... 145**
**Chapter 7 Experimental methods and materials ..... 149**
7.1 Materials ..... 149
7.2 Synthesis of fluorescent nanomaterials ..... 149
7.2.1 Synthesis of fluorescent nanoparticles (FNPs) ..... 149
7.2.2 Conjugation of biotin on $FNP^-$ ..... 151
7.2.3 Conjugation of antibody on $FNP^-$ ..... 152
7.2.4 Synthesis of fluorescent polymer chains (FPCs) ..... 153
7.2.5 Synthesis of fluorescent pH-sensitive nanoparticles (FANPs) ..... 155
7.3 Characterization of fluorescent nanomaterials ..... 157
7.3.1 Absorption and fluorescence spectroscopy ..... 157
7.3.2 Hydrodynamic diameter ..... 157
7.3.3 Size exclusion chromatography (SEC) ..... 158
7.3.4 Critical micelle concentration (CMC) ..... 158
7.3.5 Titration of $FNP^-$ or $GFPC^-$ with Methylene blue ..... 159
7.3.6 Surface Plasmon Resonance (SPR) experiment ..... 159
7.3.7 pH measurements ..... 159
7.3.8 Photostability and reversibility assessment of FANPs ..... 160
7.4 Toxicity assessments of fluorescent nanomaterials on *E.coli* ..... 160
7.4.1 Bacteria growth medium ..... 160
7.4.2 Toxicity assessments of FNPs and FPCs on *E.coli* ..... 161
7.5 Techniques to insert FNPs inside bacteria ..... 161
7.5.1 Chemical treatment to introduce FNPs in *E.coli* Bacteria ..... 161
7.5.2 Electroporation to introduce FNPs in *E.coli* Bacteria ..... 162
7.6 Techniques of “Sandwich system” and “Nanoparticle-antibody system” formation ..... 162
7.6.1 Process of “sandwich system” formation ..... 162
7.6.2 Secondary fluorescent antibody labelling ..... 163
7.6.3 Process of “Nanoparticle-antibody system” formation ..... 163
7.7 Incubation to introduce FPCs into *E.coli* bacteria ..... 164
7.7.1 Incubation to introduce GFPCs into *E.coli* bacteria ..... 164
7.7.2 Incubation to introduce RFPCs into *E.coli* bacteria ..... 164
7.8 Characterization of fluorescent nanomaterials interaction with *E.coli* by flow cytometry ..... 165

7.9 Techniques for rapid detection of *Escherichia coli* growth by fluorescent pH-sensitive nanoparticles (FANPs) ..... 166
7.9.1 Screening of bacterial growth in a 96 well plate ..... 166
7.9.2 Real-Time detection of *E.coli* ..... 166
7.9.3 High-through put screening of bacterial growth inhibition by antibiotics ..... 167
7.9.4 Preparation of pH sensitive agarose culture plates ..... 167
7.9.5 Imaging of *E.coli* growth ..... 167
7.10 Bioimaging of fluorescent nanomaterials interaction with *E.coli* bacteria ..... 168
7.10.1 Fluorescence microscopy ..... 168
7.10.2 Usage of methylene blue for bioimaging experiments ..... 169
7.10.3 Usage of DRAQ 5 for labelling the DNA of *E.coli* bacteria ..... 169
7.10.4 Usage of PKH26 for labelling the membrane of *E.coli* bacteria ..... 169
7.10.5 Main preparation pathways for SEM ..... 170
7.11 Equations ..... 170
**References ..... 175**
**Acknowledgements ..... 191**

# Abbreviations

| | |
|---|---|
| AA | Acrylic acid |
| ACPA | 4,4'-azobis(4-cyanopentanoic acid) |
| AIBN | 2,2'-Azobis(2-methylpropionitrile) |
| APEG | Poly(ethylene oxide) methyl ether acrylate |
| B | Brightness |
| BODIPY | Boron-dipyrromethene |
| BDPMA1 | BODIPY methacrylate-1 |
| BDPMA2 | BODIPY methylnaphthalene-2 |
| CFU | Colony forming unit |
| CMC | Critical micelle concentration |
| CPN | Conjugated polymer nanoparticles |
| DEG | Diethylene glycol |
| $D_h$ | Hydrodynamic diameter |
| $D_t$ | Theoretical diameter |
| DLS | Dynamic light scattering |
| DMAEA | 2-(Dimethylamino)ethyl acrylate |
| *E.coli* | *Escherichia coli* |
| EDTA | Ethylenediaminetetraacetic acid |
| EDC.HCl | 1-ethyl-3-(3-dimethylaminopropyl) carbodiimide hydrochloride |
| EtA | Ethanolamine |
| FA | Fluoresceinamine |
| FANPs | FA based fluorescent pH-sensitive nanoparticles |
| FANP1 | FA based fluorescent pH-sensitive nanoparticle type 1 |
| FANP2 | FA based fluorescent pH-sensitive nanoparticle type 2 |
| FNPs | Fluorescent nanoparticles |
| $FNP^-$ | Negative fluorescent nanoparticles |
| $FNP^+$ | Positive fluorescent nanoparticles type1 |
| $FNP\text{-}PEG^+$ | Positive fluorescent nanoparticles type2 |
| FNPB | Fluorescent nanoparticle with branched chains |

| | |
|---|---|
| FPCs | Fluorescent polymer chains |
| FRET | Förster resonace energy transfer |
| FITC | Fluorescein isothiocyanate |
| GFP | Green fluorescent proteins |
| GFPCs | Green fluorescent polymer chains |
| $GFPC^-$ | Negative green fluorescent polymer chains |
| $GFPC^0$ | Neutral green fluorescent polymer chains |
| HTS | High-throughput screening |
| IgG | Immunoglobulin G |
| IR | Infrared |
| IT | integration time |
| $K_d$ | Dissociation constant |
| LB medium | Luria Broth medium |
| M9 medium | M9 Minimal growth medium |
| MB | Methylene blue |
| $M_{nth}$ | Theoretical number-average molar mass |
| $M_n$ | Average molar mass |
| $M_w/M_n$ | Polydispersity indexes |
| $M_{nSEC}$ | Number-average molar mass |
| NPs | Nanoparticles |
| OD | Optical density |
| $OD_{600}$ | Optical density at 600nm |
| OPN | Organic polymer nanoparticles |
| PAA | Polyacrylic acid |
| PBS buffer | Phosphate buffered saline buffer |
| PCR | Polymerase Chain Reaction |
| PEO | Polyethylene oxide (see PEG) |
| PEOA | Poly(ethylene oxide) methyl ether acrylate |
| PEG | Polyethylene glycol (see PEO) |
| PFA | Paraformaldehyde |

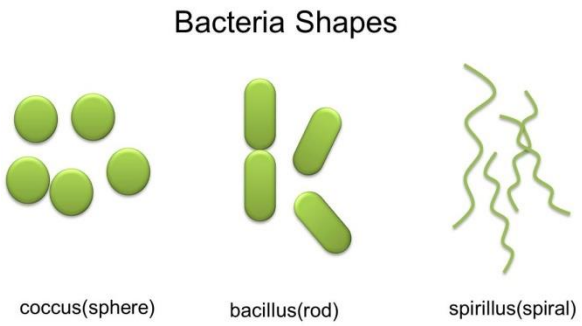
| | |
|---|---|
| PI | Propidium iodide |
| PMMA | Poly(methyl methacrylate) |
| PS | Polystyrene |
| PSNPs | Polystyrene nanoparticles |
| PSNP1 | Polystyrene nanoparticle type 1 |
| PSNP2 | Polystyrene nanoparticle type 2 |
| QDs | Quantum dots |
| RAFT | Reversible addition-fragmentation chain transfer |
| RI | Refractive index |
| RFPCs | Red fluorescent polymer chains |
| $RFPC^-$ | Negative red fluorescent polymer chains |
| $RFPC^+$ | Positive red fluorescent polymer chains |
| S | Styrene |
| SEC | Size exclusion chromatography |
| SEM | Scanning electron microscope |
| SPR | Surface Plasmon Resonance |
| THF | Tetrahydrofuran |
| TTC | Trithiocarbonate |
| TTCA | 2-methyl-2-[(dodecylsulfanylthiocarbonyl)sulfanyl] propanoic acid |
| UV | Ultraviolet |
| $\lambda_{abs}$ | Absorption wavelength |
| $\lambda_{exc}$ | Excitation wavelength |
| $\lambda_{emi}$ | Fluorescence emission wavelength |
| $\lambda_{max}$ | Maximum absorption or emission wavelength |
| $\Phi_F$ | Fluorescence quantum yield |

# Chapter 1 Introduction: bibliographical background

## 1.1 What are bacteria? Why to study them?

Bacteria are prokaryotic microorganisms. They are small (few micrometers) single cell microorganisms. They normally exist together in millions. Three different typical shapes of bacteria are encountered: spheres, rods and spirals (**Figure 1.1A**). Spherical bacteria are usually the simplest ones, called coccus. Rod shaped bacteria are known as bacillus. Spiral bacteria are known as spirillus. Unlike eukaryotic cells, most bacterial cells do not contain intracellular compartments. The study of the diffusion of proteins of different sizes inside a bacterial cell suggests that the cytoplasm is a very crowded environment[1–3]. Their cytoplasm has often been described as a complex mixture (like a "soup") containing the chromosome and all the macromolecular machineries necessary for DNA replication, gene expression and other metabolic processes. Bacteria reproduce through a binary fission process: bacterial cell mass increases until a new cell wall grows through the center thus dividing the mother cell and forming two daughter cells, each bacterium is the same as their parent cell.

**A**




**B**

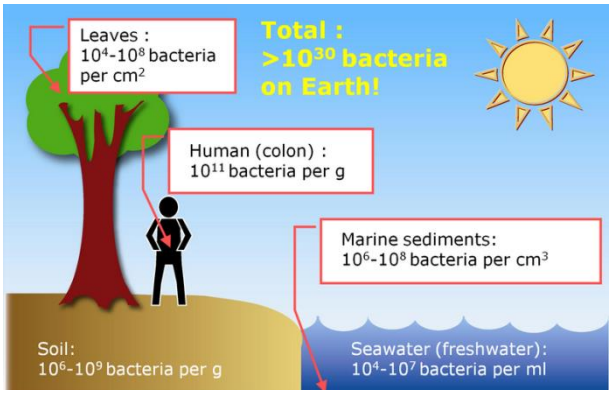



**Figure 1.1** A: Main shapes of bacteria. B: Bacteria number distribution on earth (figure from[4]).

Bacteria are the earliest and longest life forms on earth. They can inhabit every corner of the earth: water, soil, trees, human, animals, even nuclear waste[5]. A gram of soil contains about $10^6$-$10^9$ bacteria, and a piece of leaf may contains about $10^4$-$10^8$ bacteria[4] (**Figure 1.1B**). Bacteria are very common in our daily life. So it is important to do research on this unseen majority. However, until now people don't really understand how this kind of cell is organized to coordinate the different cellular processes. Studying and improved understanding of bacteria can be used for medical research[6,7], water resources[8,9], and food industry[10,11] .

Many bacteria are helpful for humans, for example, bacteria can help to digest food[10]. However people are normally scared by bacteria because some pathogens cause disease in humans race, for example, the pathogenic bacteria (e.g. *E. coli* O157:H7) hidden in food[12] and water[13] or even medical equipment may cause illness in the human body and can become life-threatening[14]. Thus, rapid detection of bacterial growth is important for medical diagnostics to identify contamination in a medical setting[15–17] and in the food-processing industry in order to prevent contamination of food, air, and water [18–20].

The *Escherichia coli* (*E.coli*) bacterium is a gram-negative bacterium that is used as a model organism for research (**Figure 1.2**). *E.coli* bacteria are surrounded by phospholipid bilayers cell membrane. As prokaryotes, unlike eukaryotic cells, *E.coli* bacteria don't have membrane-bound organelles in their cytoplasm. The cytoplasm is a complex mixture containing proteins, ribosomes, plasmid, nucleoid, which is the circular genome of the cell bound by regulatory proteins. *E.coli* bacteria also have flagella which are used for motility. *E.coli* is the most widely used and studied model organism in biotechnology and microbiology. The bacterium can be grown and cultured easily and inexpensively in a laboratory setting, and has been intensively investigated for over many years. *E.coli* cells are typically rod-shaped, and are about 3 µm long and 0.5 µm in diameter [21,22].

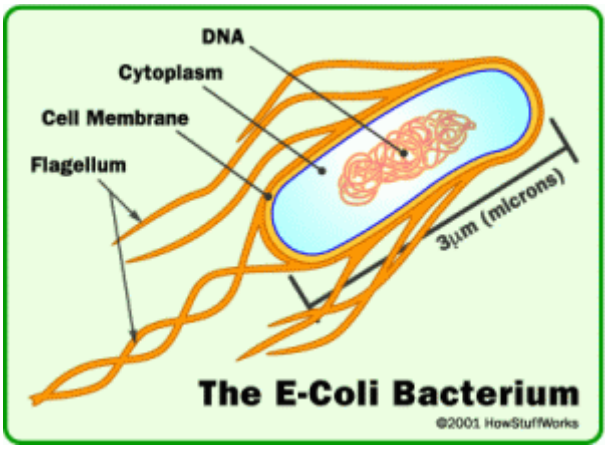



**Figure 1.2** Structure of *E.coli* bacteria (figure from[21])

For this research project, I used the *E.coli* strains K12 BW25113. This strain is adapted to laboratory setting and is not pathogenic. In this project I aim at developing and characterizing new fluorescent materials in order to develop internal and external imaging of *E.coli*. I also envision detecting growth of bacteria. Thus different fluorescent nanomaterials were synthetized: such as fluorescent nanoparticles (FNPs Chapters 2, 3, 5) and fluorescent

polymer chains (FPCs Chapter 4). I will show how these materials target internal and external parts of *E.coli* to develop bioimaging and biosensing applications of *E.coli* bacteria. Before going further, I will now introduce what fluorescence is and why I have chosen to detect such signal.

## 1.2 What is fluorescence?

Fluorescence is a radiative deactivation after absorption of a photon at appropriate energy. The emission of another photon with longer wavelength after a very brief time (few ns) is fluorescence. The processes that occur after the absorption of light by a molecule or a material are usually illustrated by the Perrin-Jablonski diagram (**Figure 1.3**). The Perrin-Jablonski diagram shows the various electronic states of a molecule, such as the ground state ($S_0$), the excited states ($S_1$, $S_2$…) and the triplet states ($T_1$, $T_2$…)[22].

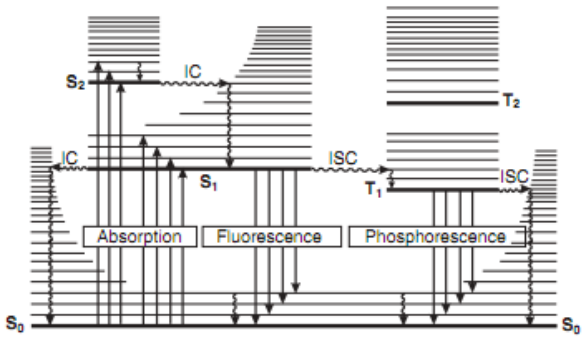



**Figure 1.3** Perrin-Jablonski diagram (figure from[22]), IC : internal conversion, ISC : intersystem crossing, $S_i$ : singlet electronic state, $T_i$ : triple electronic state.

A molecule in the ground state ($S_0$) can absorb light and be excited to higher electronic states like singlet electronic states ($S_1$, $S_2$…). Molecules in the condensed phases rapidly relax to the lowest vibrational level of $S_1$, this process is called internal conversion (IC). Molecules in the $S_1$ state can also undergo a spin conversion into the first triplet state $T_1$, such conversion is called intersystem crossing (ISC). Emission from $T_1$ to the ground state is called phosphorescence. Emission of photons accompanying the $S_1$ to $S_0$ relaxation is called fluorescence. The average time the molecule stays in its excited state $S_1$ before emitting a photon is called fluorescence lifetime.

Examination of the Perrin-Jablonski diagram (**Figure 1.3**) indicates that the energy of the emission is less than that of absorption. So, emitted fluorescent light has a longer wavelength and lower energy compared with the absorbed light. This phenomenon, known

as Stokes shift (**Figure 1.4**), is due to the energy loss in the fluorescence process. One common reason of the Stokes shift is the rapid decay to the lowest vibrational level of $S_1$. Furthermore, fluorophores usually decay to higher vibrational levels of $S_0$ (**Figure 1.3**), resulting in further loss of excitation energy by thermalization of the excess vibrational energy. Besides these effects, fluorophores can display Stokes shifts due to other reasons, such as solvent effects, excited-state reactions, complex formation, and energy transfer[22,23].

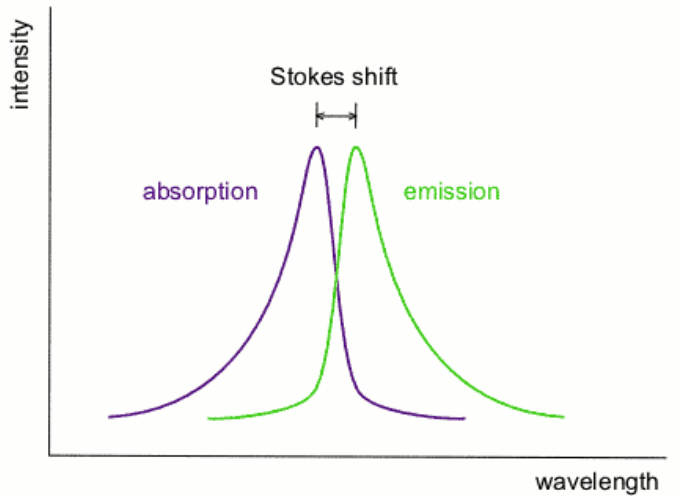



**Figure 1.4** Stokes shift (figure from [24]).

In many cases the absorption spectrum is a mirror image of the emission spectrum. This is the mirror image rule which states that electronic transitions are vertical[23]. The fluorescence quantum yield ($\Phi_F$) defines the efficiency of the fluorescence process. It is known as the ratio of the number of emitted photons to the number of absorbed photons. The quantum yield is generally independent from the excitation wavelength[25]. This is because the excited molecules normally decay to the lowest vibrational level of $S_1$ before fluorescence emission[23].

Fluorescence intensity can be decreased by a wide variety of processes which is called quenching processes (**Figure 1.5**). Quenching can occur by different mechanisms. Collisional quenching occurs when the fluorophore in the excited state is deactivated by contact with some other molecule which is called the quencher (**Figure 1.5A**). If fluorophores form non fluorescent complexes with quenchers in the ground state and do not rely on diffusion or molecular collisions the quenching is referred as static (**Figure 1.5B**).

Another important process is the Förster resonance energy transfer (FRET) (**Figure 1.5C**). This process occurs when the emission spectrum of a fluorophore (donor), overlaps with the absorption spectrum of another molecule (acceptor). The acceptor is designed to be close enough to the donor, and the acceptor does not need to be fluorescent.

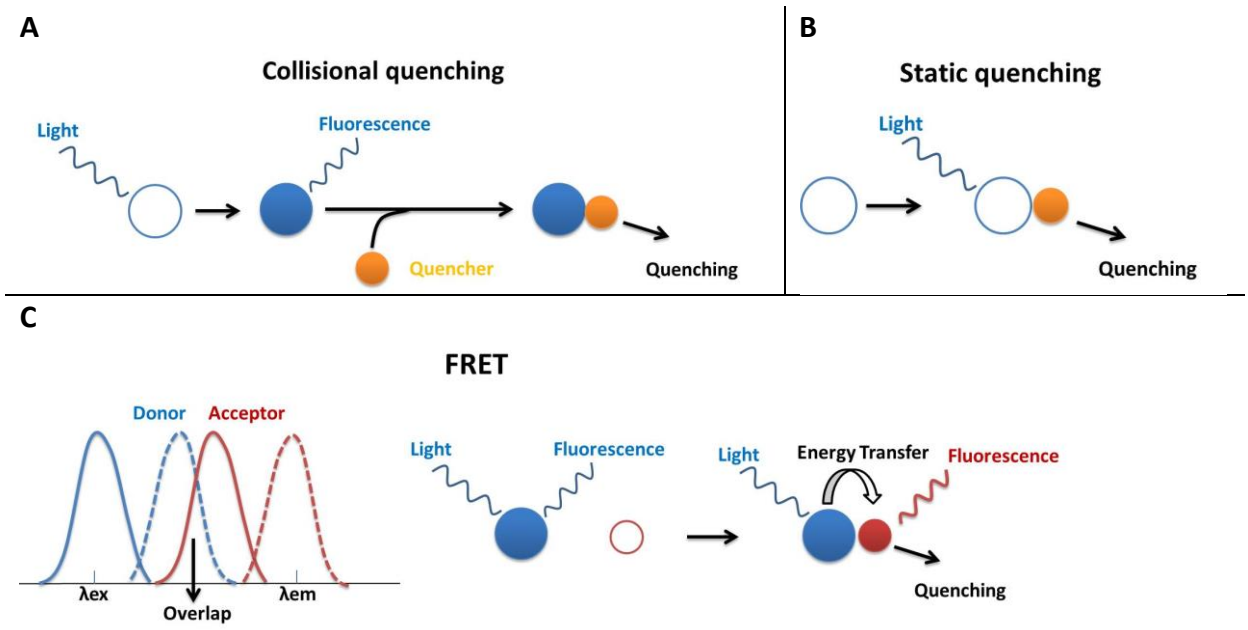



**Figure 1.5** Schemes of different types of fluorescence quenching (A: Collisional quenching, B: Static quenching, C: Förster resonance energy transfer (FRET)).

Fluorescence in life science has been widely used. People use chemical reactions to label biological macromolecules with fluorescent dyes in order to detect these biomolecules. An ideal fluorescent probe and label for bioimaging and biosensing application should carry out the following requirements:

1) High brightness.

Brightness is the total efficiency of absorption and fluorescence emission of a fluorophore. Brightness of a dye depends on two properties: molar extinction coefficient at the excitation wavelength ε(λ) and fluorescence quantum efficiency, $\Phi_F$[26].

A fluorophore with high molar extinction coefficient describes a high ability of the fluorophore to absorb light. Light absorbing ability of the fluorophore is one parameter to contribute to the brightness. Another parameter is the fluorescence quantum yield, $\Phi_F$, high quantum yield means in higher ratio of the number of emitted photons to the number of absorbed photons which resulted in high fluorescence efficiency.

The brightness (B) of a fluorophore is proportional to the molar extinction coefficient at the excitation wavelength ε(λ) and quantum yield ($\Phi_F$), as indicated in the following relationship[26]:

$$B = \varepsilon(\lambda) \times \Phi_F$$

For assemblies of fluorophores (e.g. nanoparticles), the brightness is defined as[27]:

$$B = N \times \varepsilon(\lambda) \times \Phi_F$$

Where,

N: Number of fluorophores contained inside the nanoparticle

ε(λ): molar extinction coefficient of the fluorophore at the excitation wavelength

$\Phi_F$: fluorescence quantum yield of the nanoparticle

From the equation above, one can notice that optimal excitation wavelength is also very important to high brightness. In order to achieve the highest brightness, it is important to excite fluorophore at wavelengths (λ) close to the maximum of the absorption.

2) High photostability.

During practical bioimaging experiments, after some number of excitation-emission cycles by intense light in fluorescence microscopy, almost all fluorophores can be photobleached. Photobleaching occurs because of some photochemical reactions that often involves molecular oxygen[28].

The photostability of a fluorophore can be affected by its local environment. Low photostability often limits the quality images to a short time scale which may be a serious drawback for kinetics or mapping in bioimaging (e.g. cells, tissues, bacteria…).

3) Optimal solubility, penetration, specificity, nontoxicity

High cell permeability and a good intracellular solubility of the label are important for bioimaging and biosensing. High affinity and high specificity for the target is also needed as well as nontoxic effect especially for *in vivo* research.

From all the parameters described above, one can notice that the ideal fluorescent labeling material hardly exists. Scientists have to consider about the experimental setting and different parameters to make a compromise for each application[22]. In the next paragraph **§1.3**, different selected typical fluorescent materials are briefly described, followed by the discussion about biosensing and bioimaging applications of these fluorescent materials (organic dyes, fluorescent proteins, quantum dots, silica nanoparticles, organic nanoparticles…).

## 1.3 Fluorescent probes and labels for bioimaging and biosensing

Sensing and labelling are two important methods that are widely used in life science. Different techniques and strategies based on different physical principles have been developed, such as: mass difference measurement (microcantilever)[29], electron and matter interaction (electrochemistry)[30,31], photon and matter interaction (optical sensors)[32,33], advanced microscopy (TEM[34], SEM[35]). These techniques however generally need sophisticated and expensive instrumentation which limits their application[28].

Fluorescent sensing and labelling is one of the most common methodologies used for bioanalytical purposes. Fluorescence techniques are considered to be very sensitive[28], since their sensitivity can reach in some cases the limit of single molecule. Fluorescence techniques are also considered to be very fast, the response time depends on the fluorescence lifetime which can be about $10^{-8}$-$10^{-10}$s[28]. Moreover, the most important advantage of fluorescence is the versatility. There are plenty of different fluorescent materials, more are under development. All these features distinguish fluorescence from other methods and make it great importance in sensing and labelling.

As we discussed in **§1.2**, the fundamental issues for an ideal fluorescent material are brightness and stability. In the quest of the brightest and most stable fluorescence labels, different classes of materials are currently being developed and employed as fluorescent probes and they mainly include: organic dyes (**Figure 1.6a**), fluorescent proteins (**Figure 1.6c**) and fluorescent nanomaterials (**Figure 1.6b, d**). The earlier classes of fluorescent labels such as organic dyes and fluorescent proteins, are still the most popularly used as fluorescent labels. This is because of their small size, high water solubility, commercial availability and the existence of standard protocols. However, there are several limitations for these labeling

agents such as: broad spectrum profiles, photobleaching or poor photochemical stability[36]. Nowadays, fluorescent materials with high brightness and high photostability are in great need for life science, at the same time, the developments of nanomaterial science bring a new class of labeling agent: fluorescent nanomaterials. Fluorescent nanomaterials have the great potential and ability to solve the drawbacks caused by "standard" fluorophores[36]. In this section I will concentrate on several important members of fluorescent labels: organic dyes, fluorescent proteins and fluorescent nanomaterials (e.g. semiconductor quantum dots, silica-based nanoparticles, and organic polymer nanoparticles). I will discuss their properties and evaluate their applicability for bioimaging and biosensing applications.

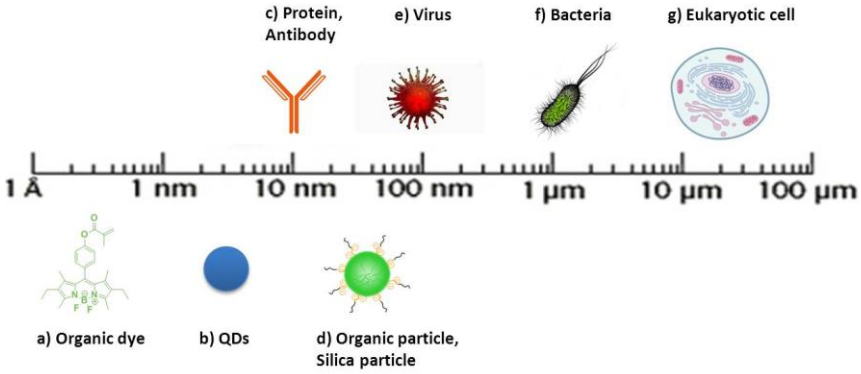



**Figure 1.6** Scale bar of the most common nanomaterials compared to that of the main biological structures (figure adapted from [37–40]).

### 1.3.1 Organic dyes

Organic dyes are the most common probes used in fluorescence bioimaging. Their main advantages are their easy availability, low price and versatility. The amount of fluorescent synthetic organic dyes is quite large and keeps increasing, therefore, I will concentrate on several main classes that are frequently used.

*Fluorescein* is a green organic dye. It is widely used as a fluorescent label for biological applications. The chemical structure and spectra of the parent fluorescein dye is presented in **Figure 1.7**. Fluorescein has an absorption maximum at 494 nm and emission maximum of 521 nm in buffer at pH 7[41]. The pKa of fluorescein is 6.4 and its ionization equilibrium leads to a pH-dependent absorption and emission over the pH range of 5 to 9[42]. Fluorescein and its derivatives are commonly used in confocal microscopy and flow cytometry applications. However, fluorescein dyes have low photostability which is an obvious disadvantage for bioimaging application. There are many different fluorescein derivatives which are widely

used as fluorescent labels, such as, fluorescein isothiocyanate (FITC)[43], 6-FAM phosphoramidite[44], OregonGreen[45], Tokyo Green[46] and SNAFL (Carboxyseminaphthofluorescein)[47] .

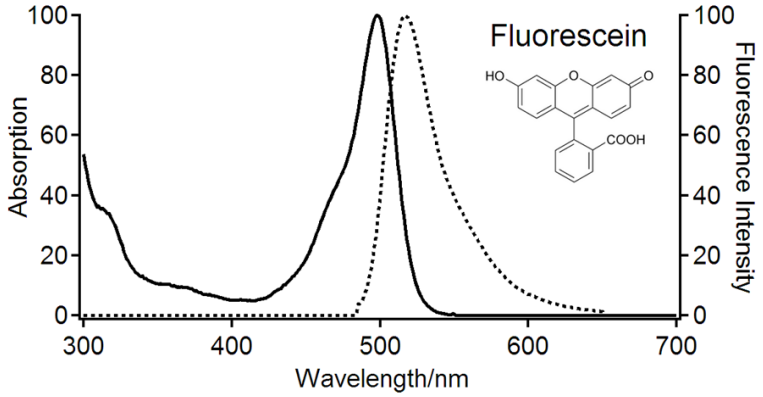



**Figure 1.7** Structure and spectra of fluorescein in buffer at pH 7: absorption (full line), fluorescence emission (dotted line)(data from life technologies[41]).

Fluoresceinamine is a common amine-reactive derivative of fluorescein. It consists of an amino group which is capable of grafting on carboxylic groups. During my research projects, fluoresceinamine is used as a fluorescent pH indicator which is grafted on polystyrene nanoparticles. I carried out investigation to test if this fluoresceinamine based fluorescent pH-sensitive nanoparticles (FANPs) can be used to detect the growth of *E.coli* bacteria and their biocompatibility (**Chapter 5**).

*Rhodamine* families are also a popular choice of dye for labeling. They are widely used in biological applications such as fluorescence microscopy, fluorescence correlation spectroscopy, flow cytometry, and enzyme-linked immunosorbent assay (ELISA). The most common Rhodamine family members are Rhodamine 6G, Rhodamine B, Rhodamine 123. This latter one (**Figure 1.8**) is a cell-permeant, cationic, water soluble green fluorescent dye. It has an absorption maximum at 507 nm and emission maximum of 529 nm in methanol[41]. Its luminescence quantum yield is 0.90[48]. Rhodamine 123 seems to bind to the mitochondrion membranes and inhibit transport processes[49].

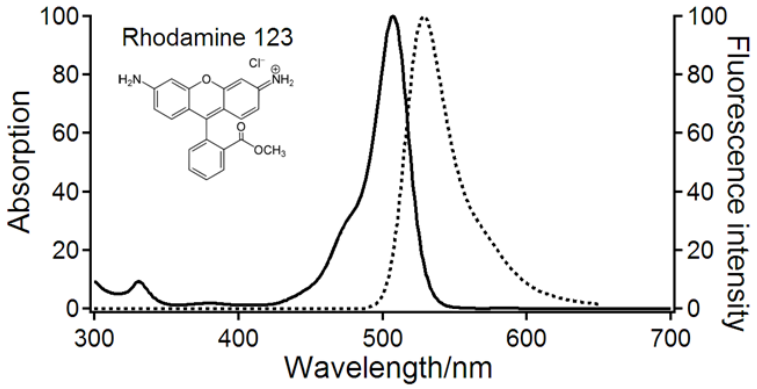



**Figure 1.8** Structure and spectra of Rhodamine 123 in methanol: absorption (full line), fluorescence emission (dotted line)(data from life technologies[50]).

*Alexa Fluor dyes*, a fluorescent dye family which is obtained by sulfonating aminocoumarin, rhodamine, or carbocyanine dyes[51]. They are widely used as cell or tissue labels in fluorescence microscopy and cell biology. Alexa fluor dyes have a very wide excitation and emission spectra. They cover the whole visible spectrum and extend to the infrared range (**Figure 1.9**). Alexa Fluor dyes are normally more stable, brighter, and less pH-sensitive than dyes like fluorescein, and rhodamine[52]. However, they are more expensive.

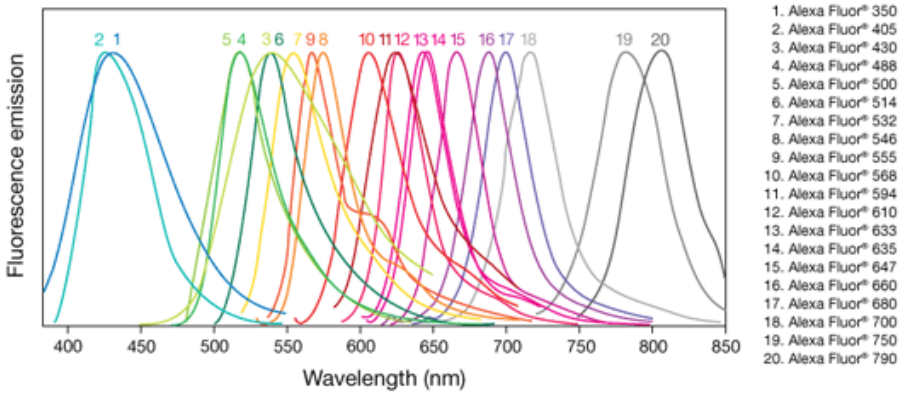



**Figure 1.9** Emission spectra for the Alexa Fluor dye series (figure from [53]).

*BODIPY* dyes (boron-dipyrromethene), is an important class of fluorescent dyes. The synthesis and spectroscopic properties have been recently summarized in a review by Loudet A et al.[54]. Normally, BODIPY molecules are uncharged[28]. The core structure of the BODIPY fluorophore is shown in **Figure 1.10**. BODIPY have shown attractive spectroscopic features such as tunable emission spectra from green to red. BODIPY dyes possesses uniquely small Stokes shift, high fluorescent quantum yield[55]. BODIPY dyes are highly soluble in many organic solvents. The combination of these characters makes BODIPY dyes an important tool in imaging applications. BODIPY dyes are considered to be very versatile[56].

Scientists can use BODIPY dyes to prepare BODIPY conjugated nucleotides[57], proteins[58], fluorescent enzyme substrates for life science[53].

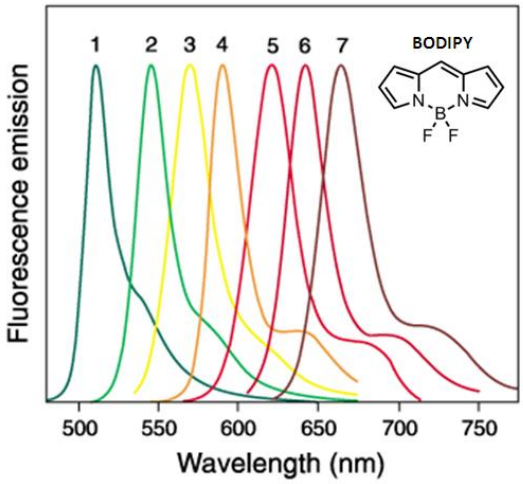



**Figure 1.10** Core structure of the BODIPY fluorophore (inserted) and normalized fluorescence emission spectra of 1) BODIPY FL, 2) BODIPY R6G, 3) BODIPY TMR, 4) BODIPY 581/591, 5) BODIPY TR, 6) BODIPY 630/650 and 7) BODIPY 650/665 fluorophores in methanol(figure adapted from[53]).

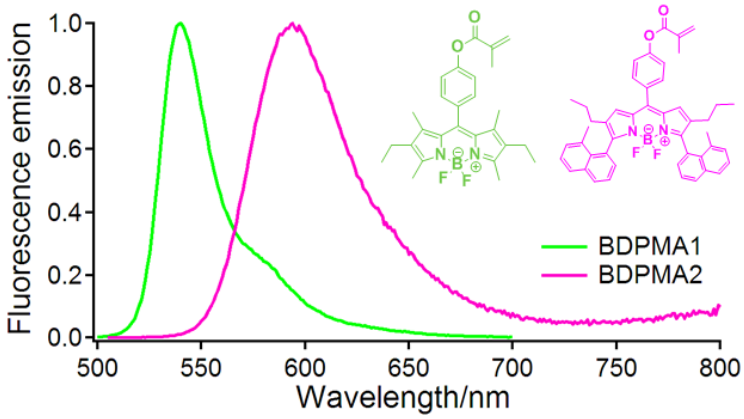



**Figure 1.11** Structures and fluorescence emissions of BDPMA1 (in toluene, $\lambda_{exc}$=495nm) and BDPMA2 (in ethanol, $\lambda_{exc}$=540nm) monomers.

During my research projects, BODIPY was selected as a main fluorophore. Its two methacrylate derivatives (BODIPY methacrylate-1 (BDPMA1), BODIPY methylnaphthalene-2 (BDPMA2)) were developed by Chloé Grazon[27] (**Figure 1.11)**. BDPMA1 emits around 540 nm (green emission) and BDPMA2 emits around 610nm (orange-red emission). The methacrylate group allows BODIPY to be polymerized. We use BDPMA1 to synthesize green core-shell fluorescent nanoparticles[27] and collect thousands of BODIPY fluorophores in one particle. This resulted in incredibly bright and stable nanoparticles. These particles were then tested to insert inside bacteria (**Chapter 2**) or to target the bacterial membrane (**Chapter 3**) for bioimaging application. We have also use BDPMA1 and BDPMA2 to synthesize green or

red fluorescent polymer chains (FPCs). I have determined whether green polymer chains (GFPCs) can enter into *E.coli* bacteria or not and how they localize. I have investigated whether red polymer chains (RFPCs) can label the membrane of *E.coli* bacteria or the cytoplasm or the DNA. Both green polymer chains and red polymer chains biocompatibility have been tested prior to any imaging application. I have done experiments to determine if they can be used for multi-color imaging of bacteria (**Chapter 4**).

Besides the dye families described above, there are also some fluorescent molecules used to target specific cell compartments or to label and distinguish dead and live cells.

*Methylene blue* is a blue fluorescent dye in its oxidized form, its maximum absorption is at 661nm, the maximum fluorescence emission is at 683nm (**Figure 1.12**). In water, methylene blue has a positive charge, and it will bind to DNA of bacteria which is negatively charged[59]. Methylene blue is easily reduced to a colorless form in viable cells leaving them unstained. However, dead cells are unable to reduce methylene blue. Thus stained cells are blue and dead. During my research projects, methylene blue is used to interact with bacteria and fluorescent particles and polymer chains (**Chapter 2**).

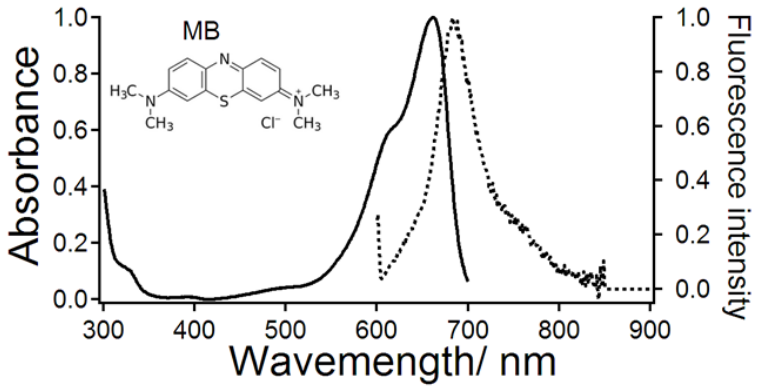



**Figure 1.12** Structure and spectra of oxidized methylene blue in water: absorption (full line), fluorescence emission (dotted line, $\lambda_{exc}$=660nm).

*DRAQ5* is a far-red fluorescent dye that is permeable across the cell membrane and commonly used to stain DNA for fluorescent cellular imaging application[60]. DRAQ5 has two absorption bands at 601nm and 644nm and a maximum emission band at 683nm (**Figure 1.13**). Because of its far-red excitation and emission, DRAQ5 can be multiplexed with many other dyes such as GFP or FITC. During my research projects, the commercial dye DRAQ5 was

used to label bacterial DNA and multiplexed to check the compatibility of green fluorescent polymer chains (**Chapter 4**).

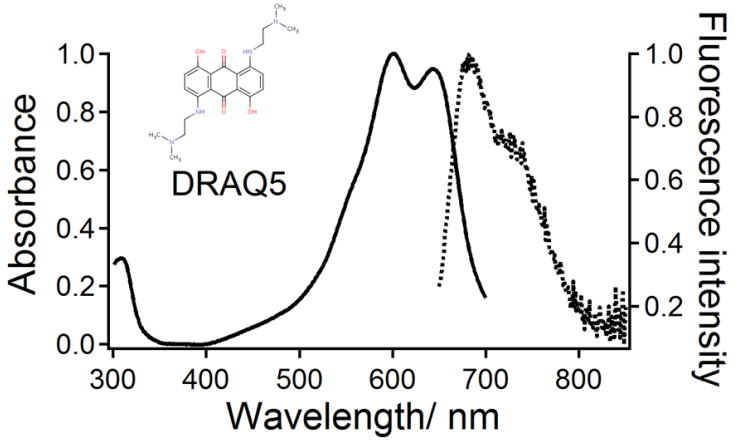



**Figure1.13** Structure and spectra of DRAQ 5 in PBS buffer: absorption (full line), fluorescence emission (dotted line, $\lambda_{exc}$=600nm) - (figure adapted from[61]).

*PKH26* is a yellow-orange fluorescent dye for cell membrane labelling. PKH26 has two absorption bands at 519nm and 553nm and a maximum emission band at 577nm (**Figure 1.14**). PKH26 is compatible with violet, green, red or far-red fluorophores in biological imaging[62,63]. During my research projects, PKH26 was used to label the bacterial membrane and multiplexed to check the compatibility of green fluorescent polymer chains (**Chapter 4**).

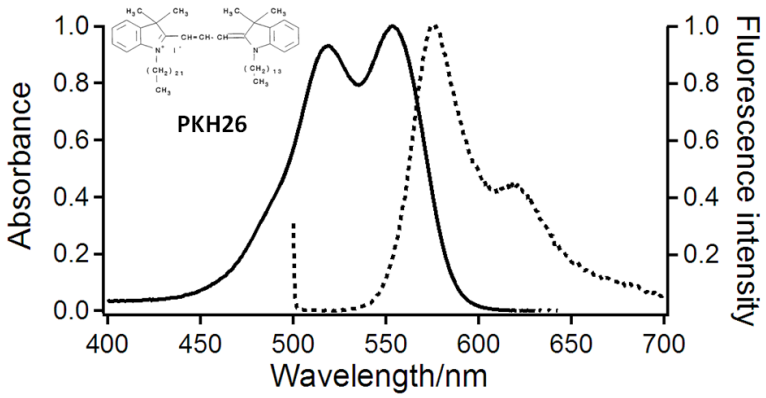



**Figure 1.14** Structure and spectra of PKH26 in PBS buffer: absorption (full line), fluorescence emission (dotted line, $\lambda_{exc}$=500nm).

*Propidium iodide* is a popular red fluorescent dye. Since propidium iodide is not permeant to live cells, it is commonly used to detect dead cells whose membrane has destabilized and become porous. It has a maximum absorption at 238nm and a maximum emission at 317nm when bound to DNA[64] (**Figure 1.15**). During my research projects, propidium iodide was used to detect live/dead *E.coli* bacteria by flow cytometry.

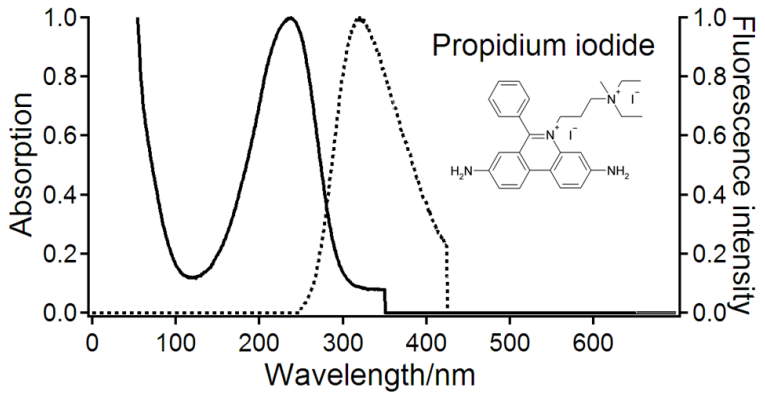



**Figure 1.15** Structure and spectra of propidium iodide bound to DNA: absorption (full line), fluorescence emission (dotted line) (data from life technologies[64]).

After focusing on molecular fluorophores, I will now make a short review about fluorescent proteins.

### 1.3.2 Fluorescent proteins

Fluorescent proteins (FP) are widely used in the life science, especially for probes and labelling in bioimaging applications[65]. The green fluorescent protein (GFP), a naturally fluorescent protein found from the jellyfish *Aequorea Victoria*, was the first in this family to isolated and characterized. The GFP from *A. victoria* has a major excitation peak at 395 nm and a minor one at 475 nm, its maximum emission peak is at 509 nm[66] (**Figure 1.16**). The fluorescence quantum yield of GFP is 0.79. Many green fluorescent proteins variants now have been developed now, scientists can therefore select the suitable FP with different light absorption and fluorescent emission properties[66]. GFP is known as a full genetically encoded label, it has become a unique tool that can provide direct visualization of structures and processes in living cells such as bacteria. Fluorescent proteins are now also available in different colors such as blue (BFP), cyan (CFP), yellow (YFP), red(RFP) fluorescent proteins[67]. The discovery and development of multiple-colored fluorescent proteins has contributed greatly to life science. These achievements were recognized by the 2008 Nobel Prize in Chemistry awarded "for the discovery and development of the green fluorescent protein, GFP"[65] (**Figure. 1.17**).

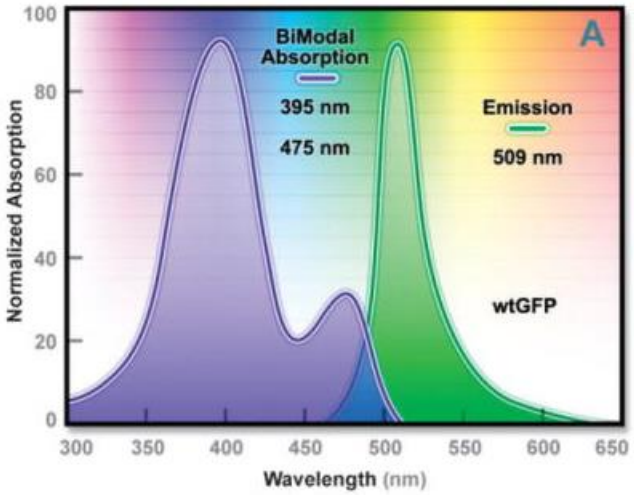



**Figure1.16** Absorption and emission spectra of *Aequorea Victoria* GFP (figure from[68]).

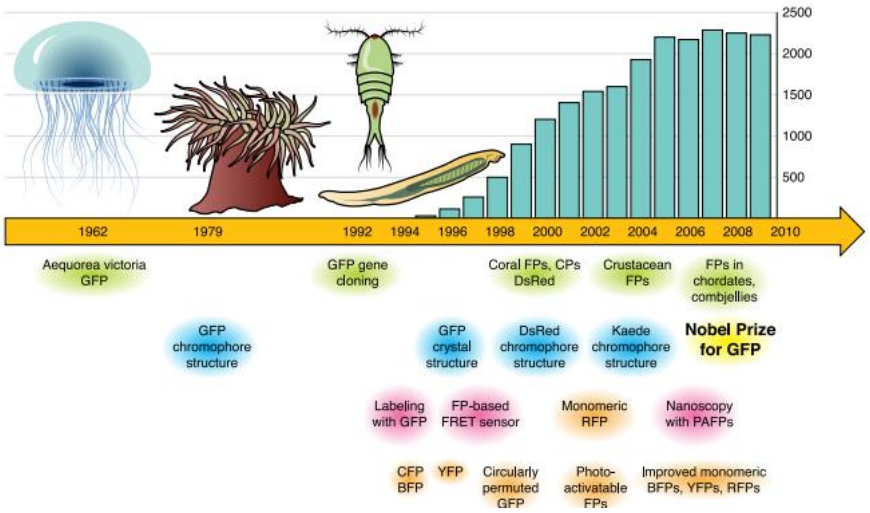



**Figure 1.17** timeline of major achievements in the fluorescent proteins field (figure from[65]).

In fluorescent proteins, the fluorophore lies within the folded protein, the mechanisms of fluorescent protein formation have been described by Miyawaki et al.[69]. The greatest advantage of fluorescent proteins is their heritability. Because of the ability to be co-synthesized and inherited inside the living cells, fluorescent proteins have become a very unique and important tool in living cell imaging[70]. In recent years, GFP and its variants in different colors[67] have been widely used in the study of organization and function of living systems by optical techniques (**Figure 1.18**). Fluorescent proteins encoded to a specific target in cells[71,72], bacteria[73], organisms[74], animals[75] allow for the study of localization, movement, function, mechanisms of this target. For example, fluorescent proteins can be used to label cell organelles, to investigate cell structure, or cell division, and to describe organelles functional process by microscopy[74,76,77]. Fluorescent proteins can also be used to

label bacteria cells and to detect their movements, to study their transient gene expression process[73] and many other important characteristics[78–80]. However, the molecular mass of fluorescent proteins can reach 26-28 kDa, which is relatively large and may interfere with the function and localization of the labelled protein and the interaction with other molecules[22,28,36].

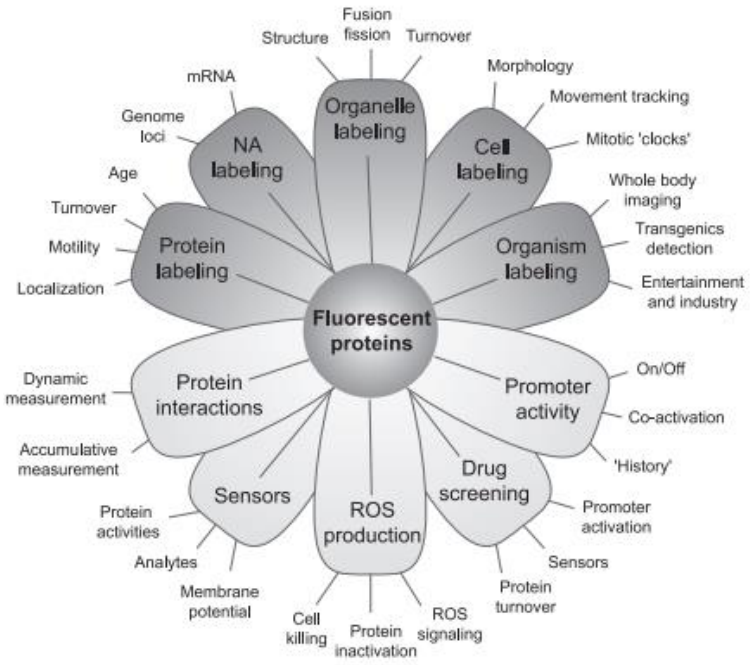



**Figure 1.18** Different areas of applications for fluorescent proteins in life science (figure from[65]).

After describing fluorescent proteins as useful macromolecules for biochemists and biophysicists, I will now focus on larger objects such as fluorescent nanomaterials.

### 1.3.3 Fluorescent nanomaterials

The combination of fluorescence and nanomaterials has developed into an attractive and emerging interdisciplinary research field combining chemistry and photophysics. Nowadays, fluorescent nanomaterials have attracted great interests due to their excellent optical properties including high photostability and high brightness. Furthermore, many developments have already been made to functionalize these nanomaterials to be more biocompatible. Additionally, most of the fluorescent nanomaterials possess tunable excitation and emission wavelength and can be used for multi-color imaging. The combination of these advanced features have made fluorescent nanomaterials to be an important and highly promising tool which can provide new roads of fluorescence imaging

and sensing for *in vitro* and *in vivo* labeling in bacteria, cells, tissues, and whole organisms. In recent years, this approach has been widely used in various areas of biology and medicine, and environmental science. Fluorescent nanomaterials can be generally classified into two categories based on their chemical nature: inorganic fluorescent nanomaterials (e.g. quantum dots,[81–83] silica nanoparticles,[84,85] carbon nanoparticles[86–88] and metal nanoclusters[81,89]) and organic fluorescent nanomaterials (e.g. fluorescent conjugated polymer nanoparticles[90–93], dye-doped polymeric nanoparticles[94–97]). I will focus on several representative fluorescent nanomaterials: quantum dots, silica nanomaterials, and organic polymer nanomaterials to discuss their properties and their biological applications.

The general steps to design functional fluorescent nanomaterials for biosensing and bioimaging are: 1) synthesis; 2) coating; 3) surface functionalization or bioconjugation; 4) biosensing and bioimaging applications[98] (**Figure 1.19)**. Surface functionalization or bioconjugation is required to make the fluorescent nanomaterials more biocompatible and able to label biological targets while at the same time preserving their original properties[99] (**Figure 1.20**). In order to increase the water solubility of fluorescent nanomaterials, different coating techniques can be applied, such as hydrophilic thiol coating, silica coating, amphiphilic polymer coating and coating nanoparticles with polyethylene glycol (PEG) (**Figure 1.20**). Fluorescent nanomaterials can be bioconjugated with biological ligands (e.g. streptavidin, antibody, peptides) in order to make them more biocompatible and also to target biomolecules in cell, bacteria, tissue and living systems (**Figure 1.20**).

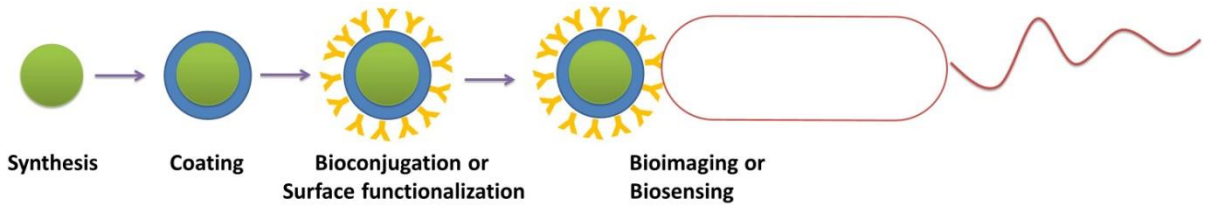



**Figure 1.19** General steps to design functional fluorescent nanomaterials for biosensing and bioimaging.

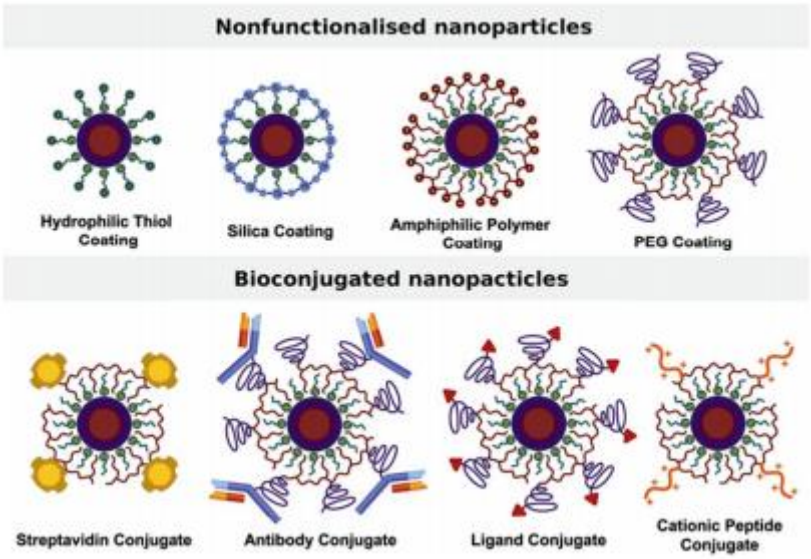



**Figure 1.20** General strategies to make surface functionalization of fluorescent nanoparticles (figure from[98,100])

### 1.3.3.1 Quantum dots

Quantum dots (QD) are semi-conducting nanocrystals. They are particularly small (2-10nm)[28]. The general structure of a QD is displayed in **Figure 1.21**. The semi-conducting materials usually used are CdTe or CdSe to design the inorganic core. A different band gap semiconductor material, for example, ZnS is often used as an inorganic shell. QDs are usually coated by an aqueous organic coating for conjugation of biomolecules[101].

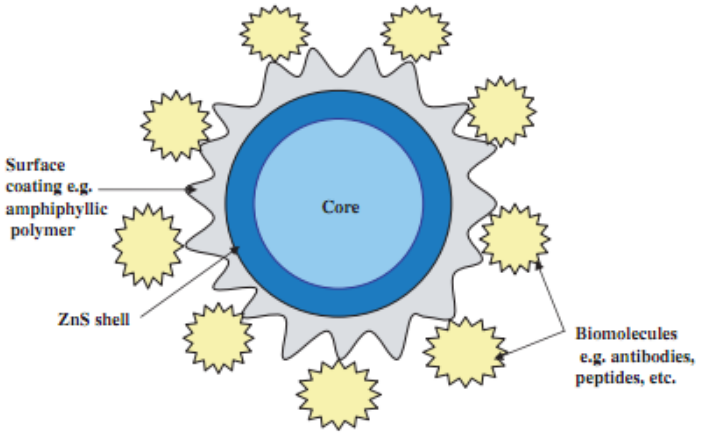



**Figure 1.21** Schematic structure of a quantum dot (figure from[101]).

Nowadays, QDs have become important nanoparticles for biological applications due to their unique optical properties that are unavailable from classical organic dyes and fluorescent proteins. QDs have high brightness, photostability, high quantum yield, and

narrow emission. Their emission of light covers the visible and near infrared range[102,103]. In comparison with organic dyes, QDs have similar quantum yields but extinction coefficients that are 10−50 times greater and significantly more reduced photobleaching rates[98,104].

When increasing the QDs size, their band gap decreases, this will shift their emission spectrum to longer wavelengths. The bigger the QDs, the more red shifted the QDs is[105]. By synthesizing QDs of different sizes, scientists can obtain required emission wavelength. QDs' luminescence covers almost the entire visible spectrum extending to the near infrared range (**Figure 1.22**).

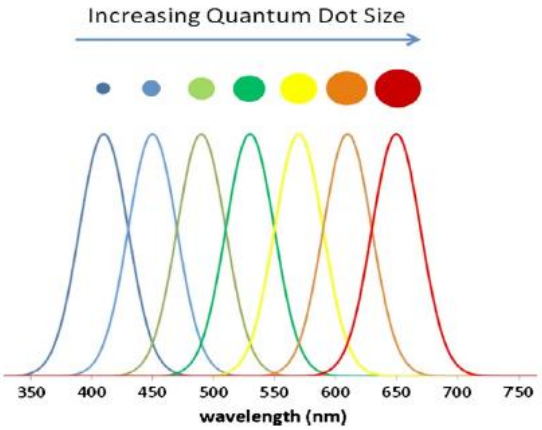



**Figure 1.22** Increasing the size of QDs resulted in a redshift in the fluorescence emission (figure from[105])

Because of their high brightness, QDs are ideal for imaging. Biological ligands such as peptides[106] and antibodies[107] are usually conjugated to the surface of the QDs for labelling of specific targets (**Figure 1.23**). Advanced applications of QDs include using QDs as fluorescent labels for intracellular sensors[108], cellular labeling [109–114], deep-tissue and tumor targeting and imaging agents [100,107,115,116].

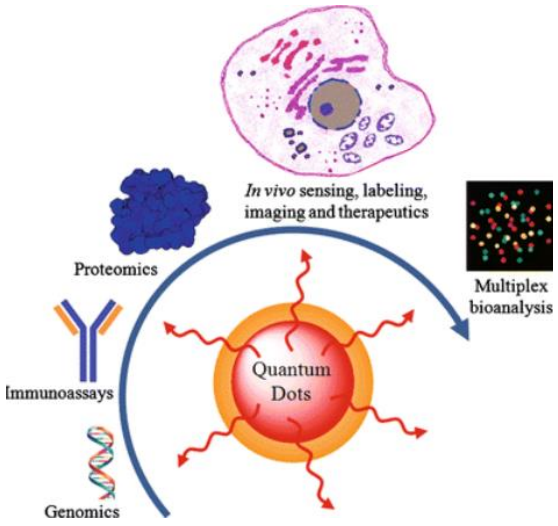



**Figure 1.23** Bioanalytical applications of bio conjugated QDs (figure from [117]).

QDs have been widely used for imaging applications in bacteria[118–120]. Sulatha Dwarakanath et al. demonstrated that CdSe/ZnS QDs exhibited fluorescence emission blue shifts when conjugated to antibodies that are bound to bacteria. The wavelength shift might be because of changes in the chemical circumstance of the antibody conjugated QDs when bound to the bacterial surface [121]. Fluorescent CdSe/ZnS QDs were used for super-resolution fluorescence microscopy on *Shewanella oneidensis* bacteria (**Figure1.24**). Experiments show that after 1.5 hour incubation, amino-poly(ethylene glycol) surface functionalized QDs clusters of a size of 10-15 nm are associated with the bacterial cell surface. They partially penetrated inside bacterial membrane. The reason why the QDs can't be internalized inside bacteria is perhaps due to the relatively large size of the particle or the lack of pathways of the bacterial rigid cell structure.[122]

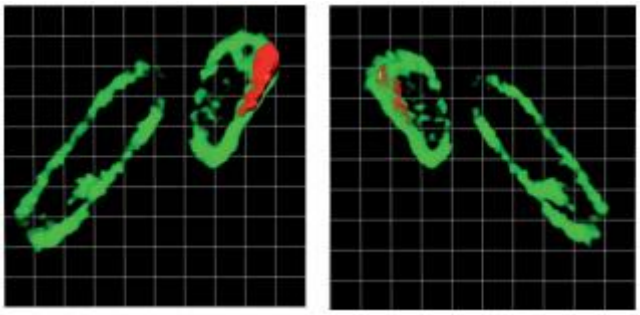


**Figure 1.24** Structured illumination microscopy (SIM) images of *Shewanella oneidensis* bacteria with associated amino-PEG QDs, each square has side length 0.42 µm (figure from[122]).

In comparison with traditional organic dyes, QDs are more photostable and brighter, however, the drawbacks such as irreproducibility, toxicity issues, blinking and complex

fluorescence decays are to be considered when developing fluorescent labels with QDs[22]. Thus chemists developed silica-based NPs which have less toxicity and higher fluorescence stability.

### 1.3.3.2 Silica-based nanoparticles

Another type of fluorescent nanomaterial which has been extensively developed for fluorescent labelling and bioimaging is silica nanoparticles. Generally speaking, silica provides a stable vehicle to protect the encapsulated fluorophores from external perturbations[123]. The silica nanoparticles matrix is capable of encapsulating a variety of fluorescent agents such as inorganic dyes[124–126], organic dyes[127–129] (**Figure 1.25**), QDs and metal NPs without affecting their spectral features[98,124,130].

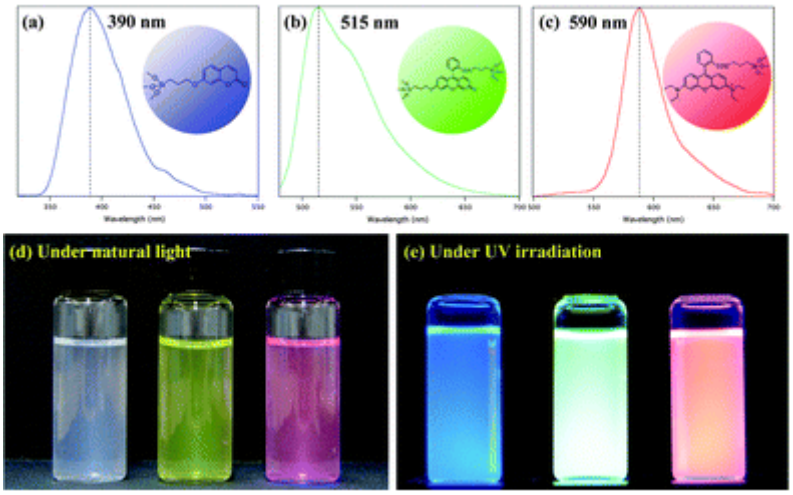



**Figure 1.25** Fluorescence emission spectra and photographs of organic dye-incorporated silica nanoparticle(50nm) in water (figure from[129]).

Silica nanoparticles have attracted great interests due to their unique properties such as abundant, nontoxic, optical transparency. Furthermore, the ability to capture a large amount of fluorescent dye molecules together in one particle resulted in high brightness, and the silica vehicle can protect fluorophores from molecular oxygen resulting in improved stability. At the same time, the surface of silica nanoparticles can be efficiently conjugated with different biomolecules for biological analytical purpose.

Nowadays, this newer class of fluorescent nanomaterial with high photostability and sensitivity compared with traditional organic dyes has been developed intensively for fluorescent labeling and sensing in life science such as DNA hybridization analysis,[126,128] drug

delivery,[131] nucleic acid analysis,[132] antibodies,[133] cells,[134] multiplexed bioanalysis,[135] bacteria[136,137]. Anti-bacterial antibody can be conjugated on the surface of silica nanoparticle and be used to detect bacteria[138–140]. Weihong Tan and his team[139] demonstrated that *Escherichia coli* O157:H7 can be readily and specifically labeled by fluorescent silica nanoparticles doped with Rubpy and conjugated with anti-*E.coli* antibody. The bioconjugated silica nanoparticle provides an extremely high fluorescent signal which can be used for bioanalysis (**Figure 1.26**).

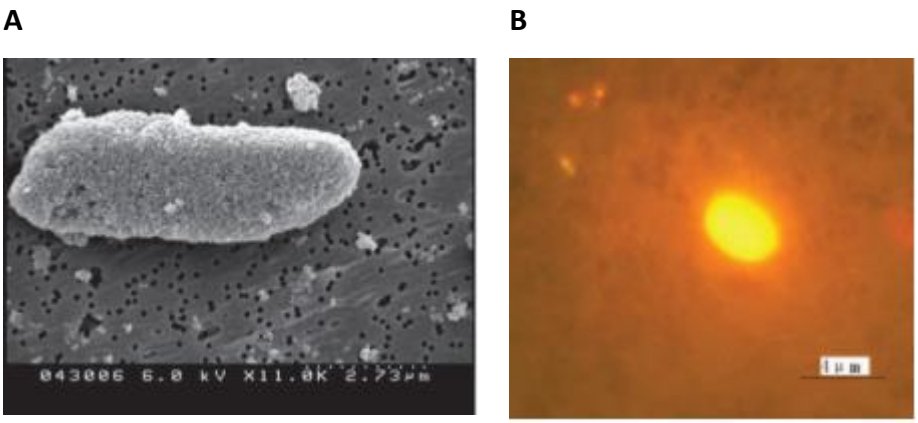



**Figure 1.26** Images of *E.coli* O157:H7 cells. A: SEM image of *E.coli* O157:H7 coated with antibody conjugated silica nanoparticles. B: Fluorescence image of *E.coli* O157:H7 after incubation with antibody conjugated silica nanoparticles (figure from[139]).

Recently, multi-shell silica nanoparticles have also been developed for multi-functional purpose in drug delivery and fluorescent labeling applications. For example, the multi-shell architecture displayed in **Figure 1.27** is formed with a gold nano shell for near infrared plasmon imaging and a silica outer shell for drug delivery. By varying the chemical properties of each layer, this kind of particle can be used for different tasks such as drug delivery, bioimaging and sensing[141].

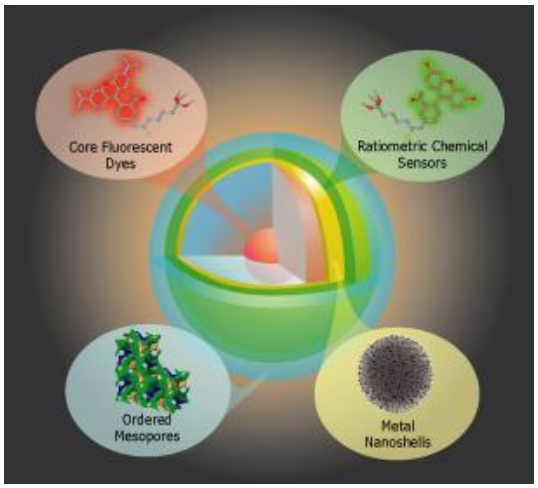



**Figure 1.27** multi-shell architecture of silica nanoparticle applications (figure from[141]).

Compared with conventional organic dyes, silica nanoparticles are more hydrophilic, biocompatible and more stable. However, silica particles also have some drawbacks, such as particle aggregation[142] and organic dyes spill-over from particles[36] that may limit their applications.

Although inorganic nanomaterials have been intensively developed for fluorescent imaging *in vitro*, the potential bioincompatibility of the inorganic nanomaterials have hindered the development of their practical applications for imaging *in vivo*[143–145]. Nowadays, the U.S. Food and Drug Administration(FDA) has only approved one inorganic nanomaterial: the nonporous silica nanoparticle for the phase I clinical trial[146]. In contrary, organic fluorescent nanomaterial imaging agents are obtained from organic molecules that are less toxic. Furthermore, in order to develop organic materials, there are already many FDA-approved biocompatible molecules, such as the fluorescent dye indocyanine green (ICG) [147] and the biodegradable polymers poly(methyl methacrylate) (PMMA), poly(lactic acid) (PLA), poly(lactic-co-glycolic acid) (PLGA) derivatives and poly(ethylene glycol) (PEG)[148]. In the next section, I will discuss the organic fluorescent nanomaterials.

### 1.3.3.2 Organic polymer nanoparticles (OPNs)

It is well known that the major problem with traditional organic dyes is their poor photostability, this major drawback results in low sensitivity for biological labeling and sensing studies. Fluorescent nanomaterials are brighter and more photostable compared with classical organic dyes. This is because every nanoparticle can carry a large number of

fluorescent species which are insulated by the particle matrix. Indeed this matrix can protect enfolded fluorophores from complex environment. Moreover, the large surface to volume ratio of nanoparticles offers a suitable platform for surface modification and bioconjugations[149].

Organic fluorescent nanomaterials attract great attention for fluorescent labelling and sensing technologies because of their high brightness, high photostability, abundant surface modification and easily bioconjugation, and most importantly low toxicity for living systems. During my research project I found that all the fluorescent organic nano-objects used for fluorescent labeling and sensing are nontoxic for bacterial growth and can be used for live bacterial imaging applications.

The principle of design for any fluorescent organic polymer nanoparticles is the same: gathering as many fluorohores as possible together in one nano-object. Unlike single organic dye such as FITC or rhodamine, each organic nano-object can contain thousands of embedded fluorophores that are encapsulated in a polymer shell and protected from the outside environment. Because of the high number (up to thousands) of dye molecules incorporated into one single particle, organic polymer particles are much brighter than individual organic molecules. At the same time, since they are encapsulated, fluorophore molecules are protected from outside environment and less affected by the external environment and are more stable (less photobleaching or blinking as well)[150]. Bioconjugation of various biological functional groups such as biotin, avidin, antibody, antigenic peptides, to the surface of polymer nanoparticles allow for their labeling of cells, tissues, organisms, bacteria and other living systems (**Figure 1.28**).

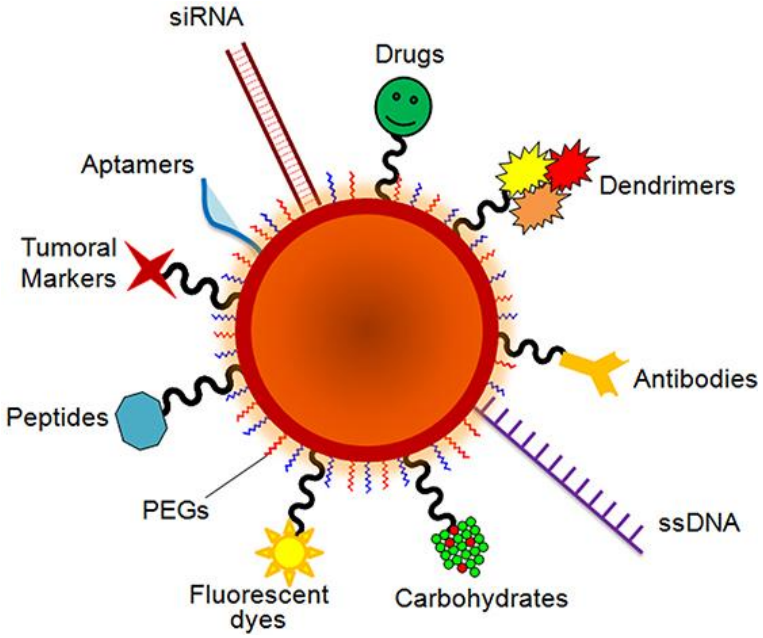



**Figure 1.28** Organic polymer nanoparticles with multifunctional bioconjugations (figure adapted from[151]).

Organic polymer nanoparticles are known as highly versatile nanostructured materials. As we discussed above, the advantages of organic polymer nanoparticles includes high brightness, high photostability, high quantum yield, low toxicity, and rich surface modification. In order to prepare organic polymer nanoparticles, there are several methods available: macro-/micro-/miniemulsion, precipitation, self-assembly, direct polymerization. Each of them will be described below.

***Methods of synthesize organic polymer nanoparticles***

Landfester and co-workers have synthesized organic polymer nanoparticles by the miniemulsion method[152,153] (**Figure 1.29**). To prepare organic polymer nanoparticles, the polymer is dissolved in an organic solvent and then the solution is injected into an aqueous solution of an appropriate surfactant[154]. The mixture is then rapidly stirred by ultrasonicating to generate stable miniemulsion which contains small droplets of the polymers. Finally, the organic solvent is evaporated and leaving a stable dispersion of polymer nanoparticles in water. Depending on the polymer concentration, the size of this kind of particle can vary from 30 to 500 nm[155].

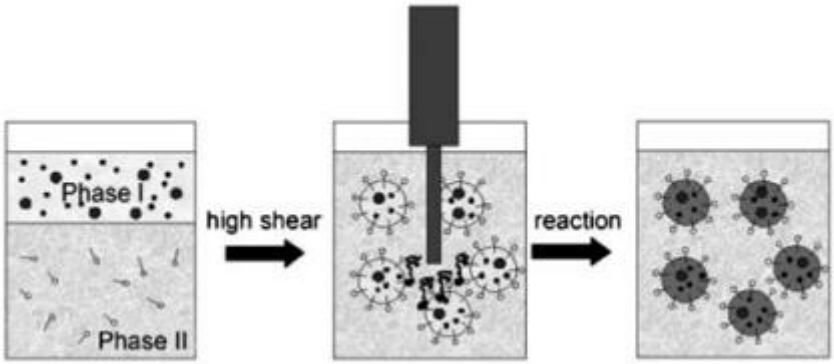



**Figure 1.29** Preparation of polymer nanoparticles by the miniemulsion method (figure from [155]).

During precipitation, hydrophobic conjugated polymers are dissolved in a good solvent such as THF, and then the mixture is poured into a poor solvent such as water which is miscible with the good solvent (**Figure 1.30**). The main force for the formation of the nanoparticles is the hydrophobic effect. When the solution of polymer in good solvent is added into the water, polymer chains tend to avoid facing with water and fold into spherical shapes in order to achieve minimum exposure to water. The solution is also stirred powerfully with a sonicator to help the formation of nanoparticles[155]. The particle diameter is dependent on the starting concentration of the conjugated polymers[156,157]. Higher polymer starting concentration will result in larger particle diameter.

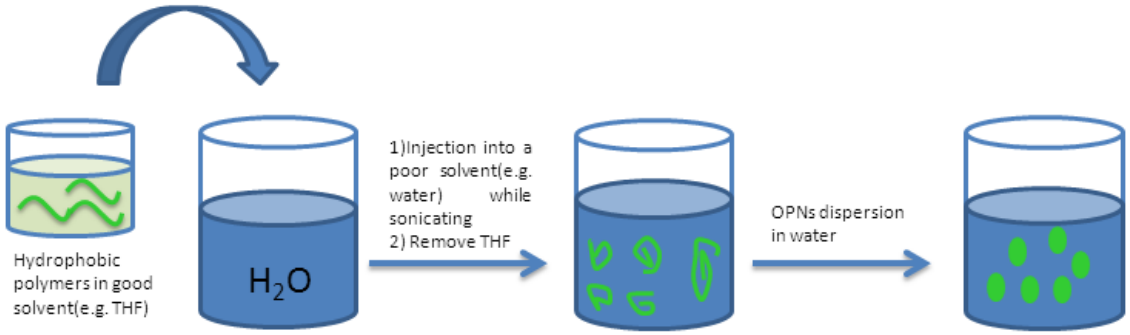



**Figure 1.30** Preparation of polymer nanoparticles by the reprecipitation method.

In self-assembly process, amphiphilic polymers are used. These polymers contain a hydrophobic part and a hydrophilic part such as PEG or PAA which is responsible for the increase in the particles' solubility and allow further biofunctionalization. The hydrophobic part (for instance polystryrene) might be fluorescent thanks to the copolymerization or encapsulation of fluorophores (such as BODIPY and FITC). When these amphiphilic polymers are facing with aqueous solution, they form a core-shell structure nanoparticle. The hydrophobic part is the core and hydrophilic part is the shell (**Figure 1.31**).

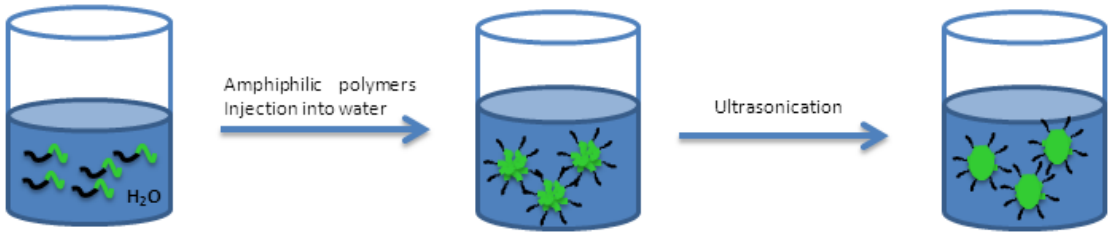



**Figure 1.31** Schematic preparation of polymer nanoparticles by the self-assembly method.

In direct polymerization, monomers and organic dyes are dissolved in the organic solvent, and then the mixture is added into the aqueous solution with an emulsifier. With ultrasonification, stable and small oil droplets will be formed inside the mixture solution. After adding initiators into the emulsion, monomers in oil droplets will start the polymerization to obtain organic nanoparticles dispersion (**Figure 1.32**)[158,159] .

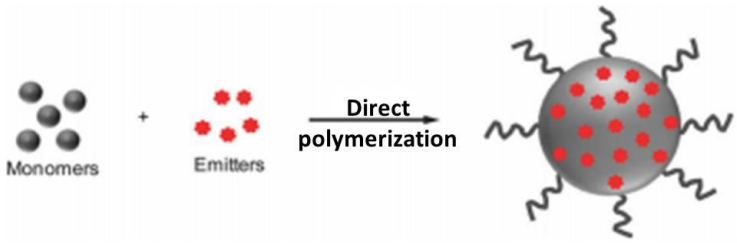



**Figure 1.32** Schematic preparation of polymer nanoparticles by direct polymerization (figure adapted from[160]).

***Fluorescent labelling and sensing applications***

After a brief description of the methodologies of preparation of organic polymer nanoparticles, I will describe the main applications of these ONPs for fluorescent labelling and fluorescent sensing.

As I have described before, due to their biocompatible natures, organic polymer nanoparticles have relatively low cytotoxicity compared with inorganic nanoparticles. Small organic polymer nanoparticles can be internalized by living cells through the process of endocytosis without extra modification of the particle surface or addtional technologies. Various fluorescent organic nanoparticles have been used to label cells including fluorescent conjugated polymer nanoparticles[90–93], self-fluorescent biodegradable nanoparticles[161], dye-doped polymeric nanoparticles[94–97]. Moon, J.H. et al.[162] demonstrated that conjugated polymer nanoparticles generated by using an amine containing poly(p-phenylene ethynylene) (PPE) can be used to perform live cell imaging. Different cells including baby-hamster kidney (BHK) and BALB/C 3T3 (mouse embryonic fibroblast) were incubated with conjugated polymer nanoparticles for different times varying from one hour to several days in culture

media to study the cell permeability, cellular toxicity and photostability of conjugated polymer nanoparticles. Microscopy images of live BALB/C 3T3 (a) and fixed 3T3 cells (b) stained by the conjugated polymer nanoparticles overnight are shown in **Figure 1.33**. The images show that the conjugated polymer nanoparticles were cell permeable without any inhibition of cell viability and can accumulate particularly in the cytosol. Furthermore, compared with commercial dyes, conjugated polymer nanoparticles possess high resistance to photobleaching[162].

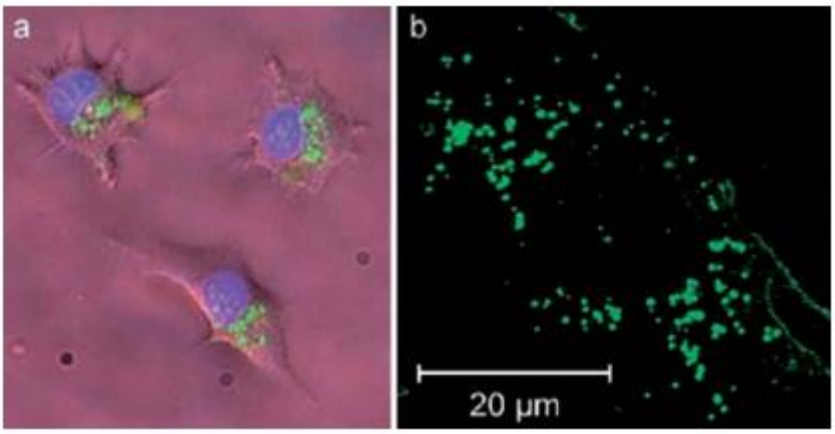



**Figure 1.33** Fluorescence images of live (a) and fixed (b) cells. (a) BALB/C3T3 cells were incubated conjugated polymer nanoparticles (green) and Hoechst dye (blue). (b) Fixed BALB/C 3T3 cells for confocal microscopy[162].

Organic polymer nanoparticles can also be used to coat the bacterial surface to form bacteria-nanoparticle microparticles to perform multiplex biological imaging and analysis. Wang and co-workers[163] prepared four different colored conjugated polymer nanoparticles (P1 blue, P2 green, P3 yellow and P4 red) with diameters from 50 to 100 nm. By electrostatic and hydrophobic interactions, *E. coli* bacteria were coated with particles. These fluorescent organic nanoparticles were bounded to the outer membrane of *E.coli*. Under excitation from a single wavelength, multi-step intermolecular FRET processes between these particles occurred. By monitoring the proportions of P1, P2, P4 on *E. coli* bacteria, different colored bacteria-nanoparticle microparticles can be obtained (**Figure 1.34**).

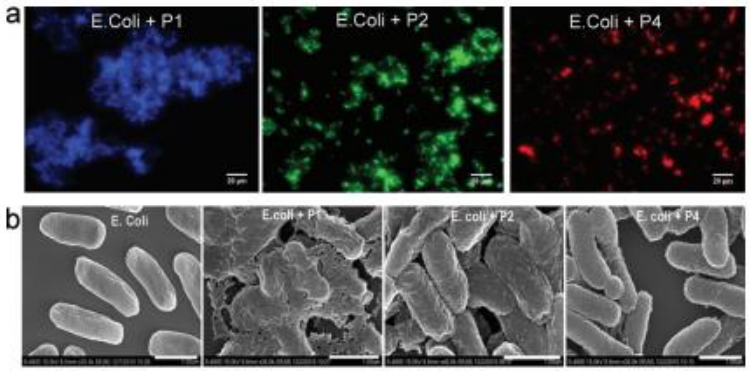



**Figure 1.34** (a) Fluorescence microscopy images of coating conjugated polymer nanoparticle on *E. coli* to form microparticles (b) SEM images of *E. coli* alone and *E. coli* microparticles (figure from[163]).

Because of their nontoxic properties, organic polymer particles can be used not only for cell imaging but also for drug delivery[164,165]. Interestingly, multifunctional nanoparticle-bacteria system can be developed for drug delivery and loading which open up new strategies for drug delivery application[166]. Additionally, organic polymer nanoparticles which are used as antibiotics drug nanocarrier have recently been developed thanks to the versatile functional possibilities. Omid C. Farokhzad and his group[167] developed a drug-encapsulated, pH-responsive, surface charge-switchable PLGA-PLH-PEG (poly(D,L-lactic-co-glycolic acid)-b-poly(L-histidine)-b-poly-(ethylene glycol)) nanoparticles system for bacterial infections therapy (**Figure 1.35**). These nanoparticle drug carriers are negatively charged and they are designed to switch their surface charge to positive and bind strongly to the bacterial membrane which is negatively charged in an acidic environment and deliver drugs to bacteria with decreasing pH. These PLGA-PLH-PEG NPs are considered to be the first step for developing drug carriers systemically which can target and potentially treat bacterial infections associated with acidic activity[167].

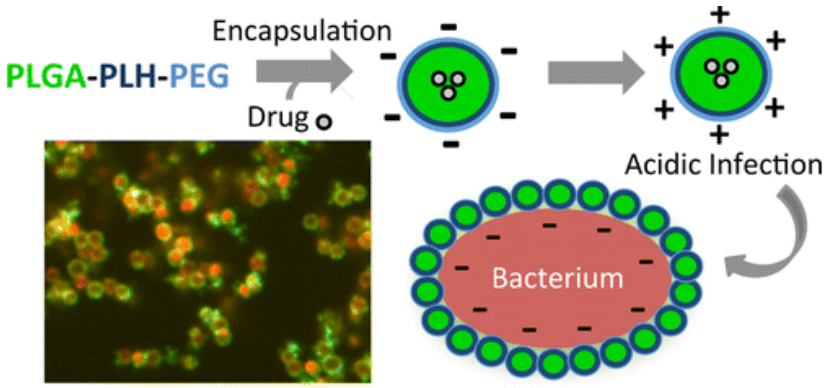



**Figure 1.35** Drug-encapsulated, pH-responsive, surface charge-switchable PLGA-PLH-PEG nanoparticles system for bacterial infections therapy (figure from[167]).

Besides electrostatic interactions between organic polymer particles and bacteria, bioconjugation of the particles surface with various biological functional groups such as avidin, biotin[168] and antibodies[169,170] allows them to target the bacterial surface for various biological applications. The surface of polystyrene (PS) beads can be coated by antibody[171–173] or streptavidin[174]. Rashid Bashir and his group[174] have used streptavidin-coated nanoparticles which can bind with a biotinylated-antibody to target bacteria in order to form a bacteria cargo for tracking and drug delivery application as displayed in **Figure 1.36**. David H. Gracias and his team[171] developed a two-antibody-based technique to attach and release bacteria to polystyrene beads (around 500nm) to form bacteria cargo from patterned surfaces. Polystyrene beads were coated with FITC-labeled bacteria-capturing antibody and were bound to a second antibody which is stabilized on gold patterns. These PS beads can be used to capture *E.coli* bacteria (**Figure 1.37 left**). The bacteria–nanoparticle cargo can be released on-demand from the gold patterns with imidazole or EDTA, and these motile bacteria are observed to propel their cargo swimming in growth media (**Figure 1.37 right**).

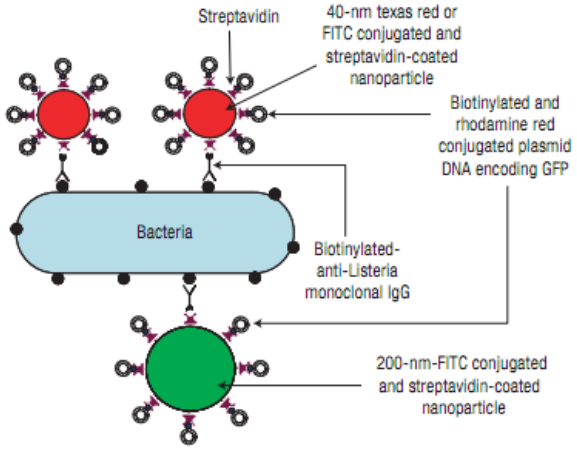



**Figure 1.36** Streptavidin conjugated nanoparticle to form bacteria-nanoparticles cargo (figure from[174]).

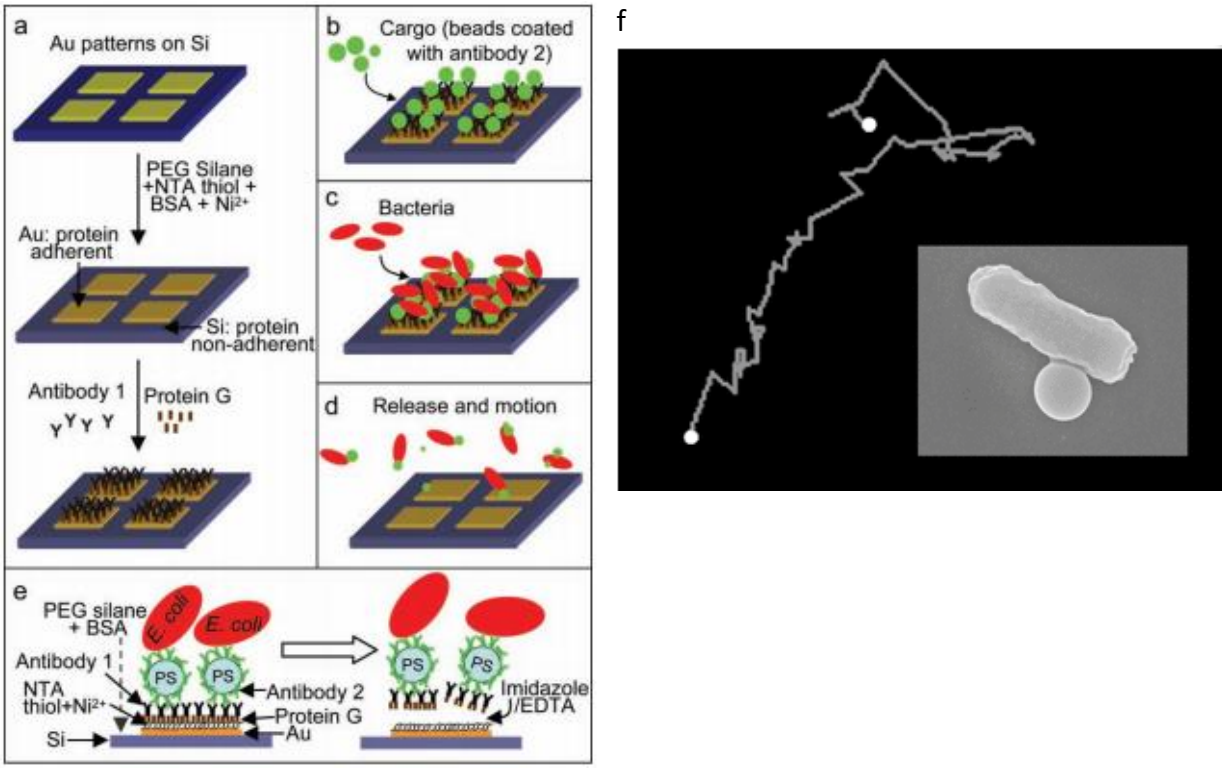



**Figure 1.37** Two-antibody-based techniques to attach and release bacteria by polystyrene beads to form bacteria cargo from patterned surfaces. a) Au-patterned Si substrate. b) Cargo beads coated with anti-*E.coli* antibody can bind to second antibodies on the Au patterns. c) PS beads capture *E.coli* bacteria d) bacteria–nanoparticle cargo released on demand from the gold patterns with imidazole or EDTA. e) Schematic showing bound and released cargo-carrying bacteria. f) a single bacteria–PS bead and its tracking in solution (figure from[171]).

Organic polymer nanoparticles can also be used for bacterial detection and monitoring bacterial growth. The growth of bacteria is often associated with a pH decrease of the growth medium due to a release of acidic metabolites such as acetic acid, lactic acid and $CO_2$. Different kinds of organic nanoparticles pH sensors have therefore been used to measure the growth of bacteria based on this principle[175,176]. Bhawana Thakur et al.[175] demonstrated that a polyaniline nanoparticle based colorimetric pH sensor could monitor bacterial growth. Polyaniline is highly sensitive to the presence of protons and it will change from blue to green visible color. In this work, polyaniline nanoparticles were synthesized and incorporated in agarose gel to form sensor film. The films were then used for real time monitoring for bacterial growth and exhibited a visible color change from blue to green as shown in **Figure 1.38**.

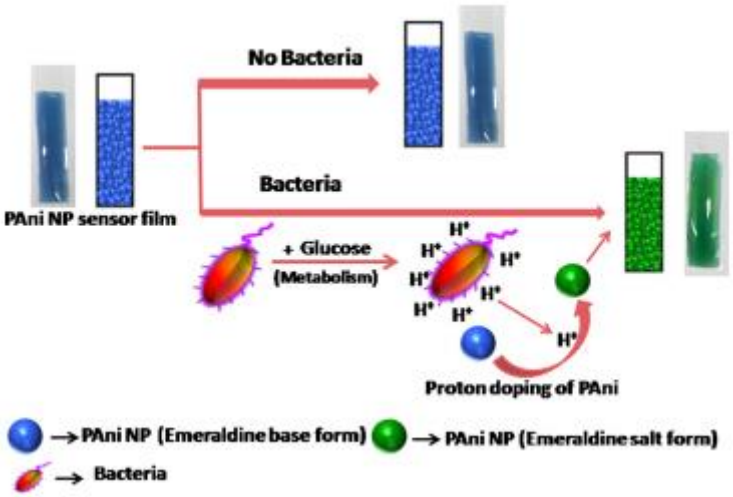
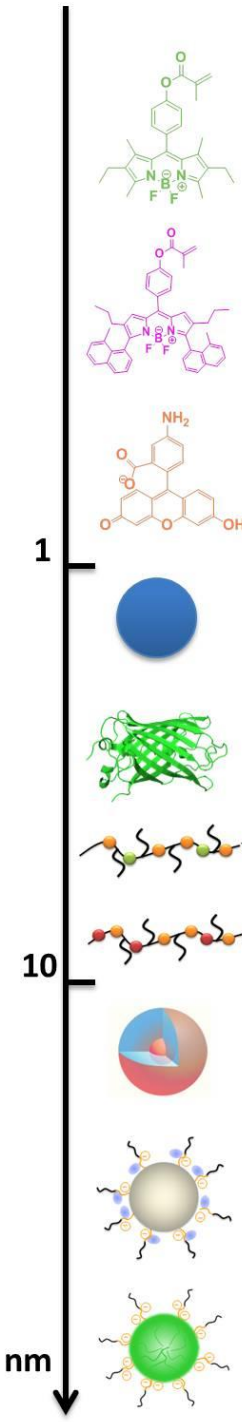



**Figure 1.38** Representation of the mechanism for monitoring bacterial growth by polyaniline nanoparticles based colorimetric sensor (figure from[175]).

## 1.4 Novel fluorescent nanomaterials for bioimaging and biosensing: application on *E.coli* bacteria

In the quest for very bright and stable labels, we envisioned the design and characterization of novel polymer-based, self-stabilized, fluorescent nanoparticles (FNPs, 60nm) and fluorescent polymer chains (FPCs, 5nm). The main structure of these fluorescent organic nanomaterials are shown in **Figure 1.39 f, g, i, j**. They are compared with single organic dyes which were used to form these nanomaterials (**Figure 1.39 a, b, c**) and common fluorescent labels which have been described in last section such as: GFP, QDs, dye doped silica nanoparticles (**Figure 1.39 e, d, h**). I have used these nanomaterials to study the internal and external bioimaging and biosensing application on *E.coli* bacteria, the strategies are generally shown in **Figure 1.40**.




| | Label | $\lambda_{nm}$ | $\Phi_F$/% | B /$10^3$ $M^{-1}$ $cm^{-1}$ | Size |
|---|---|---|---|---|---|
| a) | BDPMA1 | 528 | 70 | 51 | <1 |
| b) | BDPMA2 | 558 | 53 | - | <1 |
| c) | Fluoresceinamine | 494 | 79 | 70 | <1 |
| d) | QDs/CdSe | 470-660 | ~90 | 60-600 | 2-10 |
| e) | GFP | 509 | ~70 | 39 | <10 |
| f) | GFPC$^-$ | 528 | 20 | 30 | 4-6 |
| g) | RFPC$^-$ | 553 | 10 | - | 4-6 |
| h) | Silica nanoparticle | 470-660 | - | - | <100 |
| i) | FANP1 | 488 | 12 | $10^3$ | 73 |
| j) | FNP$^-$ | 529 | 36 | $10^4$ | 65 |

**Figure 1.39** Main structures of fluorescent organic nanomaterials and their comparison. a) BDPMA1 (BODIPY methacrylate-1), b) BDPMA2 (BODIPY methylnaphthalene-2), c) FA (Fluoresceinamine[27,177]), d) QDs (Quantum dots[28,178]), e) GFP (Green fluorescent proteins[179]), f) GFPC$^-$ (negative Green fluorescent polymer chains), g) RFPC$^-$ (negative Red fluorescent polymer chains), h) Silica nanoparticle[141], i) FANP1 (fluoresceinamine based fluorescent pH-sensitive nanoparticles), j) FNP$^-$ (negative Fluorescent nanoparticles).

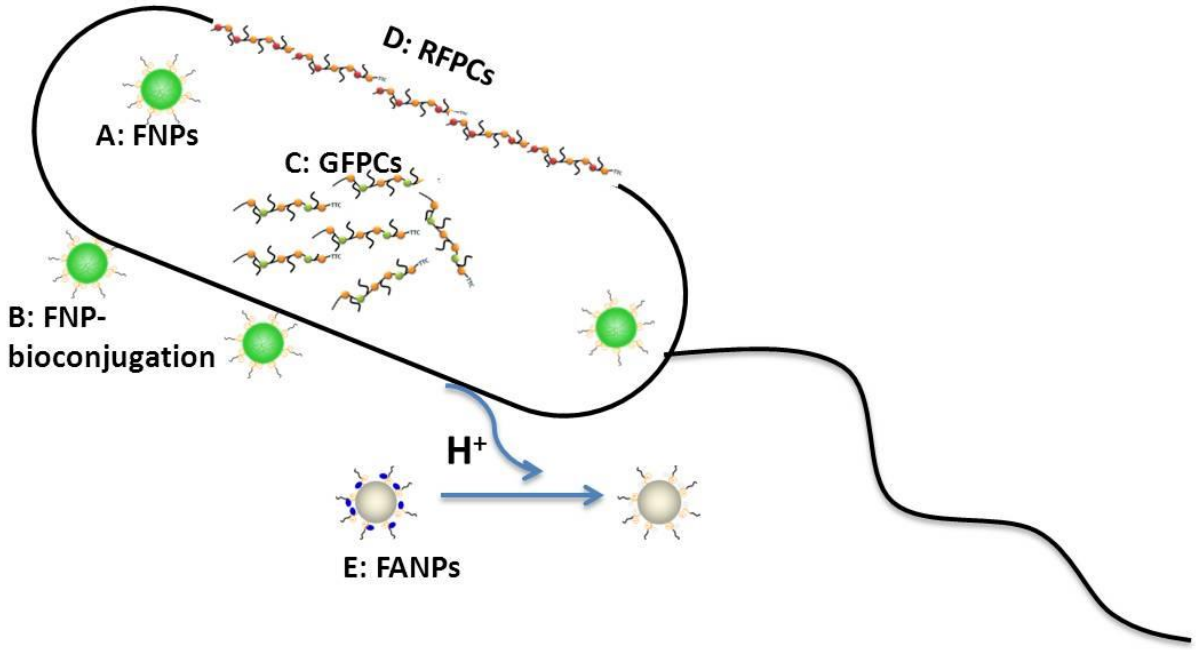



**Figure 1.40** Scheme of the envisioned fluorescent nanomaterials for bioimaging and biosensing: application on *E.coli* bacteria. (A) FNPs: Fluorescent nanoparticles. (B) FNP-bioconjugation. (C) GFPCs: Green fluorescent polymer chains. (D) RFPCs: Red fluorescent polymer chains. (E) FANPs: Fluorescent pH-sensitive nanoparticles

The core-shell structure fluorescent nanoparticles were synthesized and characterized by Chloé Grazon[27], a former PhD student in PPSM (CNRS UMR8531) laboratory. One particle is formed with around 1750 amphiphilic self-assembled polymer chains bearing about one to two BODIPY per chain. Thus about 3000 BODIPY fluorophores are inside the core, this resulted in very high brightness. These FNPs are also stable and photobleach slowly due to the protection of fluorophores in the hydrophobic core. Thanks to the poly-acrylic acid groups all around the particle, it can be functionalized easily with biomolecules such as biotin and antibodies.

These FNPs are an ideal tool for biolabeling and bioimaging applications in life science due to their high brightness, high photostability and rich surface functionalization ability. In order to investigate the biological applications of FNPs on *E.coli* bacteria, different strategies have been developed as shown in **Figure 1.40**. One strategy is to internalize fluorescent nanomaterials (**Figure 1.40A:** FNPs, **C:** GFPCs, **D:** RFPCs) in *E.coli* bacteria, and investigate which part of bacteria is labeled (or not). The second idea is that we can conjugate biomolecules on the surface of the particles to target the bacterial membrane (**Figure 1.40B:**

FNP-bioconjugation). The third strategy is that fluorescent nanoparticles can be used as pH-biosensor to detect the growth of bacteria for biosensing application (**Figure 1.40E:** FANPs).

In this manuscript I described the investigation of the biocompatibility of FNPs on *E.coli* bacteria. I will describe a methodology to insert the described FNPs (**Figure 1.40A**) into *E.coli* bacteria. To control if the FNPs are indeed internalized, I developed a protocol based upon FNPs luminescence quenching by methylene blue (see **Chapter 2**).

I then performed bioconjugation of biotin to FNPs (**Figure 1.40B**). Biotin conjugated FNPs can target bacteria surface membrane. By using a streptavidin-biotin link, I can obtain a "sandwich" to build a bridge between particles, specific antibodies and bacteria. SPR, fluorescence images and SEM images have been used to demonstrate the interaction of biotin conjugated FNPs with *E.coli* bacteria. An antibody specific to the bacterial outer membrane can also be conjugated on the particle surface, I will describe how we can use these antibody coated FNPs to target bacteria (see **Chapter 3**).

We also have designed green fluorescent polymer chains (GFPCs, **Figure 1.40C**) which are much smaller compared with FNPs. I have studied whether they can enter into *E.coli* bacteria or not. I have tried to answer several questions such as: Are these polymer chains toxic to bacteria? Can these GFPCs label the cytoplasm or the DNA of bacteria? Are these polymer chains compatible with other commercial dyes? At the same time, we have also recently prepared red fluorescent polymer chains (RFPCs, **Figure 1.40D**). I have investigated the interaction of these RFPCs with *E.coli* bacteria, to study which part of the bacteria they label (see **Chapter 4**).

More recently, fluoresceinamine based fluorescent pH-sensitive nanoparticles (FANPs, **Figure 1.40E**) are used to measure the presence of *E.coli* bacteria growth. I will show how bacteria influence the fluorescence intensity of FANPs after incubating *E.coli* bacteria with pH sensitive FANPs. I have demonstrated that these FANPs can be used for a rapid, accurate, reproducible and highly sensitive detection of *E.coli* bacterial growth. I will show that such FANPs can be used for continuous monitoring for real-time detection in long time scales and can be used for screening of a large number of samples for high-throughput applications (see **Chapter 5**).

After a general introduction, I will describe in details the interation of these fluorescent nanomaterials with *E.coli* bacteria and the bioimaging and biosensing applications of them on bacteria in following chapters. Now, I will begin with fluorescent nanoparticles (FNPs) in chapter 2, I will show you three different fluorescent nanoparticles and the methology to insert them inside bacteria for internal bioimaging of *E.coli*.

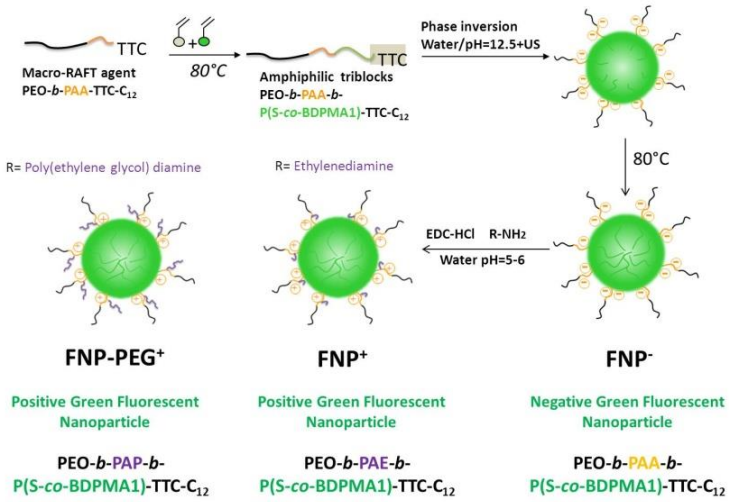
# Chapter 2 Fluorescent nanoparticles (FNPs) for internal bioimaging of *E.coli* bacteria

In this chapter, I will present three different fluorescent nanoparticles: one negatively charged ($FNP^-$) and two positively charged fluorescent nanoparticles ($FNP^+$ and $FNP\text{-}PEG^+$). I will discuss their photophysical characterizations and use for internal bioimaging of *E.coli* bacteria.

## 2.1 Synthesis of fluorescent nanoparticles (FNPs)

The synthesis of the fluorescent nanoparticles presented here has been optimized by Dr. Chloé Grazon[180]. The one-pot synthesis is based on a reversible addition-fragmentation chain-transfer (RAFT) polymerization in miniemulsion conditions using a surfactant-free one-pot phase inversion process (**Scheme 2.1**)[180].

Briefly, the particles are obtained from a hydrophilic chain PEO-*b*-PAA (poly(ethylene oxide)-*block*–poly(acrylic acid)) macromolecular RAFT agent (experimental details in **Chapter 7, §7.2.1**). These hydrophilic chains were first extended with a hydrophobic block by a bulk polymerization of styrene (S) and BODIPY methacrylate-1 (BDPMA1). Then, the polymerization was stopped after 70 minutes. Basic water (pH 12.5) was added to the reaction mixture at room temperature and ultra-sound treatment in an ice bath allowed the formation of nano sized monomer droplets (amphiphilic copolymer PEO-*b*-PAA-*b*-P(S-co-BDPMA1)) were obtained. Finally, the RAFT polymerization was reinitiated by simple degasing with argon and heating to 80°C. After re-polymerization, a core-shell structure negatively charged nanoparticle was obtained with poly(styrene-*co*-BDPMA1) in the core and poly(ethylene oxide)-*block*–poly(acrylic acid) in the shell. The particle is negatively charged in water because the carboxylic acid group (-COOH, pKa around 4) will dissociate into $H^+$ cations and ($-COO^-$) anions in water (pH 6.8-7.0). The obtained $FNP^-$ are well-defined in size with a mean hydrodynamic diameter of 65 nm (**Table 2.1**).




**Scheme 2.1** Synthetic path way for fluorescent nanoparticles ($FNP^-$, $FNP^+$, $FNP\text{-}PEG^+$)(adapted from[180]).

In order to obtain positively charged particles, the acrylic acid sites on FNPs were reacted with ethylenediamine or poly(ethylene glycol) diamine by a coupling reaction involving activation of the carboxylic acid with *N*-(3-Dimethylaminopropyl)-*N*'-ethylcarbodiimide hydrochloride (EDC-HCl) (**Scheme 2.1**). These particles are positively charged in water because the amine group ($NR^3$, pKa around 9) will dissociate into $N^+$ cations and ($R^{3-}$) anions in water (pH 6.8-7.0). Two different positive fluorescent nanoparticles were obtained: $FNP^+$ and $FNP\text{-}PEG^+$ with very small difference on the shell where $FNP\text{-}PEG^+$ has slightly longer side chains than $FNP^+$ as shown in **Scheme 2.1**.

## 2.2 Characterizations of fluorescent nanoparticles (FNPs)

Fluorescence and absorption spectroscopy analysis of FNPs are displayed on **Figure 2.1** and their main spectroscopic data are given in **Table 2.1**. The BDPMA1 monomer in toluene shows the expected spectra for BODIPY fluorophores[54] with an intense band in the visible region located at 528 nm (corresponding to $\pi \rightarrow \pi*$ transition) and a vibrational shoulder at higher energy. A second, less intense band is located in the UV region at around 380 nm[180]. The maximum of fluorescence emission is found at 540 nm, exhibiting a Stokes shift of 421 $cm^{-1}$ (12 nm).

The $FNP^-$ exhibits very similar absorption and fluorescence spectra with a maximum absorption at 529 nm and a maximum fluorescence emission at 543 nm. The Stokes shift of the nanoparticles (487 $cm^{-1}$, 14nm) is slightly higher than the monomer. Similar slight red

shift of fluorescence emission has previously been observed from free monomer to monomer immobilized in a rigid environment[181]. One can also notice that the $FNP^-$ absorption spectra exhibit a more intense vibrational shoulder which might result from the confinement of BODIPY in a rigid polymer matrix (**Figure 2.1A**)[181,182]. The excitation spectra for $FNP^-$ and BDPMA1 monomer have the same aspect and superimpose to their respective absorption spectra (**Figure 2.1B**), showing that the absorbing and emitting species are identical. The fluorescence quantum yield of $FNP^-$ is 36% while that of BODIPY in toluene is 70%. The decrease may be due to quenching between closely associated BODIPY monomers in the polystyrene matrix. However since there are about 2975 BODIPY molecules[27] inside one particle, the brightness of the particle is about $7.8 \times 10^7$ $M^{-1}$ $cm^{-1}$, which is 1500 times higher than the one of BODIPY monomer alone. The very high brightness of $FNP^-$ shall be a good advantage for bioimaging applications (see **Chapter 1 §1.2**).

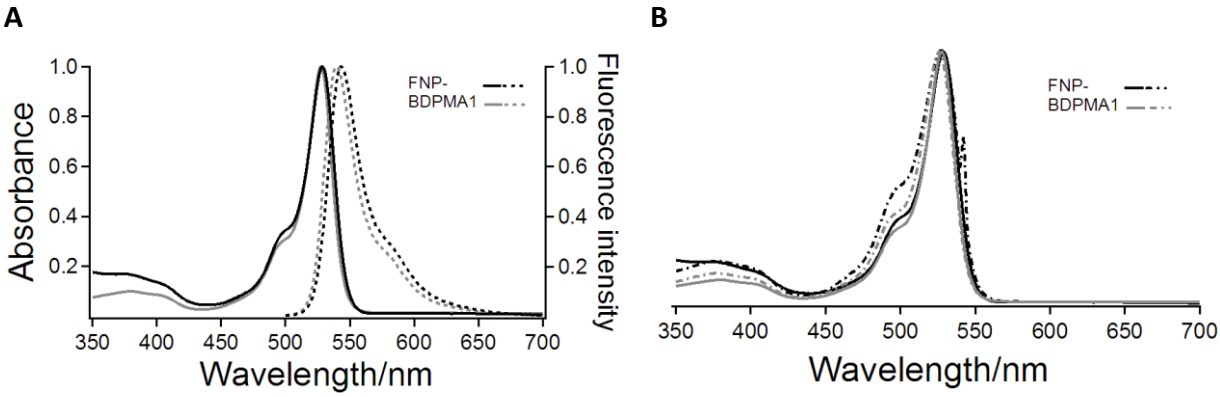



**Figure 2.1** BDPMA1 monomer in toluene (black lines) and $FNP^-$ (grey lines) in water (pH=7.0): absorption (A, B full lines), fluorescence emission (A dotted lines, $\lambda_{exc}$=495nm) and excitation (B dotted lines, $\lambda_{emi}$=543nm) normalized spectra.

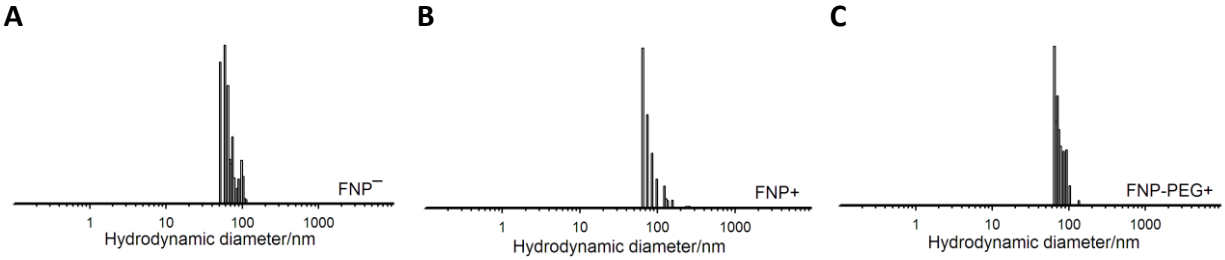



**Figure 2.2** DLS signals of $FNP^-$ (A), $FNP^+$(B) and FNP-$PEG^+$(C) in water (pH 7).

**Table 2.1** Main spectroscopic properties of BDPMA1 and FNPs

| Sample | Structure | $\lambda_{abs}$ /nm | $\lambda_{em}$ /nm | $\Phi_F$/% water[a] | $\Phi_F$/% toluene[27] | BDPMA1 per particle[27] | Brightness/ $M^{-1}$ $cm^{-1}$[b] | $D_h$/nm[c] |
|---|---|---|---|---|---|---|---|---|
| BDPMA1 | - | 528 | 540 | - | 70 | - | 51100 | - |
| $FNP^-$ | PEO-*b*-PAA-*b*-P(S-*co*-BDPMA1)-TTC-$C_{12}$ | 529 | 543 | 36 | - | 2975 | $7.8x10^7$ | 65 |
| $FNP^+$ | PEO-*b*-PAE-*b*-P(S-*co*-BDPMA1)-TTC-$C_{12}$ | 529 | 543 | 24 | - | 2975 | $5.25x10^7$ | 79 |
| $FNP\text{-}PEG^+$ | PEO-*b*-PAP-*b*-P(S-*co*-BDPMA1)-TTC-$C_{12}$ | 529 | 543 | 24 | - | 2975 | $5.16x10^7$ | 71 |

[a] Error of 15%[182], [b] Brightness is determined by **Equation 7.5 in Chapter 7**, [c] hydrodynamic diameter ($D_h$) determined by DLS.

Both the absorption and emission spectra of $FNP^+$ and $FNP\text{-}PEG^+$ are identical in shape and position with the $FNP^-$ which demonstrates that the change of the charge doesn't change the spectrum behavior of FNPs (**Figure 2.3**). However the fluorescence quantum yield of $FNP^+$ and $FNP\text{-}PEG^+$ is 24%, which is lower than the one of $FNP^-$ (36%). This is perhaps because of the charge effect on BDPMA1. DLS signals of $FNP^-$ (65nm), $FNP^+$ (79nm) and $FNP\text{-}PEG^+$ (71nm) are shown in **Figure 2.2.** The size of $FNP^-$ (65nm) is in agreement with the one reported (63nm)[180]. $FNP^+$ (79nm) and $FNP\text{-}PEG^+$ (71nm) show larger measured diameters. Even if aggregation of positively charged FNPs cannot be ruled out, the increase of the hydrodynamic diameter probably comes from the larger size of the couterion ($Cl^-$ for $FNP^+$ and $FNP\text{-}PEG^+$ and $Na^+$ for $FNP^-$).

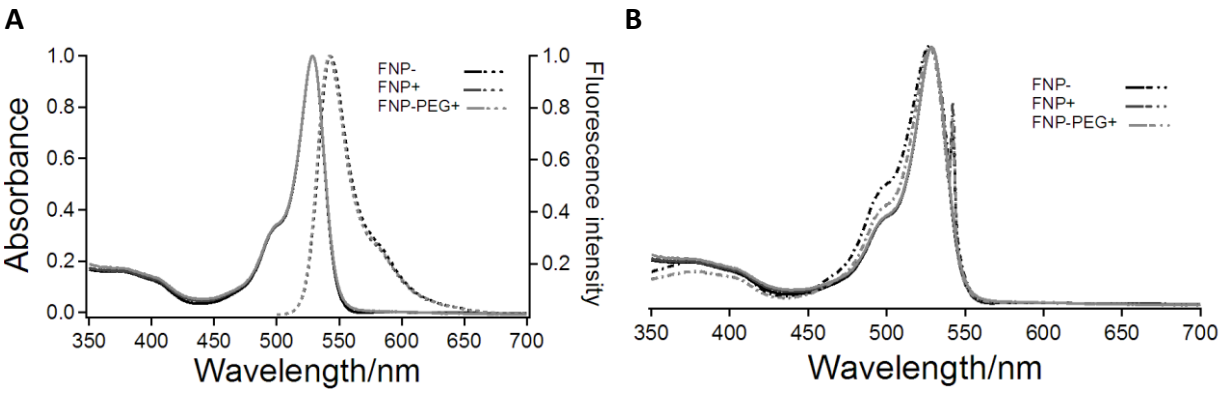



**Figure 2.3** $FNP^-$ (black lines), $FNP^+$ (dark grey lines), $FNP\text{-}PEG^+$ (light grey lines) in water (pH=7.0): absorption (A, B full lines), fluorescence emission (A dotted lines, $\lambda_{exc}$=495nm) and excitation (B dotted lines, $\lambda_{emi}$=543nm) normalized spectra.

## 2.3 Toxicity assessments of FNPs on *E.coli*

Having synthesized and characterized the FNPs, I next assessed the toxic effect of FNPs on *E.coli*. In order to do this, the growth rates of bacteria in the presence of FNPs were compared with the growth rate of *E.coli* bacteria alone. The growth rate was measured by using a 96-well plate reader. The FNPs concentration used was $6.6x10^{-3}$µM ($4x10^{12}$particles/mL).

Here, *E.coli* bacteria with $FNP^-$, $FNP^+$ or $FNP\text{-}PEG^+$ were incubated in the 96-well plate reader at 37°C in the dark overnight. A control with only bacteria was also prepared. Every nine minutes the growth rate of the cells was monitored by measuring the optical density at 600nm (**Figure 2.4**). For over ten hours incubation, the growth curves of bacteria with FNPs were practically the same as the growth curve of bacteria alone both in LB (rich) and M9 (poor) media. This means that, at this concentration, FNPs have no toxicity effect on bacterial growth in a long time scale, independently of the charge of the FNPs.

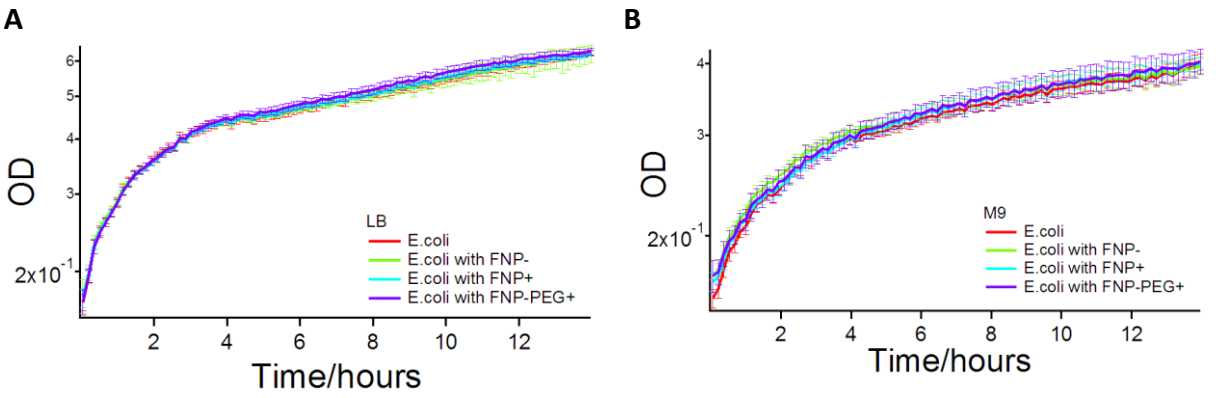



**Figure 2.4** Growth curves of *E.coli* bacteria alone (red lines) and *E.coli* bacteria incubated with $FNP^-$ (yellow lines), $FNP^+$ (blue lines) and $FNP\text{-}PEG^+$ (purple lines) at $6.6x10^{-3}$µM in LB (A) or M9 media(B). The error bars indicate the difference between the three replicates in the experiment (<9%).

## 2.4 FNPs for internal bioimaging of *E.coli*

### 2.4.1 Chemical treatments of *E.coli* with FNPs

After having shown that FNPs have no toxicity effect on *E.coli* bacterial growths, the FNPs were tested for internal imaging application with *E.coli*. The *Escherichia coli* cytoplasmic membrane is composed of two phospholipid bilayers with a peptidoglycan layer sandwiched between them and has the function of acting as a permeability barrier for most molecules. There are two means of transportation of molecules or biochemical agents into

the cell: active transport or passive transport. Passive transport is a movement of molecules across the bacterial membrane. It is driven by the increase of entropy of the system. Active transport is also a movement of molecules (such as ions, glucose and amino acids…) across bacterial membrane in the direction from lower concentration to higher concentration. Unlike passive transport it requires an input of cellular energy. Particles under 5nm can be transported into bacterial cell by active transport[183]. As a matter of fact, the size of FNPs (60-80nm) is too big to enter inside *E.coli* and we need to find another way to insert them. One way to remove the limitation of membrane barrier is to partially destroy it[184]. Historically, a variety of chemicals were found to penetrate *E.coli*. For example, the cell membrane may be gently lysed and disorganized by chemical treatment with di(ethylene glycol) (DEG)[185]. Thus, in the following experiments, *E.coli* bacteria are permeabilized by a brief exposure to DEG before incubation with FNPs.

An initial *E.coli* bacterial concentration of $5x10^7$ CFU/mL (OD=0.5) in the LB growth medium (rich medium, **§7.4.1**) was placed inside an Eppendorf Safe-Lock Tube in the presence of $FNP^-$ (at 3 different concentrations-$2.6x10^{-2}$µM, $3.9x10^{-2}$µM, $5.2x10^{-2}$µM) and 5% DEG. The samples were incubated at 37°C in the dark shaking for one hour and washed twice with PBS to remove free $FNP^-$. The cells were then fixed by adding a fixing solution (4% PFA, 0.03% glutaraldehyde in 1x PBS), then washed three times with PBS and finally re-suspended in PBS before flow cytometry measurements and bioimaging experiments.

Accurate measurements of fluorescent cells (**Figure 2.5**) after incubation of *E.coli* with different concentrations of $FNP^-$ ($2.6x10^{-2}$µM, $3.9x10^{-2}$µM, $5.2x10^{-2}$µM) were obtained by Flow Cytometry.

After incubating *E.coli* with $FNP^-$ and DEG, the percentage of total fluorescent cells increased when increasing the $FNP^-$ concentration and it reaches a plateau when the $FNP^-$ is about $3.9x10^{-2}$µM. The percentage of total fluorescent cells after DEG treatment could reach 80%. I choose the $FNP^-$ concentration of $2.6x10^{-2}$µM as a suitable concentration to continue the chemical treatment experiments.

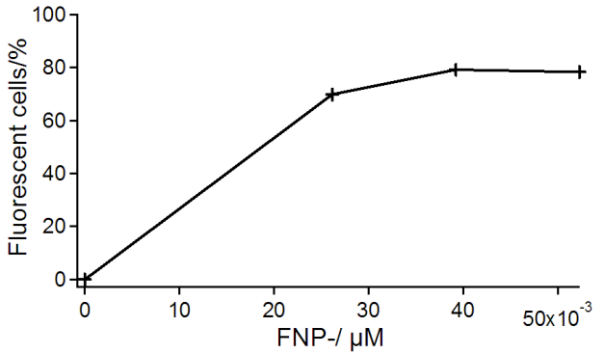



**Figure 2.5** Percentage of fluorescent cells for *E.coli* incubation with $FNP^-$ after DEG (5%) treatments.

*E.coli* interacting with $FNP^-$ after chemical treatment was observed by epifluorescence microscopy. In **Figure 2.6** one can see that some cells are associated with the $FNP^-$ and several FNPs are sometimes found on one bacterium. However, the FNPs seemed to be attached to the membrane and not inside the cells.

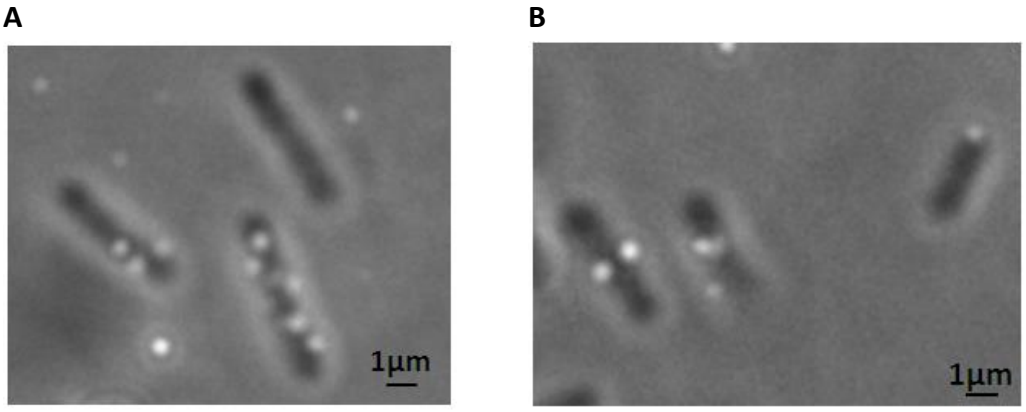



**Figure 2.6** Epifluorescence microscopy images of *E.coli* interacting with $FNP^-$ after DEG treatment. Additional images are shown in **Figure S2.1 in Section 2.6**.

Since the chemical treatment was not efficient to insert FNPs inside *E.coli* bacteria, I turned to another method: electroporation.

## 2.4.2 Electroporation of *E.coli* bacteria with FNPs

### 2.4.2.1 Characterization of electroporation by flow cytometry

Another method to partially destroy the membrane barrier in order to insert the FNPs into the *E.coli* is electroporation. Electroporation consists in the application of an electric pulse on the bacterial cell, pores will form on the cell membrane, and the fluorescent particles may enter inside the membrane through these holes. During incubation, cells can repair their membranes while the particles stay inside the cell. Electrocompetent cells are

needed for this process; competence is the ability of a cell to take up extracellular elements or materials from its environment. Electrocompetent cells are prepared by a chemical treatment (see experimental part for details in **Chapter 7, §7.5.2**).

50µL electrocompetent cells ($8x10^7$ bacteria /µL) were mixed with different volumes of $FNP^-$, $FNP^+$, $FNP\text{-}PEG^+$ to reach different final concentrations ($2.7x10^{-4}$-$5.2x10^{-2}$µM). This mixture was placed on ice for 10 minutes before electroporation at the specified voltage (15kV/cm). Immediately after electroporation, the cells were then incubated at 37°C for one hour in rich growth medium to repair their membranes.

After incubation, cells were centrifuged to remove unattached nanoparticles and fixed with 4% formaldehyde. Then the cells were re-suspended in PBS (1mL) prior to flow cytometry measurement and bioimaging.

Accurate measurements of live, dead, total bacteria and fluorescent cells percentage after *E.coli* electroporation with different concentrations of $FNP^-$ ($2.7x10^{-4}$-$5.2x10^{-2}$µM) are obtained by Flow Cytometry (**Chapter 7, §7.8**) (**Figure 2.7**). Live cells have intact membranes and are impermeable to dyes such as propidium iodide (PI- see **Chapter 1 §1.3.1**), which only leaks into dead cells when the membrane is compromised. After addition of PI, we can measure the percentage of dead cells in each sample.

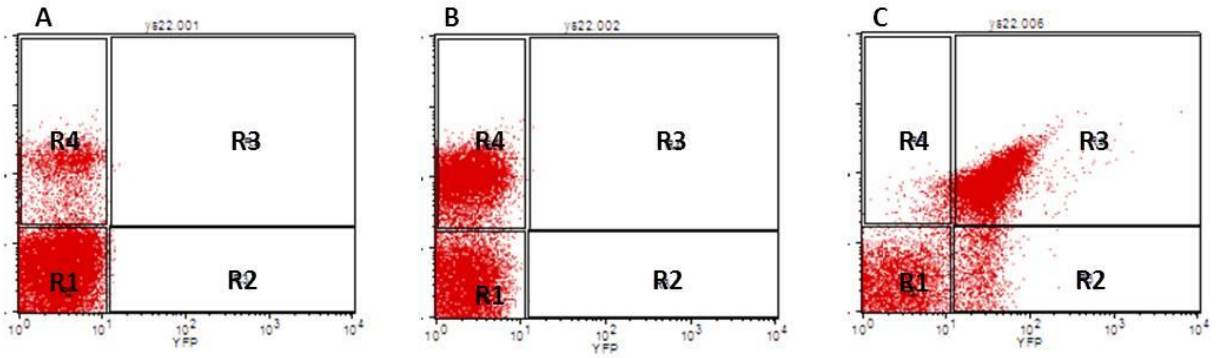



**Figure 2.7** Flow Cytometry of *E.coli* interacting with $FNP^-$ after electroporation, A) competent cells, B) competent cells after electroporation, C) competent cells and $FNP^-$ after electroporation ($2.7x10^{-9}$ M). X axis: green fluorescence, Y axis: red fluorescence. (R1: live non-fluorescent cells, R2: live green fluorescent cells, R3: dead red-green fluorescent cells, R4: dead red fluorescent cells).

As shown in **Figure 2.7A**, 10% cells (R4) are dead after competent cells preparation while in **Figure 2.7B** one can see that 50% (R4) of the cells are dead after electroporation. In **Figure 2.7C** when competent cells are exposed to $FNP^-$ and electroporation then 60% of cells are dead and labeled by $FNP^-$ (R3), 40% of cells survived, only 8% of cells are alive and labeled by FNPs (R2). When the particle concentration is increased, the percentage of live

cells decreases (**Figure 2.8A**). Since the particle itself has no toxicity effect on bacterial growth as described in section 2.3, the decreases in live cells may come from the effect of $FNP^-$ on the electroporation process. This induces an increased number of dead bacteria. However, at the concentration $2.7x10^{-3}$µM, 40% percent cells survived which is an encouraging result (**Figure 2.7C**).

The percentage of total fluorescent cells increases when increasing the particle concentration. Its value reaches a plateau when the concentration is about $1.4x\ 10^{-2}$µM. For the live fluorescent cells, the percentage increases at the beginning, and reaches the plateau at the concentration of $2.7x10^{-3}$ µM. The percentage of fluorescent live cells remains at about 8% (**Figure 2.8B**).

The percentage of total fluorescent cells could reach 90%, but because of the combination of electroporation and addition of $FNP^-$, the percentage of live fluorescent cells is not very high, remaining at about 8%. Taking into account the percentage of live cells and live fluorescent cells, I chose the particle concentration of $2.7x10^{-3}$ µM as a suitable concentration for the following experiments (**Figure 2.8B**).

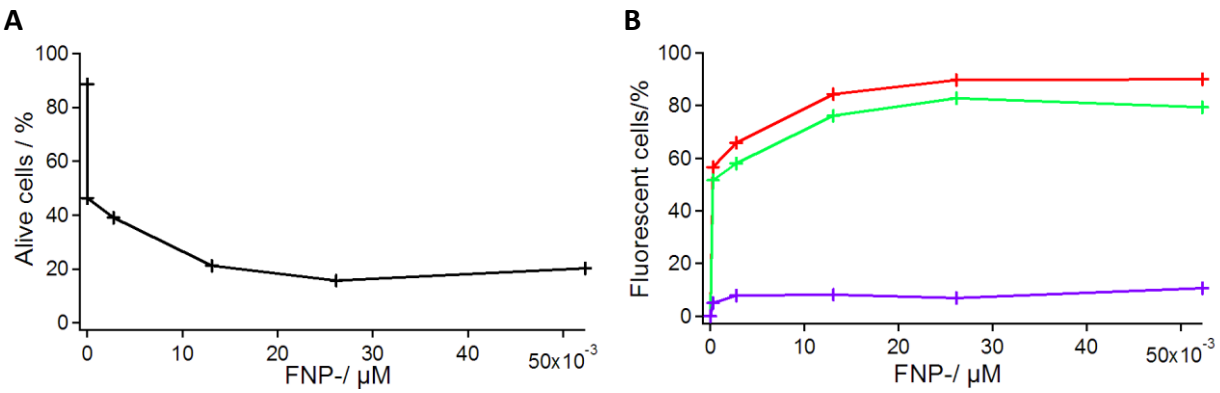



**Figure 2.8** Assessment of incorporation of $FNP^-$ on *E.coli* after electroporation (A): Live cells percentage with $FNP^-$ (B): total green fluorescent cells (red lines), dead green fluorescent cells (green lines) and live green fluorescent cells (purple lines).

After this primary study with $FNP^-$, I decided to compare three different FNPs interacting with *E.coli* bacteria: $FNP^-$, $FNP^+$ and FNP-$PEG^+$. Different FNPs are added to an *E.coli* electrocompetent cells suspension (50µL). Samples are electroporated with an initial field strength of 15kV/cm.

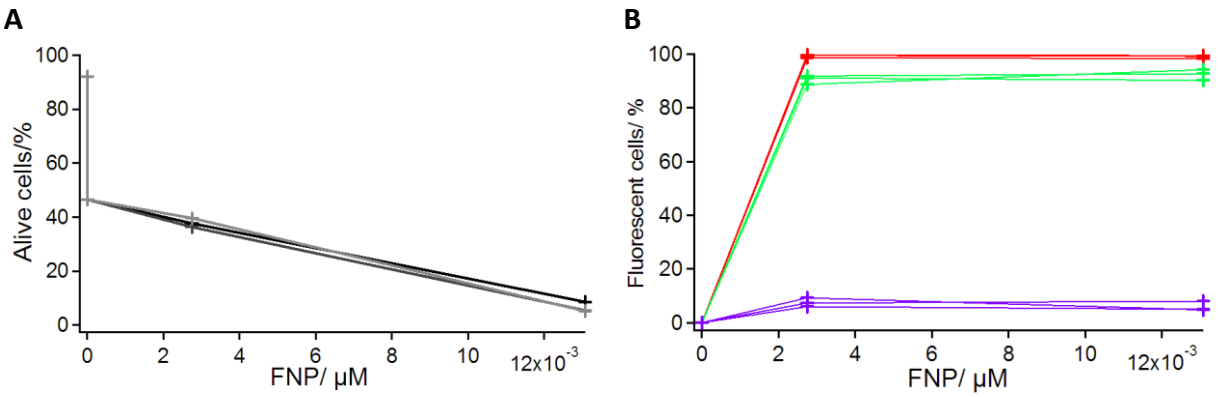



**Figure 2.9** Assessment of incorporation of $FNP^-$(black lines), $FNP^+$ (dark grey lines) and FNP-$PEG^+$ (light grey lines) on *E.coli* after electroporation (A): Llive cells percentage with FNPs (B): total green fluorescent cells (red lines), dead green fluorescent cells (green lines) and live green fluorescent cells (purple lines).

The three different FNPs have almost the same behavior when electroporated with *E.coli* no matter what the charge of the particle is (**Figure 2.9 A**). This means that the charge is not a significant parameter for the effect on *E.coli*. Moreover, the percentage of fluorescent cells has the same tendency as in the previous measurement (**Figure 2.8**). The percentage of live fluorescent cells is about 8% for all three different FNPs (**Figure 2.9B**).

### 2.4.2.2 Fluorescence bioimaging of *E.coli* interacting with FNPs after electroporation

*E.coli*'s interaction with $FNP^-$, $FNP^+$, FNP-$PEG^+$ was assessed by fluorescence microscopy. Phase contrast images and fluorescence images were taken. **Figure 2.10** shows how $FNP^-$ interacts with bacteria *E.coli* after electroporation. **Figure 2.10A** is the phase contrast image and **Figure 2.10B** is the fluorescence image of the same bacterium. There are some green spots on the fluorescence image of this bacterium corresponding to the $FNP^-$. In order to visualize more clearly, images A and B were overlapped (**Figure 2.10C**), and one can notice that all the particles are associated with the bacterium. At this point it cannot be confirmed whether the particles are inside or on the surface of the bacteria

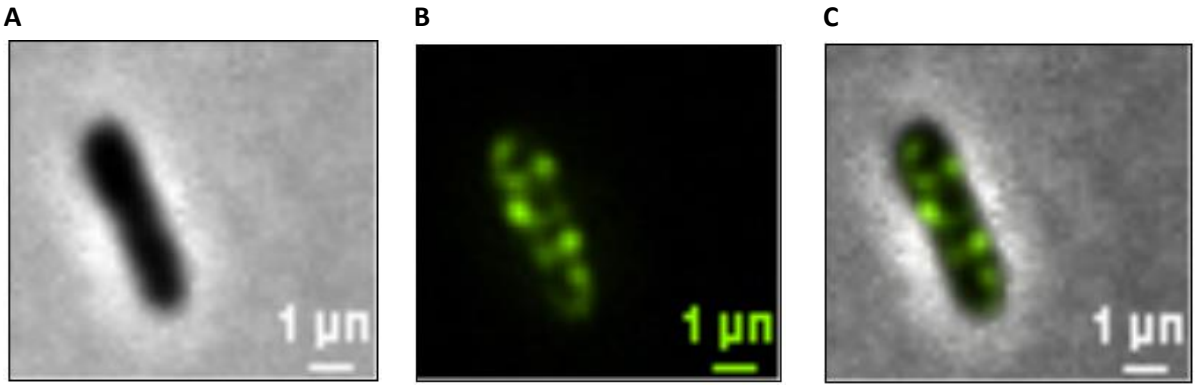



**Figure 2.10** Bioimaging of one *E.coli* interacting with $FNP^-$ after electroporation. (A): phase contrast image, IT=400ms; (B): fluorescence image, IT=5s; (C): overlap of images A and B (60X objective, Particle concentration: $2.7x10^{-3}$ µM).

Larger images (**Figure 2.11**) show that after electroporation, many cells are associated with $FNP^-$ and several nanoparticles on one bacterium are often observed.

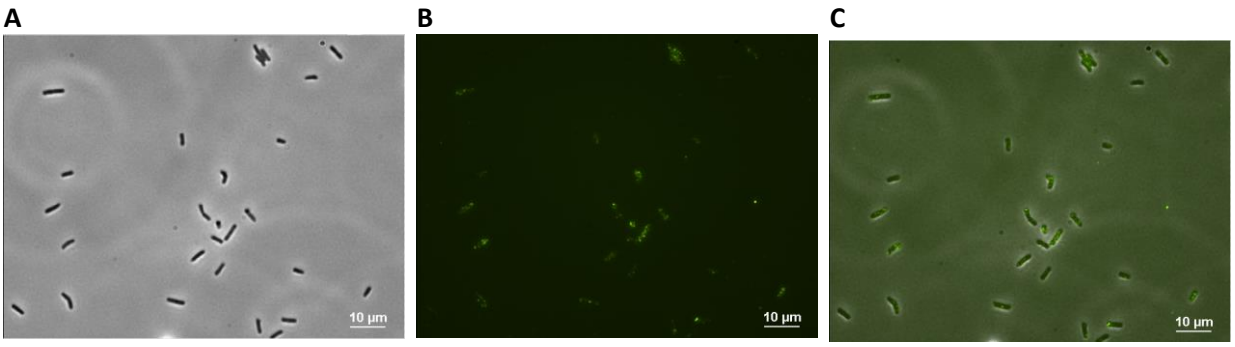



**Figure 2.11** Bioimaging of *E.coli* interacting with $FNP^-$ after electroporation. (A): phase contrast image, IT=400ms; (B): fluorescence image, IT=5s; (C): overlap of images A and B (60X objective, Particle concentration: $2.7x10^{-3}$ µM). Additional images are shown on **Figure S2.2 in Section 2.6**.

*E.coli* cells interact also with positively charged $FNP^+$ and $FNP\text{-}PEG^+$ (**Figure 2.12**). As it was observed with the $FNP^-$, most of the cells are associated with particles, and several FNPs on one *E.coli* bacterium are often observed. As mentioned previously we cannot say whether FNPs are on the membrane or inside the bacteria. From the images and as already observed by flow cytometry, we found that the probability of the interaction of *E.coli* with FNPs is not dependent on the particle charge.

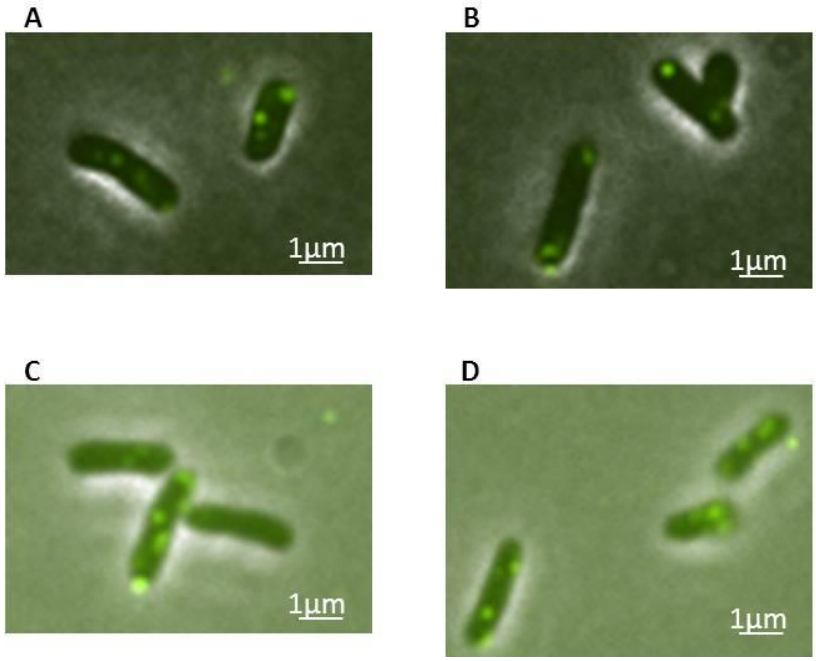



**Figure 2.12** Overlap of phase contrast and fluorescence images of *E.coli* interacting with $FNP^+$ (A, B) and FNP-$PEG^+$ (C, D). (60X objective, Particle concentration: $2.7x10^{-3}$ µM). Additional images are shown on **FigureS2.3 in Section 2.6**.

After observation of FNPs interaction with *E.coli* bacteria, we found that the FNPs can be associated with the cell after electroporation. However, only 8% of cells are fluorescent and alive. Furthermore, it is difficult to determine whether the particles are inside the bacteria from the microscopy images, since they could also be on the surface of bacteria. So, in order to discriminate between these two hypotheses, another dye, methylene blue, was introduced in the experiments.

### 2.4.3 Emission quenching of $FNP^-$ with Methylene Blue (MB)

In order to determine whether after electroporation the FNPs were inside or outside *E.coli*, methylene blue was used. Methylene blue (MB- see **Chapter 1 §1.3.1**) is a cationic blue biocompatible dye, it will bond to the DNA of bacteria which is negatively charged. Methylene blue is reduced in viable cells leaving them unstained, dead cells are unable to reduce the oxidized methylene blue and the cells are stained blue. However, the labeling of bacteria by methylene blue is requires a longer time (around 10 minutes)[186] compared with the quenching process and a particular protocol is needed for the staining process[187,188], so it is possible to use the methylene blue to quench the particles outside the bacteria. I will first demonstrate that MB can interact with FNPs (without bacteria) and quench their emission.

Here, I take $FNP^-$ as an example to continue the following experiments since the probability of the interaction of *E.coli* with FNPs is not dependent on the particle charge. The results of the fluorescence and absorption spectroscopy analysis of $FNP^-$ and methylene blue are displayed on **Figure 2.13A**. The overlap between the emission spectrum of $FNP^-$ and the absorption spectrum of MB indicates a possible quenching process of $FNP^-$ by MB. Titration experiments were conducted to characterize the quenching process of $FNP^-$ by MB. A $FNP^-$ solution was placed inside a cuvette and the methylene blue solution was added gradually. Emission spectra were taken after each addition until the emission of $FNP^-$ stopped decreasing.

The titration experiment of $FNP^-$ with methylene blue is displayed on **Figure 2.13B**. After the addition of MB, the fluorescence intensity of $FNP^-$ decreases continually while the fluorescence intensity of MB increases slightly at the same time. In the same condition without FNPs, MB does not exhibit emission of fluorescence (**Figure 2.13C**). Thus the fluorescence intensity decrease of FNPs is correlated with the increase of MB emission. It is likely to indicate an energy transfer from FNPs to MB.

It was found that, at first, the fluorescence intensity of $FNP^-$ decreases dramatically until 90% fluorescence of $FNP^-$ was quenched and then decreased slower even with the addition of more methylene blue (**Figure 2.13D**). When the concentration of methylene blue was about 6-20 µM, the decrease reached the plateau. At the end up to 98% fluorescence intensity of $FNP^-$ has been quenched. Taking into consideration the results of the titration experiment, MB with a concentration of 16 µM was used during the following bioimaging experiment in order to quench the fluorescence of $FNP^-$ outside the membrane of *E.coli* under the microscope.

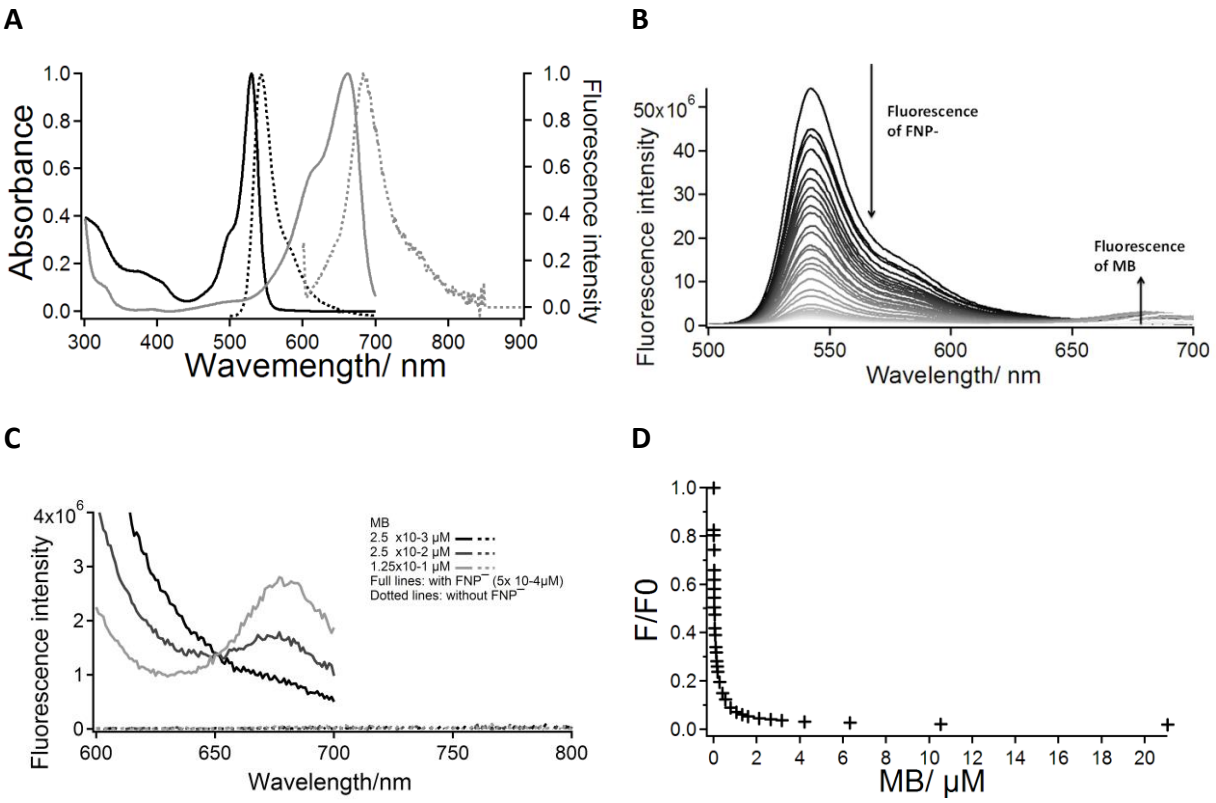



**Figure 2.13** Absorption (full lines) and emission (dotted lines) spectra of $FNP^-$ (black) and MB (grey) in water (A); Fluorescence spectra recorded during the titration of $FNP^-$ with MB (B, $\lambda_{exc}$=495nm); Fluorescence spectra recorded of MB in the same condition without FNPs (C, $\lambda_{exc}$=495nm); Relative decrease of fluorescence intensity of $FNP^-$ as a function of the concentration of methylene blue (D).

In order to understand the mechanism of the quenching process, the data was plotted according to Stern-Volmer equation shown in **Figure 2.14** (**Equation 7.3 in Chapter 7**). A linear Stern-Volmer plot is generally indicative of a single class of fluorophores, all equally accessible to quencher[23]. Since in our case the Stern-Volmer plot deviates from linearity toward the x-axis, it means that two or more populations of fluorophores are present, one of which is not accessible to the quencher. However in $FNP^-$, BPDMA1 is the only fluorophore, so it can be assumed that there are two populations of BDPMA1s, one of which is accessible (a) to methylene blue and the other is not (b). In this case the Stern-Volmer plot will display a downward curvature which is exactly what is observed in **Figure 2.14A.** In addition, a slight blue shift of the emission of $FPC^-$ is observed in the titration process (**Figure2.13B**): the emission spectrum shifts progressively to shorter wavelengths with increasing MB concentrations. This is also probably due to selective quenching of exposed BDPMA1 versus buried BDPMA1. Thus it indicates that those BDPMA1 emitting at longer wavelengths are quenched more readily than the shorter wavelength BDPMA1. These spectra show that the

quenched BDPMA1 display an emission maximum at 543 nm and the protected BDPMA1 display an emission maximum at 540 nm. A modified Stern-Volmer plot (**Figure 2.13B**) was made according to the modified Stern-Volmer equation (**Equation 7.4 in Chapter 7**). The plot is practically linear, and the fraction of the initial fluorescence of $FNP^-$ that is accessible to quencher MB is determined to be 0.94 which means that 94% of the initial fluorescence is accessible to MB and has been quenched directly. This is identical with what we observed in **Figure 2.13C.** Since the core of the particle is formed by poly(styrene-*co*-BDPMA1), the BODIPY fluorophores are in distinct environments. The plot proves our hypothesis that there are two populations of BDPMA1s inside the particle, one on the surface of the core is more accessible (a) to quencher methylene blue and the other one deep in the core is being inaccessible or buried (b). These results corroborate a previous study on the $FNP^-$ where a dual population was also postulated to explain their fluorescence decays[4].

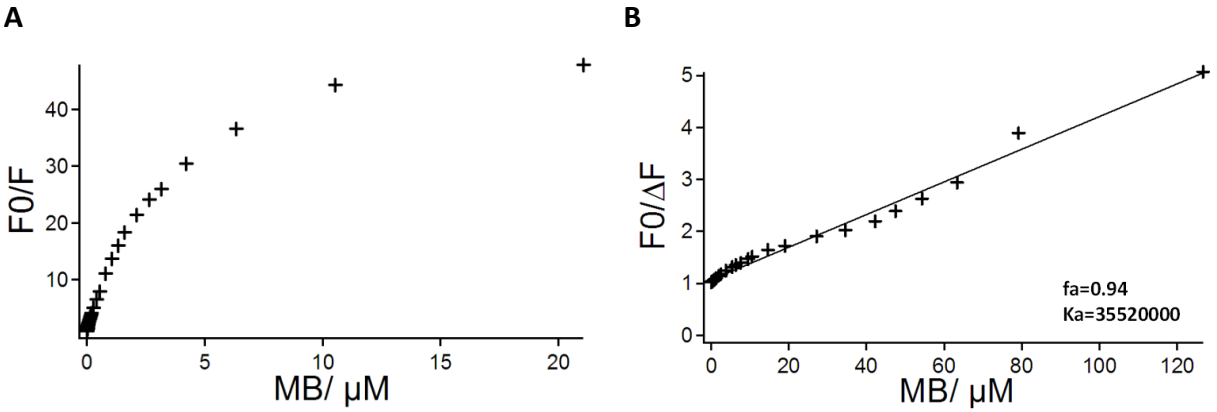



**Figure 2.14** Stern-Volmer (A) and modified Stern-Volmer plots (B) for $FNP^-$ quenched by methylene blue.

### 2.4.4 Fluorescence bioimaging of *E.coli* with $FNP^-$ after quenching with MB

After characterization of the quenching process of $FNP^-$, methylene blue was used in the bioimaging experiments of *E.coli* electroporated with $FNP^-$. *E.coli*'s interaction with $FNP^-$ after the addition of methylene blue was measured by epifluorescence microscopy. So, if there is a bacterium with particle inside and outside (**Figure 2.15**), after the addition of methylene blue, the particles outside the bacteria will be quenched and cannot be detected under the microscope, however the particles inside the bacteria will be protected by the membrane and cannot be quenched by the methylene blue due to that MB interaction time

with bacteria is too short to go through the cell membrane. As a result, they will remain fluorescent and detected under microscope.

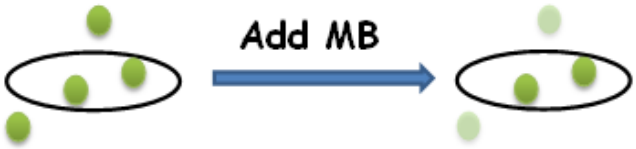



**Figure 2.15** Mechanism of differentiation of particles inside or outside bacteria by addition of methylene blue and selective quenching. Light green refers to a quenched FNP, while dark green refers to a fluorescent FNP (unquenched).

After adding methylene blue, indeed, the $FNP^-$ outside the cells were quenched while some bright spots remain. This means that there were $FNP^-$ inside the cells. They were protected by the cell membrane and thus remained fluorescent under microscope (**Figure 2.15B**). This means that $FNP^-$ can successfully enter inside *E.coli* bacteria after electroporation. However, when I tried to incubate bacteria with $FNP^-$ inside under the microscope, they did not grow. This is probably because, after electroporation, most of the cells were dead as determined by flow cytometry experiments, where only 8% cells were found alive and fluorescent. It is then difficult to identify them and watch them growing under the microscope.

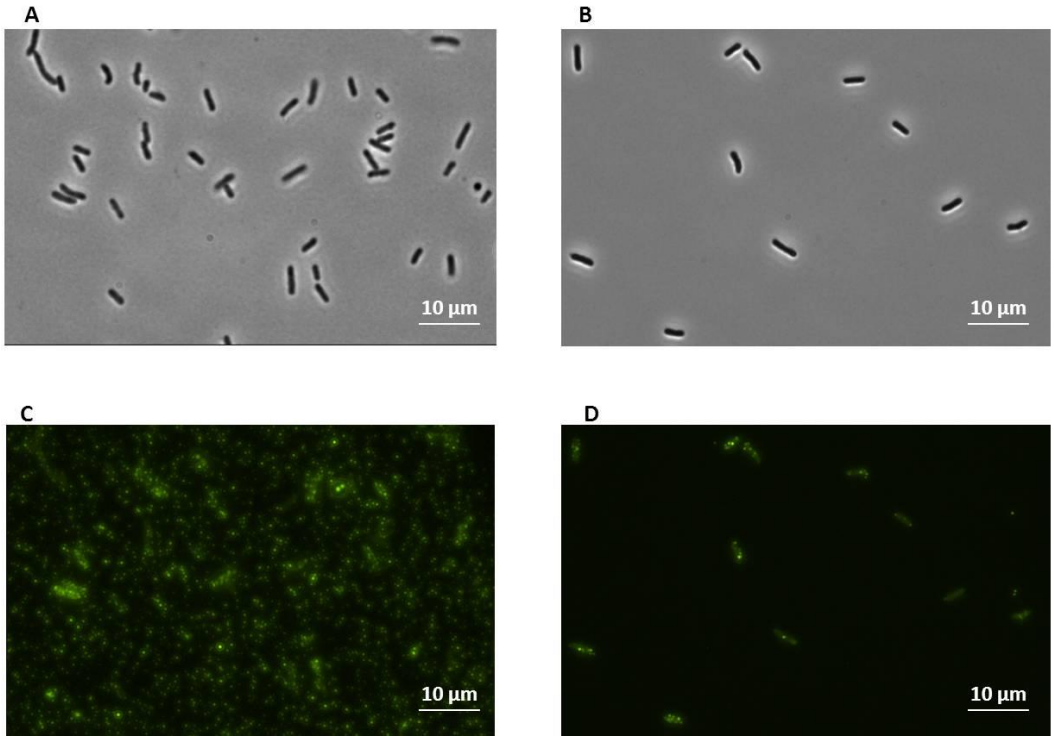



**Figure 2.15** Comparison of electrocompetent *E.coli* interacting with $FNP^-$ before (A, C) and after (B, D) quenching with methylene blue (60X objective, A, B: phase contrast images, IT=200ms; C, D: fluorescence images, IT=5s). Additional images are shown in **Figure S2.4 in Section 2.6.**

### 2.4.5 SEM images of *E.coli* interacting with $FNP^-$

Scanning electron microscope (SEM) was used in order to get more detailed information on *E.coli* interacting with $FNP^-$ after electroporation. A scanning electron microscope (SEM) is a type of electron microscope that produces images of a sample by scanning it with a focused beam of electrons. The resolution of SEM images can reach 1nm.

For SEM, a specimen is normally required to be completely dry, since the specimen chamber is under high vacuum. But living cells and tissues are soft and hydrated, so cells need to be fixed to be transformed into a solid state to preserve and stabilize their structure. Fixation is usually performed by incubation in a solution of a buffered chemical fixative (with a fixing solution). In our case we used glutaraldehyde which kills cells quickly by crosslinking their proteins. The fixed tissues are then dehydrated. However air-drying in SEM is not suitable because air-drying causes collapse and shrinkage. For example, for fresh porcinis, when water is evaporated, high surface tension of water leads to a collapse of structures and air dried porcini are shrinking (**Figure 2.16**). Clearly the structure of bacteria would be destroyed under air-drying. Because air-drying causes collapse and shrinkage, dehydration in

SEM is done by a process of substitution of water in the cells with ethanol, and then exchange of ethanol with liquid carbon dioxide.

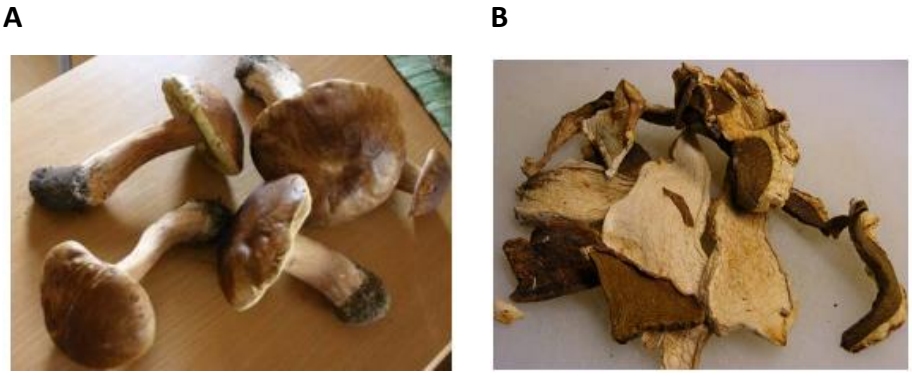



**Figure 2.16** Fresh porcinis (A) and air dried porcinis (B) (adapted from[189]).

After substitution of ethanol, it was exchanged with a transitional liquid carbon dioxide by critical point drying. **Figure 2.17** is a phase diagram of $CO_2$. For liquid $CO_2$ to become gas, it needs to cross the phase boundary. When the liquid changes into gas at a finite rate, while the amount of liquid decreases, it causes a surface tension that would break apart the cells' structure. To avoid this, we use critical point drying, on the high-temperature, high-pressure side. Phase transition of $CO_2$ from liquid to gas does not cross a phase boundary anymore, instead it will pass through the supercritical region where the difference between gas and liquid does not exist. The liquid and vapor phases become equal at the critical point.

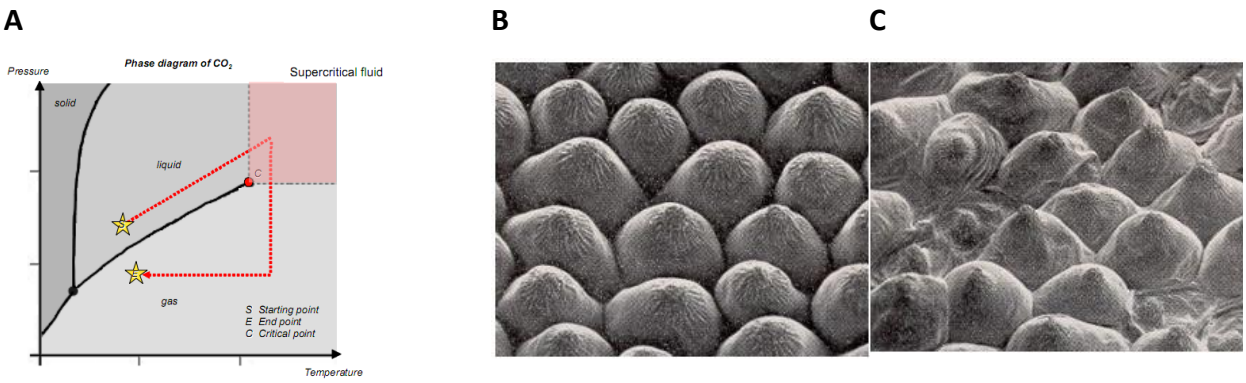



**Figure 2.17** Phase diagram of $CO_2$ (A); Surface of rose blossom after critical point drying (B) and air drying (C) (figure from[189]).

Generally speaking, ethanol was used to replace water inside cells, and then ethanol was exchanged by high pressure liquid carbon dioxide. The liquid carbon dioxide is then heated until its temperature goes beyond the critical point, at which time the pressure can be gradually released, allowing the gas to escape and leaving a dried bacteria. A thin heavy

metal platinum layer is applied to the specimen surface by coating in order to increase contrast by localization of the signal to the surface of the specimen.

As described in the beginning of electroporation experiments of bacteria (**§2.4.2**), electrocompetent cells are used in the experiments, because they have the ability to take up extracellular material (FNPs) from its environment. The difference between untreated cells (K-12 BW25113) and competent cells is shown in **Figure 2.18**. Membrane of the untreated wild type *E.coli* is different from the competent *E.coli* because of reconstruction of the membrane during the competent cells preparation process.

**A** **B**

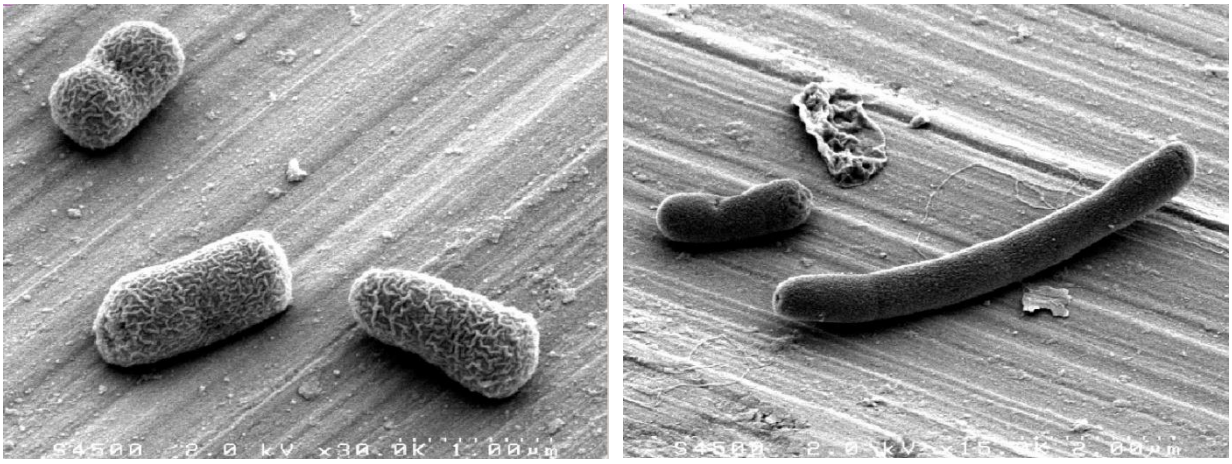


**Figure 2.18** SEM images of untreated *E.coli* (A) and electrocompetent cells (B). Additional images are shown in **Figure S2.5 in Section 2.6**.

From the flow cytometry experiments, one can notice that 50% cells were dead after electroporation. And indeed, electroporation causes serious damages to bacteria as shown in **Figure 2.19**. After electroporation, holes form on the bacteria membrane, especially at the poles of the bacteria which appeared to be more frangible. After electroporation, cells in different states were also observed (**Figure 2.19B**). After the breakage, some cells released their cytoplasm and are dead.

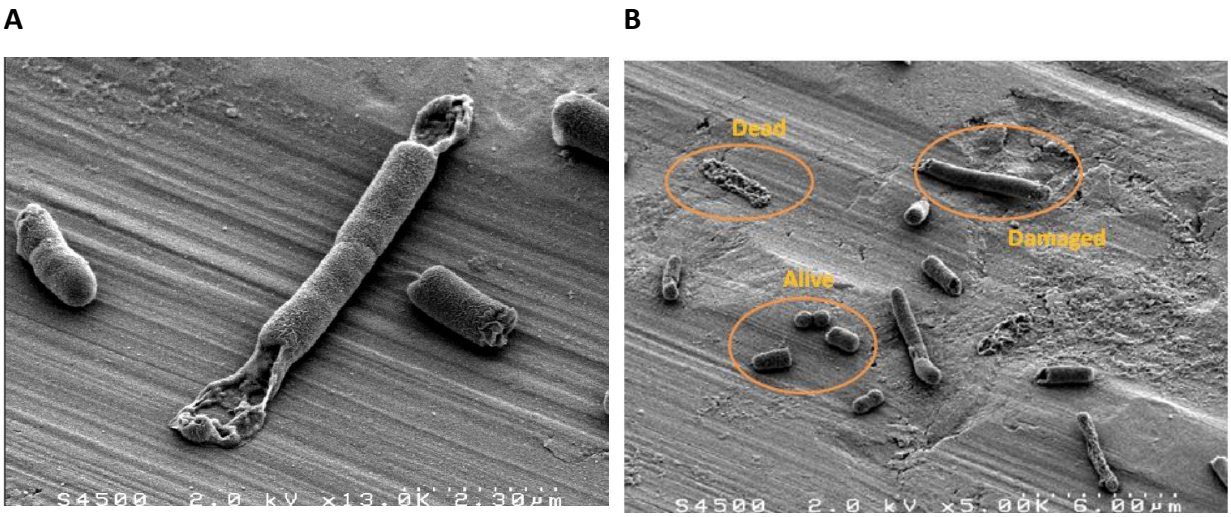



**Figure 2.19** SEM images of damaged electrocompetent cells (A) and electrocompetent cells in different states (B). Additional images are shown in **Figure S2.6 in Section 2.6**.

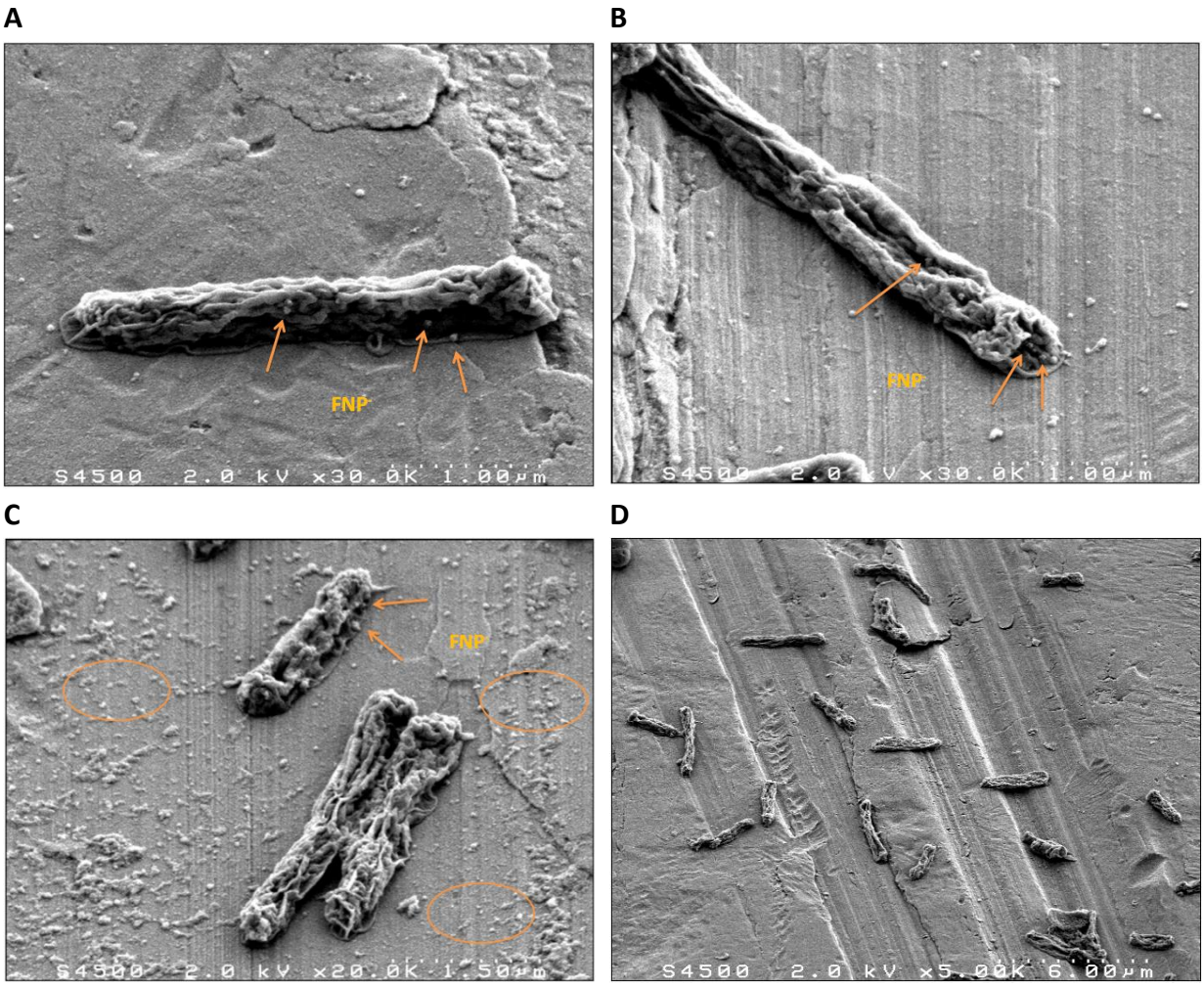



**Figure 2.20** SEM images of *E.coli* interacting with $FNP^-$ after electroporation. Additional images are shown in **Figure S2.7 in Section 2.6**.

SEM images of *E.coli* electroporated with $FNP^-$ are shown in **Figure 2.20**. Particles could be found easily on or under the membrane of the bacteria which confirms the fluorescence

microscopy results presented previously. But with the presence of particles, after electroporation, bacteria were exposed to too much stress and, most of them were dead (**Figure 2.20D**). It was difficult to find alive *E.coli* with $FNP^-$.

## 2.5 Conclusion

In this chapter, I presented three different fluorescent nanoparticles: negatively charged fluorescent nanoparticle ($FNP^-$), positively charged fluorescent nanoparticles ($FNP^+$, $FNP\text{-}PEG^+$) and their bioimaging on *E.coli* bacteria.

FNPs have been shown to be nontoxic on bacterial growth in a long time scale independently of the charge and of the growth medium. Electroporation was used to insert particles inside bacteria. After electroporation, the percentage of total fluorescent cells could reach 90%, but because of the electroporation and the addition of FNPs, the percentage of live florescent cells decreased to about 8%.

Bioimaging experiments indicated that *E.coli* bacteria interacted with both negative and positive fluorescent nanoparticles, most of the cells are associated with particles. In order to make sure that FNPs were really inside the bacteria, methylene blue was introduced to quench the fluorescence of particles outside the bacteria. $FNP^-$ inside the cells were protected by the cell membrane and remained fluorescent after the addition of methylene blue while the particles outside the membrane could be quenched. This indicates that $FNP^-$ can successfully enter inside bacteria after electroporation.

SEM images of *E.coli* electroporated with $FNP^-$ have also shown that particles could be easily found on or under the membrane of bacteria, but bacteria are too much stressed and most of them were dead.

Only 8% cells are alive and fluorescent after electroporation which makes it difficult to identify them and watch them grow under the microscope. So, new strategies are needed to apply the particles to bioimaging of *E.coli*. One way is to try to decrease the size of the nanomaterials and synthesize smaller nano-objects for internal bioimaging of *E.coli*. Another way is to use the particles for external bioimaging of *E.coli*, for instance, we can try to link particles to the surface of bacteria which will be described in detail in next chapter. Finally,

the labeling of dead bacteria by the $FNP^-$ could be used to measure the toxicity of potential antibiotics in a very sensitive manner due to the high brightness of the particles.

## 2.6 Additional images

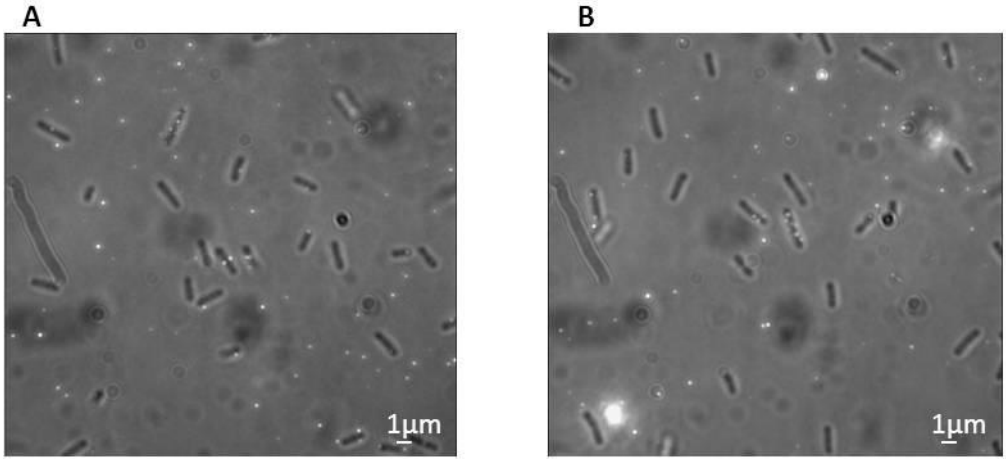



**Figure S2.1** Epifluorescence microscopy imaging of *E.coli* interacting with $FNP^-$ after DEG treatment.

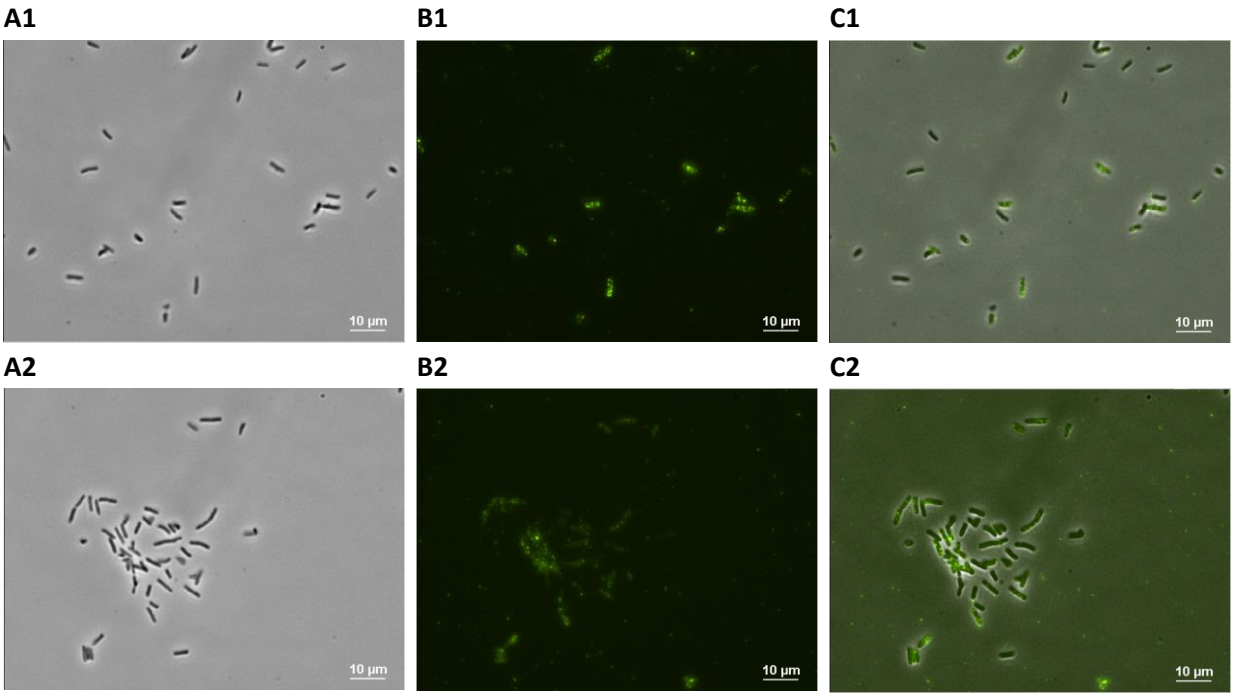



**Figure S2.2** Bioimaging of *E.coli* interacting with $FNP^-$. (A): phase contrast images, IT=400ms; (B): fluorescence images, IT=5s; (C): overlap of images A and B (60X objective, Particle concentration: $2.7x10^{-3}$ µM).

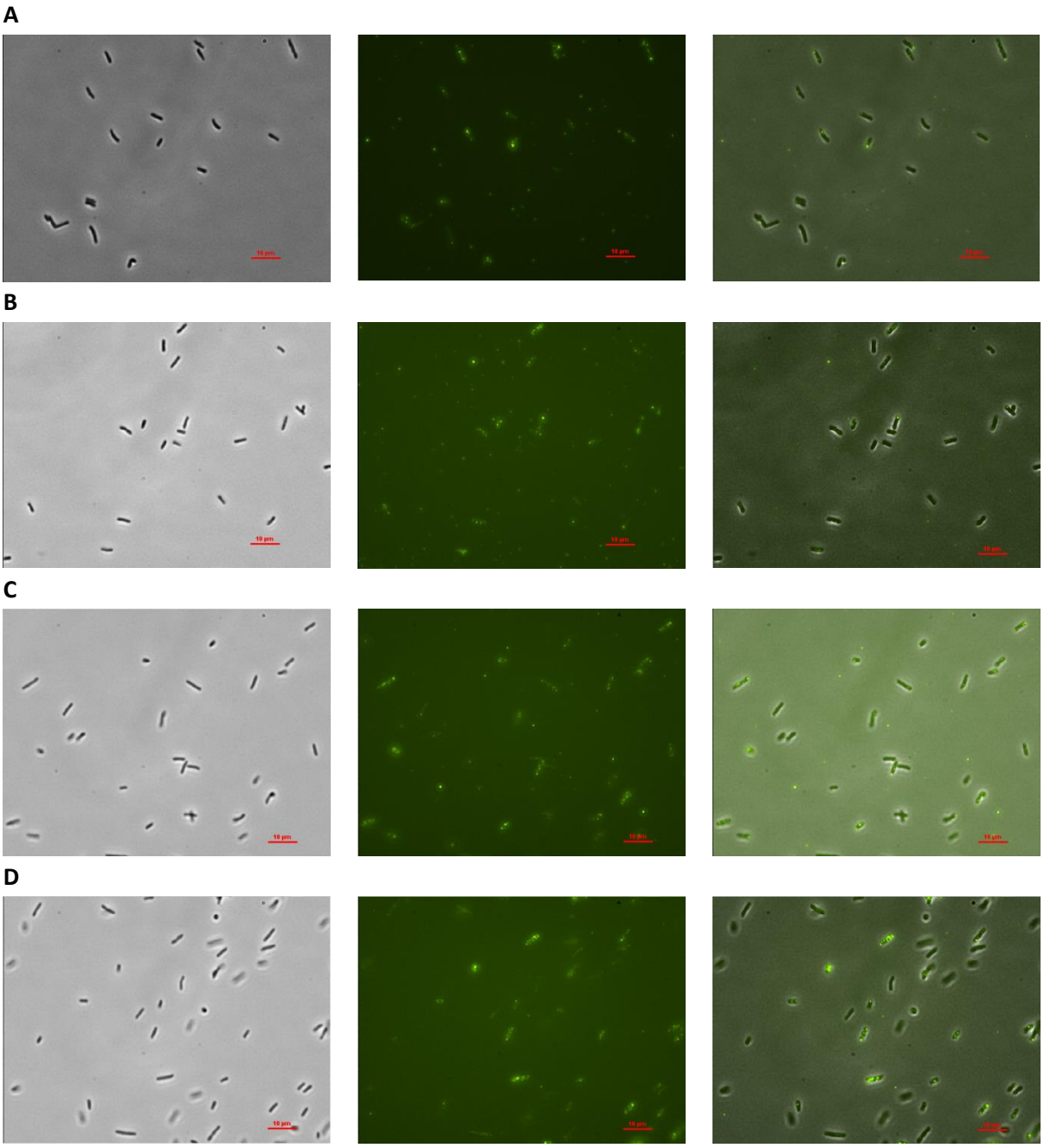



**Figure S2.3** Bioimaging of *E.coli* interacting with $FNP^{+}$ (A, B) and FNP-$PEG^{+}$ (C, D); first column: phase contrast images (IT=400ms); second column: fluorescence images (IT=5s) and third column: overlap of images phase contrast images and fluorescence images (60X objective, Particle concentration: $2.7x10^{-3}$ µM).

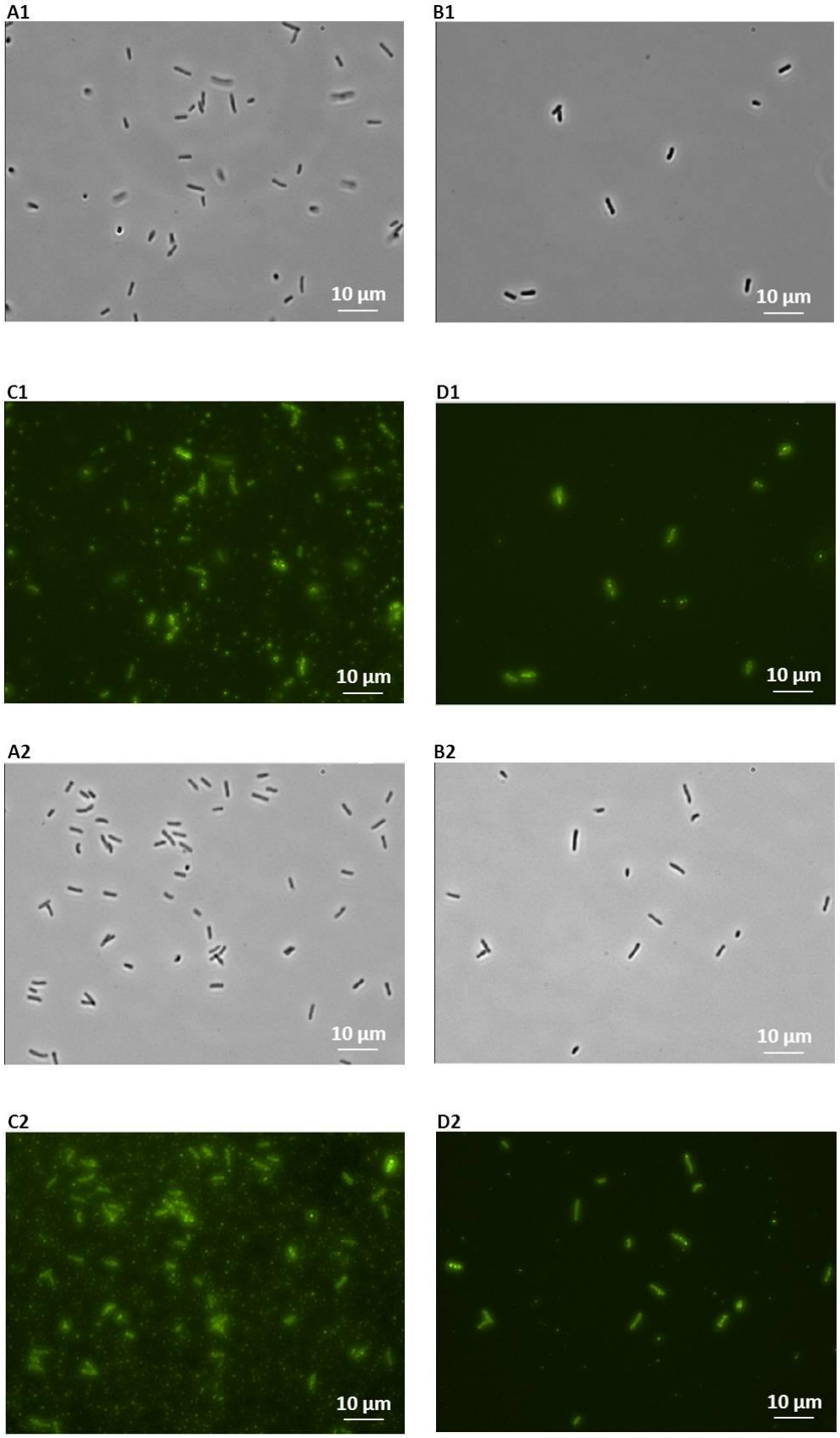



**Figure S2.4** Comparision of electrocompetent *E.coli* interacting with $FNP^-$ after electroporation and before (A, C)- after (B, D) quenching with methylene blue (60X objective, A, B: phase contrast images(IT=200ms); C, D: fluorescence images(IT=5s)).

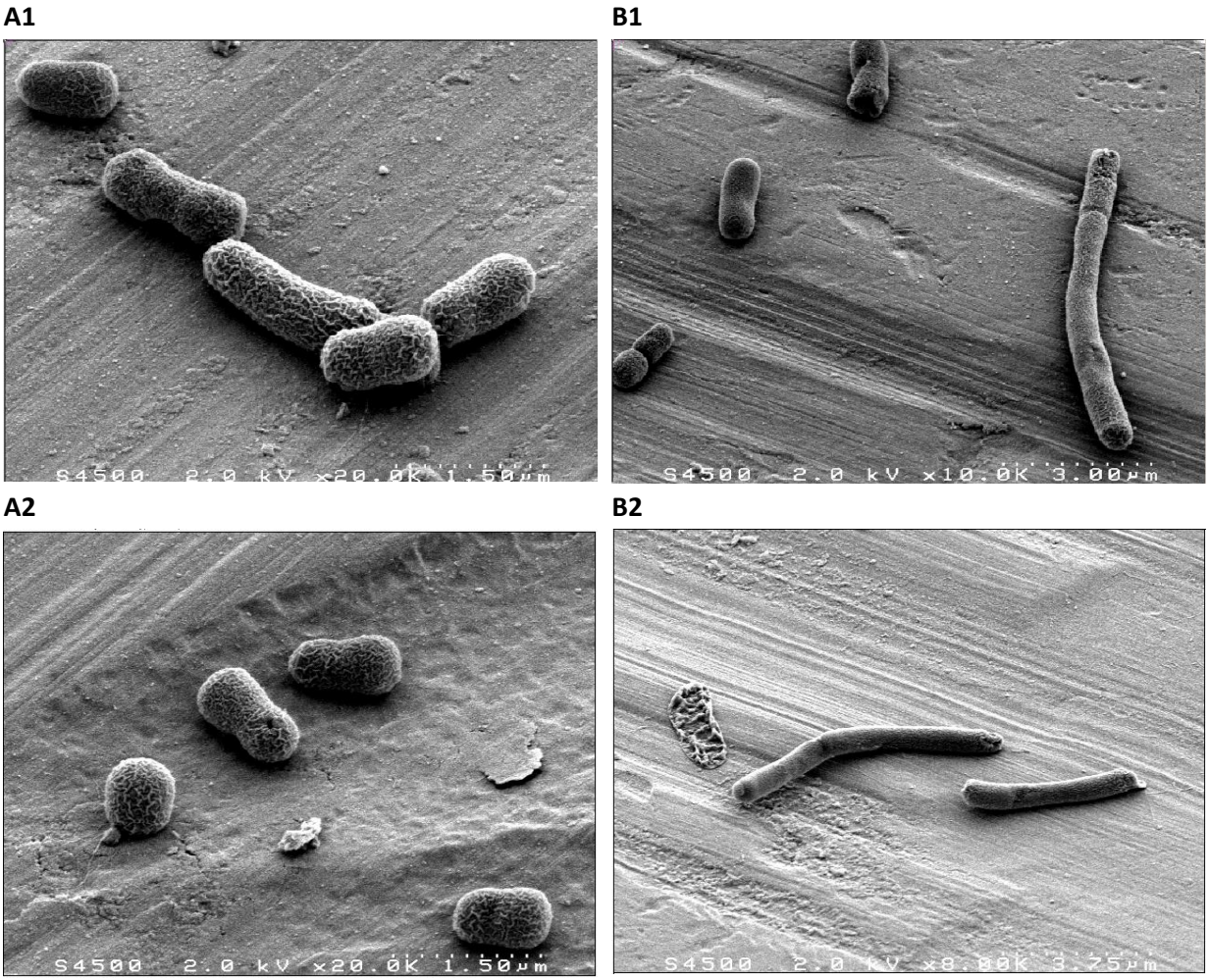
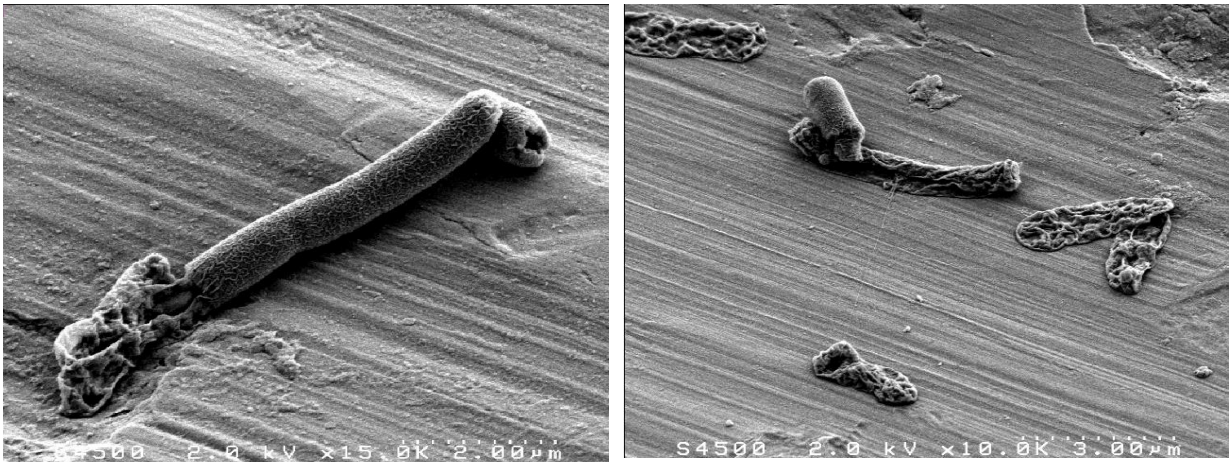



**Figure S2.5** SEM images of untreated *E.coli* (A) and electrocompetent cells (B).

**A1** **B1**




**A2** **B2**

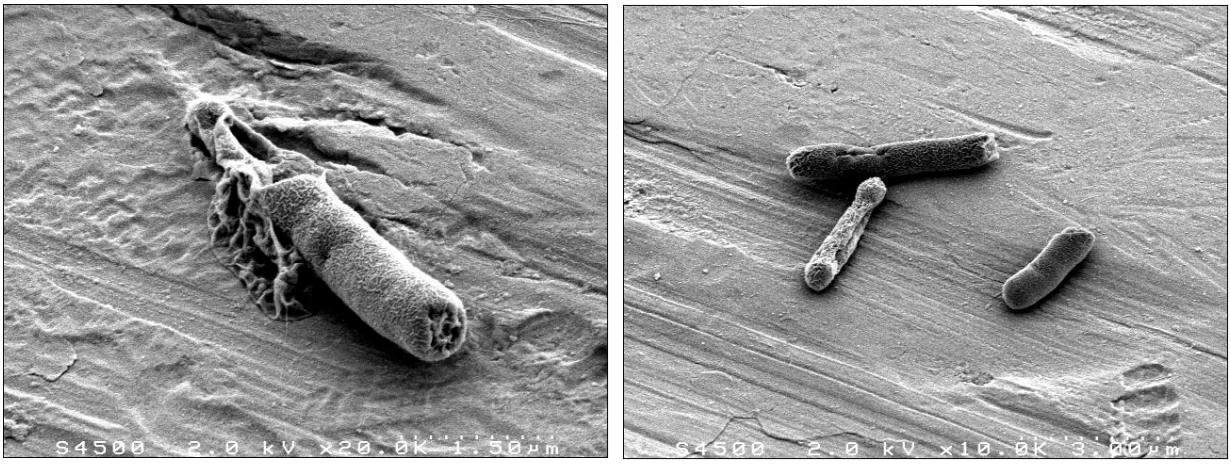



**Figure S2.6** SEM images of damaged electrocompetent cells (A) and electrocompetent cells in different states (B).

**A** **B**




**Figure S2.7** SEM images of *E.coli* interacting with $FNP^-$ after electroporation.

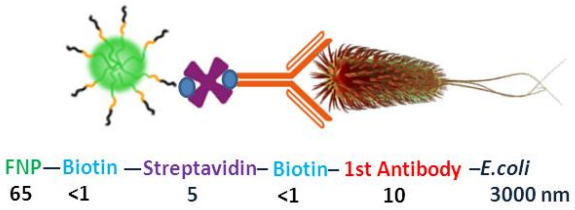
# Chapter 3 Fluorescent nanoparticles (FNPs) for external bioimaging of *E.coli* bacteria

In the previous chapter, I have shown that particles can be successfully inserted inside bacteria by electroporation, however, only very few bacteria survived after this treatment. So, new strategies were needed to develop particles applied to fluorescent bioimaging of *E.coli*. If it is difficult to use them for internal labeling, could they be useful for external labeling of *E.coli* bacterial surface? The answer is yes. In this chapter, I will show how I modified the particles to link them to *E.coli* surface through the elaboration of a "sandwich system". Full characterization of the targeting process will be presented. Moreover the first step toward a microfluidic device designed to immobilize *E.coli* on a surface for further bio-imaging will be shown. I also prepared a "nanoparticle-antibody" system to bind to the surface of *E.coli* bacteria. Preliminary imaging results of "nanoparticle-antibody" system will be presented.

## 3.1 Design of "Sandwich" for targeting bacterial surface

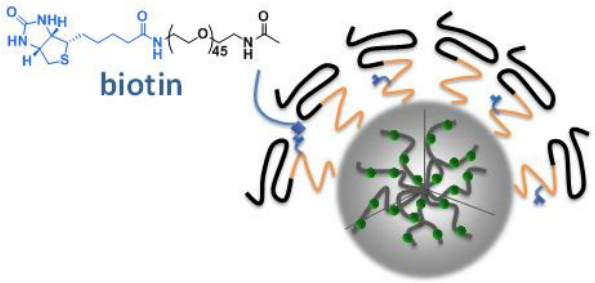
### 3.1.1 Conjugation of biotin on FNPs

After studying fluorescent nanoparticles for internal bioimaging application of *E.coli* bacteria, $FNP^-$ were then modified for bioimaging of bacterial surface. In order to target *E.coli*'s outer membrane with $FNP^-$, a "sandwich system" was created (**Scheme 3.1**). *E.coli* can be easily targeted with an antibody conjugated with biotin. The binding of biotin to streptavidin is one of the strongest non-covalent interactions known in nature. If we can conjugate biotin to nanoparticles, then with a streptavidin, we can easily use the particle based "sandwich system" to target the bacteria *E.coli*'s outer membrane.




**Scheme 3.1** Hypothesis of particle based "sandwich system"

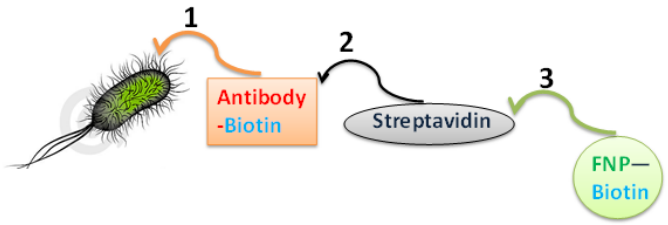
A schematic representation of $FNP^-$ conjugated with biotin is shown in **Scheme 3.2**. The chemical bonding of the biotin to the nanoparticle was possible starting from the commercially available poly(ethylene glycol)$_n$-2-aminoethyl ether biotin (with n≈45) which possesses a terminal amine function that can react with the carboxylic acids present on the surface of $FNP^-$. It was thus possible to apply the same reaction used to transform $FNP^-$ into $FNP^+$ presented in **Chapter 2 (§2.1)**. In a typical experiment, the total number of acrylic acid units present on the surface of the fluorescent nanoparticles ($FNP^-$) was taken as 1 equiv. Poly(ethylene glycol) 2-aminoethyl ether biotin (1 equiv. ) and EDC.HCl (4 equiv.) were added to react with the acrylic acids on the surface of the $FNP^-$ and get maximum conversion. It was difficult to characterize the conjugation by conventional method (*e.g.* NMR or IR). Absorption and fluorescence spectra of $FNP^-$ and $FNP^-$-biotin were recorded but it turned out that they are almost identical (**Figure 3.1**). The successful reaction of the amino-biotin with the carboxylic acids could be proved by Surface Plasmon Resonance (SPR) as described in **§3.2.2**.




**Scheme 3.2** Conjugation of biotin on the $FNP^-$

### 3.1.2 Target *E.coli*'s outer membrane with "sandwich system"

After conjugation of biotin on $FNP^-$, $FNP^-$-biotin was then used to target bacterial membrane by building the "sandwich system" (see experimental details in **§3.1.2**). Briefly, *E.coli* bacteria were firstly labelled by a primary antibody which was already conjugated with biotin. Then, the primary antibody conjugated with biotin was bonded to streptavidin. Since streptavidin has four identical peptide chains which can each bind to a biotin, the $FNP^-$-biotin was added to bond the free streptavidin sites. Finally, by using a streptavidin-biotin link, I built a bridge between particles, antibodies and bacteria (**Scheme 3.3**).




**Scheme 3.3** Process of sandwich system formation

## 3.2 Characterizations of the "Sandwich"

### 3.2.1 Spectroscopy analysis

In order to characterize the formation of the sandwich, I divided our study into four different parts: $FNP^-$, $FNP^-$-biotin, $FNP^-$-biotin-streptavidin, $FNP^-$-biotin-streptavidin-antibody. I analyzed each step of the sandwich formation, and did a comparative study of the properties of the subunits.

Fluorescence and absorption spectroscopy analysis of $FNP^-$, $FNP^-$-biotin, $FNP^-$-biotin-streptavidin, $FNP^-$-biotin-streptavidin-antibody are displayed on **Figure 3.1** and their main spectroscopic data are given in **Table 3.1**. The $FNP^-$ exhibits a maximum absorption at 529nm and a maximum fluorescence emission at 543nm. After conjugation of biotin, bonding with streptavidin or bonding with antibody didn't change the position of the maximum of absorption and emission. The only difference one can notice is that, $FNP^-$-biotin-streptavidin and $FNP^-$-Biotin-streptavidin-antibody exhibit a more intense band located in the UV region at around 380nm compared with $FNP^-$ and $FNP^-$-biotin which may come from the light scattered by the larger sized "sandwich" compared to the starting $FNP^-$. From literature, we can find that the sizes of biotin, streptavidin and antibody are about 1nm[190], 5nm[191,192] and 10 nm [193,194] respectively. Since the size of $FNP^-$ is about 65nm, theoretically, the formation of $FNP^-$-biotin-streptavidin and $FNP^-$-biotin-streptavidin-antibody complexes should give objects with a size of 77nm and 97nm respectively, much larger than $FNP^-$ and $FNP^-$-biotin (67nm) resulting in an increase of scattered light.

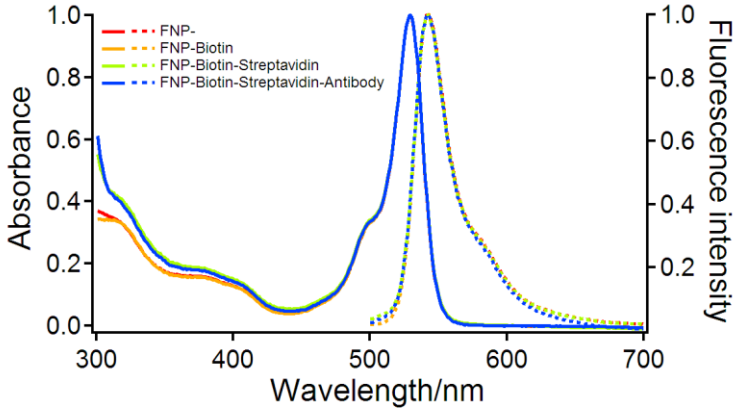



**Figure 3.1** FNP$^-$ (red lines), FNP$^-$-Biotin (orange lines, FNP$^-$-biotin-streptavidin (green lines), FNP$^-$-biotin-streptavidin-antibody (blue lines) in PBS: absorption (full lines) and fluorescence emission (dotted lines, $\lambda_{exc}$=495nm) normalized spectra.

**Table 3.1** Main spectroscopic properties of FNP$^-$, FNP$^-$-Biotin, FNP$^-$-Biotin-streptavidin, FNP$^-$-Biotin-streptavidin-antibody

| Sample | $\lambda_{abs}$ /nm | $\lambda_{em}$ /nm | $\Phi_F$/% PBS[a] | Brightness/ $M^{-1}$ $cm^{-1}$[b] | $D_t$/nm[c] | $D_h$/nm[d] |
|---|---|---|---|---|---|---|
| FNP$^-$ | 529 | 543 | 36 | $7.8x10^7$ | 65 | 65 |
| FNP$^-$-biotin | 529 | 543 | 35 | $7.6x10^7$ | 67 | 67 |
| FNP$^-$-biotin-streptavidin | 529 | 543 | 34 | $7.4x10^7$ | 77 | 78 |
| FNP$^-$-biotin-streptavidin-antibody | 529 | 543 | 30 | $6.5x10^7$ | 97 | 92 |

[a] Error of 15%[182]; [b] Brightness is determined by **Equation 7.5 in Chapter 7**; [c] theoretical diameter ($D_t$); [d] hydrodynamic diameter ($D_h$) determined by DLS.

In PBS the fluorescence quantum yield of FNP$^-$ is 36% and there is practically no difference for FNP$^-$-biotin (35%), FNP$^-$-biotin-streptavidin (34%) and FNP$^-$-biotin-streptavidin-antibody (30%). Thus formation of the "sandwich" does not markedly alter the photophysical properties of FNP$^-$.

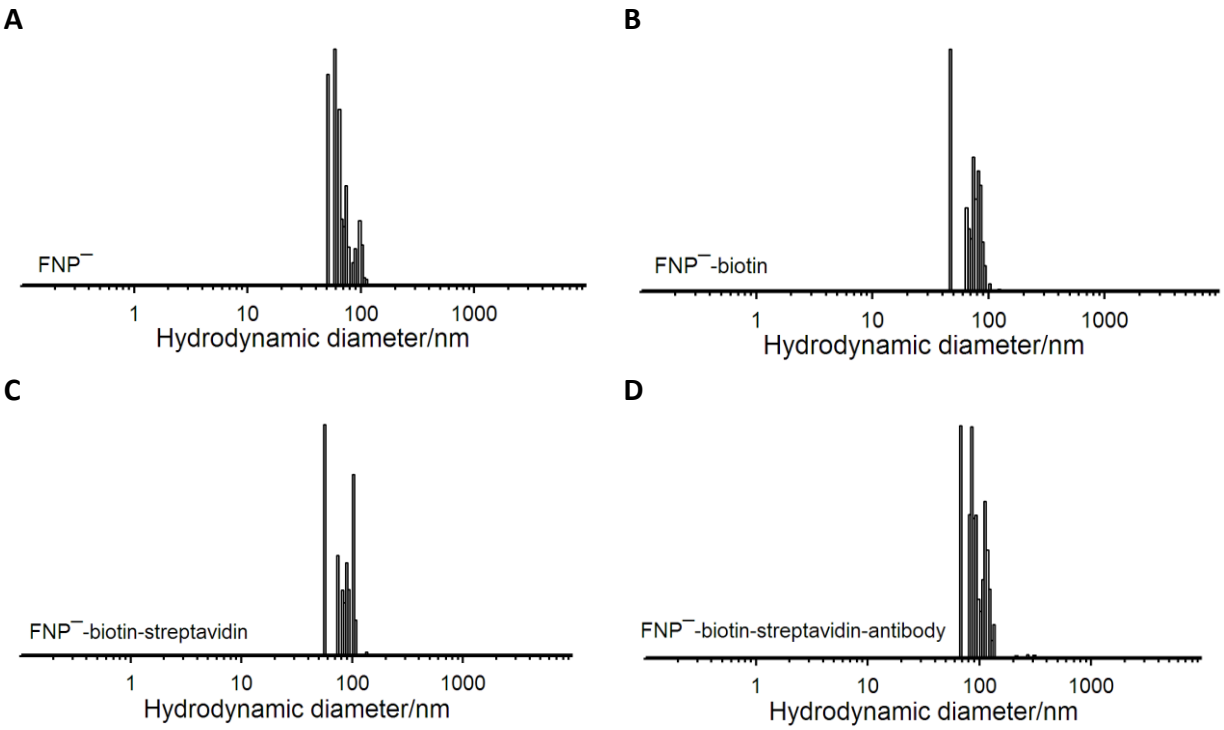



**Figure 3.2** DLS signals of $FNP^-$ (A), $FNP^-$-biotin (B), $FNP^-$-biotin-streptavidin(C) and $FNP^-$-biotin-streptavidin-antibody (D) in PBS (pH 7).

From the DLS measurements (**Figure 3.2**), one can notice that there is very little difference between the theoretical diameter and the hydrodynamic diameter (**Table 3.1**). This is likely to prove that the addition of each element is effective. There is only a slight deviation after the addition of antibody. This is probably because an antibody is relatively large (150 kDa[194]) and it is difficult for them to cover the whole surface of a particle. Thus it is likely that only a few antibodies bond to the surface of particle resulting in a smaller size than the theoretical one for the $FNP^-$-biotin-streptavidin-antibody complex.

### 3.2.2 Surface Plasmon Resonance

Surface Plasmon Resonance (SPR) experiments (cooperation with Dr. Claude Nogues[†]) were performed to measure the affinity of streptavidin and the $FNP^-$-biotin. SPR is a method that measures the interaction between a ligand and a receptor bound to a metallic surface. The detection is based on the refractive index variation during the bio-molecular interaction.

Streptavidin solutions at different concentrations (10 µM and 1 µM in phosphate buffer (0.4 M) at pH 7.4) were spotted on a prism surface freshly covered with gold (**Figure 3.3**, see experimental part for details in **Chapter 7 §7.3.6**). The prism was then inserted into

[†] LBPA laboratory (UMR 8113) ENS-Cachan, France

the SPRi apparatus and a 1 nM $FNP^-$ solution was flowed. Different images before and after the injection were taken. After the washing, a 1 nM $FNP^-$-biotin solution was flowed across the SPRi surface containing the spotted streptavidin and different images were taken before and after the injection.

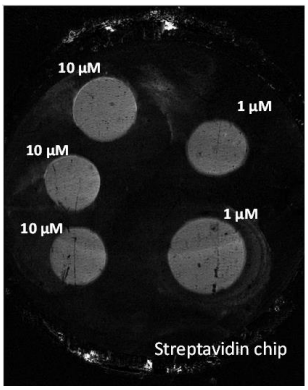



**Figure 3.3** Streptavidin gold chip for SPR.

Kinetics of $FNP^-$/ streptavidin and $FNP^-$-biotin/ streptavidin complex formation and dissociation are measured. The differential images at different time points during flooding of $FNP^-$ across the spots of streptavidin are presented in **Figure 3.4**. Kinetic curves, characteristic of interactions between 1nM of $FNP^-$ or $FNP^-$-biotin and streptavidin, are shown in **Figure 3.5**.

**Figure 3.4A** corresponds to the differential image at time t=0 where no $FNP^-$ was injected. **Figure 3.4B, C, D** are images taken during the association step, at a total $FNP^-$ concentration of 1 nM. Since there is no biotin conjugation, we observed a non-specific binding between particles and streptavidin. The spots became slowly bright and the contrast increased until it reached a maximum (**Figure 3.4D**). The kinetic curve of $FNP^-$ and streptavidin interaction confirms this observation (**Figure 3.5A**). Moreover, there is a higher relative reflectivity intensity for the spots at 10 µM streptavidin than the one at 1 µM which indicates that increasing the streptavidin concentration favors the non-specific interaction between particles and streptavidin. Immediately following the injection of $FNP^-$, the surface was continuously rinsed with buffer. The background signal returned to its original level while the relative reflectivity intensity in the streptavidin containing spots went back to low level (**Figure 3.4E**). We also observed a huge decrease of relative reflectivity intensity from the kinetic curve after washing for both concentrations of streptavidin (**Figure 3.5A**).

Therefore, the non-specific interaction of the $FNP^-$ with streptavidin was not strong enough and particles have been washed away.

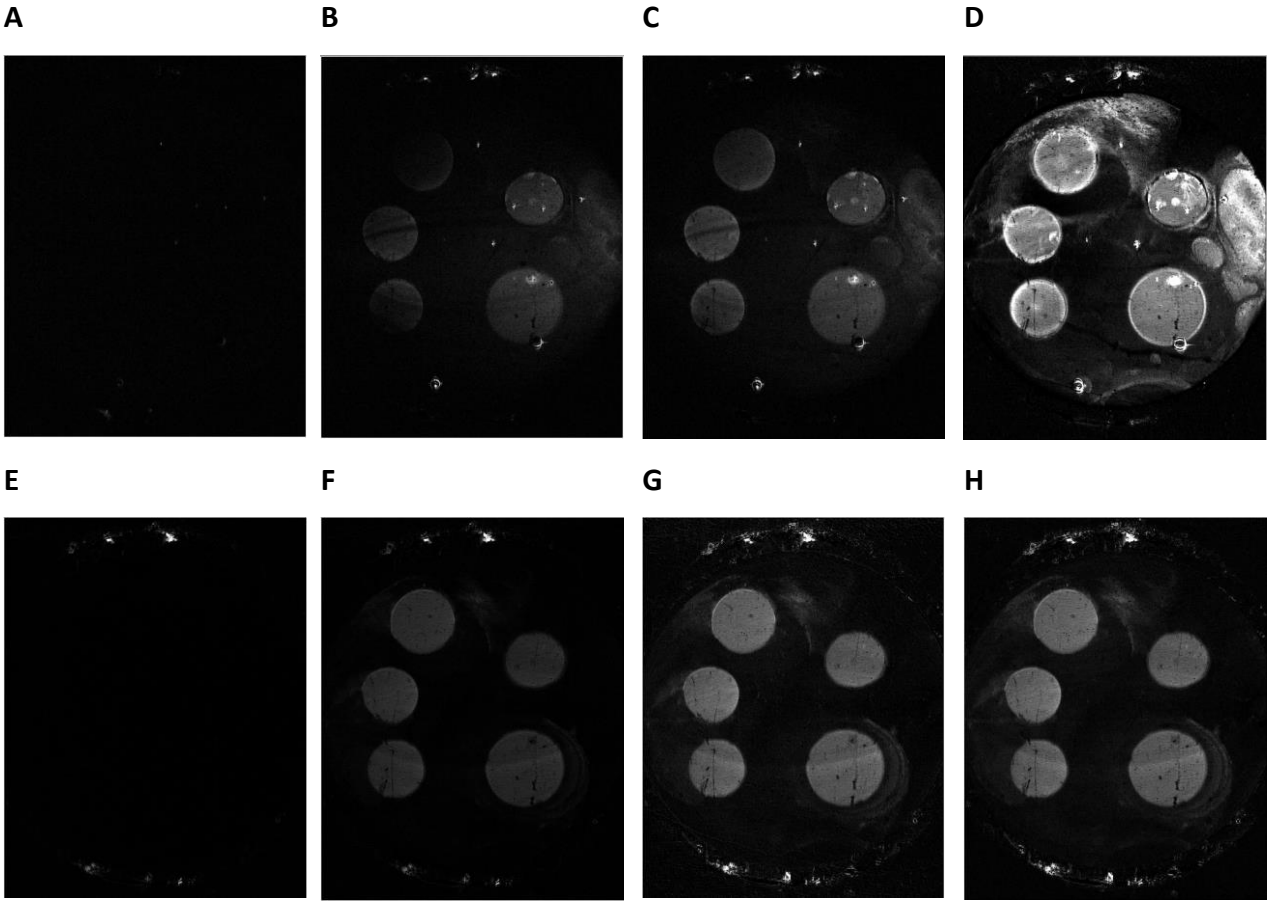



**Figure 3.4** SPRi difference images of the biochip surface at different times during the course of the experiment. 2 different streptavidin solution concentrations (10 µM, 1 µM) were spotted as shown in Figure 3.3. A: t = 0 s, no $FNP^-$ injected. B, C, and D are images taken at t = 1min, t = 2 min and t = 4 min respectively after 1 nM $FNP^-$ injection. E is the image taken 30 min after the injection was stopped and washed by buffer. F, G and H are images taken at t = 30 s, t = 2 min, t = 4 min respectively after 1 nM $FNP^-$-biotin injection.

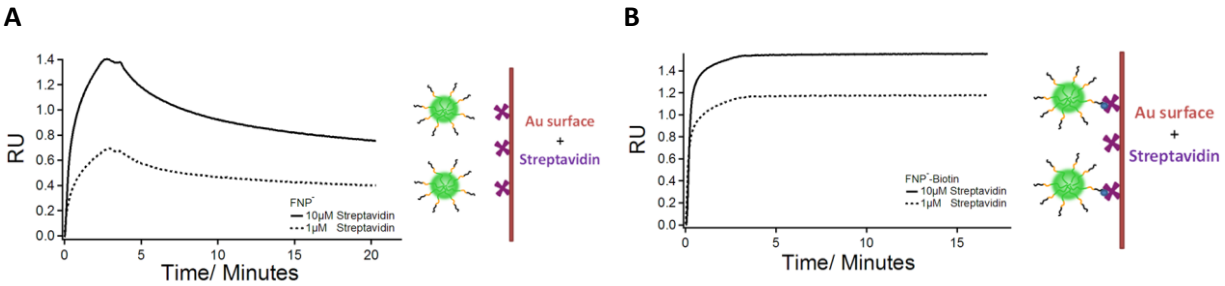



**Figure 3.5** SPRi kinetic curves of $FNP^-$ (A) and $FNP^-$-biotin (B) at selected spots on the SPRi surface as a function of time as particles pass over the prism surface interacting with streptavidin (10 µM (solid lines), 1 µM (dotted lines)) on the pre-treated surface. The kinetic curves are subtracted from the background.

After the washing process, 1 nM $FNP^-$ -biotin solution was flowed across the SPRi surfaces containing the spotted streptavidin. **Figure 3.4 F, G, H** are images taken during the association step. As we know, streptavidin–biotin bonding is one of the strongest known non-covalent interactions ($K_d$ of $10^{-14}$ mol/L)[195]. With biotin conjugated particles, there is a very strong non-covalent interaction between particles and streptavidin, the spots became bright quickly and the contrast increased to reach the maximum very quickly (**Figure 3.4 H**). The kinetic curve of $FNP^-$ -Biotin and streptavidin interaction confirms this observation (**Figure 3.5B**). The curve increased dramatically at the beginning and reached quickly a maximum proving the strong non-covalent interaction between particles and streptavidin. Moreover, there is a higher relative reflectivity intensity for the spots at 10 µM streptavidin than the one at 1 µM which indicates that increasing the streptavidin concentration increases the non-covalent bonding between particles and streptavidin. Immediately after injection of $FNP^-$ -biotin, the surface was continuously rinsed with PBS buffer. However the background signal remains while the relative reflectivity intensity in the streptavidin containing spots remained high unlike the ones flowed with $FNP^-$. Similarly on the kinetic curve, the relative reflectivity intensity remained constant and didn't decrease at all even during washing (**Figure 3.5B**). Therefore, the non-covalent interaction between $FNP^-$-biotin and streptavidin is much stronger compared to the non-specific interaction of the $FNP^-$ and streptavidin. Moreover, the SPR experiments also proved the successful conjugation of biotin on $FNP^-$.

### 3.2.3 Secondary fluorescent antibody

The efficiency of primary antibody to target *E.coli* bacteria was measured by introducing a secondary green fluorescent antibody: Anti-rabbit IgG (H+L), F(ab')2 Fragment conjugated with Alexa Fluor®488. The absorption ($\lambda_{max}$=499nm) and emission ($\lambda_{max}$=520nm) spectra of Alexa Fluor® 488 are shown in **Figure 3.6 B**. After targeting bacterial membrane with a primary antibody conjugated biotin, a secondary fluorescent antibody is added to label the primary antibody on bacterial surface (**Figure 3.6A**).

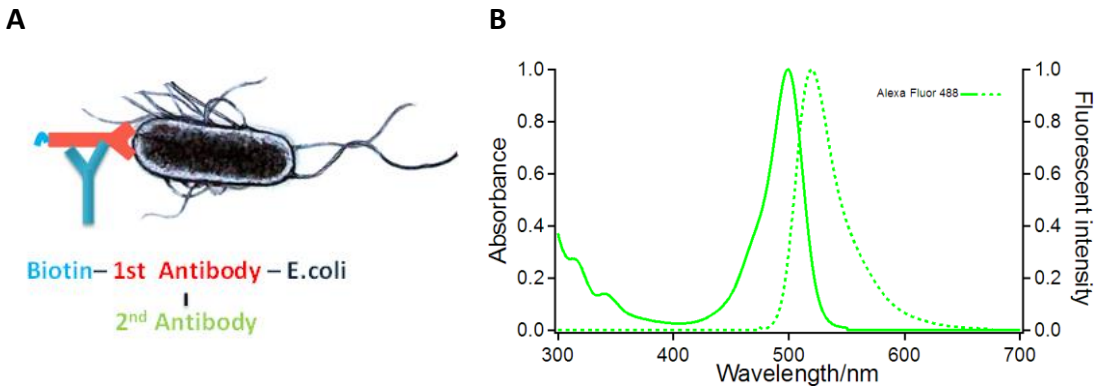



**Figure 3.6** A: Principle of secondary antibody labeling primary antibody on bacteria. B: Absorption and emission spectra of Alexa Fluor® 488 (data from life technologies[196]).

From the bioimaging experiments, we can see that without the addition of primary antibody, the bacteria did not become green after adding the secondary fluorescent antibody (**Figure 3.7B**). However, with the presence of the primary antibody, the bacteria became green fluorescent after the addition of the secondary fluorescent antibody which proved the successful bonding of the primary antibody on bacterial membrane (**Figure 3.7D**).

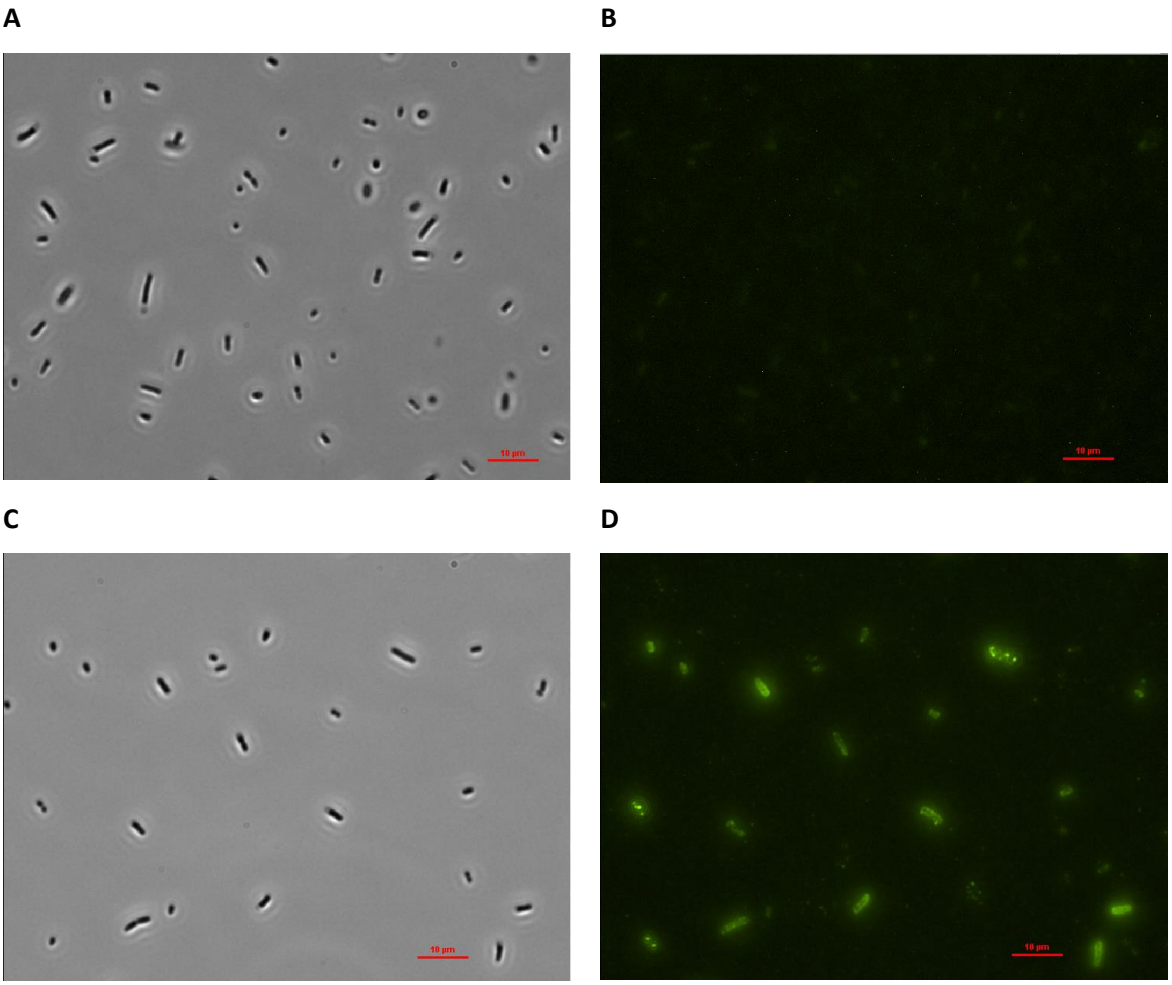


**Figure 3.7** Comparison of *E.coli* - secondary fluorescent antibody (A, B) and *E.coli*- primary antibody-secondary fluorescent antibody (C, D). (60X objective, A, C: phase contrast images, IT=200ms. B, D: fluorescence images, IT=5s) Additional images are shown in **Figure S3.1 in Section 3.5**.

### 3.2.4 Fluorescence bioimaging of "sandwich" labelling bacterial surface

After characterization of each part of the "sandwich" system by spectroscopy, DLS, SPR and secondary antibody labeling, I demonstrated each part of the "sandwich system" are functionable and the "sandwich system" were successfully obtained. I applied it to label the bacterial membrane. Bioimaging of the particle based sandwich system targeting bacterial membrane were measured by fluorescence microscopy. **Figure 3.8A** is the phase contrast image of bacteria, after formation of sandwich system and particles could label the bacterial membrane as shown by fluorescence in **Figure 3.8B**.

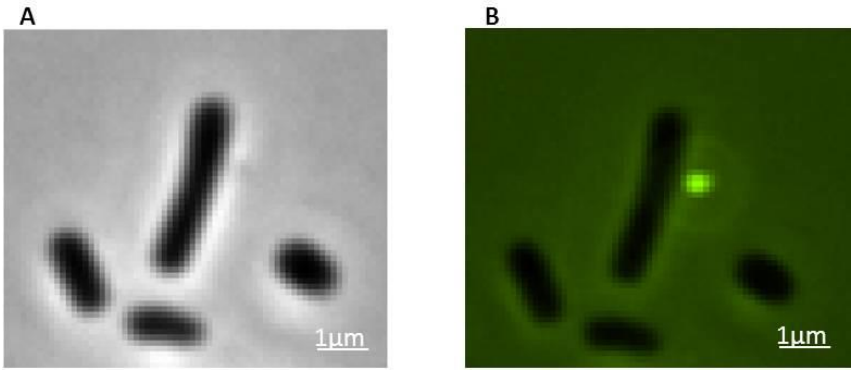



**Figure 3.8** Bioimaging of particle based sandwich system targeted on bacterial surface. (60X objective, A: phase contrast image, IT=200ms. B: fluorescence image overlap with phase contrast image, IT=5s). Additional images are shown in **Figure S3.2 in Section 3.5**.

However, even if we proved the formation of the "sandwich" system, it was very difficult to observe many cells targeted by particles. Moreover it was difficult to tell if the particles were really linked to the surface of bacteria.

In order to confirm the interaction of the sandwich with the bacteria, SEM images were also recorded.

### 3.2.5 SEM images of "sandwich" labelling bacterial surface

Scanning electron microscope (SEM) was used in order to get more detailed information on the sandwich system at the surface of *E.coli*. The cells were prepared like

described in **Chapter 2 (§2.4.5)**. One control without adding streptavidin was made to compare with the one with streptavidin.

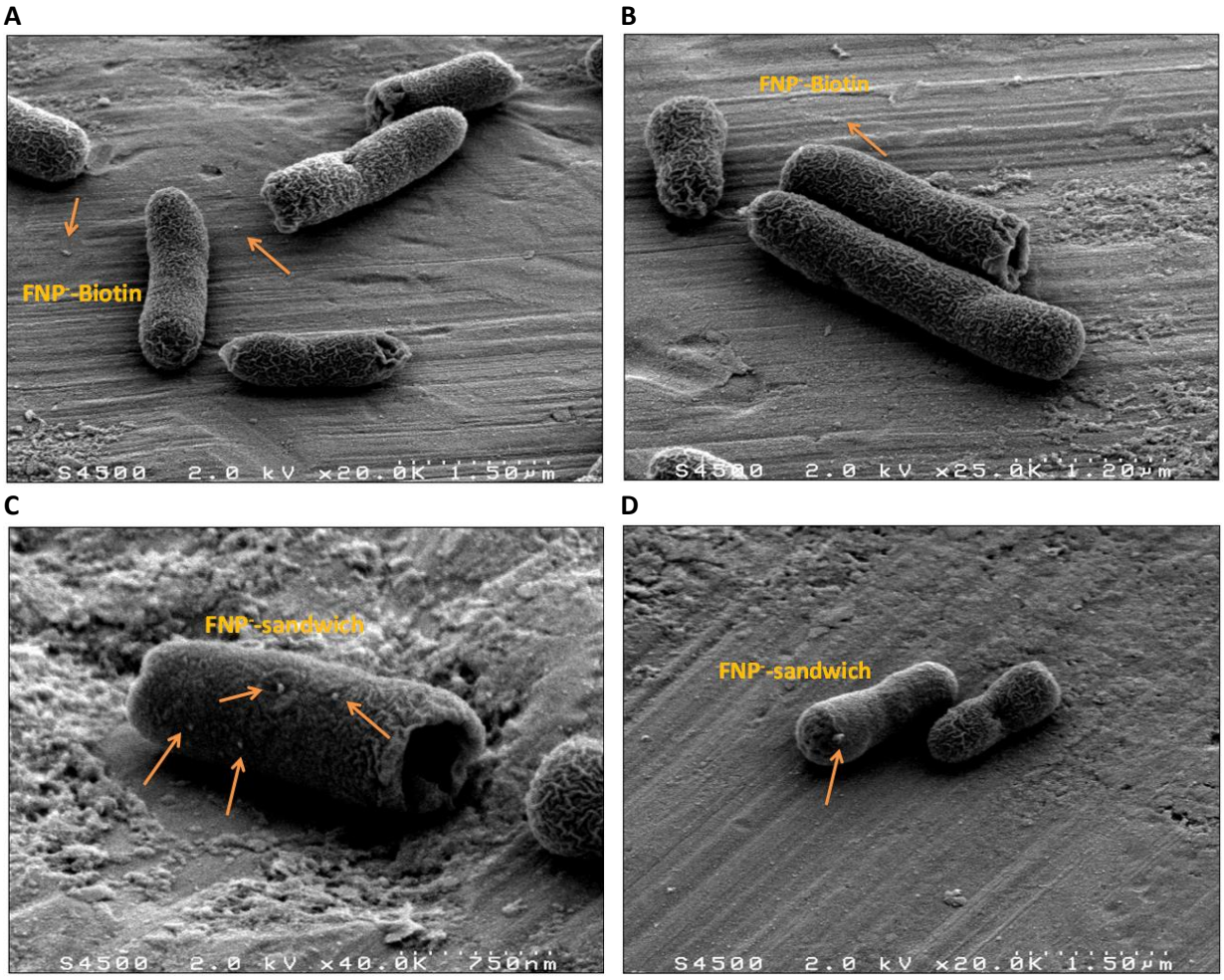



**Figure 3.9** SEM images of *E.coli* with FNP⁻-biotin without streptavidin (A, B) and with streptavidin (C, D). Additional images are shown in **Figure S3.4 in Section 3.5**.

Without adding streptavidin, the sandwich is not built, and particles are hardly found on the membrane of bacteria (**Figure 3.9A, B**). When adding streptavidin, the sandwich is built and, we can find particles bound to the surface membrane of the bacteria which indicates the successful formation of the sandwich system (**Figure 3.9C, D**).

### 3.2.6 Sandwich complex in a microfluidic device

In order to improve and also to develop a new device to target bacteria, microfluidic system was introduced in our experiments. From previous experiments, I often observed a strong affinity of FNP⁻ for glass surface: particles tended to attach to microscope slides. They proved out to be difficult to wash away after bonding. This unique property gave us the idea

to build a sandwich system on a microscope slide to "catch" bacteria and target bacterial membrane more efficiently than in solution.

In order to measure the affinity of $FNP^-$-biotin particle to glass and to determine which suitable $FNP^-$-biotin amount is needed, a 6 channel µ-Slide (µ-Slide VI 0.4, IBIDI) was used as shown in **Figure 3.10**. 30 µL $FNP^-$-biotin particle solutions in PBS at different concentrations (0.01, 0.04, 0.07, 0.1 nM) were injected into the µ-Slide channels. After 10 minutes waiting to let the particles attach on the surface, 1mL PBS was flowed three times to wash away excess $FNP^-$.

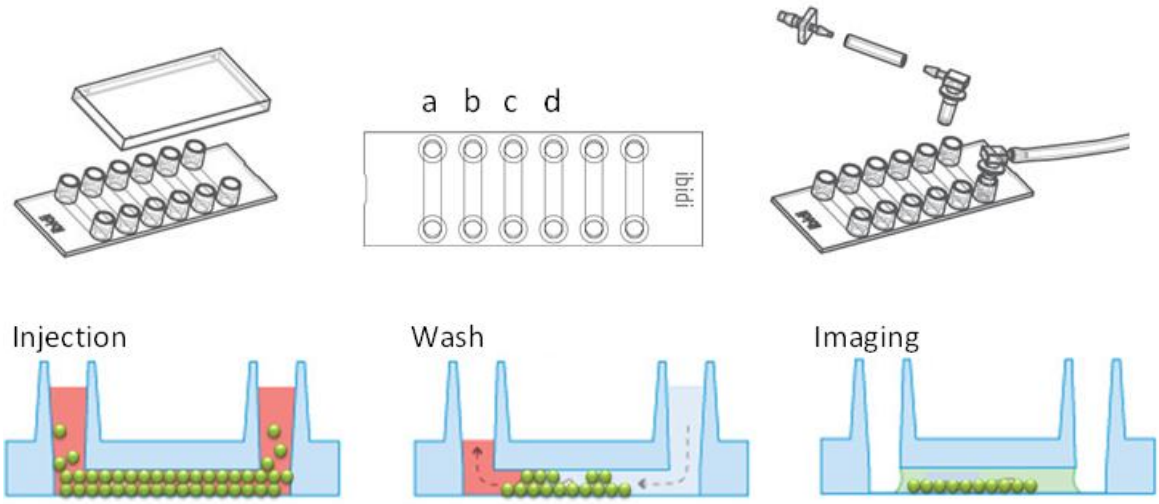



**Figure 3.10** Flow experiments for $FNP^-$-biotin (a: 0.01, b: 0.04, c: 0.07, d: 0.1 nM) on µ-Slide channel (figure adapted from IBIDI[197]).

Images of $FNP^-$-biotin particles attached on the slide surface before and after washing are shown in **Figure 3.11**. After injection of particles inside the channels, $FNP^-$-biotin particles stick on the surface (**Figure 3.11 A**). It is noteworthy that even with the lowest concentration (0.01 nM) of particle solution, the number of $FNP^-$-biotin is huge. A lot of particles stick to the surface giving a strong fluorescent background and particles can't be identified. After the first washing (**Figure 3.11 B**), the background signal became less strong, however particles could still not be identified clearly , the particles surface density seems too high, we aim at less surface coverage. After the second washing (**Figure 3.11 C**), a lot of particles still stick on the surface and there is no visible difference between the four different concentrations of $FNP^-$-biotin used. It means that the lowest concentration (0.01nM) is already enough, so I washed channel "a" (**Figure 3.10**) which contained the

lowest concentration of particles twice more. And finally, after the fourth washing, I obtained a channel with particles stuck on the surface quite homogeneously and $FNP^-$-biotin particles fluorescent signal could be identified clearly. This seems to be a suitable condition to build the "sandwich system" (**Figure 3.11E**).

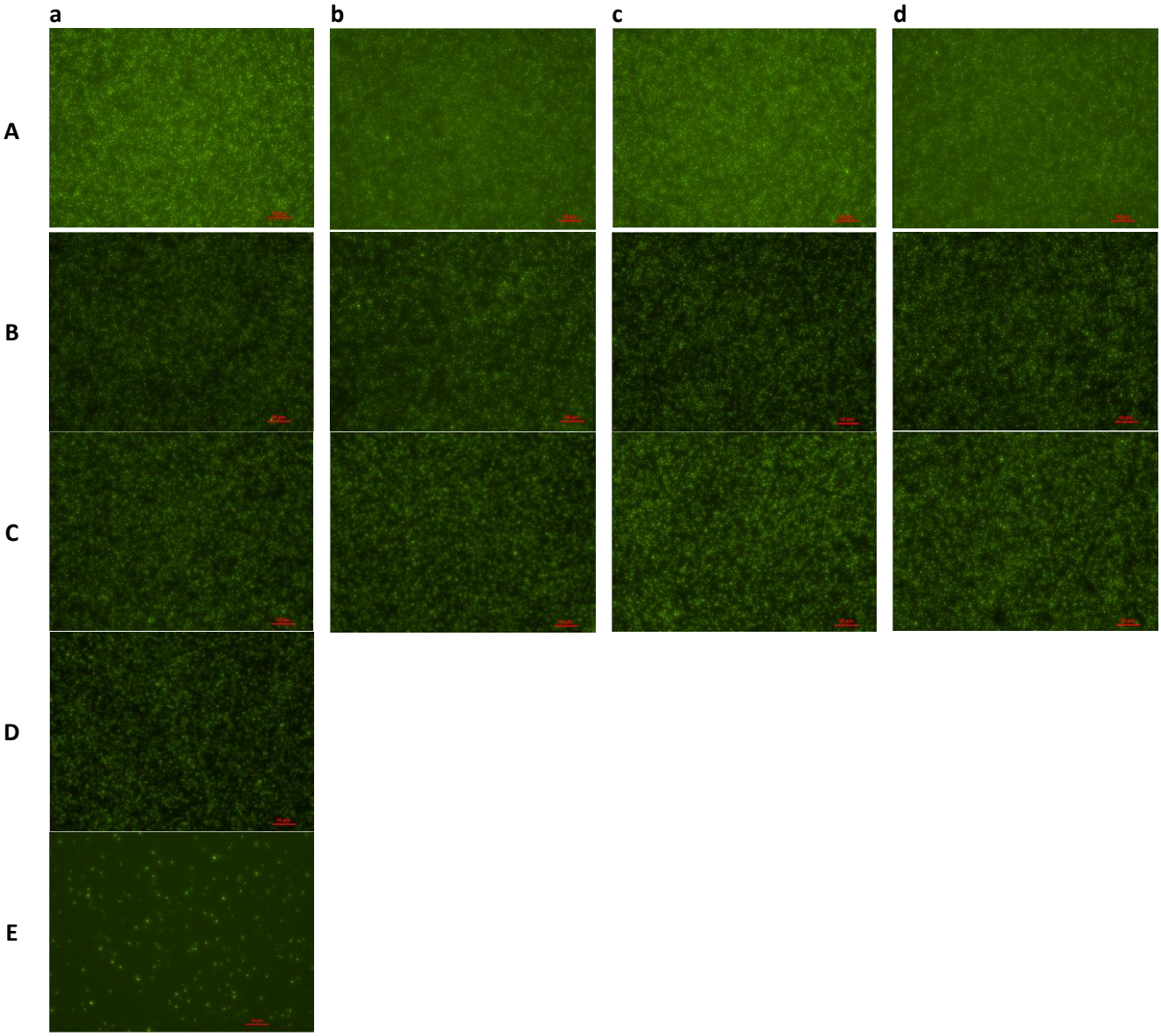



**Figure 3.11** Fluorescence images of particles $FNP^-$-biotin (a: 0.01, b: 0.04, c: 0.07, d: 0.1 nM) attached on the slide surface before (A) and after washing (B: wash once, C: wash twice, D: wash three times, E: wash four times)-(60X objective, IT=5s).

After optimizing and obtaining a suitable $FNP^-$-biotin particle surface, streptavidin solution (4nM) was injected to the channel in order to bind the $FNP^-$-biotin particles. After gently washing away the unattached streptavidin, primary antibody solution (88nM) was injected to the channel to bind the streptavidin and build the "sandwich system". Finally, 30 µL bacterial solution with an initial concentration of 5x $10^7$ CFU/mL (OD=0.5) was injected

inside the channel and left for about one hour at room temperature. The whole process is depicted in **Figure 3.12**.

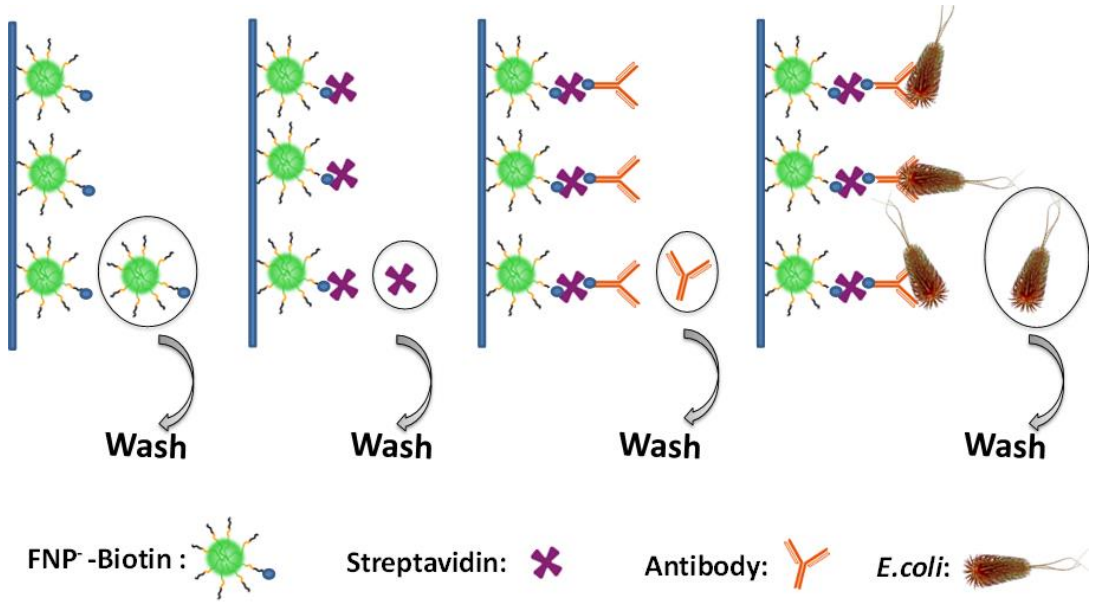
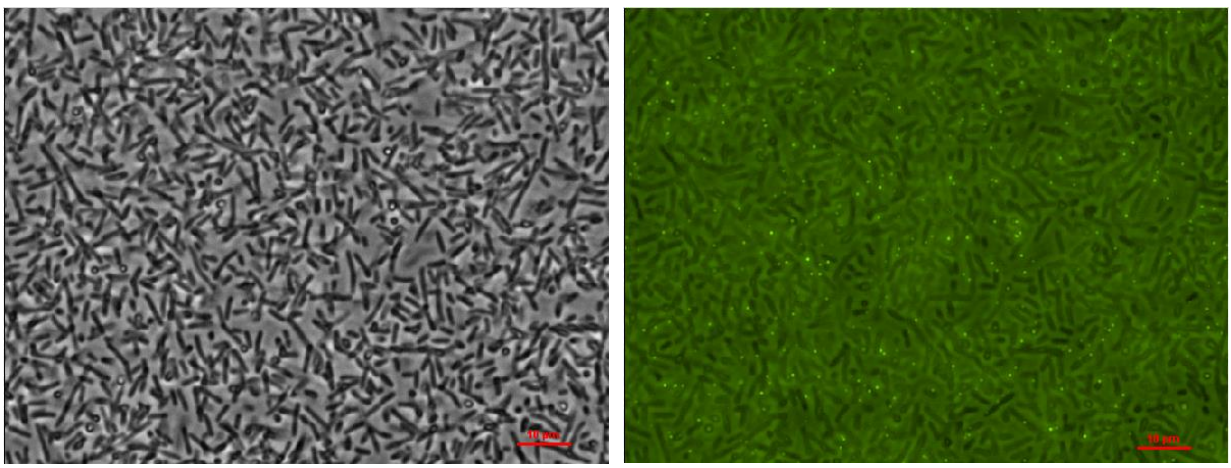



**Figure 3.12** Process to form the "sandwich system" on a microscope slide.

It is not possible to detect bonding of streptavidin and antibody to FNP⁻-biotin by microscopy. However, after one hour incubation, bacteria filled the channel as shown in **Figure 3.13A**. It is very difficult to distinguish individual cell or to tell if they are linked to particle from the fluorescence image (**Figure 3.13B**), so I tried to wash free bacteria away. The cells are gently washed by PBS twice. After the first wash, most of the unbound cells have been washed away (**Figure 3.13C**). However there are still a lot bacteria remaining. Even if all the bacteria are associated with particles (**Figure 3.13D**), it is still difficult to identify each bacteria and particle location.

**A** **B**



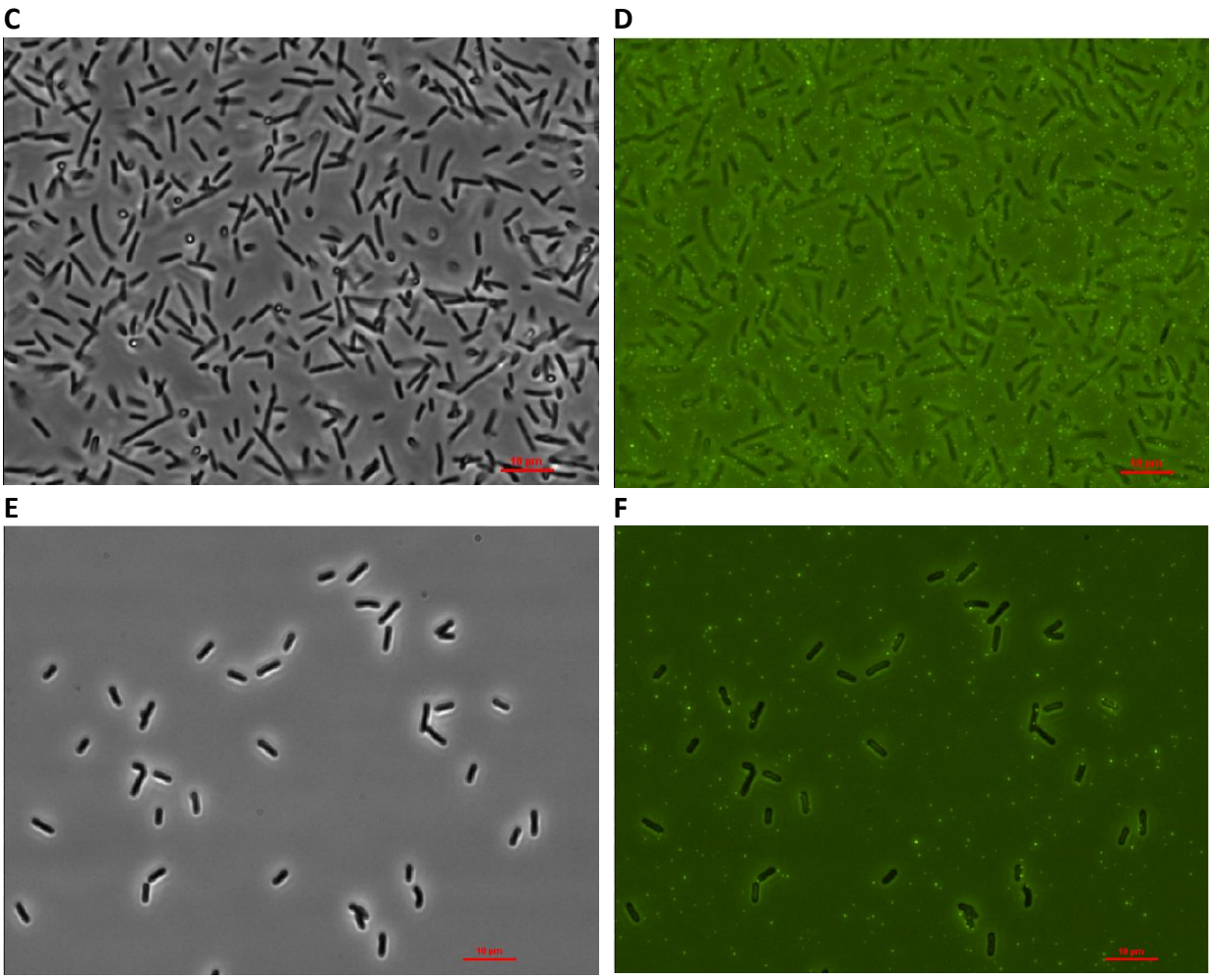



**Figure 3.13** Images of particle $FNP^-$ based "sandwich system" on microscope slide to "catch" bacteria before (A, B) and after washing (C, D: wash for once, E, F: wash for twice). (60X objective, A, C, E: phase contrast image, IT=200ms. B, D, F: fluorescence image overlap with phase contrast image, IT=5s). Additional images are shown in **Figure S3.3 in Section 3.5**.

After the second washing process, all the unattached bacteria have been washed away (**Figure 3.13E**) and only the ones targeted by the "sandwich" are left behind. Each individual bacterium is clearly and easily identifiable. Fluorescence images have shown that particles and bacterium can be been seen clearly, and are very homogenously distributed on the slide. Moreover every bacterium is linked to particles indicating that the "sandwich system" on microscope slide can "catch" bacteria and target bacterial membrane effectively.

## 3.3 Design of "Nanoparticle-Antibody" for targeting bacterial surface

In the "sandwich system", it takes three agents to link the $FNP^-$ to antibody which can target bacteria ($FNP^-$-biotin-streptavidin-biotin-antibody). Even if it is proved that "sandwich system" was successfully obtained, the targeting efficiency on bacteria is not very high. This may come from the several formation steps of "sandwich". Is it possible to link $FNP^-$ directly

on primary antibody? The answer is yes. On the surface of antibody , there are a lot of amino acid residues[198]. Since the $FNP^-$ surface is covered with acrylic acids groups, we can conjugate directly antibody on the particles' surface by coupling reaction.

As I described in **Chapter 2**, $FNP^-$ is a core shell structure nanoparticle with poly(styrene-*co*-BDPMA1) in the core and poly(ethylene oxide)-*block*–poly(acrylic acid) (PEO-*b*-PAA) in the shell (**Figure 3.14A**). The poly(acrylic acid) block used in the particle is designed for post-functionalization. In the "sandwich system", I introduced biotin conjugated to these acrylic acids units. However, from the structure displayed in **Figure 3.14A**, one can notice that these acrylic acids units are "hidden" by the poly(ethylene oxide) (PEO) which in the most outside layer of the shell. This structure may affect the accessibility of the reaction between the biotin and acrylic acids. Thus, I changed to another type of fluorescent nanoparticle (FNPB, **Figure 3.14B**) synthesized by Chloé Grazon[27] with a different shell architecture which might be more efficient for antibody conjugation experiments.

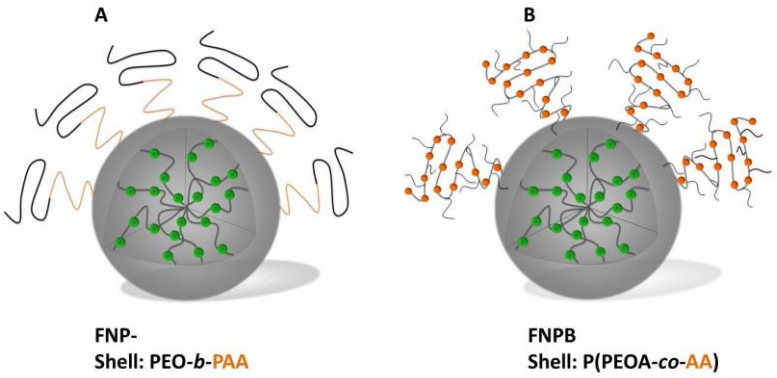
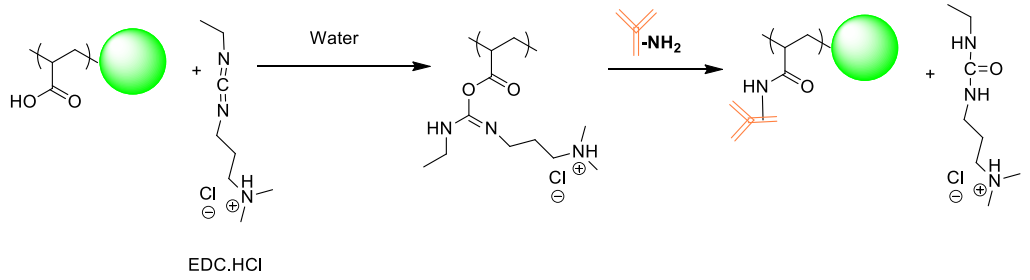



**Figure 3.14** Structures of $FNP^-$(A) and FNPB (B)-(figure adapted from[27]).

In FNPB, the PEO-*b*-PAA shell was replaced by a randomly distributed copolymer of acrylic acid (AA) and poly (ethylene oxide) methyl ether acrylate (PEOA) as P (PEOA-*co*-AA). Structure of $FNP^-$ and FNPB are displayed in **Figure 3.14**, one can notice that the linear chains (PEO-b-PAA) in $FNP^-$ is replaced by branched chains (P (PEOA-*co*-AA)) in FNPB. Acrylic acids units are now more accessible and some of them lie in the outside layer of the shell. This architecture is better for bioconjugation experiments. The full characterization of the FNPB was investigated by Chloé Grazon[27]. Here, I carried on experiments to conjugate anti-*E.coli* antibody on FNPB, and made some preliminary tests on *E.coli* bacteria labeling.

A schematic representation of FNPB conjugated with antibody is shown in **Scheme 3.4**. The chemical bonding of the antibody to the nanoparticle was possible starting from amino acid residues on antibody that can react with the carboxylic acids present on the surface of FNPB. It was thus similar to the reaction used to transform $FNP^-$ into $FNP^+$ presented in **Chapter 2 (§2.1)**. In a typical experiment, the total number of acrylic acid units present on the surface of the branch chains fluorescent nanoparticles (FNPB) was taken as 1 equiv. Anti-*E.coli* antibody (4 equiv.) and EDC.HCl (4 equiv.) were added to react with the acrylic acids on the surface of the $FNP^-$ and get maximum conversion.




**Scheme 3.4** Synthetic pathway for antibody conjugated on FNPB.

As said before, it was difficult to characterize the conjugation by conventional method (*e.g.* NMR or IR). Absorption and fluorescence spectra of FNPB and FNPB-antibody were recorded as shown in **Figure 3.15** and their main spectroscopic data are given in **Table 3.2**. The FNPB particle in PBS shows a maximum absorption band at 529nm, and a maximum emission band at 541nm. The FNPB-antibody shows very similar absorption and fluorescence spectra as FNPB (**Figure 3.15A**) except that the FNPB-antibody exhibits a more intense bond in the UV region at around 380nm. This is probably due to the light scattering by the conjugated antibody which are relatively large (150 kDa[194]). The excitation spectra for FNPB and FNPB-antibody have the same aspect and superimpose to their respective absorption spectra (**Figure 3.15B**). In PBS the fluorescence quantum yield of FNPB is 42% and the one for FNPB-antibody is 28% indicating that formation of the "nanoparticle-antibody" may decrease the quantum yield of FNPB.

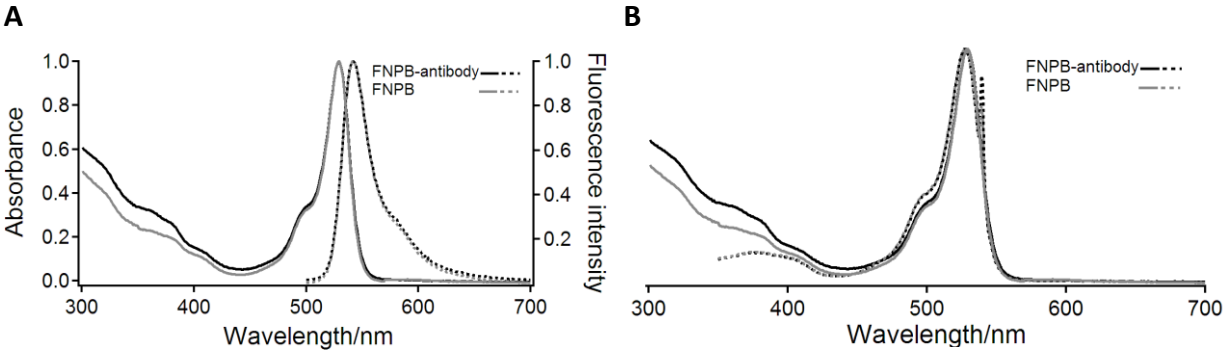



**Figure 3.15** FNPB (grey lines), FNPB-antibody (black lines) in PBS: absorption (A, B full lines) and fluorescence emission (A, dotted lines, $\lambda_{exc}$=495nm) and excitation (B dotted lines, $\lambda_{emi}$=541nm) normalized spectra.

**Table 3.2** Main spectroscopic properties of FNPB, FNPB-antibody

| Sample | $\lambda_{abs}$ /nm | $\lambda_{em}$ /nm | $\Phi_F$/% PBS[a] | Brightness/ $M^{-1}$ $cm^{-1}$[b] |
|---|---|---|---|---|
| FNPB | 529 | 541 | 42 | $5.3x10^7$ |
| FNPB-antibody | 529 | 541 | 28 | $3.5x10^7$ |

[a] Error of 15%[182]; [b] Brightness is determined by **Equation 7.5 in Chapter 7**.

After a preliminary characterization of antibody conjugated nanoparticle, I applied the FNPB-antibody to label the bacterial membrane. Bioimaging of the FNPB-antibody targeting bacterial membrane was measured by fluorescence microscopy. **Figure 3.16A** is the phase contrast image of bacteria, FNPB-antibody can label the bacterial outer membrane as shown in fluorescence image in **Figure 3.16B**.

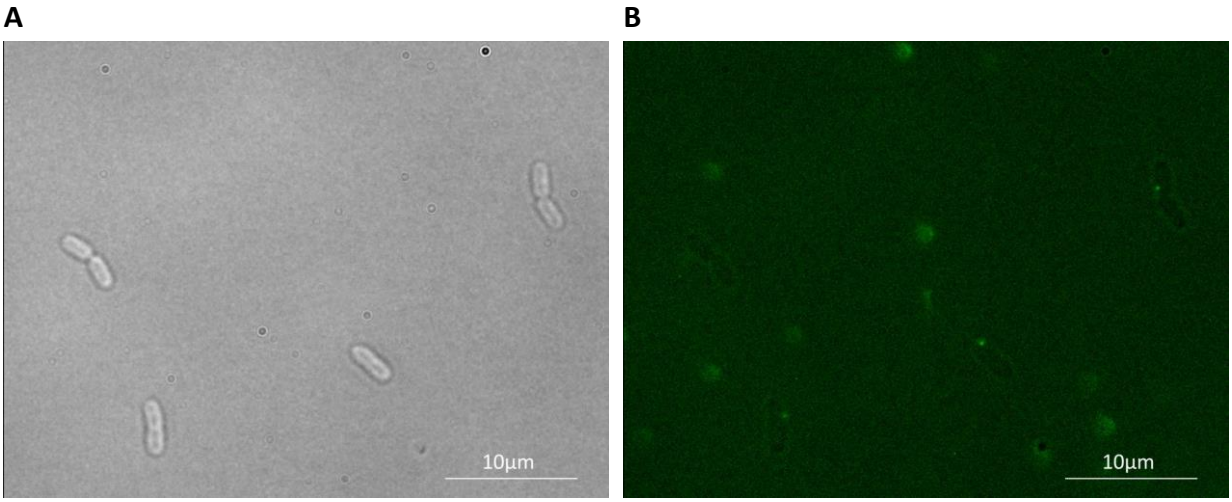



**Figure 3.15** Bioimaging of "nanoparticle-antibody" targeted on bacterial surface. (100X objective, A: bright field image, IT=500ms, B: fluorescence image overlap with bright field image, IT=500ms). Additional images are shown in **Figure S3.5 in Section 3.5**.

However, these are very preliminary results, more investigations are needed such as more characterizations of FNPB-antibody, and more experiments to confirm the microscopy

experiments. The FNPB-antibody method is easier to be generated compared with the "sandwich" method. If the reproducibility can be proved, we can change the general anti-*E.coli* antibody to specific antibody for particular protein on bacterial membrane such as the antibody for protein controlling the growth of flagella. Using "nanoparticle-antibody" system to label this specific protein may allow us tracking the growth of flagella.

## 3.4 Conclusion

In this chapter, I presented two methods to target bacterial membrane with fluorescent nanoparticles: the "sandwich system" and the "nanoparticle-antibody" system.

In order to target *E.coli*'s outer membrane with $FNP^-$, a "sandwich system" was created (**Figure 3.16**). *E.coli* can be targeted with an antibody conjugated with biotin. The binding of biotin to streptavidin is one of the strongest non-covalent interactions known in nature. After conjugating the biotin to nanoparticles and then with a streptavidin, we can use the particle based "sandwich system" to target the bacteria *E.coli*'s outer membrane.

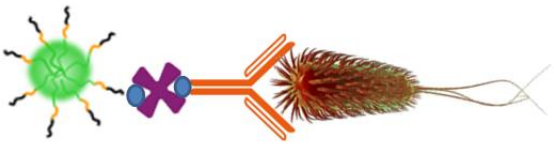


**Figure 3.16** Strategy for particle based "sandwich system"

In order to characterize the formation of sandwich, I divided it into four different parts: $FNP^-$, $FNP^-$ -biotin, $FNP^-$ -biotin-streptavidin, $FNP^-$ -biotin-streptavidin-antibody. I analyzed each part of the sandwich, and studied their properties and compared them with each other.

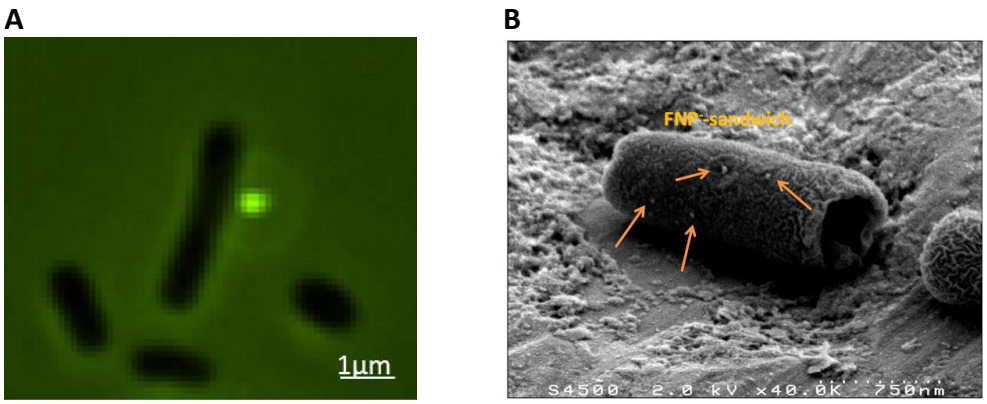



**Figure 3.17** Bioimaging of particle based "sandwich system" targeted on bacterial surface. A: Epifluorescence image. B: SEM image

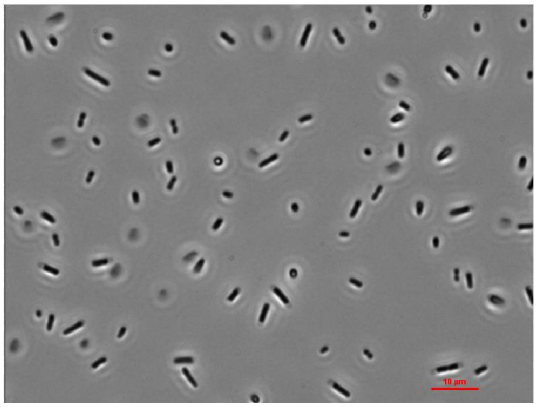
In the "sandwich system", it takes three agents to link the $FNP^-$ to antibody which can target on bacteria ($FNP^-$ -biotin-streptavidin-biotin-antibody). Even if it is proved by fluorescence (**Figure 3.17A**) and SEM (**Figure 3.17B**) that the "sandwich system" was successfully obtained, after applying it to label bacterial membrane, the targeting efficiency on bacteria is not very high. This may come from the several steps to form the sandwich. It was very difficult to obtain many cells targeted by particle. Moreover it was difficult to tell if the particle were really linked on the surface of bacteria.

In order to simplify this approach, we attempted to directly graft the anti-*E.coli* antibody to the FNPB but the characterization of the reaction is still underway. I applied the FNB-antibody to label the bacterial membrane, after a preliminary test, the particles conjugated with antibody can label bacterial outer membrane. However, this approach needs to be investigated more.

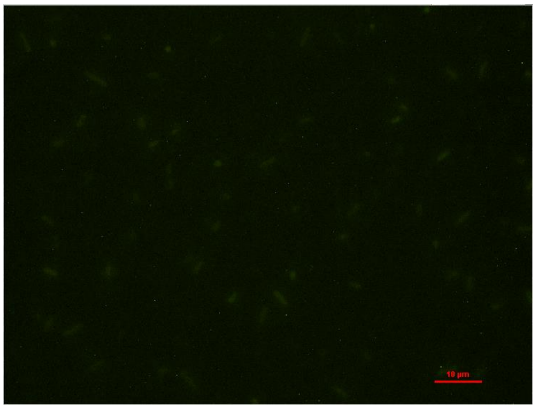
In the next chapter, I will describe several smaller fluorescent nanomaterials: Fluorescent polymer chains (FPCs). I will show the interaction of FPCs with *E.coli* bacteria and the bioimaging applications of these FPCs.

## 3.5 Additional images

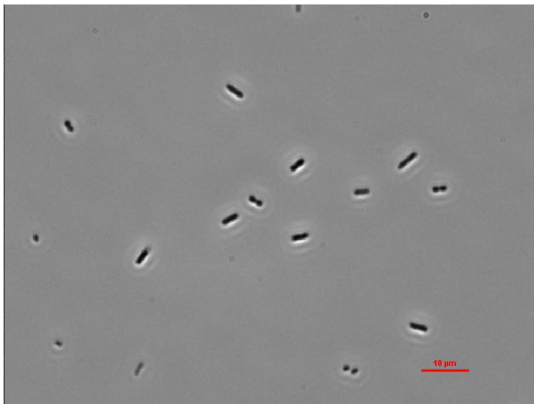
**A1**



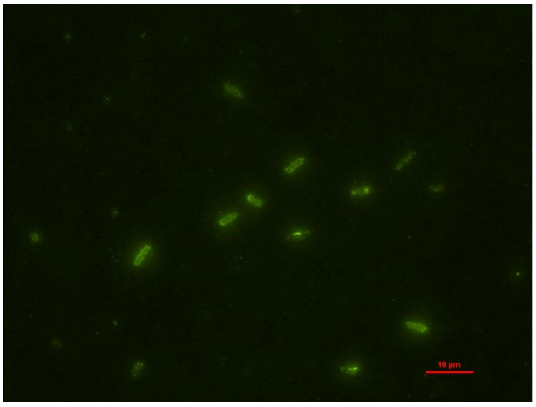
**B1**



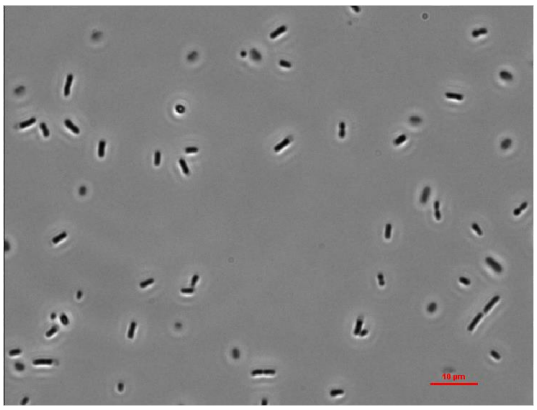
**C1**



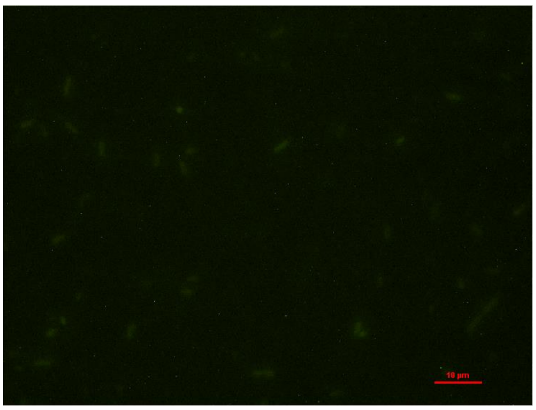
**D1**



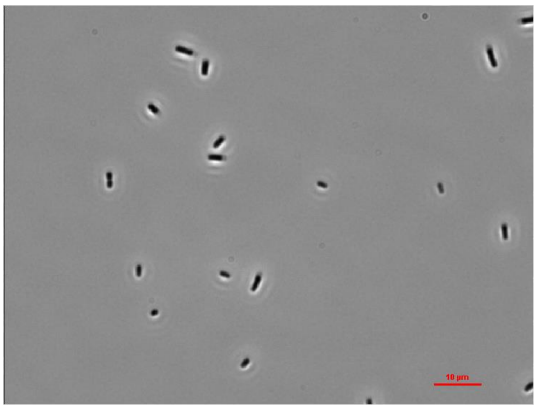
**A2**



**B2**



**C2**



**D2**

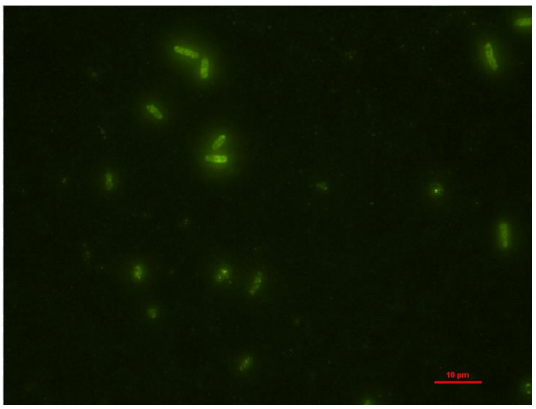


**Figure S3.1** Comparison of *E.coli* - secondary fluorescent antibody (A, B) and *E.coli*- primary antibody-secondary fluorescent antibody (C, D)(60X objective, A,C: phase contrast image, IT=200ms. B, D: fluorescence image, IT=5s).

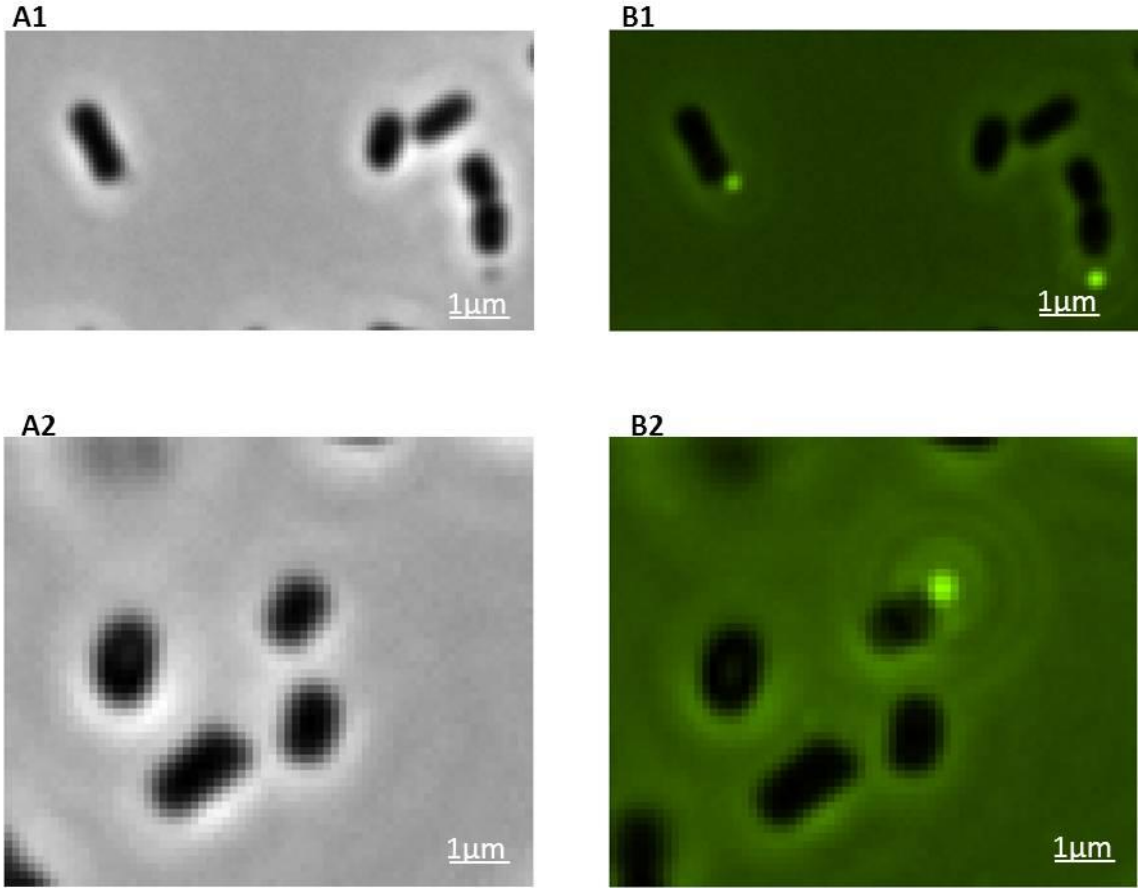



**Figure S3.2** Bioimaging of particle based sandwich system targeted on bacterial surface. (60X objective, A: phase contrast image, IT=200ms. B: fluorescence image overlap with phase contrast image, IT= 5s).

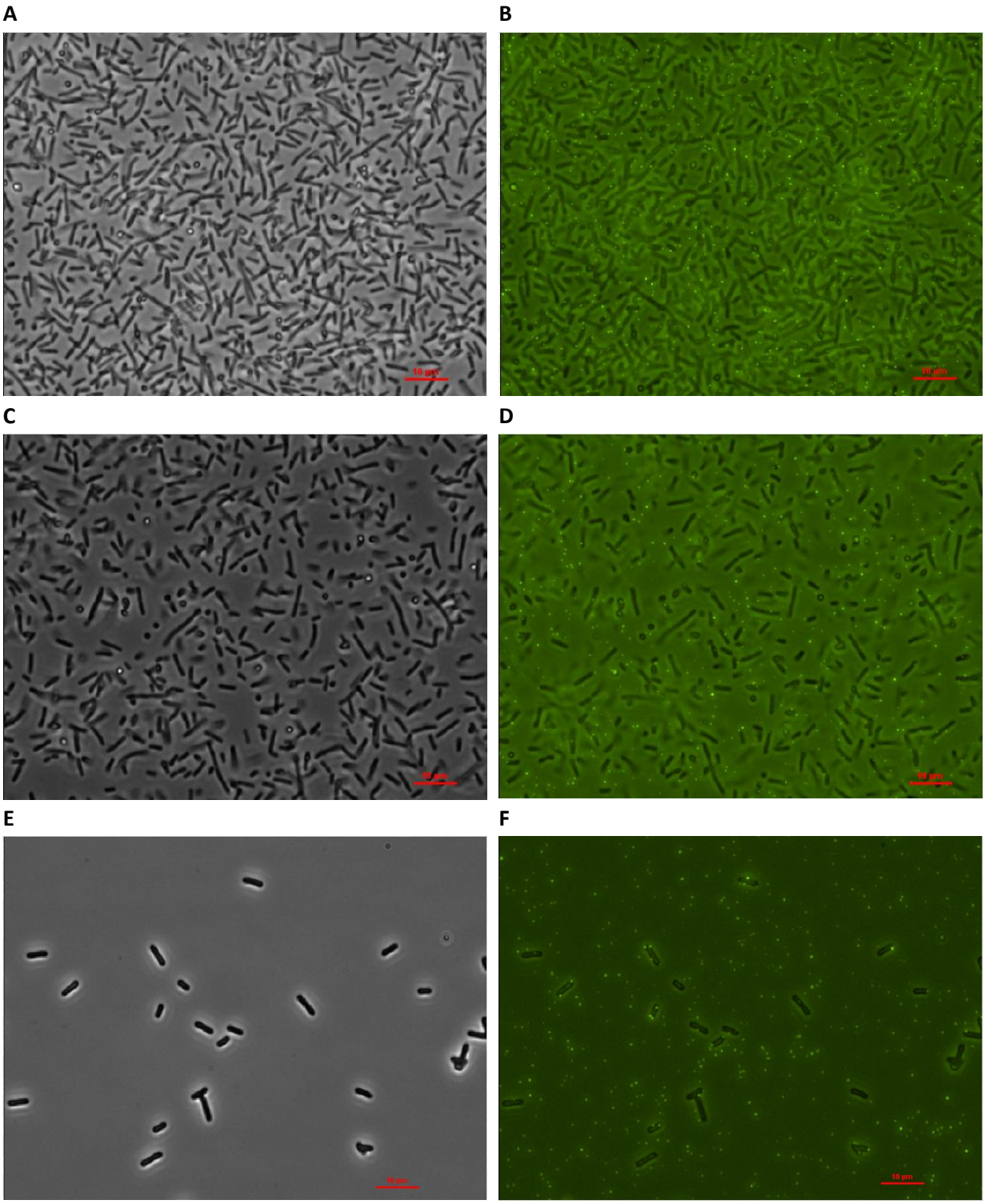



**Figure S3.3** Images of particle $FNP^-$ based "sandwich" system on microscope slide to "catch" bacteria before (A, B) and after washing (C, D: one time wash, E, F: two times wash). (60X objective, A, C, E: phase contrast image, IT=200ms. B, D, F: fluorescence image overlap with phase contrast image, IT=5s).

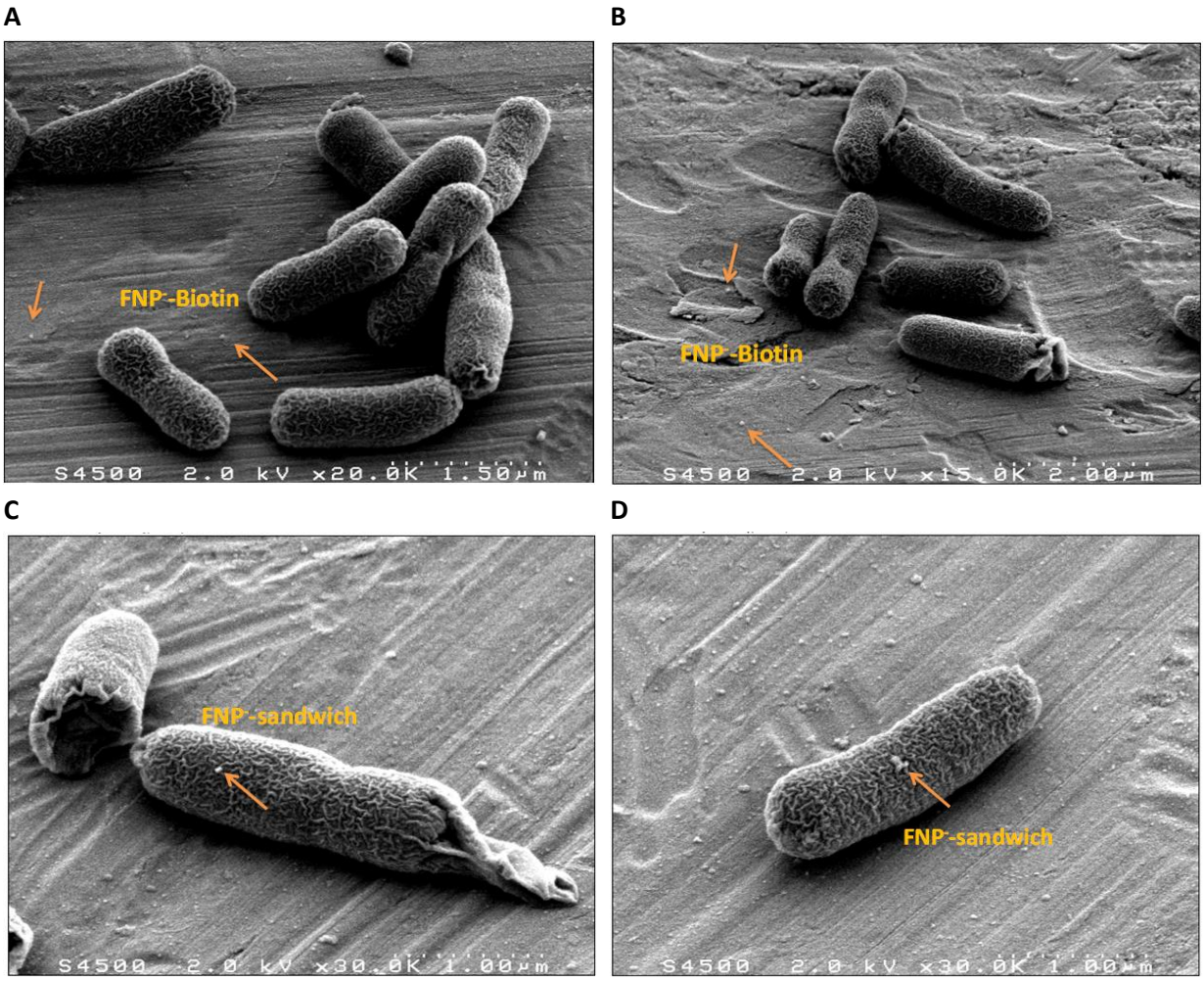



**Figure S3.4** SEM images of "sandwich" without streptavidin (A, B) and with streptavidin (C, D) labelling bacterial surface.

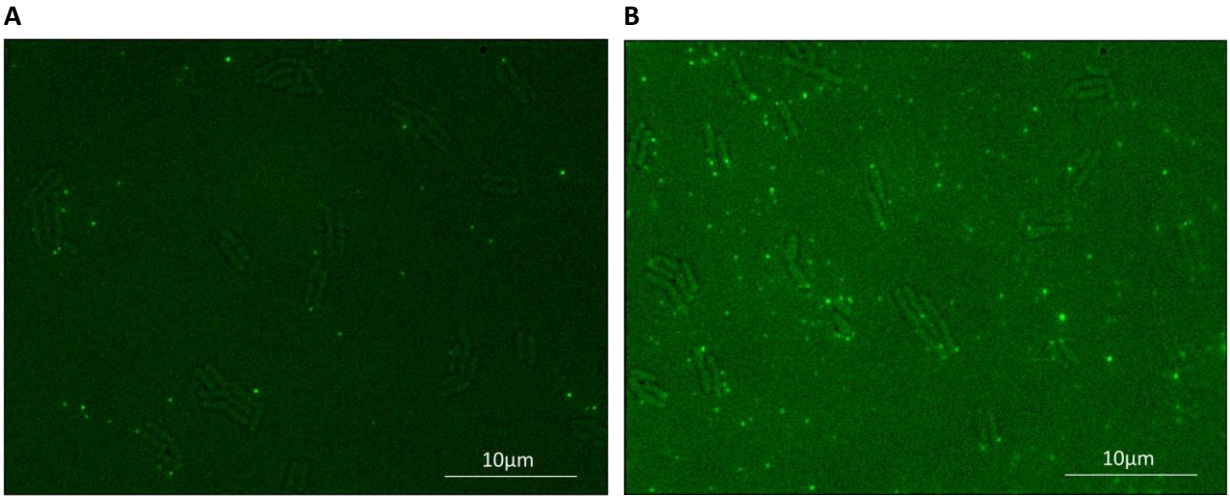



**Figure S3.5** Bioimaging of "nanoparticle-antibody" targeted on bacterial surface. (100X objective, fluorescence image overlap with bright field image).

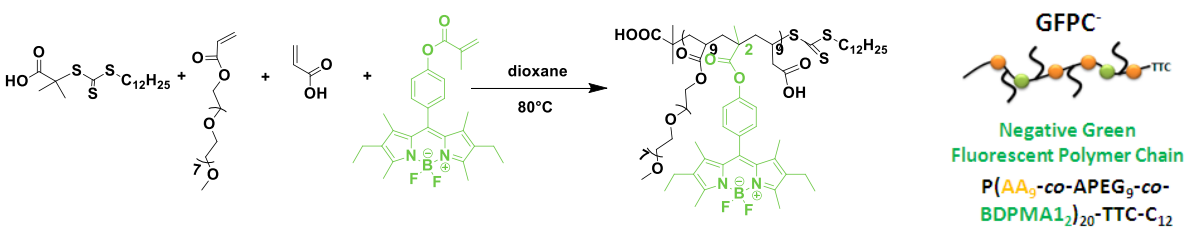
# Chapter 4 Fluorescent polymer chains (FPCs) for bioimaging of *E.coli* bacteria

In previous chapters, fluorescent nanoparticles were used for internal and surface bioimaging of *E.coli* bacteria. In chapter 1, we found that nanoparticles (65nm) are quite big and they can only be internalized in bacteria by electroporation. But it killed quite a lot of bacteria by this (40% survive). So, we wondered if it was possible to synthesize some small fluorescent nanomaterials which can enter easier inside bacteria. So, we had the idea to synthesis some polymer chains with a theoretical size of 4-6 nm.

In this chapter, I will present four different fluorescent polymer chains: negative green fluorescent polymer chain ($GFPC^-$), neutral green fluorescent polymer chain ($GFPC^0$), negative red fluorescent polymer chain ($RFPC^-$), positive red fluorescent polymer chain ($RFPC^-$). I will discuss their physical characterizations and their interaction with *E.coli* bacteria for potential internal and membrane fluorescent labelling application.

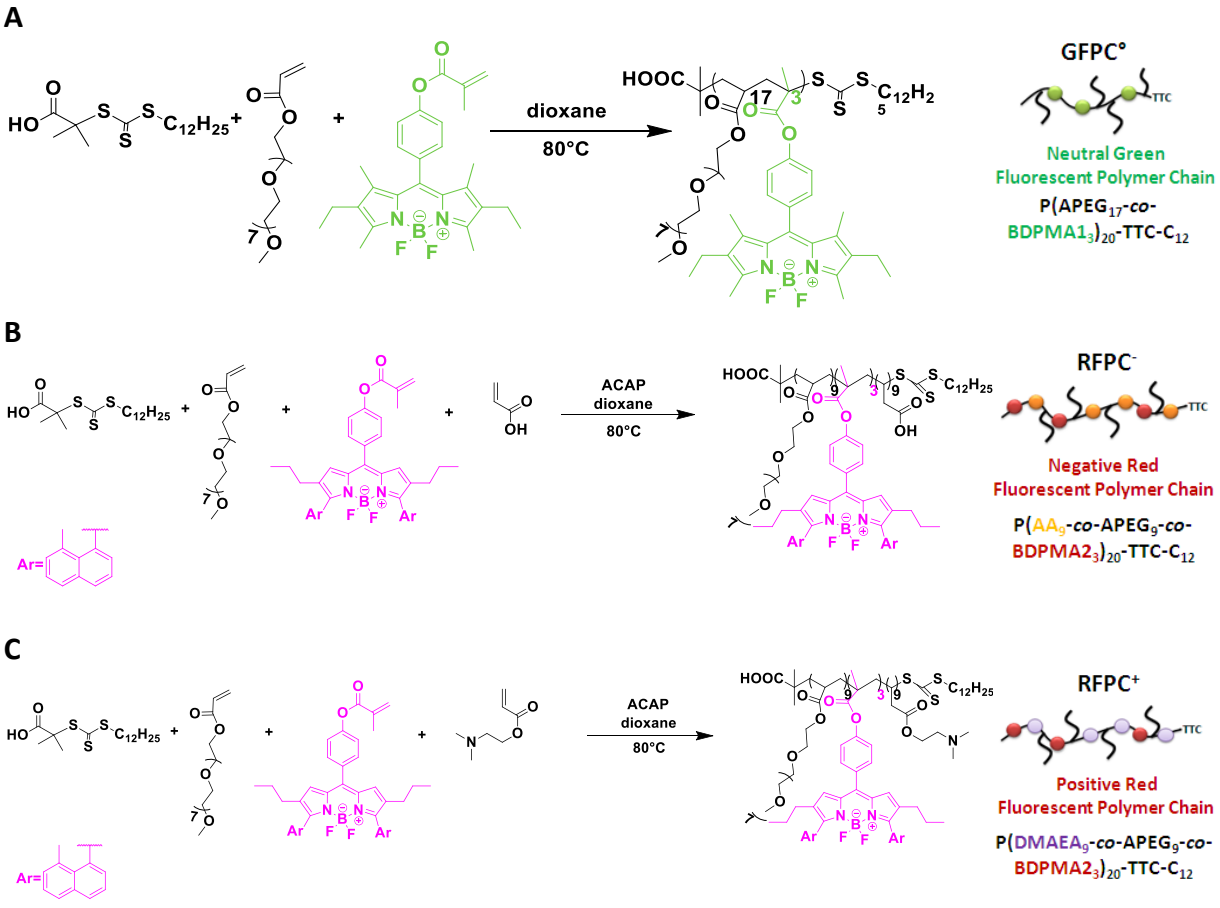
## 4.1 Synthesis of fluorescent polymer chains (FPCs)

The synthesis of fluorescent polymer chains was performed in a novel one-pot process based on a reversible addition-fragmentation chain-transfer (RAFT) polymerization method: a small RAFT agent and three different monomers: APEG, AA and BODIPY methacrylate-1 (BDPMA1) were dissolved in 1,4-dioxane at room temperature. After it was purged with nitrogen, the reaction of the mixture was initiated by simple heating to 80°C for 90 minutes. After RAFT polymerization, the reaction was stopped by immersion of the flask in iced water. Finally, after complete polymerization, a statistic and random copolymer (negative green polymer chain $GFPC^-$) was formed: $P(AA_9\text{-}co\text{-}APEG_9\text{-}co\text{-}BDPMA1_2)_{20}\text{-}TTC\text{-}C_{12}$ (**Scheme 4.1**). This polymer chain is negatively charged in water because the carboxylic acid group (-COOH, pKa around 4) will dissociate into $H^+$ cations and ($-COO^-$) anions in water (pH 6.8-7.0).




**Scheme 4.1** Synthetic pathway for negative green fluorescent polymer chain ($GFPC^-$).

All four different FPCs have been synthesized (see experimental detail in **Chapter 7, §7.2.4**) with a similar architecture but different monomers in order to obtain products with a different charge and color: In GFPC°, the AA monomer was not added during the one-pot polymerization process in order to obtain a neutrally charged green polymer chain: P(APEG$_{17}$-*co*-BDPMA1$_3$)$_{20}$-TTC-C$_{12}$ (**Scheme 4.2A**). In order to make RFPC$^-$, the BODIPY methylnaphthalene-2 (BDPMA2) monomer was used in order to obtain a red shift in absorption and fluorescence emission and we obtained the negative red polymer chain: P(AA-*co*-APEG-*co*-BDPMA2)-TTC-C$_{12}$ (**Scheme 4.2B**). In order to obtain RFPC$^+$, 2-(Dimethylamino)ethyl acrylate (DMAEA) was used instead of acrylic acid (AA) in order to obtain positively charged red polymer chain: P(DMAEA-APEG-*co*-BDPMA2)-TTC-C$_{12}$ (**Scheme 4.2C**). It is positively charged in water because the amine group (NR$^3$, pKa around 9) will dissociate into N$^+$ cations and R$^{3-}$ anions in water (pH 6.8-7.0). All polymer chains have a theoretical size of around 4-6 nm.




**Scheme 4.2** Synthetic pathways for neutral green fluorescent polymer chain (GFPC$^0$)(A), negative red fluorescent polymer chain (RFPC$^-$)(B), positive red fluorescent polymer chain (RFPC$^-$)(C).

## 4.2 Characterizations of Green fluorescent polymer chains (GFPCs)

In order to characterize the green fluorescent polymer chains (GFPCs), samples were withdrawn regularly during polymerization, dried and analyzed by size exclusion chromatography (SEC, cooperation with Dr. Jutta Rieger[‡]) in THF solution after methylation of the carboxylates. The SEC traces of copolymers obtained at different stages of the polymerization of GFPC$^-$ and GFPC° are displayed in **Figure 4.1**. The BDPMA1 conversion is determined by SEC using UV-vis detection ($\lambda_{abs}$= 528 nm)**.** It shows narrow symmetric peaks that are shifted towards shorter retention volumes (corresponding to higher molecular weight and longer polymer chains) upon progressing polymerization (**Figure 4.1A, C**). For GFPC$^-$, the polymerization reached 60% conversion of BDPMA1 after 4 hours (**Figure 4.1B**) which is slower compared with GFPC° (80%, **Figure 4.1D**). For GFPC$^-$, a reaction plateau period was observed after 4 hours and after 8 hours it reached a final conversion of 70% for BDPMA1. While for GFPC°, the final conversion of BDPMA1 is around 95%. This proves that along the chain of GFPC°, there is about 25% more BDPMA1 converted which resulted in there is one fluorophore more than the one of GFPC$^-$. The average molar mass, $M_n$, increase linearly with monomer conversion and are close to the theoretical values. Polydispersity indexes, $M_w/M_n$, are low (<1.3, **Table 4.1**). The miniemulsion copolymerization of fluorescent monomer thus exhibits the features of a living well-controlled polymerization.

**Table 4.1** Kinetic study of the synthesis of GFPC$^-$ and GFPC°

| Sample | Time/mins | BDPMA1 conv./%[a] | $M_{nth}$/ g/mol[b] | $M_{nSEC}$/ g/mol[c] | $M_w/M_n$[c] |
|---|---|---|---|---|---|
| GFPC$^-$a | 140 | 41 | 2741 | 2552 | 1.21 |
| GFPC$^-$b | 250 | 61 | 3710 | 3219 | 1.23 |
| GFPC$^-$c | 500 | 68 | 4452 | 4377 | 1.24 |
| GFPC$^-$d | 600 | **69** | 4841 | 4553 | 1.27 |
| GFPC°a | 80 | 7 | 1803 | 2126 | 1.11 |
| GFPC°b | 140 | 64 | 3597 | 4031 | 1.30 |
| GFPC°c | 250 | 81 | 6035 | 4932 | 1.25 |
| GFPC°d | 500 | 85 | 7412 | 5654 | 1.23 |
| GFPC°e | 600 | **95** | 7902 | 5958 | 1.27 |

[a] BDPMA1 conversion is determined by SEC (**Equation 7.1 in Chapter 7**), [b] theoretical number-average molar mass ($M_{nth}$) (**Equation 7.2 in Chapter 7**), [c] number-average molar mass ($M_{nSEC}$) and polydispersity index ($M_w/M_n$) are determined by SEC using a polystyrene calibration.

[‡] LCP laboratory (UMR 7610), UPMC Univ Paris 06, France

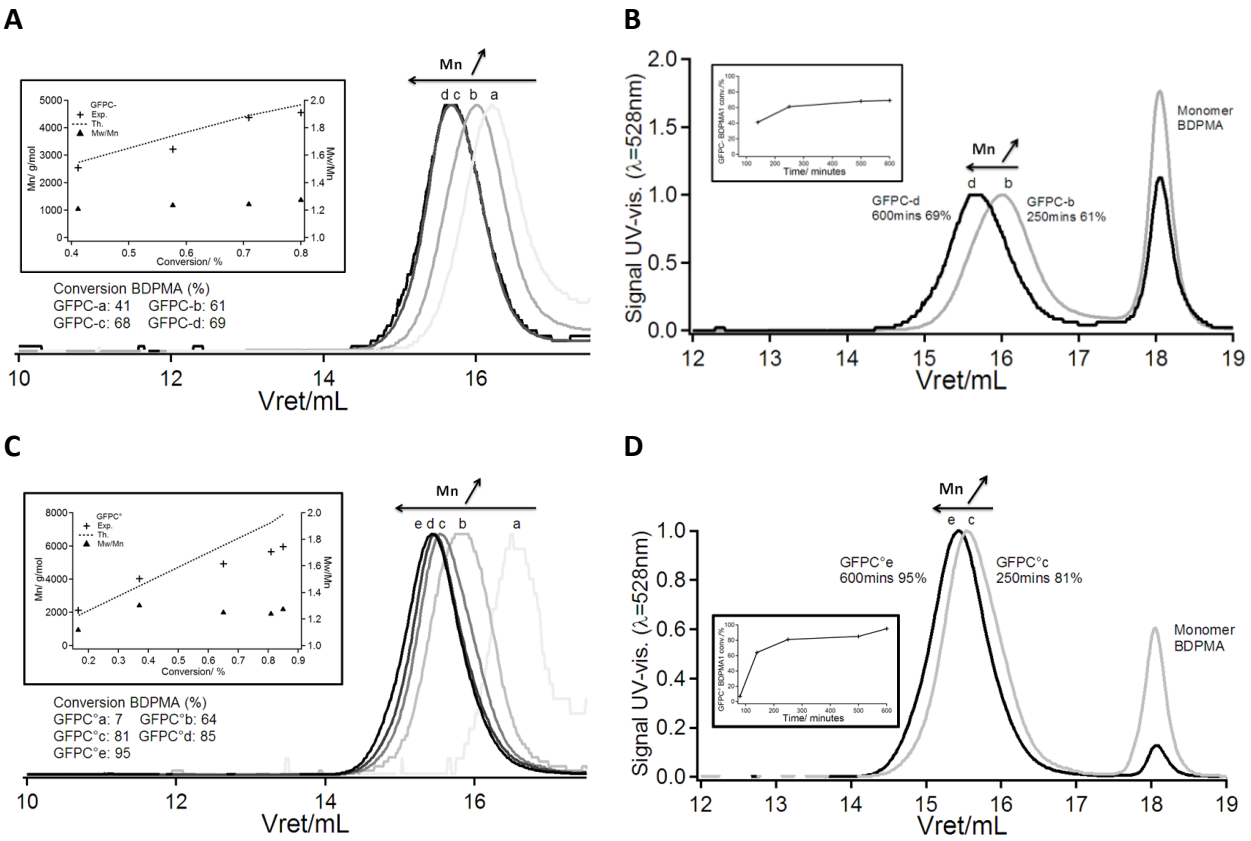



**Figure 4.1** Normalized size exclusion chromatograms (UV signal, $\lambda_{abs}$ = 528 nm) in THF for GFPC$^-$(A, B) and GFPC°(C, D), at different times of monomer conversions, and (inset A, C) evolution of the number-average molar mass ($M_n$, PS calibration) and $M_w/M_n$ vs. monomer conversion, and (inset B, D) evolution of BDPMA1 conversion/% vs. time/minutes. The straight line corresponds to the theoretical $M_n$ values (**Equation 7.2 in Chapter 7**). The indicated percentages % corresponds to the BDPMA1 conversion.

The critical micelle concentration (CMC) of GFPCs in water was determined at 20°C or in LB medium at 37°C by dynamic light scattering (DLS, cooperation with Dr. Jutta Rieger[§]) in order to determine the influence of temperature and growth medium. Different concentrations of GFPC$^-$ and GFPC$^0$ solutions were prepared and, the scattered light intensity at 90° was collected for these different samples. By plotting the intensity of scattered light as a function of GFPC$^-$ or GFPC$^0$ concentration, the CMC was determined at the intersection of the straight lines (**Figure 4.2**).

The critical micelle concentration (CMC) of GFPC- is about 0.3mg/mL in water at 20°C and 0.4mg/ml in LB medium at 37°C. For GFPC$^0$, the CMC is about 0.38mg/mL in water at 20°C and 0.5mg/ml in LB medium at 37°C (**Table 4.2**). The CMC of both GFPC- and GFPC$^0$ at 20°C is slightly higher than the one at 37°C, this is because the increase in temperature will

[§] LCP laboratory (UMR 7610), UPMC Univ Paris 06, France

cause entropy increases which induce the structure to break apart, and thus a higher concentration of surfactants is needed to form micelles. The CMC of $GFPC^-$ is always lower than the one of $GFPC^0$, this is perhaps because $GFPC^-$ is charged and the polar head of $GFPC^-$ are better located and organized than $GFPC^0$ which is more unorganized, randomly distributed in solution. The concentration of GFPCs that will be used in experiments with *E.coli* bacteria should be below the CMC so that the GFPCs are not aggregating to form micelles when incubated with *E.coli* bacteria.

**Table 4.2 Critical micelle concentration(CMC) for GFPCs**

| CMC/ $mg.ml^{-1}$ | 20°C/ water | 37°C/ LB |
|---|---|---|
| $GFPC^-$ | 0.3 | 0.4 |
| $GFPC^0$ | 0.38 | 0.5 |

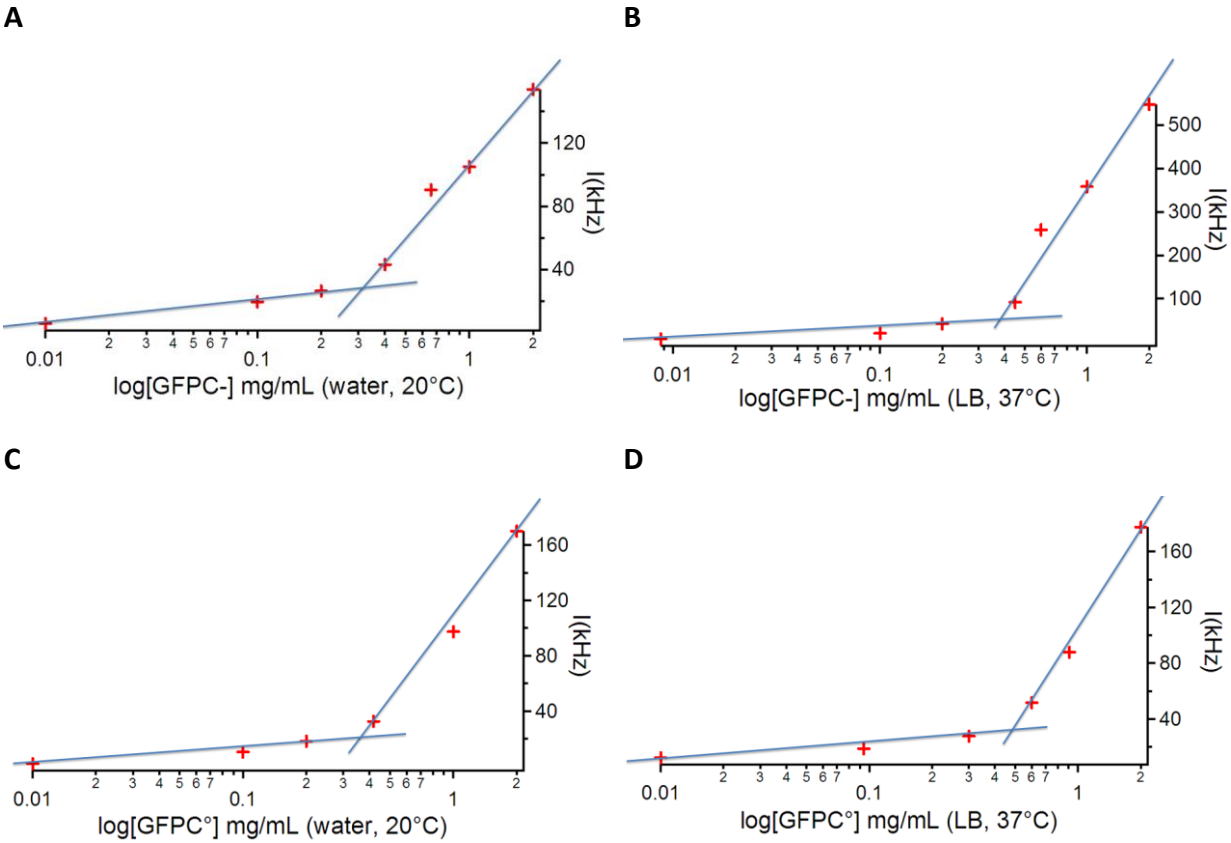



**Figure 4.2** Intensity of scattered light *vs.* molar concentration of $GFPC^-$ (A, B) and $GFPC^0$ (C, D). The intersection of the straight lines corresponds to the critical micelle concentration (CMC).

Fluorescence and absorption spectroscopy analysis of GFPCs are displayed on **Figure 4.3** and their main spectroscopic data are given in **Table 4.3**. The BDPMA1 monomer in toluene shows the expected spectra for BODIPY fluorophores[54] with an intense band in the

visible region located at 528 nm (corresponding to $\pi \rightarrow \pi*$ transition) and a vibrational shoulder at higher energy. A second, less intense band is located in the UV region at around 380 nm. The maximum of fluorescence emission is found at 540 nm, exhibiting a Stokes shift of 421cm$^{-1}$ (12nm).

The GFPCs exhibit very similar absorption and fluorescence spectra with a maximum absorption at 528 nm and a maximum of fluorescence emission at 548 nm. Both GFPC$^{-}$ and GFPC° are identical in shape and position, this shows that the addition of the AA monomer doesn't change the spectrum of GFPCs. The Stokes shift of the nanoparticles (691cm$^{-1}$, 20 nm) is slightly higher than the monomer. The red shift of the fluorescence emission is observed from the free monomer to the monomer copolymerized in a rigid environment[180]. One can also notice that the GFPCs absorption spectra exhibit a more intense vibrational shoulder which might also result from the BODIPY confined in a rigid polymer matrix (**Figure 4.3A**)[181]. The excitation spectra for GFPCs and the BDPMA1 monomer virtually superimpose with their respective absorption spectra (**Figure 4.3B**), showing that the absorbing and emitting species are identical. DLS signals of GFPC$^{0}$ (142nm) and GFPC$^{-}$ (84nm) are shown in **Figure 4.4,** compared with theoretical diameter (4-6nm), the measured diameters are much higher indicating presence of aggregation of GFPCs inside aqueous solutions.

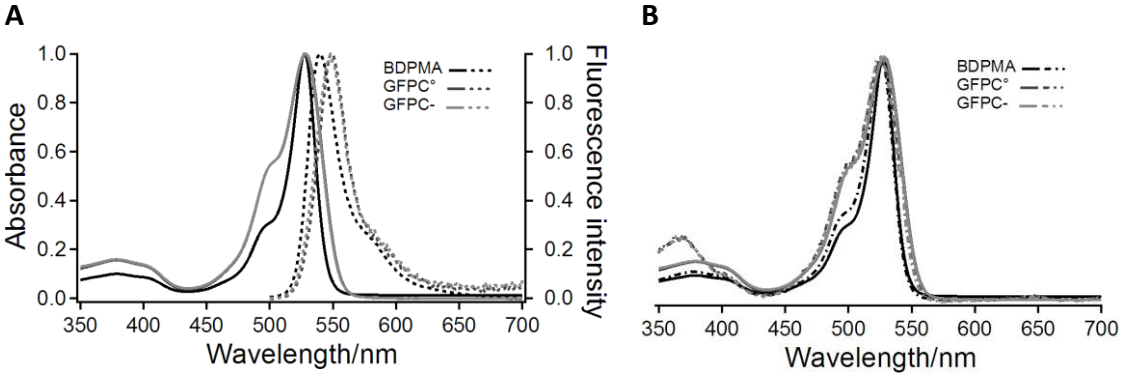



**Figure 4.3** BDPMA1 monomer in toluene and GFPCs in water (pH=7.0): absorption (A, B full lines), fluorescence emission (A dotted lines, $\lambda_{exc}$=495nm) and excitation (B dotted lines, $\lambda_{emi}$=548nm) normalized spectra.

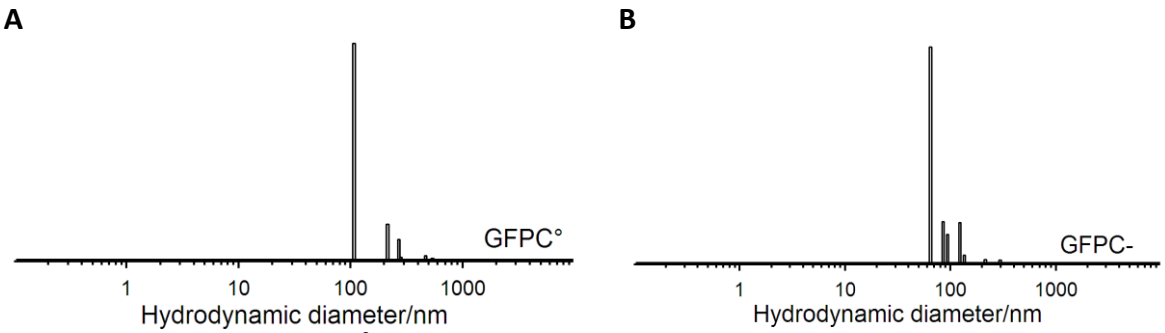



**Figure 4.4** DLS signals of $GFPC^0$ (A) and $GFPC^-$ (B) in water (pH 7).

**Table 4.3** Main spectroscopic properties of BDPMA1 and GFPCs

| | | water | | | toluene | | | | | | |
|---|---|---|---|---|---|---|---|---|---|---|---|
| Sample | Structure | $\lambda_{abs}$ /nm | $\lambda_{em}$ /nm | $\Phi_F$ /%[a] | $\lambda_{abs}$ /nm | $\lambda_{em}$ /nm | $\Phi_F$ /%[a] | BDPMA1 per chain | Brightness /$M^{-1}$ $cm^{-1}$[b] | $D_t$[c] /nm | $D_h$[d] /nm |
| BDPMA1 | - | - | - | - | 528 | 540 | 70 | - | 51100 | - | - |
| GFPC° | P(APEG$_{17}$-*co*-BDPMA1$_3$)$_{20}$-TTC-C$_{12}$ | 528 | 548 | 29 | 528 | 542 | 78 | 3 | 63510 | 4-6 | 142 |
| GFPC- | P(AA$_9$-*co*-APEG$_9$-*co*-BDPMA1$_2$)$_{20}$-TTC-C$_{12}$ | 528 | 548 | 20 | 528 | 542 | 74 | 2 | 29200 | 4-6 | 84 |

[a] Error of 15%[182], [b] Brightness is determined by **Equation 7.5 in Chapter 7**, [c] theoretical diameter($D_t$) [d] hydrodynamic diameter ($D_h$) determined by DLS in water.

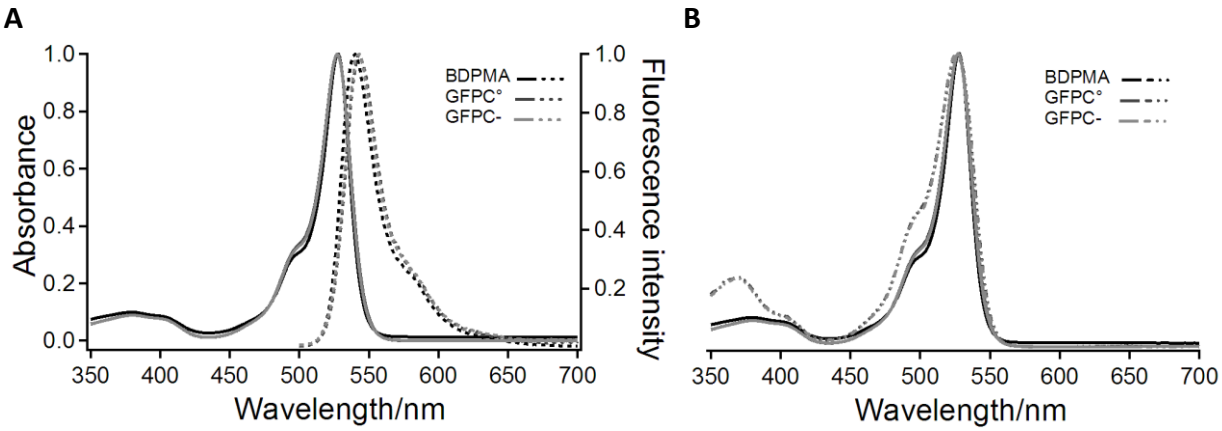



**Figure 4.5** BDPMA1 monomer and GFPCs in toluene: absorption (A, B full lines), fluorescence emission (A dotted lines, $\lambda_{exc}$=495nm) and excitation (B dotted lines, $\lambda_{emi}$=548nm) normalized spectra.

In water the fluorescence quantum yield of $GFPC^0$ is 29% while the one for $GFPC^-$ is 20%. The fluorescence quantum yield of BDPMA1 in toluene is 70%. This difference may be due to the aggregation of BODIPY along the same polymer chain. To confirm this hypothesis, I analyzed the $GFPC^0$ and $GFPC^-$ spectra in toluene (**Figure 4.5**). The fluorescence quantum yield is 78% for $GFPC^0$ and 74% for $GFPC^-$ (**Table 4.3**). Since toluene is a good solvent for this kind of polymer chains, they will be reformulated in it. The spectra of GFPCs in toluene are identical with the one of BDPMA1. So, there will not be any aggregation of BODIPY along the

same polymer chain. That is probably why the quantum yield of GFPCs in toluene is higher than the GFPCs in water.

## 4.3 Toxicity assessments of GFPCs on *E.coli*

Having synthesized and characterized the GFPCs, I next assessed the toxic effect of GFPCs on *E.coli*. In order to do this, the growth rates of bacteria in the presence of GFPCs were compared with the growth rates of *E.coli* bacteria alone. The growth rate was measured by using a 96-well plate reader (Perkin Elmer Victor3 1420 Multilabel Plate Counter). The GFPCs concentration used was $6.6x10^{-5}$M. The concentration of $GFPC^0$ or $GFPC^-$ (0.015-0.025 mg/mL) in all samples is below the CMC (0.3-0.5 mg/mL) of GFPCs, means that GFPCs are not aggregating to form micelles when incubated with *E.coli* bacteria.

Here, *E.coli* bacteria with GFPC° or $GFPC^-$ were incubated in the 96-well plate in plate reader at 37°C in the dark overnight. A control with only bacteria was also prepared. Every nine minutes the growth rate of the cells was monitored by measuring the optical density at 600nm (**Figure 4.6**). For over ten hours incubation, the growth curves of bacteria with GFPCs were practically the same as the growth curve of bacteria alone both in LB medium and M9 medium. This means that this concentration of GFPCs has no toxicity effect on bacterial growth in a long time scale independently of the charge of the GFPCs. After make sure that GFPCs have no toxic effect on *E.coli* bacteria, and then I investigated their interaction with bacteria by imaging.

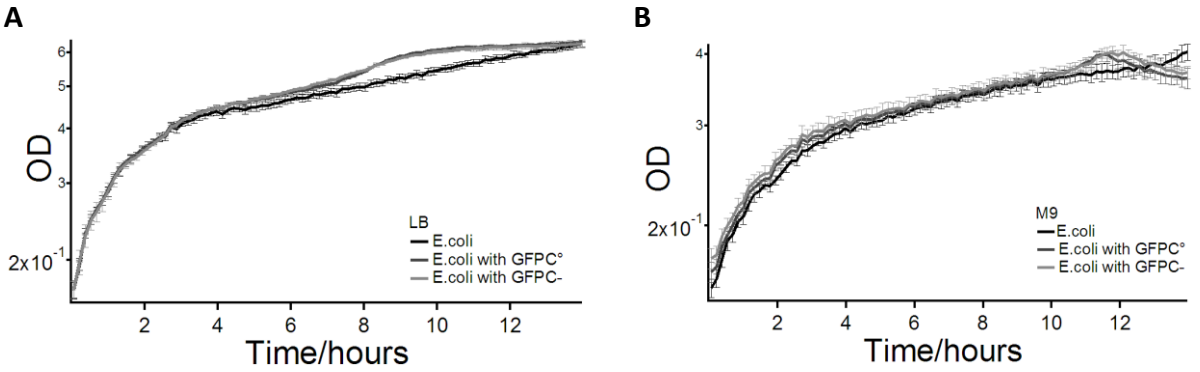



**Figure 4.6** Growth curves of *E.coli* bacteria alone (black lines) and *E.coli* bacteria incubated with $GFPC^-$ (dark grey lines) and $GFPC^0$ (light grey lines) at $6.6x10^{-5}$M in LB medium(A) or M9 medium(B). The error bars indicate the difference between the three replicates in the experiment (<6.6%).

## 4.4 GFPCs for internal bioimaging application of *E.coli* bacteria

### 4.4.1 Bioimaging of *E.coli* interacting with GFPCs

#### 4.4.1.1 Characterization by flow cytometry

After having shown that both $GFPC^-$ and $GFPC^0$ have no toxicity effect on *E.coli* bacterial growths, the GFPCs were tested for bioimaging application with *E.coli*. As the theoretical size of the GFPCs is around 5 nm, they should enter inside bacteria just by incubation[183].

In order to measure whether the GFPCs can enter inside *E.coli* successfully, the LB growth medium with an initial *E.coli* bacterial concentration of $5x10^7$ CFU/mL (OD=0.5) was placed inside an Eppendorf Safe-Lock Tube in the presence of GFPCs. The samples were incubated at 37°C in the dark shaking for one hour and washed for twice with PBS to remove free GFPCs. The cells were then fixed and then washed three times with PBS and re-suspended in PBS before flow cytometry measurements and bioimaging experiments.

Accurate measurements of live, dead, total bacteria and fluorescent cells percentage (**Figure 4.7**) after incubation of *E.coli* with different concentration of GFPCs ($6.6x10^{-4}$M, $6.6x10^{-5}$M, $6.6x10^{-6}$M) were obtained by Flow Cytometry.

After incubation of *E.coli* with $GFPC^0$, the percentage of total fluorescent cells increased when increasing the concentration of $GFPC^0$, and it reached the plateau when the concentration is $6.6x10^{-5}$M (**Figure 4.7A**). For the fluorescent cells which are alive, the percentage increases at the beginning, and reaches the plateau at the concentration of $6.6x10^{-5}$M as well. The percentage of fluorescent live cells could reach at about 80%. From the plate reader experiments described in last section, GFPCs have no toxic effect on *E.coli* bacteria, so the 20% loss of bacteria may come from sample preparation (washing, fixing process…).

After incubation of *E.coli* with $GFPC^-$, the percentage of total fluorescent cells increases quite fast from the beginning and it remains at the plateau no matter what the concentration is (**Figure 4.7B**). For the live fluorescent cells, the percentage remains at about 80% from the beginning. As well as the $GFPC^0$, $GFPC^-$ also has almost no toxicity effect on *E.coli*'s growth.

Comparing $GFPC^0$ and $GFPC^-$ interacting with the *E.coli* bacteria (**Figure 4.7**), we found that $GFPC^-$ will associated to the *E.coli* at a lower concentration. However $GFPC^0$ can also reach a high percentage of cell labeling if we increase its concentration. This is a surprising result because $GFPC^-$ is negatively charged, and $GFPC^0$ is neutral, and the membrane of *E.coli* bacteria is also negatively charged,[199] thus one could expect that $GFPC^-$ should have lower probability to associate with cells, which is not the case from the experiments results. Taking into account the percentage of live cells and live fluorescent cells, $6.6x10^{-5}$M proved to be a suitable concentration for the following experiments.

Additionally, In **Figure 4.7D**, one can notice that all bacteria become green fluorescent no matter if they were dead or alive. Since $GFPC^-$ can label all cells while PI can label only dead cells, we can use $GFPC^-$ and PI to distinguish and quantitative live and dead bacteria with the aid of a flow cytometer. The viability is measured according to the proportion of bound strains by $GFPC^-$ and PI[200].

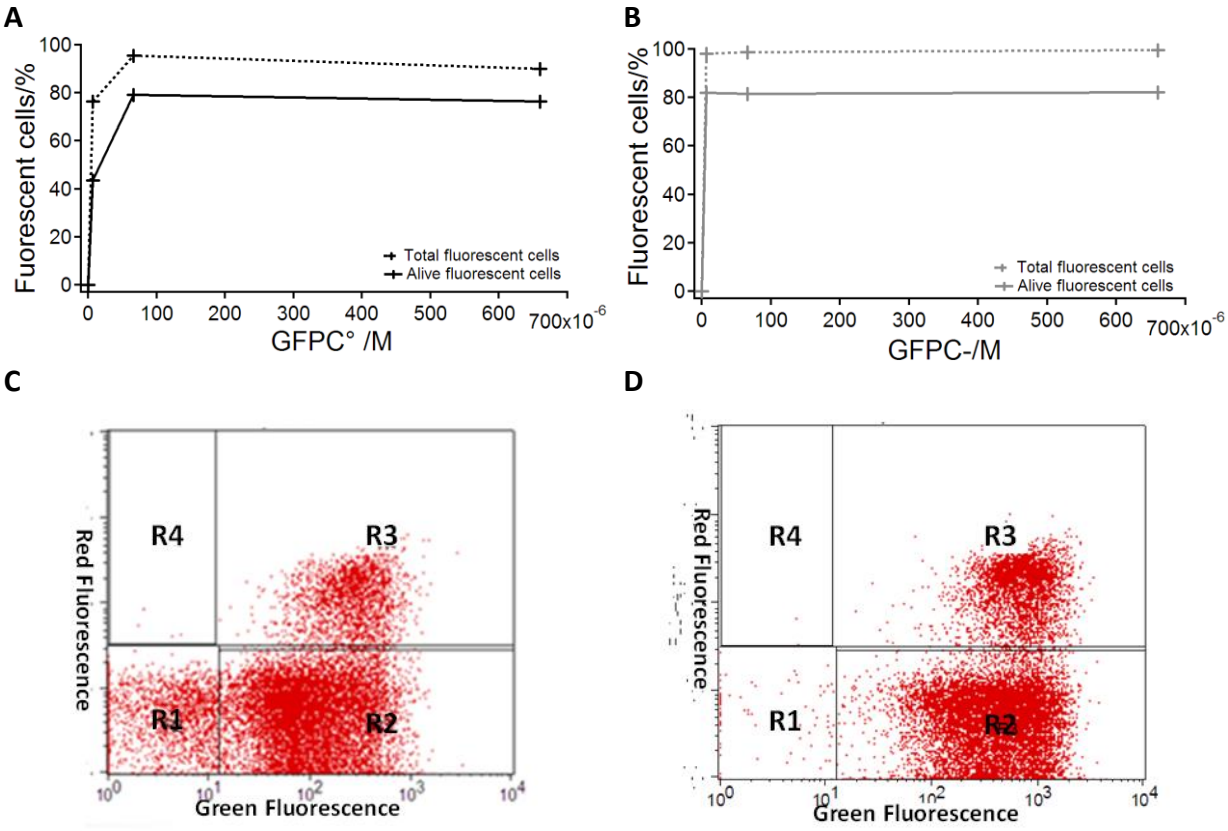



**Figure 4.7** Percentage of fluorescent cells for $GFPC^0$ (A), $GFPC^-$(B) total fluorescent cells (dotted lines), live fluorescent cells (full lines). Flow cytometry analysis of *E.coli* incubation with $GFPC^0$ (C), $GFPC^-$(D) at the concentration of $6.6x10^{-5}$M, x axis: green fluorescence, y axis: red fluorescence(R1: live non-

fluorescent cells percentage, R2: live green fluorescent cells percentage, R3: dead red-green fluorescent cells percentage, R4: dead red fluorescent cells percentage).

### 4.4.1.2 Bioimaging of *E.coli* interacting with GFPCs

*E.coli's* interaction with $GFPC^0$ and $GFPC^-$ was measured by epifluorescence microscopy. The fluorescence images of *E.coli* alone (**Figure 4.8A**) show the auto-fluorescence of *E.coli*. After incubation of *E.coli* with GFPCs, under the microscope the *E.coli* cells becomes green, it seems that the GFPCs entered into the cells, (**Figure 4.8**). Compared with $GFPC^0$ (**Figure 4.8B**) and $GFPC^-$ (**Figure 4.8C**), it is found out that under the same concentration and bioimaging conditions, the bacteria in **Figure 4.8C** are brighter than the one in **Figure 4.8B**. From previous section , we found out that the quantum yield of $GFPC^0$(29%) is higher than $GFPC^-$ (20%) in water and brightness of $GFPC^0$ is twice as high compared with $GFPC^-$ (**Table 4.3**), from image, it seems that under the same condition more $GFPC^-$ will be incorporated into *E.coli* than $GFPC^0$. However, until now, it is difficult to tell if these GFPCs enter inside bacteria or attach on the membrane of the bacteria.

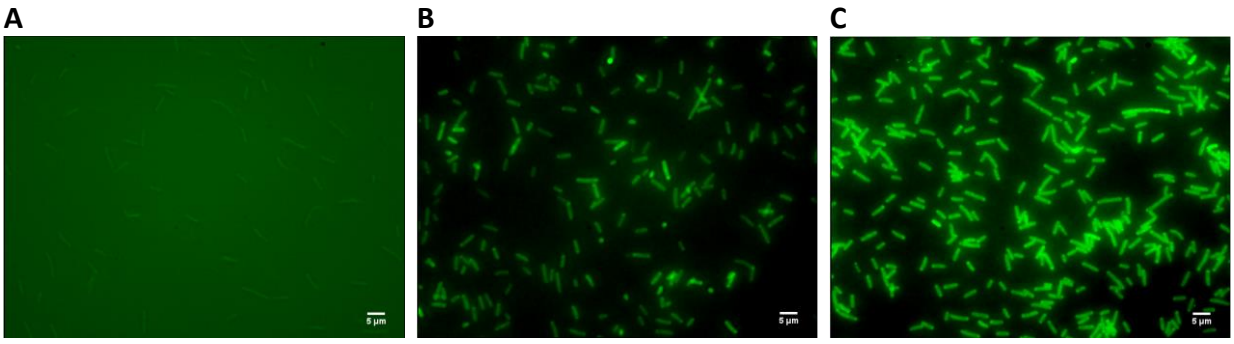



**Figure 4.8** Fluorescence image (60X objective, IT=10s) of *E.coli* alone (A) and *E.coli* interacting with $GFPC^0$ (B) and $GFPC^-$ (C). Additional images are shown in **Figure S4.1 in Section 4.9**.

From the flow cytometry characterization, I determined that 80% of the cells are alive and fluorescent after incubation with the GFPCs, and from the fluorescence microscopy images, we can also conclude that GFPCs (4-6 nm) can associated with the bacteria, especially for the negatively charged $GFPC^-$.For the $GFPC^0$, each bacterium "takes" a different amount of polymer chains, resulting in bacteria of different brightness. However for the $GFPC^-$, the fluorescence of the bacteria is more homogeneous. Since *E.coli* bacteria incorporated more easily the $GFPC^-$ resulting in brighter and better quality fluorescent images after incubation, in the following experiments, I decided to concentrate on $GFPC^-$.

## 4.4.2 Emission quenching of GFPC$^-$ with Methylene Blue (MB)

### 4.4.2.1 Characterization of GFPC$^-$ quenching with Methylene Blue (MB)

In order to make sure that the GFPCs were really inside *E.coli* after incubation not on the membrane; methylene blue was used during the bioimaging experiments. Methylene blue is a biocompatible dye that can quench GFPCs, the idea is similar as using MB to quench FNP$^-$ which described in **Chapter 2 (§2.4.3).**

Here we take GFPC$^-$ as an example since GFPC$^-$ has a better ability to label bacterial cytoplasm from previous experiments. Titration experiments were prepared to characterize the process of GFPC$^-$ quenching with MB. A GFPC$^-$ solution was placed inside a cuvette and methylene blue solution was added continually inside the GFPC$^-$ solution and emission spectrum was taken each time until the emission of GFPC$^-$ stopped decreasing.

The fluorescence and absorption spectroscopy analysis of GFPC$^-$ and methylene blue are displayed on **Figure 4.9 A**, the overlap between the emission spectrum of GFPC$^-$ and the absorption spectrum of MB indicates a possible quenching process of GFPC$^-$ by MB. The titration process of GFPC$^-$ with methylene blue is displayed on **Figure 4.9B**. After the addition of MB, the fluorescence intensity of GFPC$^-$ decreased continually while the fluorescence intensity of MB increased slightly at the same time.

It is found that, the fluorescence intensity of GFPC$^-$ decreases fast at first and then decreased slower and slower continually when adding more methylene blue during the whole process (**Figure 4.9C**). When the concentration of methylene blue was about 15-20 µM, a plateau is reached while 90% fluorescence intensity of GFPC$^-$ has been quenched. At the end up to 91% of the fluorescence intensity of GFPC$^-$ has been quenched by MB after the titration process. Considering the results of the titration experiment, MB with a concentration of 16 µM was used during the following bioimaging experiment in order to quench the fluorescence of GFPC$^-$ outside the membrane of *E.coli* under the microscope.

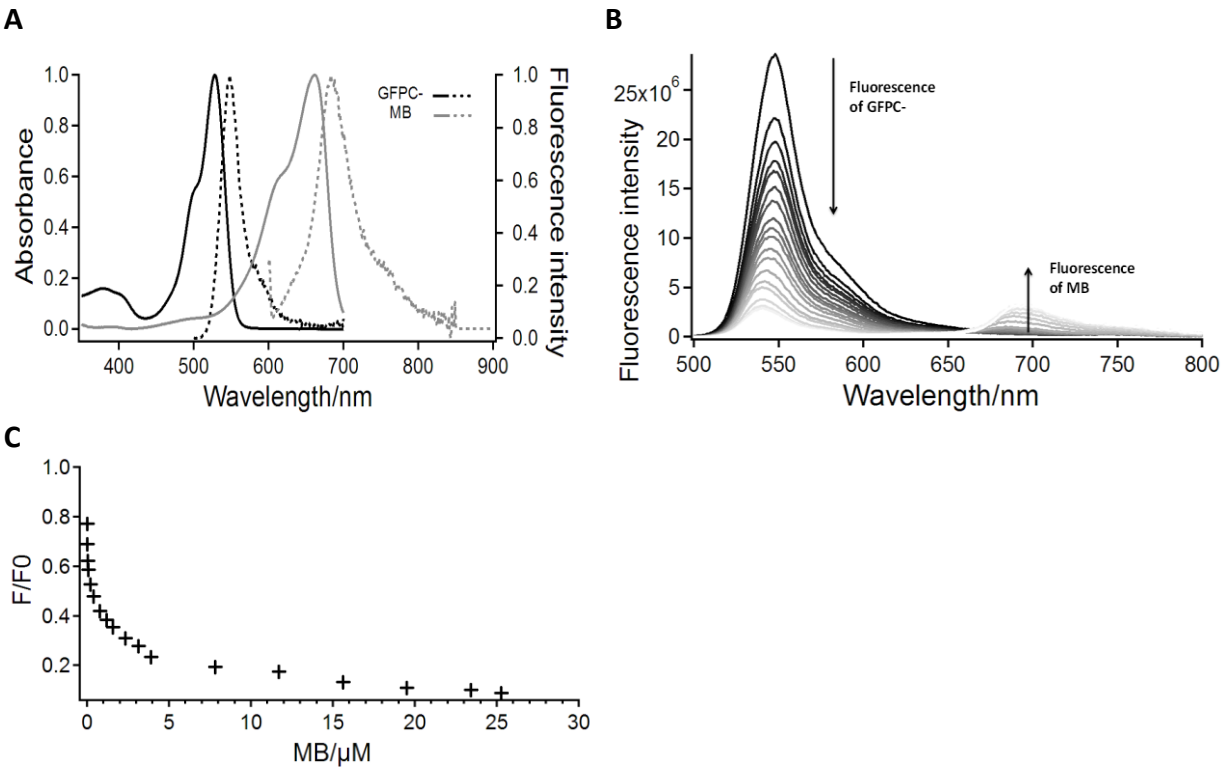



**Figure 4.9** Absorption and emission spectra of GFPC$^-$($\lambda_{exc}$= 495nm) and MB ($\lambda_{exc}$=660nm) (A), titration process of MB to GFPC$^-$(B). Percentage decrease of fluorescence intensity of GFPC$^-$ as a function of the concentration of methylene blue (C).

In order to understand the mechanism of the quenching process, the data was plotted according to Stern-Volmer equation in **Figure 4.10A** (**Equation 7.3 in Chapter 7**). A linear Stern-Volmer plot is generally indicative of a single class of fluorophores, all equally accessible to quencher[23]. Since in our case the Stern-Volmer plots deviate from linearity toward the x-axis, it means that two or several fluorophore populations are present, and there are classes are not accessible to quencher. However in GFPC$^-$, only BPDMA1 is the fluorophore, so it can be assumed that there are two or more populations of BDPMA1s, one of which is accessible (a) to quencher methylene blue and the others being inaccessible or buried (b). At the same time, in **Figure 4.9C**, there are three slopes for the fluorescence intensity decreasing process of GFPC$^-$ indicating that there might be three populations of BDPMA1 as we have hypothesized. In this case the Stern-Volmer plot will display a downward curvature which is exactly the one show in **Figure 4.10A.** In addition, a slight blue shift of the emission of GFPC$^-$ is observed in the titration process (**Figure 4.9 B**), the emission spectrum shifts progressively to shorter wavelengths with increasing MB concentrations. This is also probably due to selective quenching of exposed BDPMA1 versus buried BDPMA1 and indicates that those BDPMA1 emitting at larger wavelengths are quenched more readily than

the shorter wavelength BDPMA1. This spectrum shows that the quenched BDPMA1 display an emission maximum at 548 nm. The protected BDPMA1 display an emission maximum at 540 nm. A modified Stern-Volmer plot (**Figure 4.10 B**) is made according to the modified Stern-Volmer equation (**Equation 7.4 in Chapter 7**). However, the plot is still not linearly. However, the plot is still not linearly. The modified Stern-Volmer plot is only suitable for conditions that contain two populations of fluorophores (one accessible and one inaccessible). In the case of GFPC$^-$, the system seems more complex. We may postulate the existence of some dimers or trimers or n-mers aggregates which form a complicated "solution". So far we can't explain the dynamics by modified Stern-Volmer plot.

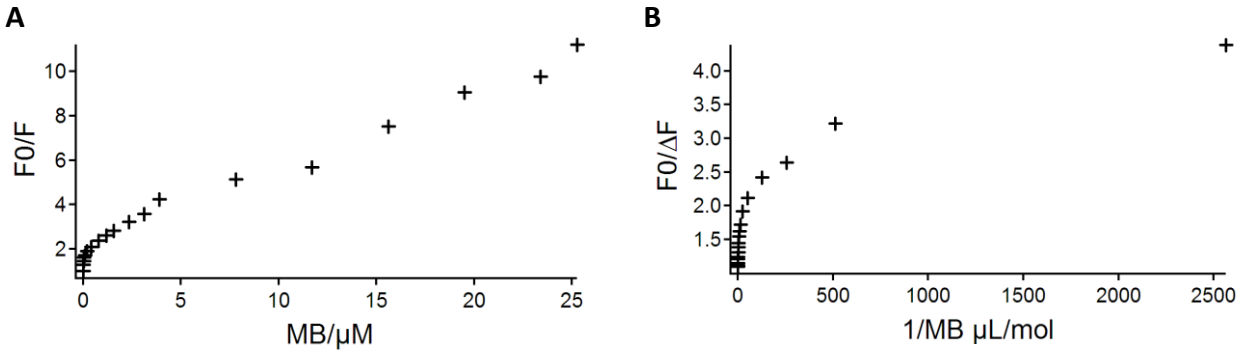



**Figure 4.10** Stern-Volmer (A) and modified Stern-Volmer plots (B) for GFPC$^-$ quenched by methylene blue.

### 4.4.2.2 Bioimaging after quenching with Methylene Blue (MB)

After characterization of the quenching process of GFPC$^-$, methylene blue was used in the bioimaging experiments of *E.coli* interacting with GFPC$^-$. *E.coli*'s interaction with GFPC$^-$ after the addition of methylene blue was also measured by epifluorescence microscopy.

After adding methylene blue, the GFPCs outside the cells were quenched by the methylene blue, thus on **Figure 4.11B**, there was no background fluorescence. However, the bacteria were still fluorescence indicating that the GFPCs inside the cells were protected by the cell membrane and were thus fluorescent under microscope (**Figure 4.11B**). This means that GFPC$^-$ can successfully enter inside *E.coli* bacteria after incubation.

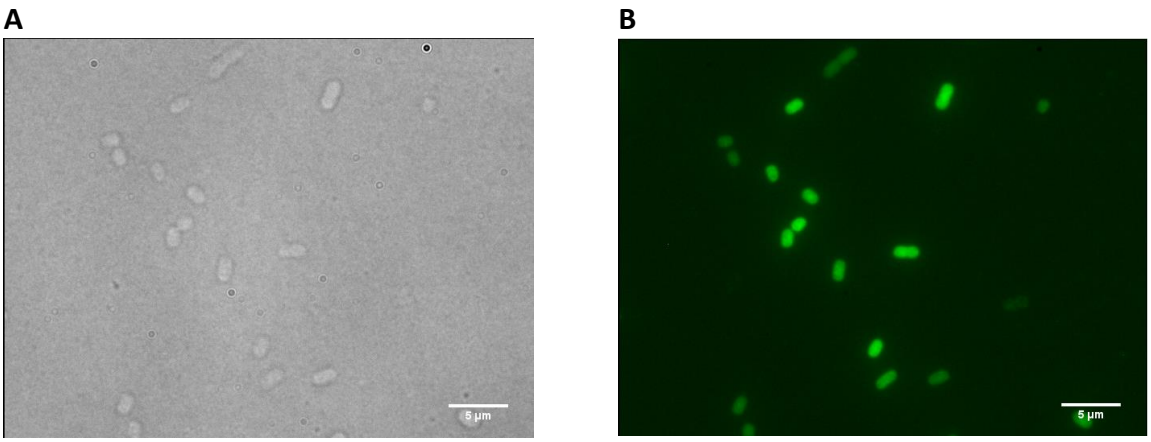



**Figure 4.11** *E.coli* interacting with GFPC$^-$ after quenching with methylene blue (100X objective, A: bright field image, IT=500ms; B: fluorescence image, IT=5s). Additional images are shown in **Figure S4.2 in Section 4.9**.

## 4.4.3 Multi-color imaging application of GFPC$^-$

### 4.4.3.1 Labelling of *E.coli*'s DNA using DRAQ 5

As shown in **Figure 4.12C**, GFPC$^-$ can enter inside *E.coli* bacteria after incubation. Moreover, some dark spots could be observed in the middle of the bacterial cells (**Figure 4.12B**). This could result from the GFPC$^-$ only labeling the cytoplasm but not the DNA. Since the DNA is negatively charged, it is possible that GFPC$^-$ will not label the DNA inside the cytoplasm. In order to prove this hypothesis, and also in order to develop the multi-color application of GFPC$^-$, another dye, DRAQ 5, was introduced in the bioimaging experiments.

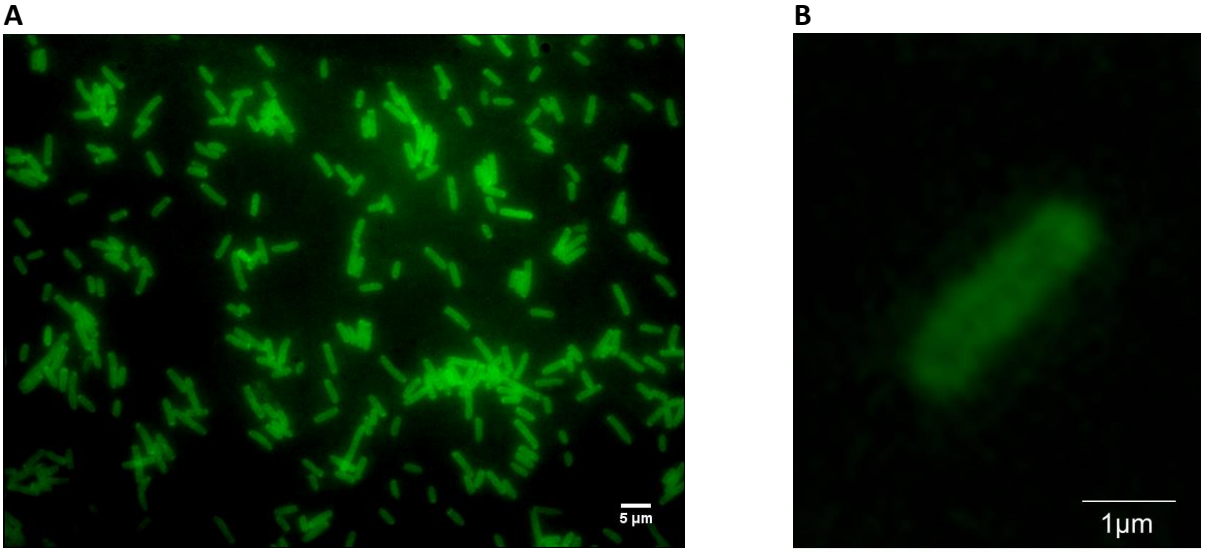



**Figure 4.12** Fluorescence image of *E.coli* interacting with GFPC$^-$, image B is a zoom of one bacteria from image A (60X objective, IT=10s).

DRAQ5 is a red fluorescent cell-permeable DNA dye that is biocompatible.[60] The chemical structure and spectral characteristics of DRAQ5 are shown in **Figure 4.14**. It has two bands of absorbance at 600nm and 646nm and it emits in the far-red / near infra-red (NIR) and has maximum band at 697nm when bound to dsDNA.

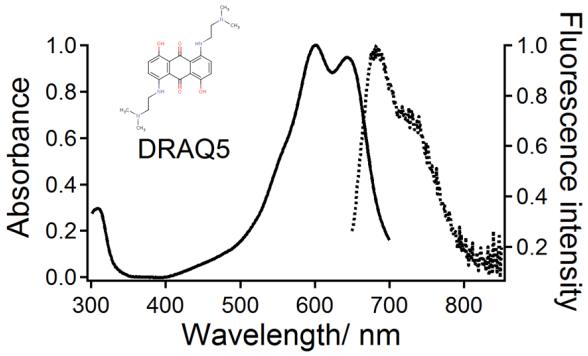



**Figure 4.13** Structure and spectra of DRAQ 5 in PBS buffer: absorption (full line), fluorescence emission (dotted line, $\lambda_{exc}$=600nm)(figure adapted from[61]).

During our experiments, DRAQ5 was used to stain the bacterial DNA in order to discriminate the location of DNA and $GFPC^-$. DRAQ5 was first tested on *E.coli* for the ability to label bacterial DNA, DRAQ5 (1:1000 dilution) with an initial concentration of 5mM was added into a bacterial suspension and incubated for one hour. Samples were washed twice with PBS before the microscopy experiments (**Figure 4.14**).

As shown in **Figure 4.14D,** DRAQ5 could be used to label bacterial DNA successfully. Since it didn't emit at the wavelength of green (**Figure 4.14B**), DRAQ5 will not influence the bioimaging results of $GFPC^-$ labelling the bacterial cytoplasm, which indicates that DRAQ5 could be used to discriminate the intracellular DNA and $GFPC^-$ location.

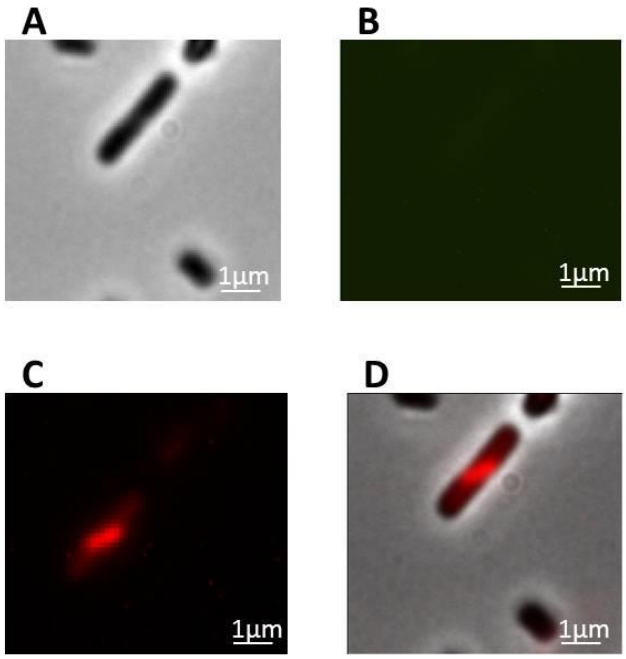



**Figure 4.14** Images of DRAQ5 labeling the DNA of *E.coli* (60X objective, A: phase contrast image, IT=100ms; B: green fluorescence image, IT= 20s; C: red fluorescence image, IT=20s; D: overlapped image of A and C). Additional images are shown in **Figure S4.3 in Section 4.9**.

After successfully using DRAQ5 to label the DNA of *E.coli*, DRAQ5 and $GFPC^-$ were then used for multi-color labelling of bacterial cytoplasm. DRAQ5 (1:1000 dilution) with an initial concentration of 5mM was added at the same time with $GFPC^-$ ($6.6x10^{-5}$M) to *E.coli* suspension in M9 medium to incubate for one hour. Samples were washed two times with PBS before the microscopy experiments.

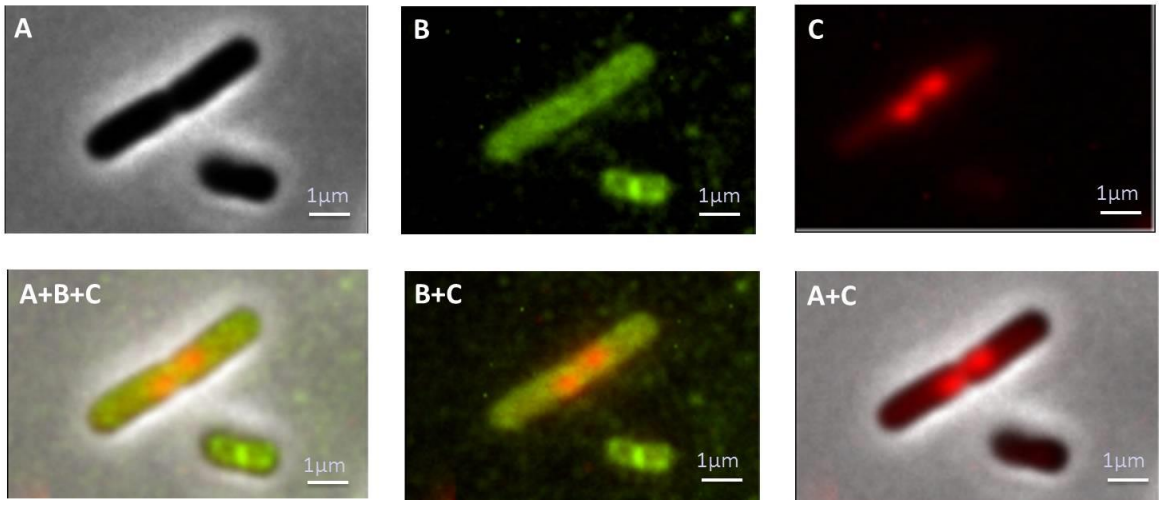



**Figure 4.15** Bioimaging of *E.coli* bacteria incubated with $GFPC^-$ and DRAQ5 (60X objective A: phase contrast image, IT=100ms; B: green fluorescence image, IT= 20s; C: red fluorescence image, IT=20s). Additional images are shown in **Figure S4.4 in Section 4.9**.

The bacterial cytoplasm was labeled by $GFPC^-$ (**Figure 4.15B**) which is the green part, and the bacterial DNA was labelled by DRAQ5 (**Figure 4.15C**) which is the red part. Since both the bacterial DNA and $GFPC^-$ are negatively charged, they supposed to exclude with each other because of the electrostatic interaction. In order to determine if $GFPC^-$ labeled bacterial DNA, we overlapped the two images together (**Figure 4.15 B+C**), it appeared that the red part and the green part do not overlap. This indicates that $GFPC^-$ could label the bacterial cytoplasm but not the DNA.

### 4.4.3.2 Labelling of *E.coli*'s membrane using PKH26

PKH26 is a yellow-orange fluorescent commercial dye that is biocompatible and it is commonly used to stain the bacterial membrane. In order to determine whether $GFPC^-$ labels the bacterial membrane PKH26 is introduced to label bacterial membrane while the bacteria are labelled by $GFPC^-$. The chemical structure and spectral characteristics of PKH26 are shown in **Figure 4.16**. It absorbs maximum at 551nm and it fluoresces peaking at 577nm.

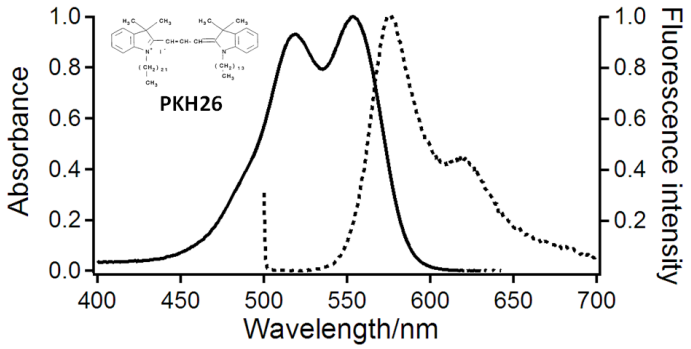



**Figure 4.16** Structure and spectra of PKH26 in PBS: absorption (full line), fluorescence emission (dotted line, $\lambda_{exc}$=500nm).

PKH26 was first tested on *E.coli* for the ability to label bacterial membrane, As show in **Figure 4.17B,** PKH26 could be used to label bacterial membrane successfully which indicates that $GFPC^-$ can be used to discriminate the membrane and $GFPC^-$ location. However the efficiency of PKH26 to label the bacterial membrane is not very high, I measured for seven images and about 10.1% cells are labelled successfully which compared with the efficiency of $GFPC^-$ (80%) to label bacterial cytoplasm, it is relatively low.

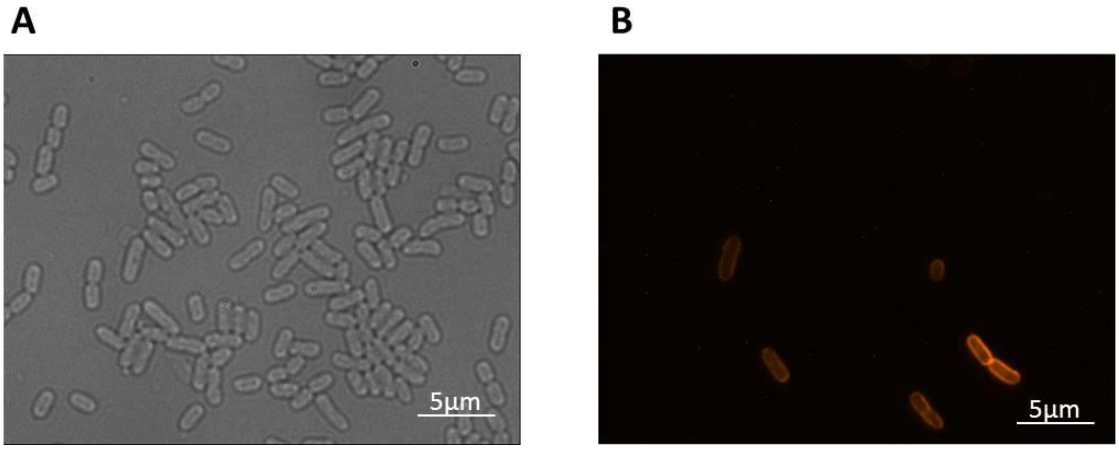



**Figure 4.17** Images of PKH26 labeling the membrane of *E.coli* (100X objective, A: bright field image, IT=500ms; B: fluorescence image, IT=5s). Additional images are shown in **Figure S4.5 in Section 4.9**.

After successfully using PKH26 to label the membrane of *E.coli*, PKH26 and GFPC$^-$ were then used for multi-color labelling of bacterial cytoplasm (**Figure 4.18**).

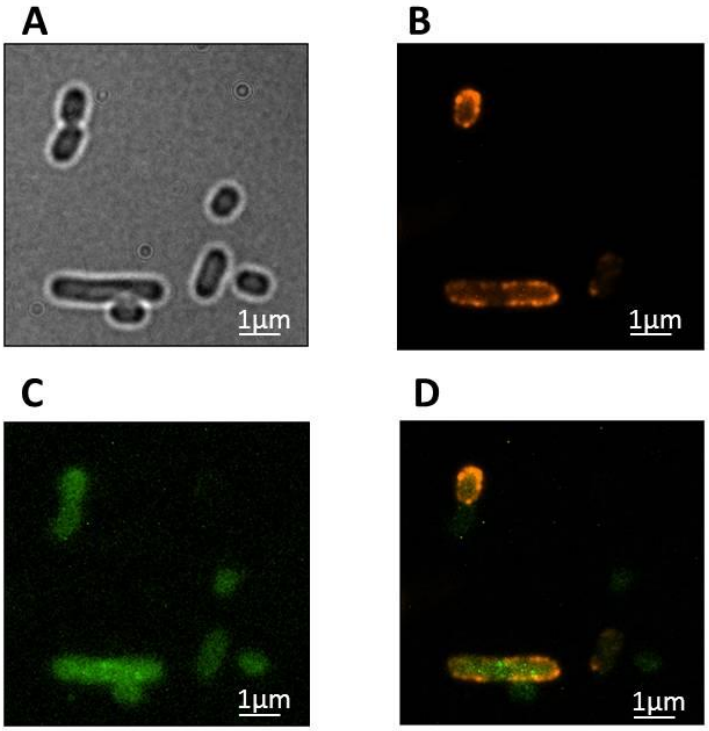



**Figure 4.18** *E.coli* interacting with GFPC$^-$ and PKH26 (A: bright field image, IT=500ms; B: orange fluorescence image, IT=5s; C: green fluorescence image, IT=5s; D: overlapped image of B+C). Additional images are shown in **Figure S4.6 in Section 4.9**.

The bacterial cytoplasm was targeted by GFPC$^-$ (**Figure 4.18C**) which is the green part, and the bacterial membrane was labelled by PKH26 (**Figure 4.18B**) which is the yellow part. It is important to notice that only a few bacterial membranes were successfully labelled by

PKH26 while almost all the bacterial cytoplasm were labelled successfully by $GFPC^-$. I overlapped the two images together (**Figure 4.18D**), and it appeared that the yellow part and the green part are not influenced by each other, and from the image it is clear that the bacterial cytoplasm is green while the membrane is yellow. This is additional evidence to show that $GFPC^-$ can label the bacterial cytoplasm. At the same time these results indicate that $GFPC^-$ are quite compatible with different types of commercial dyes that could be used to multi-color imaging.

## 4.5 Characterizations of Red fluorescent polymer chains (RFPCs)

The previous results showed that, $GFPC^-$ could be used to label the bacterial cytoplasm but not the DNA complex which is negatively charged. It would be interesting to synthesize some positively charged polymer chains that could label bacterial DNA for bioimaging. Indeed, positive and negative red fluorescent polymer chains (RFPCs, **Scheme 4.2**) have been synthesized with similar architecture as GFPCs. The BODIPY methylnaphthalene-2 (BDPMA2) is introduced in the synthesis process, the additional aromatic moieties on the pyrrole of the BODIPY monomer shift fluorescence emission to red by conjugation extension of the $\pi$ system. These RFPCs are useful to try for biological imaging application and we wish to use RFPCs and GFPCs for multi-color imaging.

RFPCs were recently synthesized by Muriel Coquelin and the characterization is still under investigation. The exact number of BDPMA2 per chain and the BDPMA2 conversion rate has not yet been determined. However, I carried out some preliminary spectroscopy measurements to obtain an overall understanding of RFPCs which are necessary for bioimaging experiments.

The fluorescence and absorption spectroscopy analysis of RFPCs are displayed on **Figure 4.19** and their main spectroscopic data are given in **Table 4.4**. The BDPMA2 monomer in ethanol shows a red shift compared with the one of BDPMA1 (**Figure 4.19A**). The maximum of absorption and fluorescence emission are found at 552nm and 594 nm, exhibiting a Stokes shift of $1281cm^{-1}$ (42nm). The RFPCs show very similar absorption and fluorescence spectra with a maximum absorption at 552nm ($RFPC^+$), 553nm ($RFPC^-$). However, the maximum band of fluorescence emission at 601nm ($RFPC^+$), 588nm ($RFPC^-$) indicates a red shift of $RFPC^+$ compared with $RFPC^-$. Moreover the emission band of $RFPC^+$ is

broader than the one of $RFPC^-$. These two facts brought together may indicate a higher aggregation state of $RFPC^+$ in water. It is observed that the RFPCs absorption spectra exhibit a more intense band located in the UV region which may come from the light scattering by the polymer chains aggregations. This is more pronounced for $RFPC^+$ than for $RFPC^-$. This is also in agreement with a higher aggregation state in $RFPC^+$ (**Figure 4.20A**). The excitation spectra for RFPCs and for the BDPMA2 monomer have the same aspect and superimpose virtually to their respective absorption spectra (**Figure 4.20B**), showing that the absorbing and emitting species are identical. DLS signals of $RFPC^-$ (17nm) and $RFPC^+$ (30nm) are shown in **Figure 4.21,** compared with theoretical diameter (4-6nm), the measured diameters are higher indicating presence of aggregation of RFPCs inside aqueous solutions. The higher hydrodynamic diameter for $RFPC^+$ compared to $RFPC^-$ probably comes from the larger size of the counterion ($Cl^-$ for $RFPC^+$ and $Na^+$ for $RFPC^-$) and/or higher aggregation state.

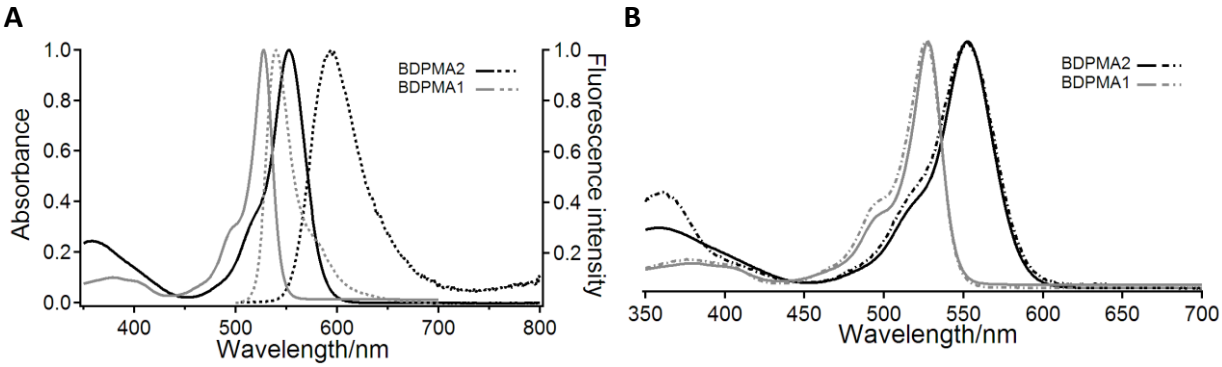



**Figure 4.19** BDPMA1 monomer in toluene and BDPMA2 monomer in ethanol: absorption (A, B full lines), fluorescence emission (A dotted lines, $\lambda_{exc\ BDPMA1}$=495nm, $\lambda_{exc\ BDPMA2}$=540nm) and excitation (B dotted lines, $\lambda_{emi\ BDPMA1}$=548nm, $\lambda_{emi\ BDPMA2}$=587nm).

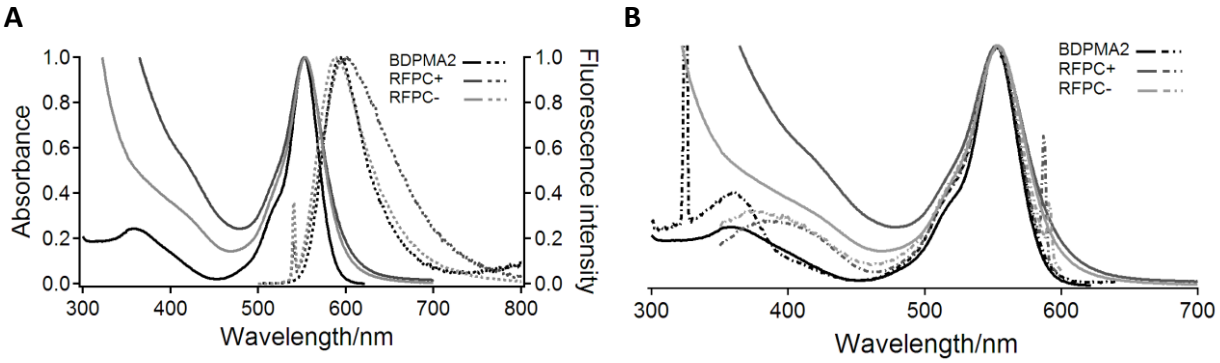



**Figure 4.20** BDPMA2 monomer in ethanol and RFPCs in water (pH=7.0): absorption (A, B full lines), fluorescence emission (A dotted lines, $\lambda_{exc}$=540nm) and excitation (B dotted lines, $\lambda_{emi}$=587nm) normalized spectra.

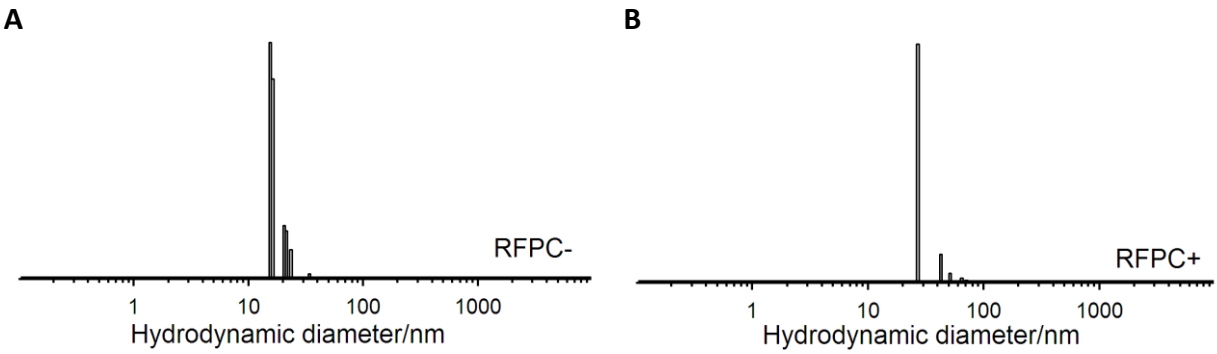



**Figure 4.21** DLS signals of $RFPC^-$ (A) and $RFPC^+$(B) in water (pH 7).

**Table 4.4** Main spectroscopic properties of BDPMA2 and RFPCs

| | | water | | | ethanol | | | | |
|---|---|---|---|---|---|---|---|---|---|
| Sample | Structure | $\lambda_{abs}$ /nm | $\lambda_{em}$ /nm | $\Phi_F$ /%[a] | $\lambda_{abs}$ /nm | $\lambda_{em}$ /nm | $\Phi_F$ /%[a] | $D_t$[b] /nm | $D_h$[c] /nm |
| BDPMA2 | - | - | - | - | 552 | 594 | 53 | - | |
| $RFPC^+$ | P(DMAEA-APEG-*co*-BDPMA2)-TTC-$C_{12}$ | 552 | 601 | 12 | 550 | 585 | 32 | 4-6 | 30 |
| $RFPC^-$ | P(AA-*co*-APEG-*co*-BDPMA2)-TTC-$C_{12}$ | 553 | 588 | 10 | 551 | 587 | 31 | 4-6 | 17 |

[a] Error of 15%[182], [b] theoretical diameter($D_t$) [c] hydrodynamic diameter ($D_h$) determined by DLS in water.

The fluorescence quantum yield of BDPMA2 in ethanol is 53% which shows about a 20% decrease from the one of BDPMA1 (70%). The additional aromatic moieties on the pyrrole of the BODIPY monomer not only shift fluorescence emission to red but also make the monomers being congested[27]. In water the fluorescence quantum yield of $RFPC^+$ is 12% while the one for $RFPC^-$ is 10%. The decrease may be due to the aggregation of BODIPY along the same polymer chain. To confirm this, I analyzed the $RFPC^+$ and $RFPC^-$ spectra in ethanol (**Figure 4.22**). The quantum yield is 32% for $RFPC^+$ and 31% for $RFPC^-$(**Table 4.4**). The spectra of RFPCs in ethanol still show intense band in UV region indicating that there were still aggregations inside the solution. That is probably why the quantum yield of RFPCs in ethanol is higher than the RFPCs in water but still lower than BDPMA2 in ethanol.

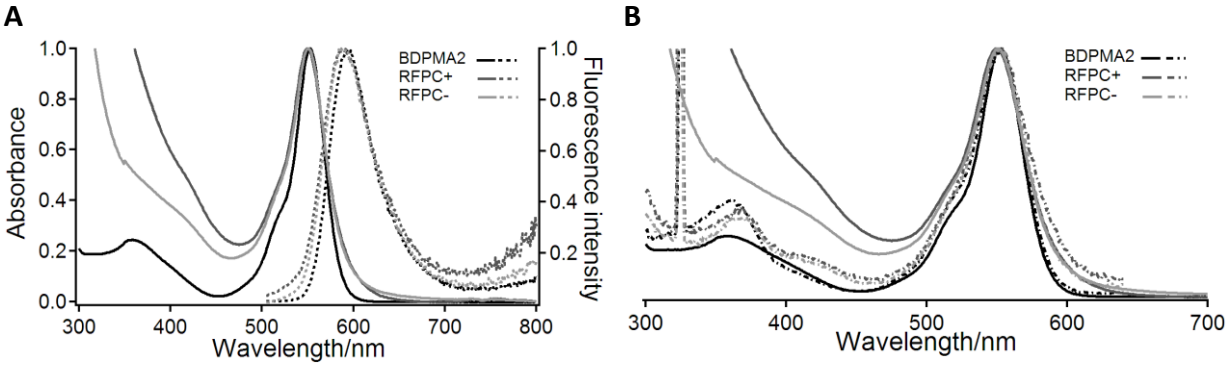



**Figure 4.22** BDPMA2 monomer and RFPCs in toluene: absorption (A, B full lines), fluorescence emission (A dotted lines, $\lambda_{exc}$=540nm) and excitation (B dotted lines, $\lambda_{emi}$=587nm) normalized spectra.

## 4.6 Toxicity assessments of RFPCs on *E.coli*

Having synthesized and having obtained a preliminary characterization of the RFPCs, I next assessed the toxic effect of RFPCs on *E.coli*. In order to do this, the growth rates of bacteria in the presence of RFPCs were compared with the growth rate of *E.coli* bacteria alone. The growth rate was measured by the plate reader (Perkin Elmer Victor3 1420 Multilabel Plate Counter). The RFPCs concentrations used was $2x10^{-10}$M.

Here, *E.coli* bacteria with $RFPC^+$ or $RFPC^-$ were incubated in the plate reader at 37°C in the dark overnight. One control with only bacteria was also prepared. Every nine minutes the growth rate of the cells was monitored by measuring the optical density at 600nm by the plate reader (**Figure 4.23**). For over ten hours incubation, the growth curves of bacteria with RFPCs were practically the same as the growth curve of bacteria alone both in LB medium and in M9 growth medium. This means that the RFPCs have no toxic effect on bacterial growth on a long time scale independently of the charge of the RFPCs.

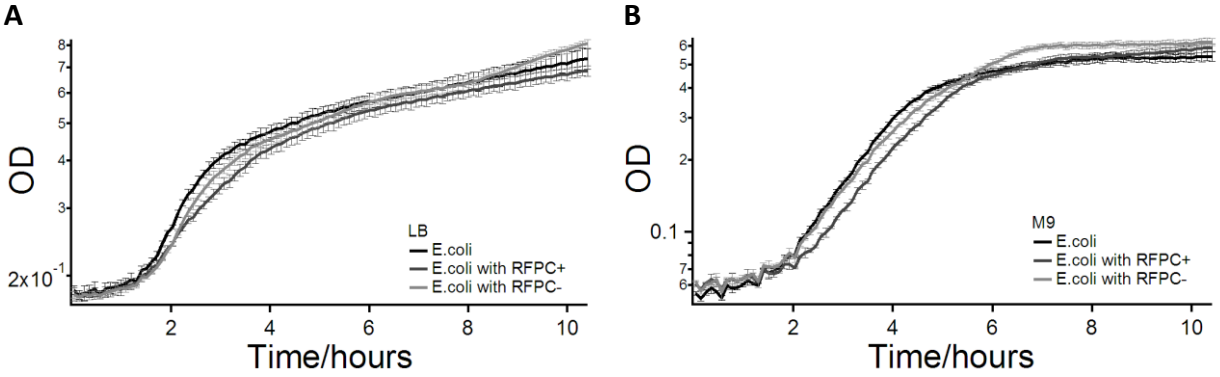



**Figure 4.23** Growth curves of *E.coli* bacteria alone (black lines) and *E.coli* bacteria incubated with $RFPC^+$ (dark grey lines) and $RFPC^-$ (light grey lines) at $2x10^{-10}$M in LB medium (A) or M9 medium (B). The error bars indicate the difference between the three replicates in the experiment (<6.8%).

## 4.7 RFPCs for external bioimaging application of *E.coli* bacteria

### 4.7.1 Bioimaging of RFPCs labelling the membrane of *E.coli*

After having shown that both $RFPC^+$ and $RFPC^-$ have no toxic effect on *E.coli* bacterial growth, RFPCs were tested for bioimaging application with *E.coli*. Taking into consideration the results from GFPCs, we expected that $RFPC^+$ would enter inside bacteria and label the DNA which is negatively charged, and $RFPC^-$ would enter inside bacteria and label the cytoplasm like the $GFPC^-$ did. However, the results are quite different from those expected.

*E.coli's* interaction with $RFPC^+$ and $RFPC^-$ was measured by epifluorescence microscope (TRITC filter). The auto-fluorescence of *E.coli* alone is shown in **Figure 4.24** which indicates that there is no red auto-fluorescence of *E.coli*.

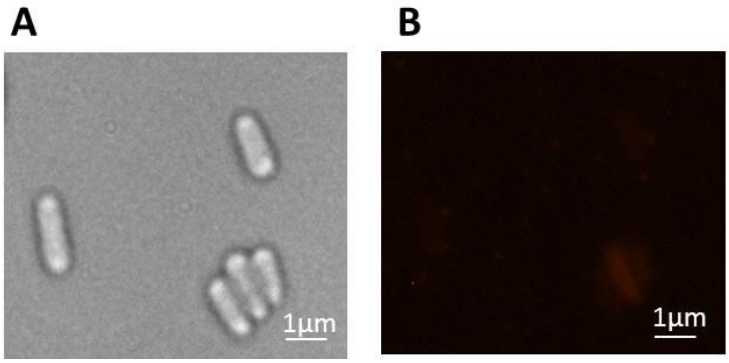



**Figure 4.24** Red auto-fluorescence images of *E.coli* alone (100x objective, A: bright filed image, IT=500ms; B: fluorescence image, IT=1s). Additional images are shown in **Figure S4.7 in Section 4.9**.

After incubation with $RFPC^+$, instead of entering inside the bacteria and labeling the DNA, $RFPC^+$ labelled the bacteria membrane in a very homogeneous way (**Figure 4.25**).

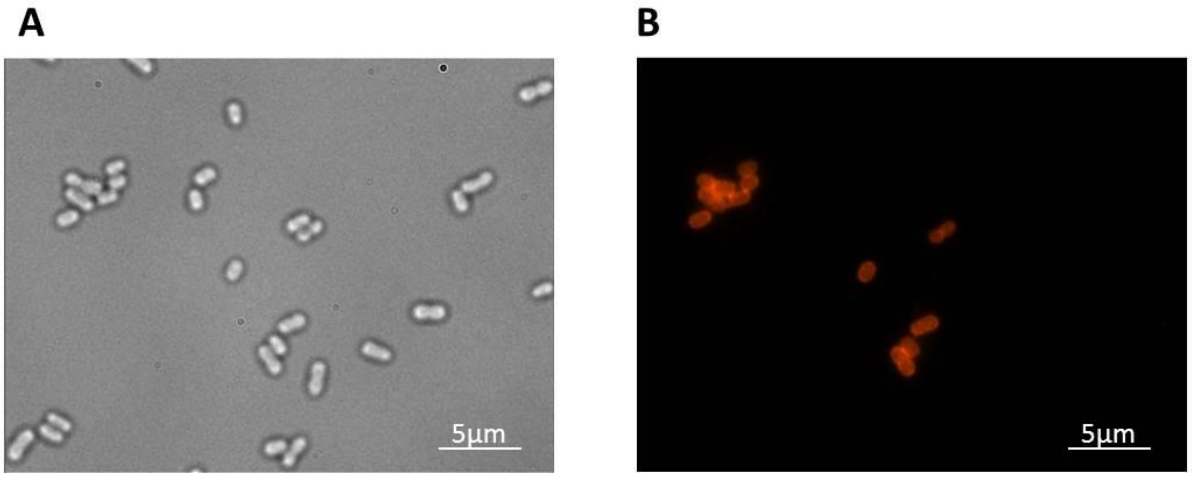



**Figure 4.25** RFPC$^{+}$ labelling the membrane of *E.coli* bacteria (100X objective, A: bright field image, IT=500ms; B: fluorescence image, IT=1s). Additional images are shown in **Figure S4.8 in Section 4.9**.

A similar observation happened to RFPC$^{-}$, instead of labelling the cytoplasm of bacteria, RFPC$^{-}$ labelled the membrane of *E.coli* (**Figure 4.26**). Bothe RFPC$^{-}$ and RFPC$^{+}$ seems label the membrane and didn't enter inside bacteria. The reason for RFPCs labelling the bacterial surface membrane instead of entering inside the bacteria is the hydrophobic head of the RFPCs would insert and remain in the hydrophobic part of the phospholipid bilayer (**Figure 4.27**). Although the membrane is negatively charged, which in theory means that RFPC$^{+}$ should label the membrane better, it is difficult to tell the difference between the RFPC$^{+}$ and RFPC$^{-}$ in their ability to stain the bacterial membrane in these experimental condition. Both of them label bacterial membrane clearly and homogeneously.

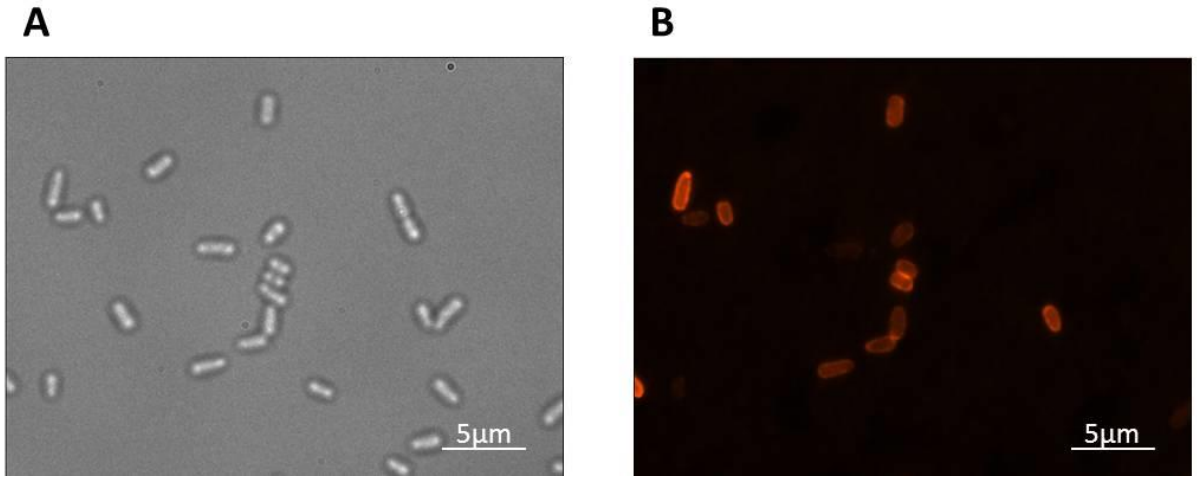



**Figure 4.26** RFPC$^{-}$ labelling the membrane of *E.coli* bacteria (100X objective, A: bright field image, IT=500ms; B: fluorescence image, IT=1s). Additional images are shown in **Figure S4.9 in Section 4.9**.

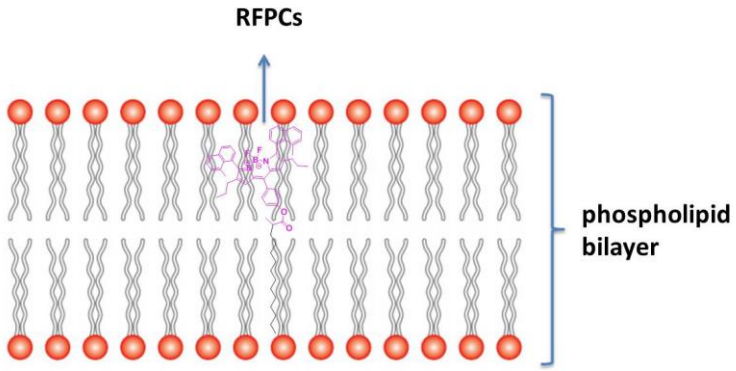



**Figure 4.27** One hypothesis of mechanism for RFPCs labelling bacterial membrane.

### 4.7.2 Multi-color Imaging application of GFPC$^-$ and RFPC$^+$

Since RFPCs can label the bacterial membrane, I next tested the multi-color internal and external bioimaging of *E.coli* bacteria with GFPC$^-$ and RFPC$^+$ together. RFPC$^+$ was added to label the bacterial membrane after GFPC$^-$ was introduced inside bacteria in order to prevent the possibilities that RFPC$^+$ may block the GFPC$^-$ to enter.

The bacterial cytoplasm was targeted by GFPC$^-$ (**Figure 4.28B**) which is the green part, and the bacterial membrane was labelled by RFPC$^+$ (**Figure 4.28C**) which is the red part. By overlapping the two images together (**Figure 4.28D**), it appeared that the green part and the red part do not overlap except for the membrane boundary. This shows that GFPC$^-$ and RFPC$^+$ are compatible with each other and that they could be used for bacteria internal and external bioimaging at the same time.

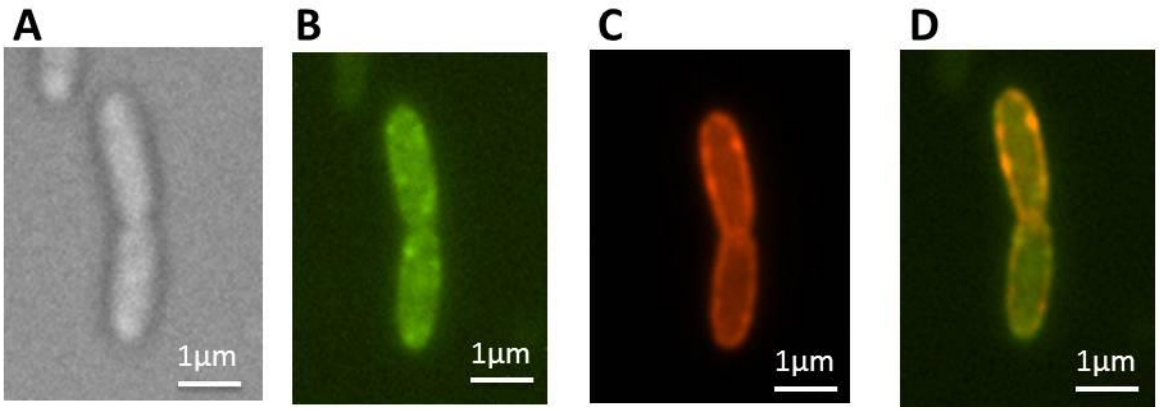



**Figure 4.28** *E.coli* interacting with GFPC$^-$ and RFPC$^+$ (A: bright field image, IT=500ms; B: green fluorescence image, IT=5s; C: red fluorescence image, IT=1s; D: overlapped of image B and C).

### 4.7.3 Comparison of PKH26 and RFPCs

From the previous experiments we can conclude that our novel highly water-soluble red fluorescent polymer chains RFPCs appear to label bacterial membrane very efficiently.

Compared with the commercial membrane dye, PKH26, used in previous experiments, RFPCs can label bacterial membrane in a clear and homogeneous way, while for PKH26, there were some holes on the membrane labelling (**Figure 4.19**) indicating to a non-uniform labelling. RFPCs are very easy and cheap to synthesize and are non-toxic to bacteria. Moreover, they can label the bacterial membrane by simple incubation in common growth medium (M9) which is very easy to handle compared to PKH26 which needs a special solvent for dilution. The spectra of PKH26 and RFPCs are displayed in **Figure 4.29**. Their maximum absorption and emission wavelength are shown in **Table 4.5**. From the spectra, one can notice that PKH26 and RFPCs share very similar maximum absorption wavelength (PKH26: 551nm, $RFPC^+$: 552nm, $RFPC^-$: 553nm), however the maximum is located at different wavelength while the Stoke Shift of RFPCs ($RFPC^+$: 1477 $cm^{-1}$, $RFPC^-$: 1076 $cm^{-1}$) are higher compared with the one of PK26 (818 $cm^{-1}$). A larger Stoke shift between absorption and emission bands allows more efficient collection of emitted light[28], which is better for imaging experiments.

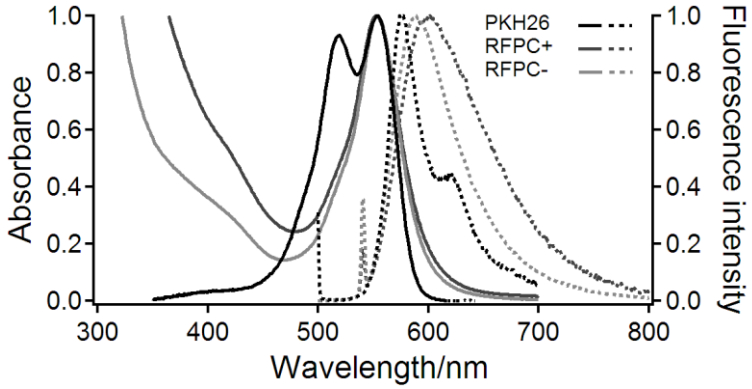



**Figure 4.29** PKH26 (black lines) in PBS and $RFPC^+$ (dark grey lines) and $RFPC^-$ (light grey lines) in water (pH=7.0): absorption (full lines), fluorescence emission (dotted lines) normalized spectra.

**Table 4.5** Maximum absorption and emission wavelength of PKH26 and RFPCs

| | $\lambda_{abs}$ /nm | $\lambda_{em}$ /nm | Stoke Shift/ $cm^{-1}$ |
|---|---|---|---|
| PKH26 | 551 | 577 | 818 |
| $RFPC^+$ | 552 | 601 | 1477 |
| $RFPC^-$ | 553 | 588 | 1076 |

The staining concentration for RFPCs during the previous experiments described above is $2x10^{-10}$M for $1x10^{8}$cells/mL. While the label concentration for PKH26 is of $2x10^{-6}$ M for $1x10^{8}$cells/ml which is 10000 times higher compared with the polymer chains. This means that we can easily use 10000 times less polymer chains to label the membrane of bacteria than PKH26. In order to test the minimum staining concentration for PKH26, I ran an experiment to decrease the quantity of PKH26 continually and to measure the extent of membrane staining by microscopy (**Figure 4.30**).

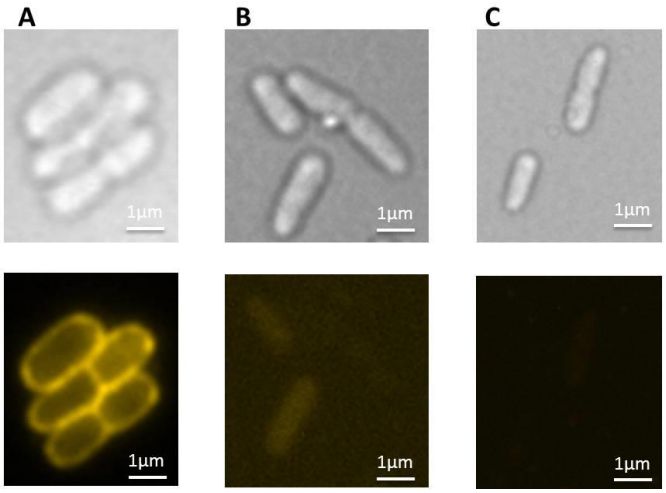



**Figure 4.30** Images of different concentration PKH26 labeling the membrane of *E.coli* (PKH26 concentration A: $2x10^{-8}$M, B: $2x10^{-9}$M, C: $2x10^{-10}$M).

From the experiments described above, a decrease in the amount of PKH26 resulted in a decrease in staining efficiency. In **Figure 4.30A**, the concentration of PKH26 is $2x\ 10^{-8}$M which is 100 times less than the concentration we used in previous experiments, and the staining is successfully made. However, when the concentration is decreased to $2x10^{-9}$M (**Figure 4.30B**), $2x10^{-10}$M (**Figure 4.30C**), the labeling is clearly less efficient. It is noticeable that we use the concentration of $2x10^{-10}$M for RFPCs as the staining concentration. In conclusion, we can use at least 100 times less RFPCs material to label the same amount of bacteria than a commercial membrane dye PKH26. And RFPCs are also very easy to handle during experiments without need of extra equipment or special conditions.

## 4.8 Conclusion

In this chapter, I presented four different fluorescent polymer chains (FPCs): neutral and negatively charged green fluorescent chains (GFPC°, $GFCP^{-}$), positively and negatively

charged red fluorescent chains ($RFPC^+$, $RFPC^-$) and their bioimaging applications on *E.coli* bacteria (**Figure 4.31**).

GFPCs have been shown to be nontoxic on bacterial growth in a long time scale, independently of the charge and of the growth medium. Since *E.coli* bacteria incorporated more easily the $GFPC^-$ resulting in brighter and better quality fluorescent images, I therefore decided to concentrate on $GFPC^-$.

I also developed the multi-color application of $GFPC^-$. DRAQ5 is introduced to label bacterial DNA while at the same time the cytoplasm of bacteria is labelled by $GFPC^-$. It is found that $GFPC^-$ could only label the bacterial cytoplasm but not the DNA. Another dye PKH26 is also introduced to label bacterial membrane while $GFPC^-$ is used for labelling the cytoplasm.

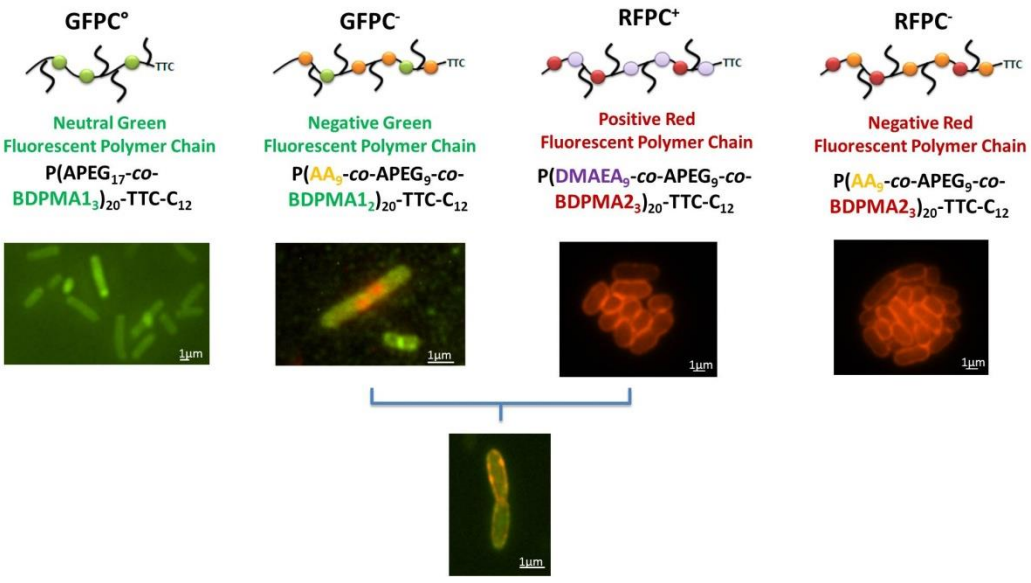



**Figure 4.31** Summary of FPCs and their bioimaging application of *E.coli* bacteria.

RFPCs also have no toxic effect on *E.coli*'s growth and they can label the bacterial membrane easily by simple incubation. $GFPC^-$ and $RFPC^+$ are compatible with each other and they can be used for bacteria internal and external bioimaging at the same time.

Compared with the commercial membrane dye PKH26, RFPCs have shown significant advantages. Our experiments show that we can use at least 100 times less RFPCs material to label the same amount of bacteria than PKH26.

Our FPCs series are highly water-soluble, biocompatible, stable and bright. With different multi-color image tests, FPCs show good compatibility with different types of commercial dyes. Moreover, they are very easy and cheap to synthesize and can be easily used to either internal (cytoplasm) or external (membrane) bioimaging applications of bacteria in any laboratory without additional expensive instruments or operators.

## 4.9 Additional images

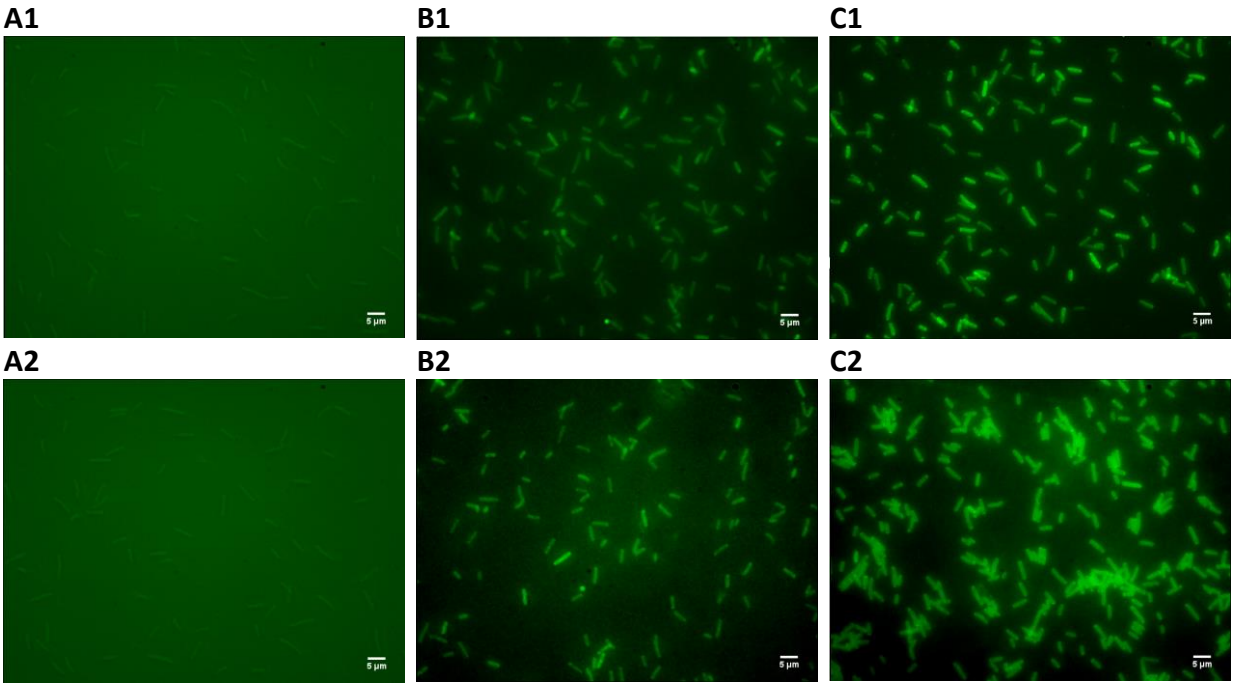



**Figure S4.1** Fluorescence image (60X objective, IT=10s) of *E.coli* alone (A) and *E.coli* interacting with $GFPC^0$ (B) and $GFPC^-$ (C).

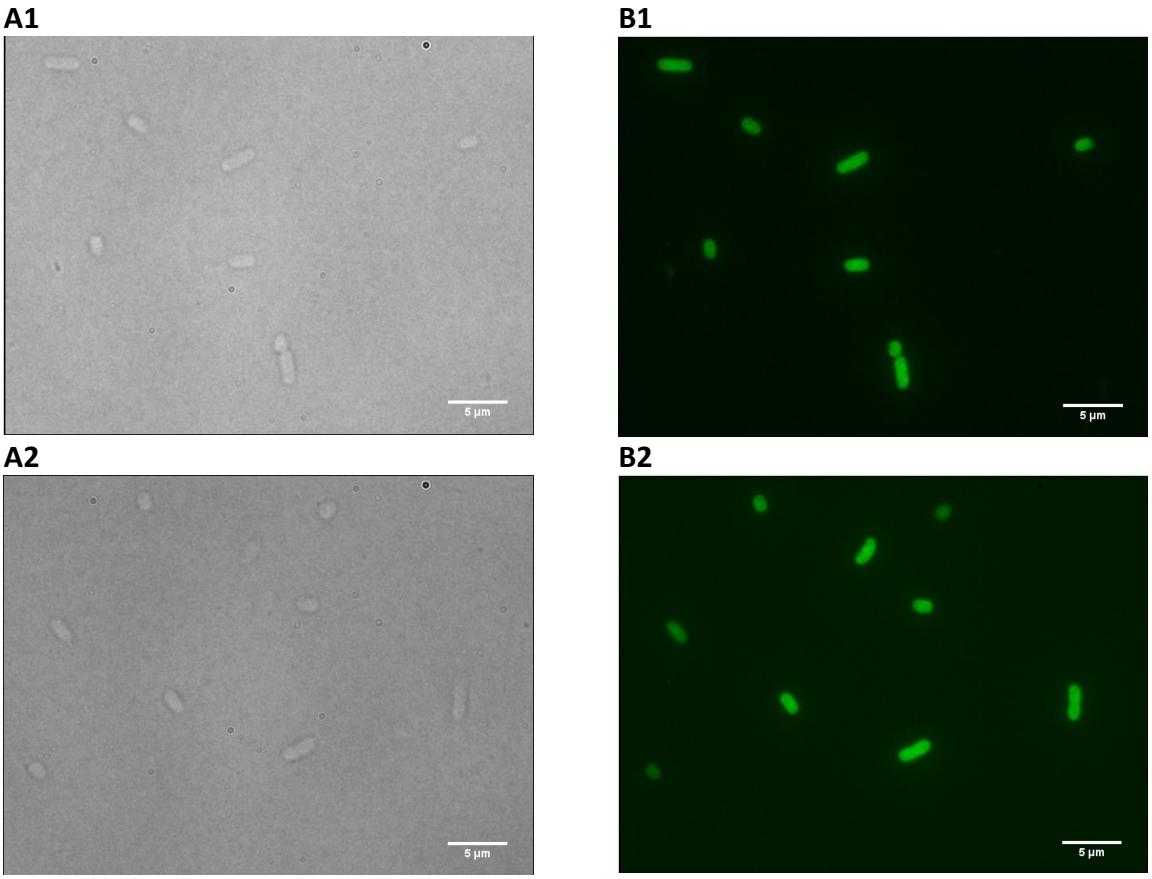



**Figure S4.2** *E.coli* interacting with $GFPC^-$ after quenching with methylene blue (100X objective, A: bright field image, IT=500ms; B: fluorescence image, IT=5s).

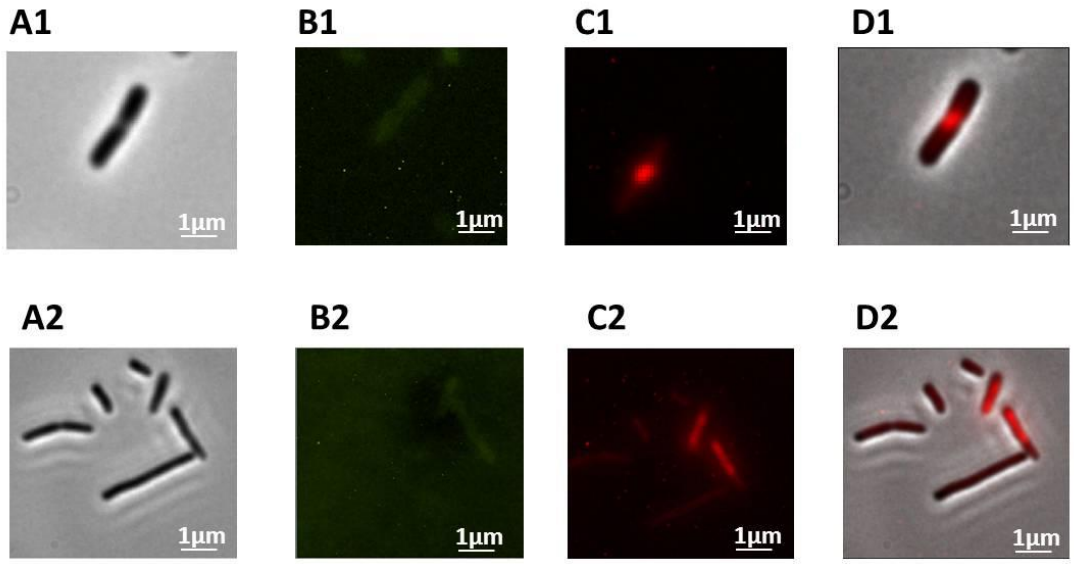
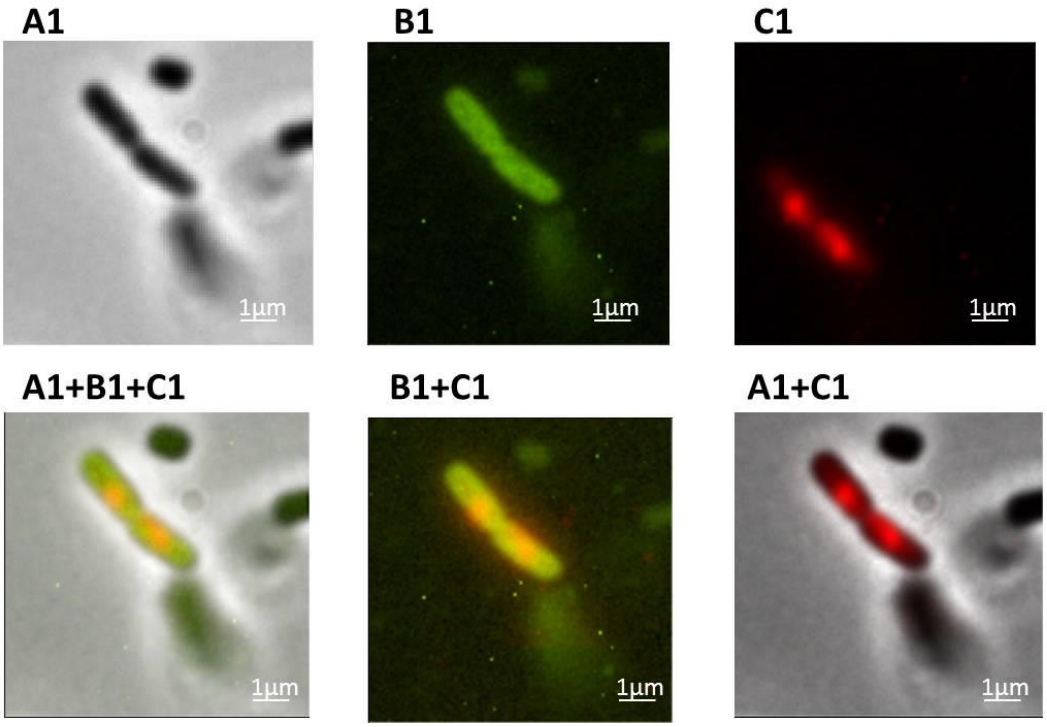



**Figure S4.3** Images of DRAQ5 labeling the DNA of *E.coli* (60X objective, A: phase contrast image, IT=100ms; B: green fluorescence image, IT= 20s; C: red fluorescence image, IT=20s; D: overlapped image of A and C).



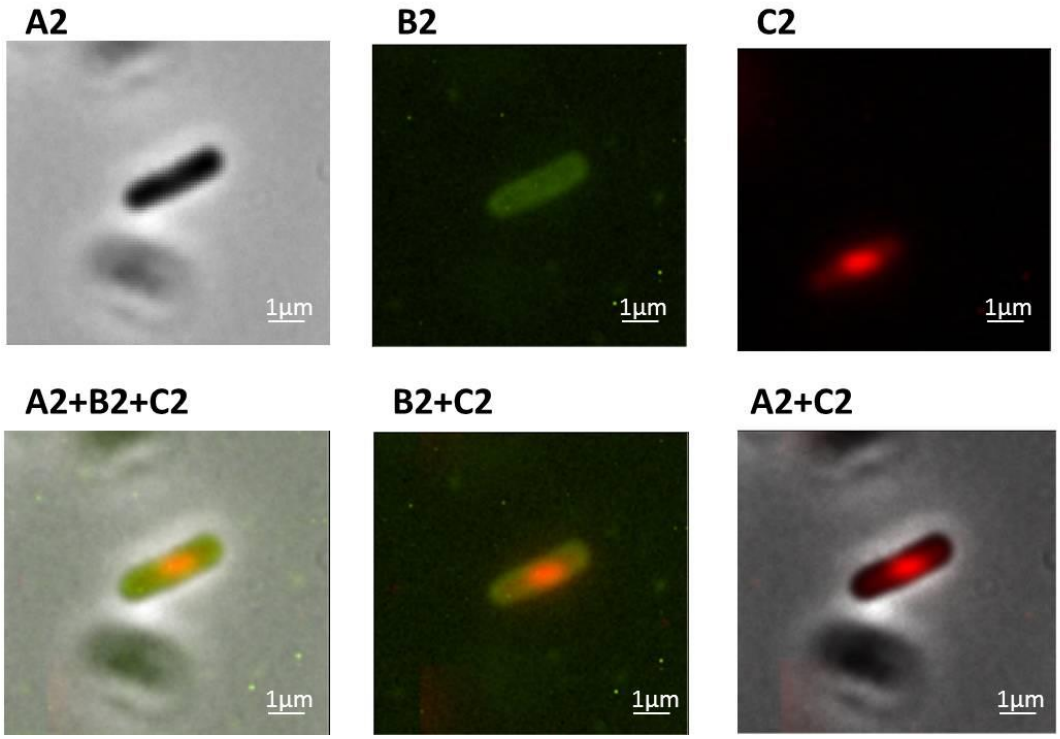



**Figure S4.4** Bioimaging of *E.coli* bacteria incubated with GFPC and DRAQ5 (60X objective A: phase contrast image, IT=100ms; B: green fluorescence image, IT= 20s; C: red fluorescence image, IT=20s). Additional images are shown in **Figure S4.4 in Section 4.9**.

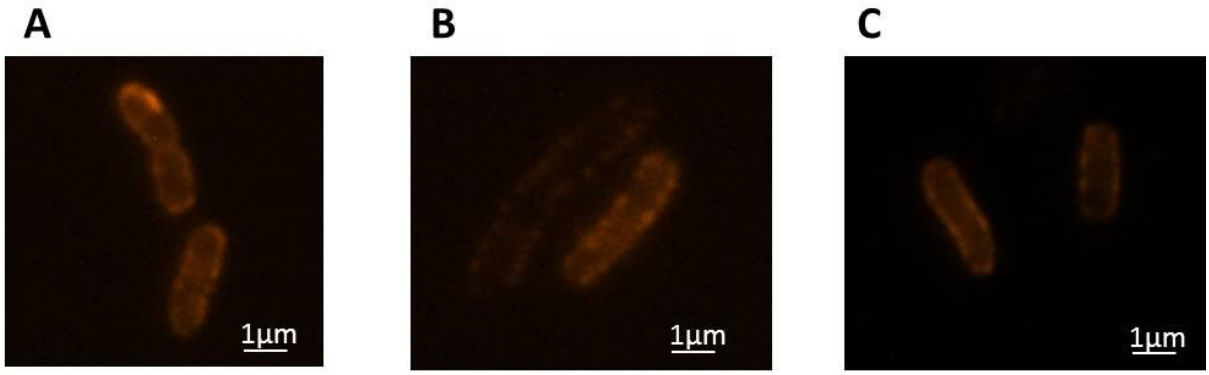



**Figure S4.5** Fluorescence images of PKH26 labeling the membrane of *E.coli* (100X objective, fluorescence image, IT=5s).

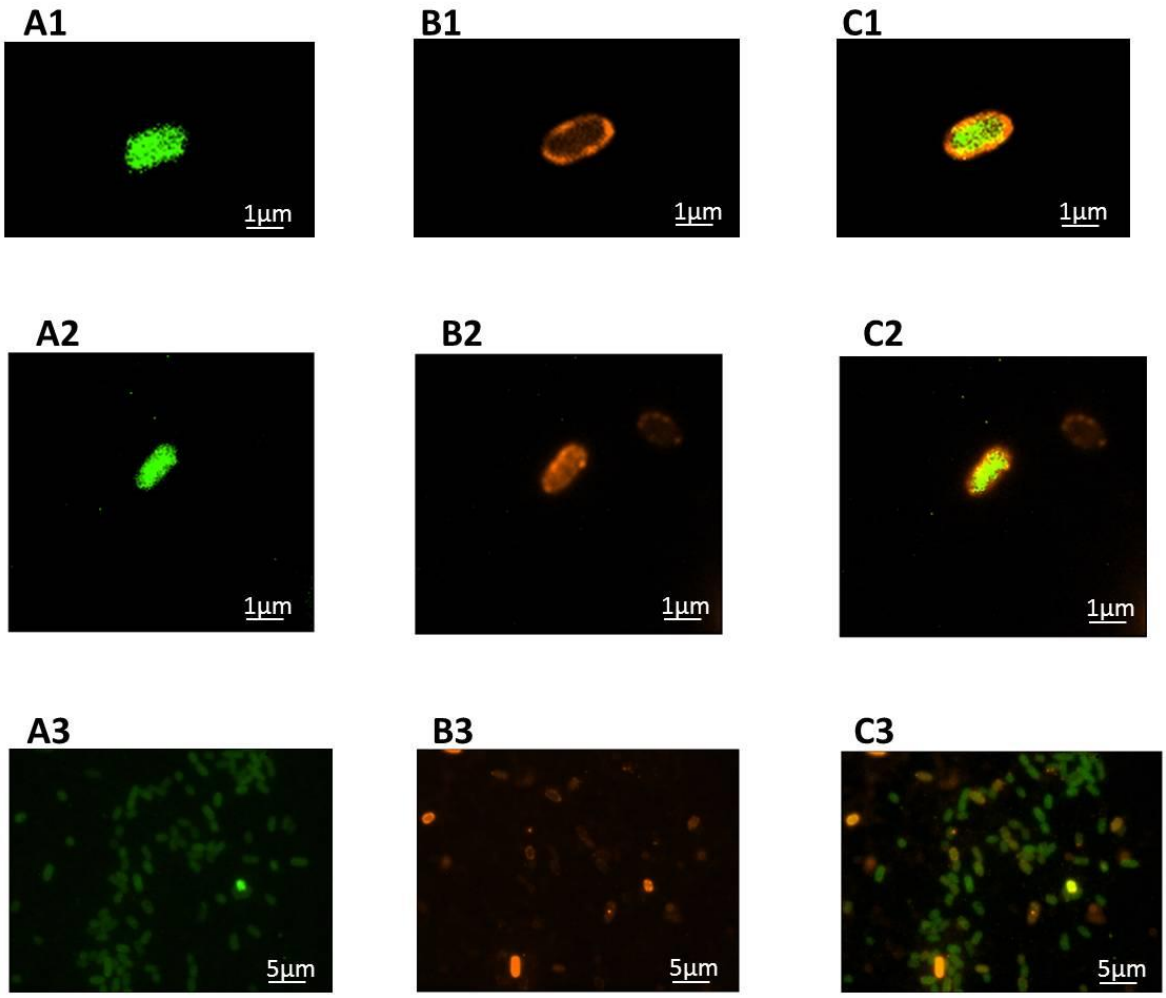



**Figure S4.6** *E.coli* interacting with GFPC$^-$ and PKH26 (A: green fluorescence image, IT=5s; B: orange fluorescence image, IT=5s; C: overlapped image of A+B).

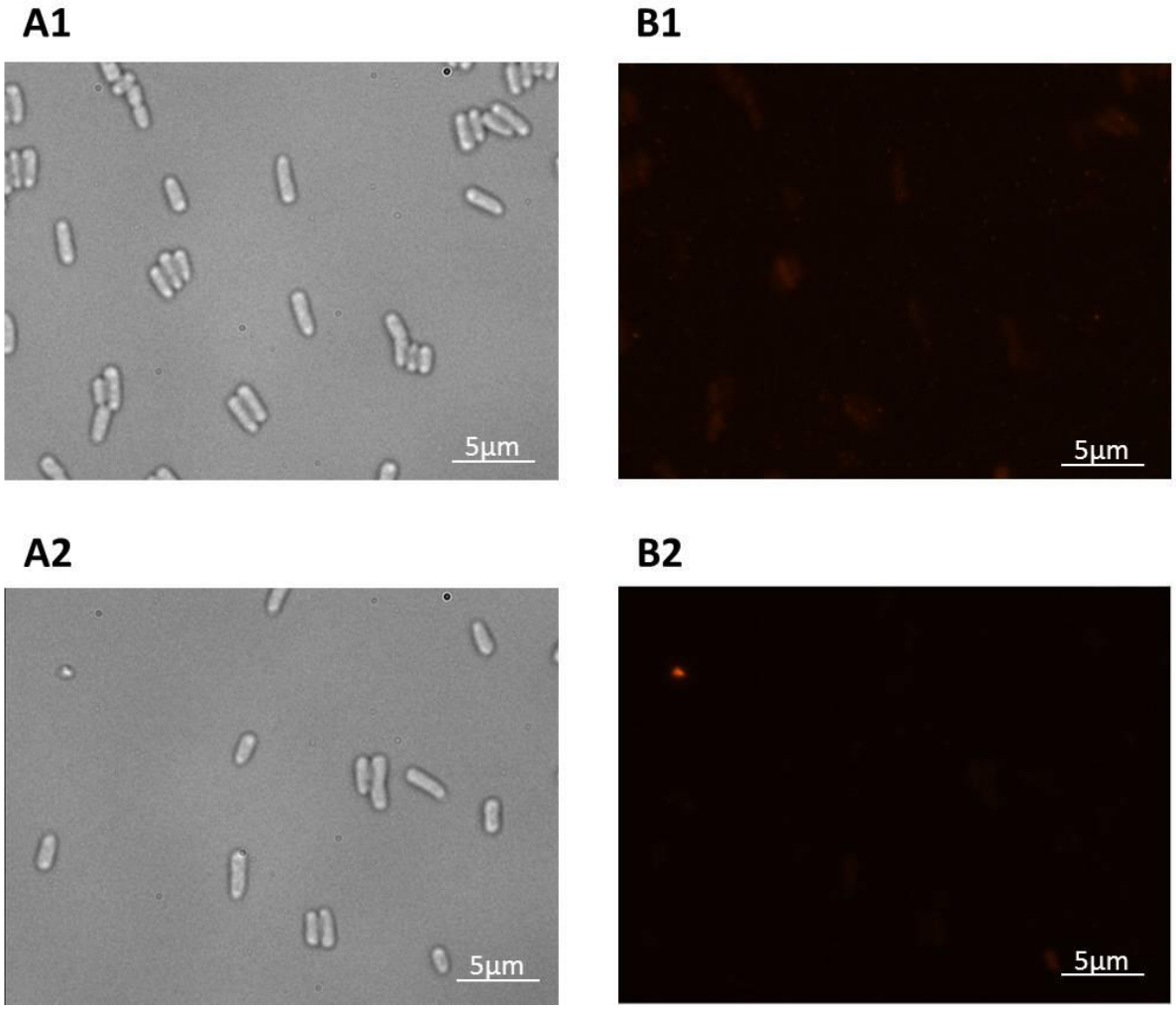



**Figure S4.7** Red auto-fluorescence images of *E.coli* alone (100x objective, A: bright filed image, IT=500ms; B: fluorescence image, IT=1s).

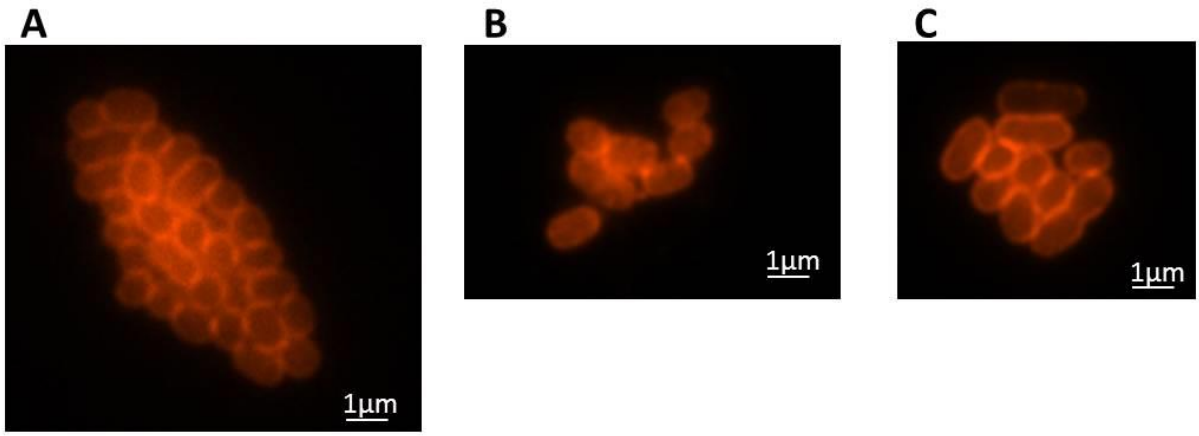



**Figure S4.8** RFPC$^{+}$ labelling the membrane of *E.coli* bacteria (100X objective, fluorescence image, IT=1s).

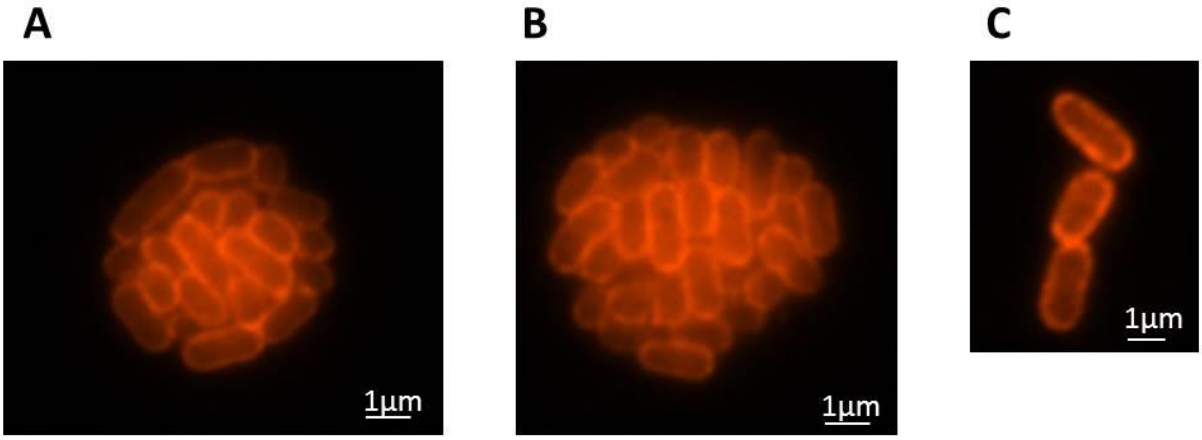



**Figure S4.9** RFPC$^-$ labelling the membrane of *E.coli* bacteria (100X objective, fluorescence image, IT=1s).

# Chapter 5 Fluorescent pH-sensitive nanoparticles (FANPs) for rapid detection of *E.coli* growth

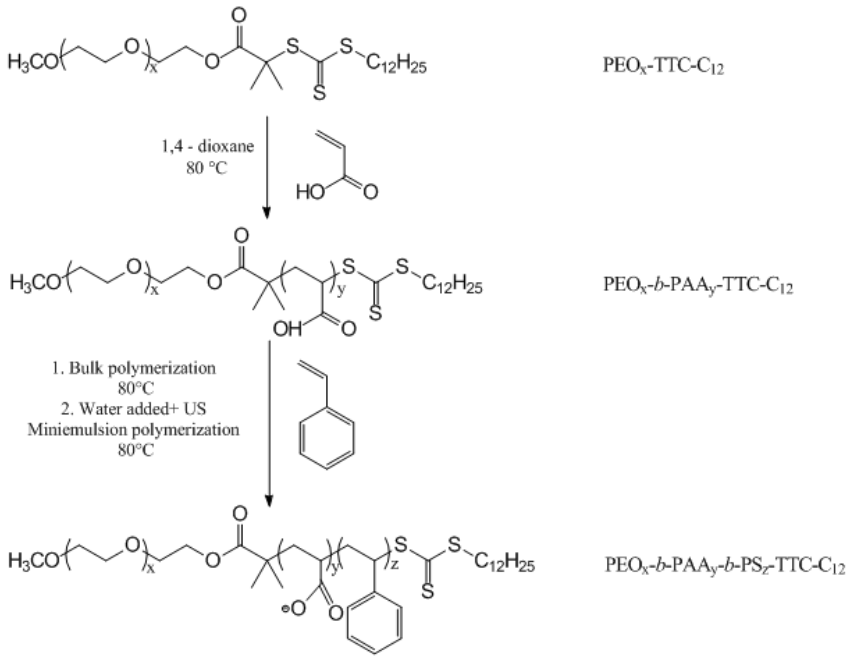
Rapid detection of bacterial growth is an important issue in the food industry and for medical research. In this chapter I will present a novel kind of fluorescent pH-sensitive nanoparticles (FANPs) that can be used for the rapid and accurate real-time detection of *Escherichia coli* growth. These organic particles are designed to be non-toxic and highly water-soluble. Here we show that the coupling of pH sensitive fluoresceinamine to the nanoparticles results in an increased sensitivity to changes in pH within a physiologically relevant range that can be used to monitor the presence of live bacteria. In addition, these FANPs do not influence bacterial growth and are stable over several hours in a complex medium and in the presence of bacteria. The use of these FANPs allows for continuous monitoring of bacterial growth via real-time detection over long time scales in small volumes and can thus be used for the screening of a large number of samples for high-throughput applications such as screening for the presence of antibiotic resistant strains. This part of work has been submitted.

## 5.1 Synthesis of fluorescent pH-sensitive nanoparticles (FANPs)

### 5.1.1 Synthesis of polystyrene nanoparticles (PSNPs)

The pH–sensitive nanoparticles presented here have been elaborated from polystyrene nanoparticles (PSNPs) as recently reported [180]. The one-pot synthesis is based on a reversible addition-fragmentation chain-transfer (RAFT) polymerization in miniemulsion conditions using a surfactant-free one-pot phase inversion process (**Scheme 5.1**). Briefly, the particles were obtained from a hydrophilic chain PEO-b-PAA (poly(ethylene oxide)-block–poly(acrylic acid)) macroRAFT agent. These hydrophilic chains were first extended with a hydrophobic block by a bulk polymerization of styrene (S). The polymerization was stopped before total consummation of styrene and, by adding basic water, droplets of the remaining styrene covered by the amphiphilic copolymer PEO-b-PAA-b-PS were obtained. A homogeneous miniemulsion was formed by ultrasound treatment. Finally, the RAFT polymerization was reinitiated by simple degasing with argon and heating to 80°C. After re-polymerization, a core-shell structure negatively charged nanoparticle was obtained with polystyrene in the core and poly(ethylene oxide)-block–poly(acrylic acid) in the shell. The

obtained PSNP1 was well-defined in size with a mean hydrodynamic diameter of 70 nm[27] (**Table 5.1**).




**Scheme 5.1** Synthetic scheme employed for the synthesis of the PSNP1.

**Table 5.1** Characterization of nanoparticles (PSNPs) having different shells[27]

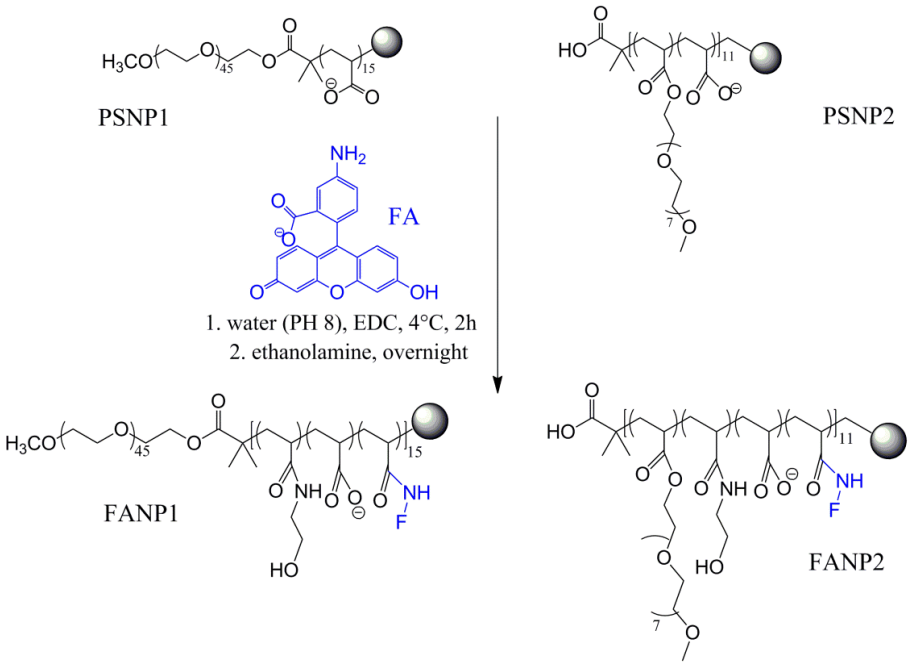
| Sample | Shell | Conv.s [a] | $D_h$ [nm] [b] |
|---|---|---|---|
| PSNP1 | $PEO_{45}$-*b*-$PAA_{19}$ | 0.97 | 80 |
| PSNP2 | $P(AA_{0.5}$-*co*-$PEOA_{0.5})_{22}$ | 0.85 | 70 |

[a] Styrene conversion[27], [b] Hydrodynamic diameter ($D_h$) determined by DLS.

In order to obtain a stable colloidal dispersions, a poly(acrylic acid) block is used in the particle design in order to have both electrostatic and steric repulsion. In addition, the introduction of carboxylic acid groups in the particle's shell is helpful for post-functionalizing of the PSNPs and the preparation of pH-sensors. Furthermore, in order to test the effect of the architecture of the hydrophilic chains on the pH-dependence of fluorescence, a PSNP2 with a different shell architecture compared with PSNP1 was designed. In this case, the PEO-b-PAA shell was replaced by a randomly distributed copolymer of acrylic acid (AA) and poly (ethylene oxide) methyl ether acrylate (PEOA) as P(PEOA-co-AA). It was found that PSNP2 nanoparticles have a similar hydrodynamic diameter compared with PSNP1 (**Table 5.1**).

### 5.1.2 Grafting pH sensitive fluorophores on the PSNPs

Fluoresceininamine was selected as a pH-sensitive molecule because it has an intense absorption band in the visible. Even though it can adopt four different forms (dianion, anion, neutral and cation) depending on the pH, it is only highly fluorescent in its dianionic form[201]. Furthermore, the pKa of the anion/dianion couple is about 6.4, which is suitable to measure changes in pH in biological media. The grafting of amino-functionalized molecules on carboxylic groups is a standard procedure[202]. The functionalization of PSNPs with fluoresceinamine (FA) was performed at pH=8 and 4 °C. The grafting of FA on PSNP1 and PSNP2 was carried out using 0.5 and 1 equivalent of FA per acrylic acid unit, respectively (**Scheme 5.2**). In all cases, the grafting did not change the hydrodynamic diameter of the nanoparticles significantly. The hydrodynamic of the fluoresceinamine conjugated nanoparticles (FANPs) remains around 50-70 nm (**Table 5.2**).




**Scheme 5.2** Preparation of pH nanosensors (FANP1 and FANP2) from PSNP1 and PSNP2.

**Table 5.2** Spectroscopic properties of FANPs in water (pH=8)[27]

| Sample | Shell | $D_h$/nm [a] | $\lambda_{abs}$/nm | $\lambda_{em}$/nm | $\Phi_F$ [b] | Number FA/FANP [c] |
|---|---|---|---|---|---|---|
| FANP1 | $PEO_{45}$-*b*-$PAA_{19}$ | 73 | 488 | 519 | 0.12 | 530 |
| FANP2 | $P(AA_{0.5}$-*co*-$APEO_{0.5})_{22}$ | 56 | 490 | 521 | 0.14 | 340 |

[a] Hydrodynamic diameter ($D_h$) determined by DLS. [b] Error of 15%[182]. [c] Styrene conversion determined by gravimetry and corrected with the loss of styrene by evaporation[203].

## 5.2 Characterization of FANPs

### 5.2.1 Spectroscopic properties of the FANPs

Absorption and fluorescence spectroscopy analysis of FANP1 and FANP2 are shown in **Figure 5.1**, their main spectroscopic data are given in **Table 5.2**. The particle suspensions have a maximum absorption at 488 and 490 nm and a maximum fluorescence emission at 519 and 521 nm in FANP1 and FANP2 respectively, in water at pH 8. There is a slight red shift compared to the free FA dye [201] which may come from the change of the local environment of the dye. The fluorescence quantum yield of the nanoparticles is between 12% and 14% for both particles at pH 8. This is lower than the free fluorescein amide dye (pH > 7, $\Phi_F$ = 79% [177]) which may be due to the formation of FA aggregates in the shell. The number of grafted fluorescein molecules is 530 and 340 for FANP1 and FANP2 respectively as estimated from the absorption spectra [204].

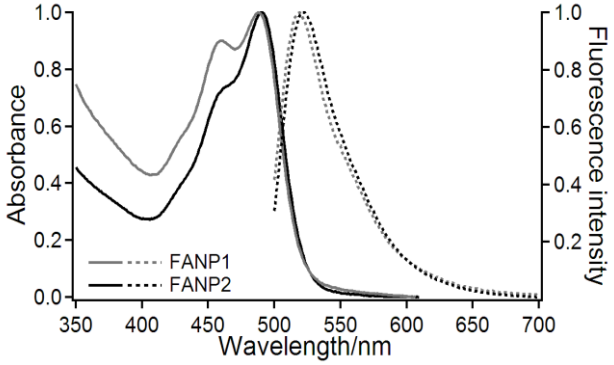



**Figure 5.1** Normalized absorption (full lines) and fluorescence emission (dotted lines) spectra (λexc=495nm) of a suspension of FANP1 (grey lines) and FANP2 (black lines) in water at pH=8.

The spectroscopic behavior of these FA-grafted nanoparticles was then studied at various pH values (**Figure 5.2**). The fluorescence spectra at pH=8 for FANP1 (**Figure 5.2A**) and FANP2 (**Figure 5.2C**) have a main band centred at 519 nm and 521 nm respectively. This main band was attributed to fluoresceinamide. The fluorescence spectra were then recorded at different pH (phosphate/citrate buffers 1mM in 140mM NaCl). Upon a decrease in the pH, the spectral intensity decreased both in the absorbance and fluorescence for FANPs. This behaviour is similar to that of fluorescein in water. Moreover the pKa was determined from the fluorescence spectra using the Henderson-Hasselbach equation:

$$I = \frac{I_A + I_B K_a 10^{pH}}{1 + K_a 10^{pH}}$$

Where I is the fluorescence intensity of the sample and $I_A$ and $I_B$ are the fluorescence intensities in the acidic and basic forms respectively[22]. The pKa for both types of nanoparticles is around 6.5 and a linear dependence of the fluorescence intensity was observed between pH 5.5 and 7.5. Both the pKa and the linear range are in agreement with the one of the free FA dye [205], therefore it seems that the grafting does not change the pH dependent fluorescent properties of FA. This is the useful pH range for the study of most biological systems. Compared to approaches reported previously [176,206], in this case the linearity of the signal covers a wider and more suitable range of pH values for detecting bacteria. The amplitude of the fluorescence intensity change between these two pH values is around 7-fold which is 3 times higher than previously reported [176,207]. These properties will thus allow a sensitive and precise determination of the change in pH in biological systems.

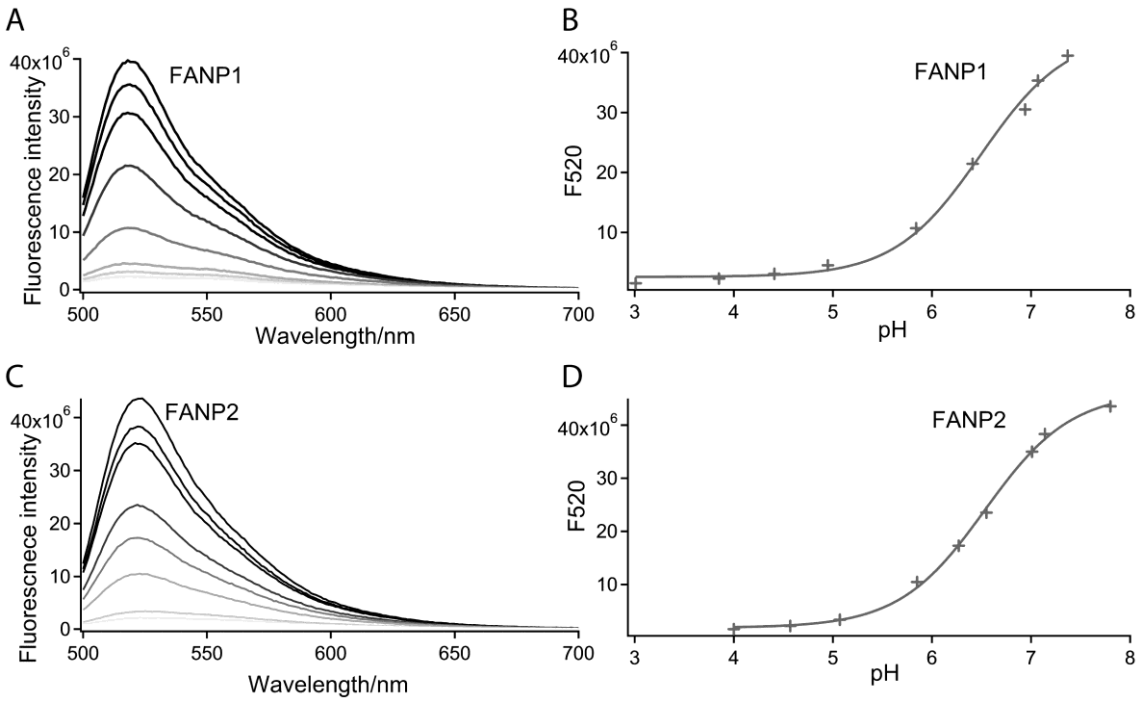



**Figure 5.2** Fluorescence emission spectra of FANP1 (A) and FANP2(C) as a function of pH ($\lambda_{exc}$=495nm; phosphate/citrate buffer 1mM and 140mM NaCl). B: Change in fluorescence intensity of FANP1 at 520nm as a function of pH. The data was fit using the Henderson-Hasselbach equation with pKa=6.49. pH values: 7.37, 7.07, 6.94, 6.41, 5.84, 4.95, 4.41, 3.85, 3.01. D: Change in fluorescence intensity of FANP2 at 520nm as a function of pH. The data was fit using the Henderson-Hasselbach equation with pKa=6.53. pH values: 7.80, 7.14, 7.01, 6.55, 6.27, 5.85, 5.07, 4.57, 4.00.

### 5.2.1 Photostability and reversibility assessments of FANPs

It is widely known that the main drawback of fluorescent sensors is the bleaching of the fluorophore over long time periods. The photostability of the FANPs was measured to determine whether photo-bleaching occurs during extended measurement of fluorescence during the incubation in the growth medium. FANPs were added to the modified M9 minimal medium at room temperature or 37°C. Every 30 minutes a fluorescence emission spectrum was recorded (**Figure 5.3**). It was found that over four hours there is no fluorescence decrease for both FANP1 and FANP2.

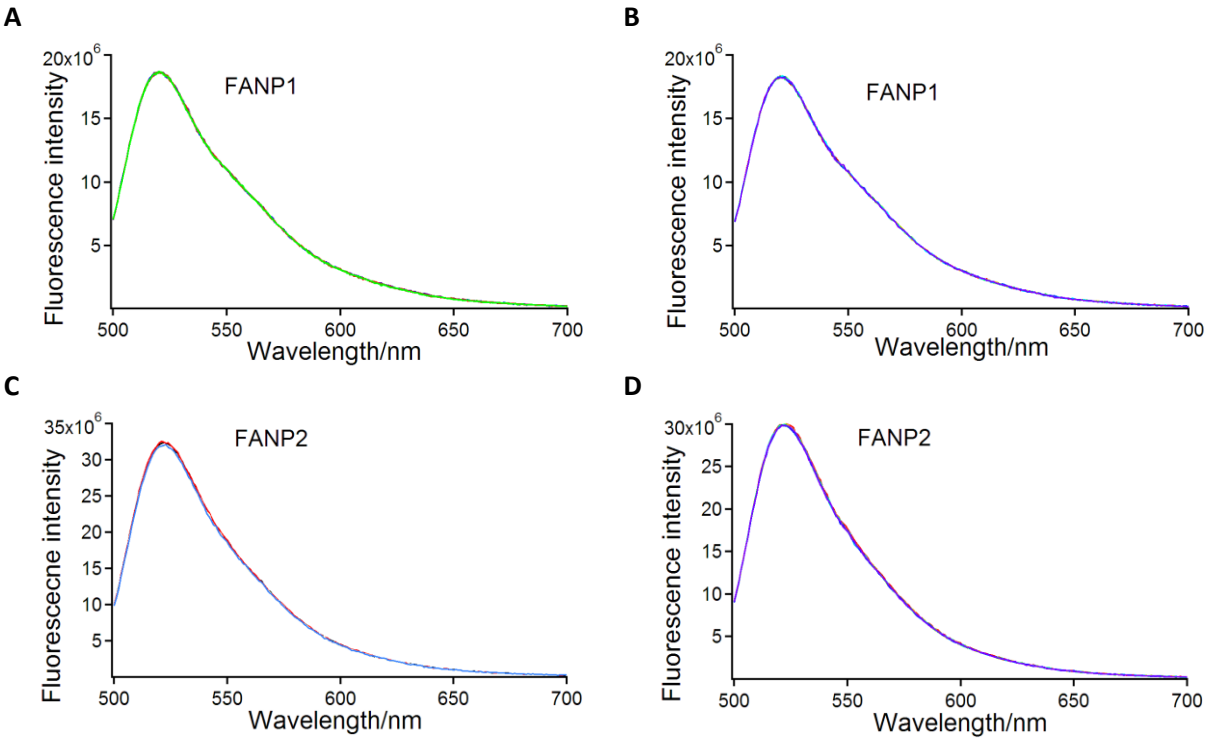



**Figure 5.3** Evolution of fluorescence emission spectra of FANP1 or FANP2 over four hours ($\lambda_{exc}$=495nm; Modified M9 Minimal Medium,). A and C are at room temperature and B and D are at 37°C. A spectrum was taken every 30mins.

In order to assess the photostability of FANPs on longer time scales, an overnight experiment was also carried out. The FANPs concentrations used were $8.2x10^{-7}$M, $4.1x10^{-7}$M and $8.2x10^{-8}$M. FANP1 or FANP2 of different concentrations in the modified M9 minimal medium were incubated in the plate reader at 37°C in the dark overnight. The fluorescence intensity of FANPs was measured every 6 minutes by using a F485/14 filter for excitation and a F535/40 filter for emission. For an incubation of over ten hours, the fluorescence intensity of FANPs at different concentrations remained practically constant (**Figure 5.4**).

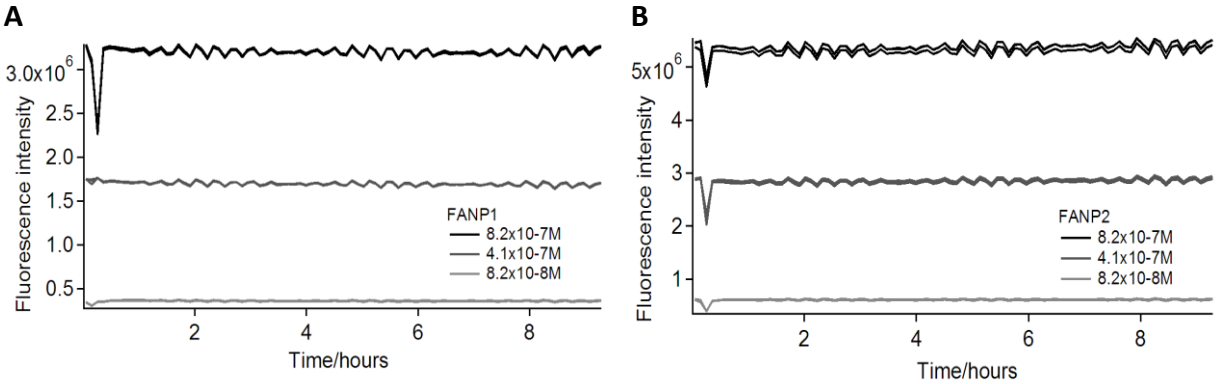



**Figure 5.4** Evolution of fluorescence intensity of FANP1 (A) or FANP2 (B) overnight. (37°C, Modified M9 Minimal Medium,). FANPs particles at $8.2x10^{-7}$M (black lines), $4.1x10^{-7}$M (dark grey lines) and $8.2x10^{-8}$M (light grey lines).

The reversibility and dynamic behaviour of the FANPs was investigated by alter the pH of medium (pH 4 and 8) several times with a presence of FANPs, respectively. The response of FANPs is shown in **Figure 5.5.** Nearly, the same response was obtained for 8 repetitions with no evidence of degradation. This indicates that our FANPs have good reversibility. The response time of FANPs at different pH medium was found to be relatively fast (less than 5 second) compared with reported literature [206,207], indicating the high proton permeability of the FANPs.

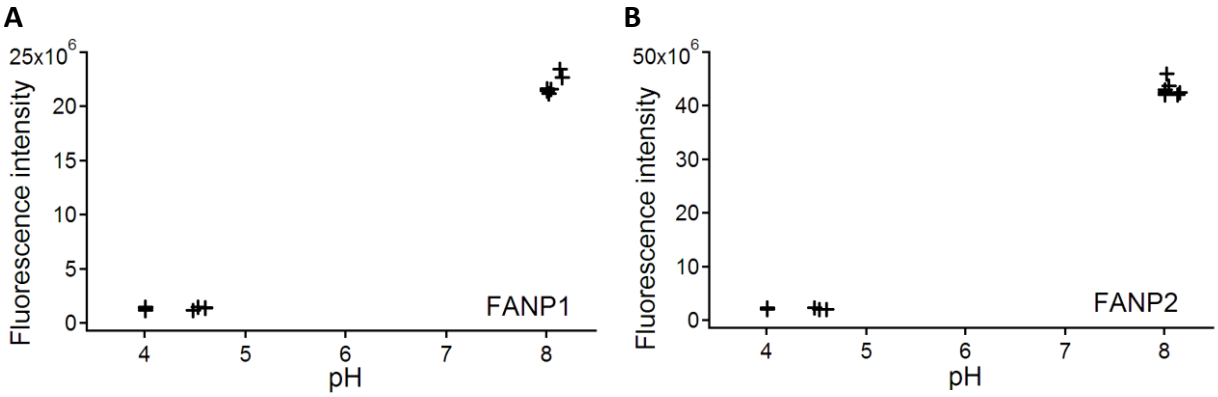



**Figure 5.5** Reversibility measurements of FANP1 (A) and FANP2 (B) fluorescence intensity in response to alter medium of pH 4 and pH 8.

The FANPs are thus very stable through time in the experimental conditions needed to monitor bacterial growth since they are not affected by the temperature and growth medium. This unique feature is very important for continuous monitoring for real-time detection on long time scale.

## 5.3 Toxicity assessments of FANPs on *E.coli*

In order to assess the toxic effect of FANPs on *E.coli*, the growth rate of bacteria in the presence of FANPs was compared with the growth rate of *E.coli* bacteria alone. The growth rate was measured by absorbance measurement (OD@600nm) in a 96-well plate reader. The FANPs concentrations used were $8.2x10^{-7}$M, $4.1x10^{-7}$M and $8.2x10^{-8}$M.

*E.coli* bacteria with different concentrations FANP1 or FANP2 were incubated in the plate reader at 37°C in the dark overnight. A control with only bacteria was also prepared. Every 6 minutes the growth rate of the cells was monitored by measuring the optical density at 600nm by the plate reader **(Figure 5.6**). For an incubation of over ten hours the growth curves of bacteria with FANPs at different concentrations were practically the same as the growth curve of bacteria alone. This means that FANPs have no toxicity effect on bacterial growth in a long time scale independently of the kind of shell present on the FANPs.

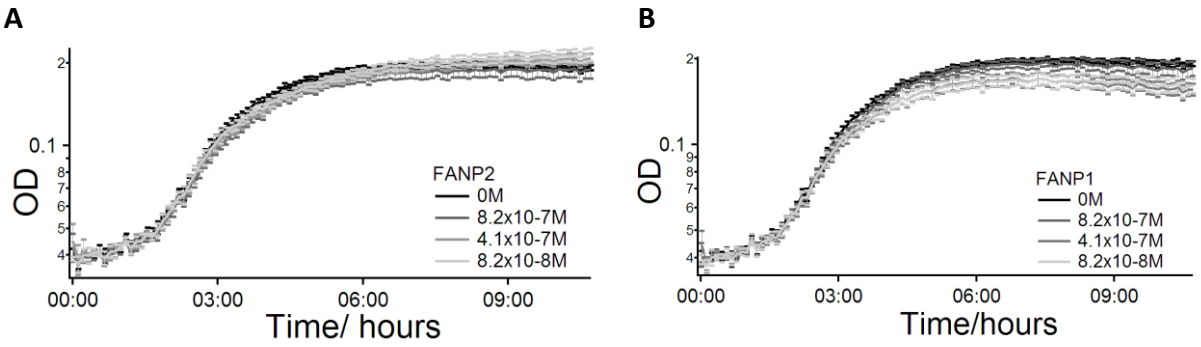



**Figure 5.6** Growth curves of *E.coli* bacteria alone and of *E.coli* bacteria incubated with FANP2 particles at $8.2x10^{-7}$M, $4.1x10^{-7}$M and $8.2x10^{-8}$M. The error bars indicate the difference between the three replicates in the experiment.

## 5.4 Detection of *E.coli* growth with FANPs

### 5.4.1 Real-time detection of *E.coli* growth

Growth of *E.coli* bacteria with glucose results in the production of $CO_2$ and acetic acid and, therefore, a decrease in pH of the growth medium. Having synthetized and characterized the pH-sensitive nanoparticles, we next tested whether they could be used to precisely monitor the pH change due to bacterial growth. In order to measure the change in fluorescence intensity of FANPs in the presence of *E.coli* bacteria, the growth medium with an initial pH of 7.0 and an initial *E.coli* bacterial concentration of $2x10^7$ CFU/mL(OD=0.2) was placed inside a cuvette in the presence of FANPs. *E.coli* bacteria samples with the FANPs

were incubated at 37°C in the dark. Every 30 minutes the growth of the cells was monitored by measuring the optical density at 600 nm using a spectrophotometer (**Figure 5.7E, F**). When the bacteria began to grow, the pH of the growth medium started to decrease. The pH of the samples was monitored at several time intervals with a pH meter. When the bacterial concentration increased to $1.1x10^8$CFU/mL (OD=1.1), the pH of the growth medium decreased to 5.8. At the same time, the emission spectra of the samples were measured. As bacterial growth increased the fluorescence intensity of both FANPs decreased significantly (**Figure 5.7A, B**).

The fluorescence intensity of FANP2 for example decreased more than 80% during bacterial growth. Thanks to the calibration curve (**Figure 5.2D**) the pH can be evaluated by recording the change in fluorescence intensity of FANP2 in the growth medium (**Figure 5.7C**). It was found that these pH values were in full agreement with those measured by a pH meter (**Figure 5.7E**). Incubating FANP1 with *E.coli* gave similar results as those obtained with FANP2 (**Figure 5.7D, F**). In conclusion, the pH-sensitive nanoparticles can be used to precisely monitor the pH variation due to bacterial growth (**Figure 5.7**).

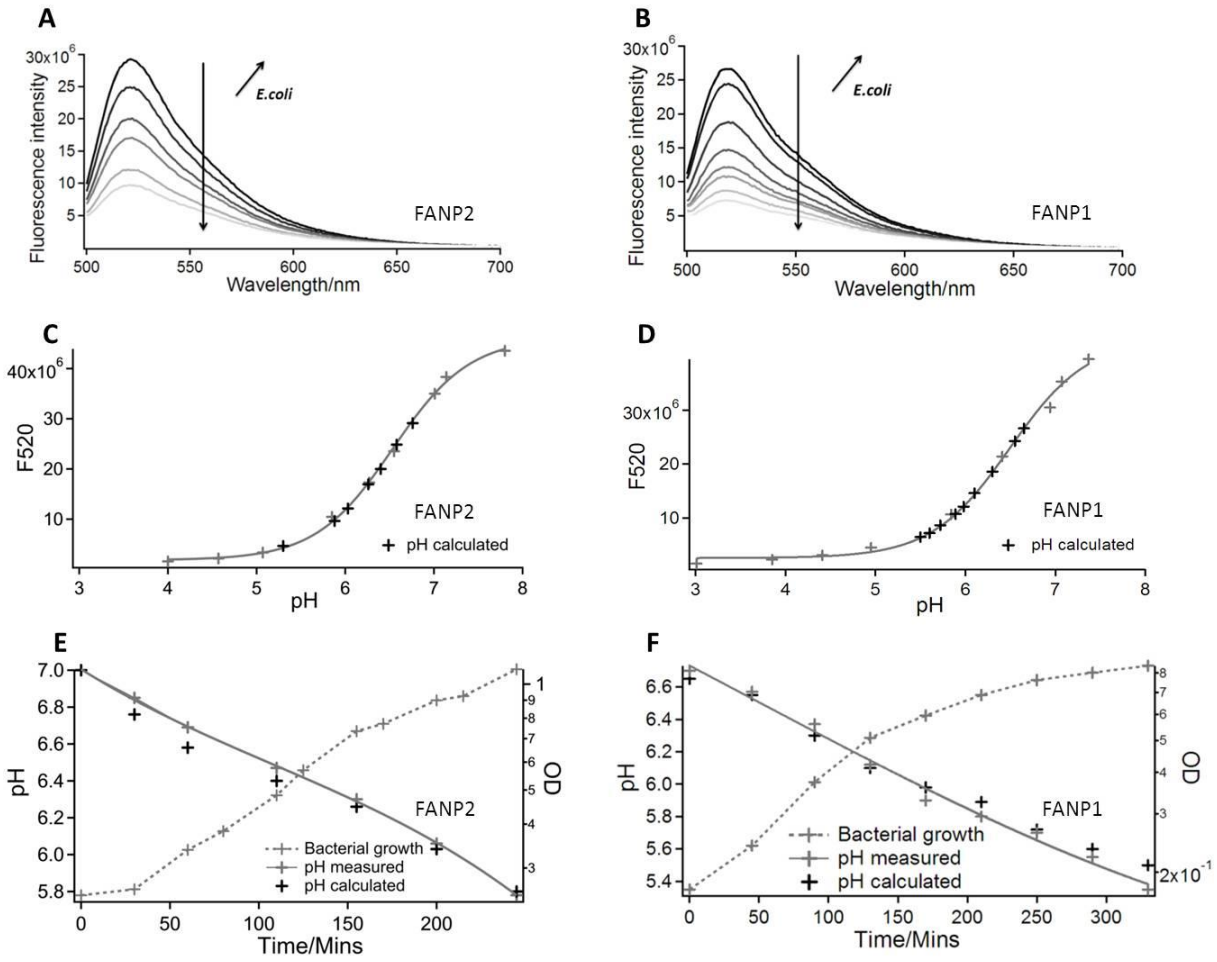



**Figure 5.7** Change in the fluorescence emission spectra of FANP2 (A) and FANP1 (B) with bacterial growth ($\lambda_{exc}$=495nm; Modified M9 Minimal Medium). B: Change in fluorescence intensity of FANP2 (C) and FANP1 (D) at 520nm and corresponding pH of the growth medium calculated by the Henderson-Hasselbach equation. Real-time bacterial growth curve (dotted line) and the corresponding pH evolution as measured by a pH meter (grey line) or the corresponding pH change calculated by the Henderson-Hasselbach equation from the change in fluorescence (black crosses)for FANP2 (E) and FANP1 (F).

## 5.4.2 Sensitivity assessments

A successful pH nano-sensor for the detection of *E.coli* growth should be both rapid and sensitive to small changes in bacterial concentrations. We therefore performed assays in order to assess the sensitivity of FANPs compared with the one of the same concentration of free fluoresceinamine (FA) molecules using a lower starting concentration of bacteria. FANP1, FANP2 or FA molecules were added to the growth medium with an initial concentration of *E.coli* bacteria of 3-6x$10^5$ CFU/mL (OD=0.003-0.006) inside a cuvette and were incubated at 37°C in the dark. Every 30 minutes the growth of the cells was monitored by using a spectrophotometer (**Figure 5.8**). At the same time, the emission spectra of the samples were

measured. The corresponding decrease in the percentage of the fluorescence intensity of FA molecules, FANP1 and FANP2 as a function of time is shown in **Figure 5.8**.

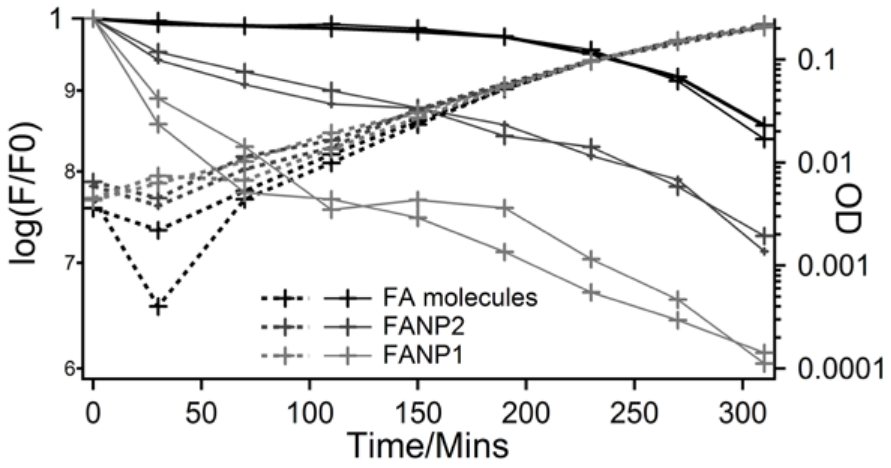



**Figure 5.8** Measurements of *E.coli* bacteria growth incubated with FA molecules (black lines), FANP1 (light grey lines) and FANP2 (dark grey lines) using either the measurement of OD@600nm (dotted lines– scale on the right axis) or the decrease (%) of fluorescence intensity (full lines– scale on the left axis) as a function of time for FA molecules, FANP1 and FANP2. The two lines represent the replicates within the experiment.

It was found that there is almost no fluorescence intensity decrease of FA molecules until after more than 3 hours of bacterial growth. After about 5 hours, the fluorescence intensity of FA molecules decreased up to 15% (**Figure 5.8**, **Figure 5.9A, B**).

However, for the FANP2, the fluorescence intensity decreases up to 10% during the first hour of bacterial growth. The fluorescence intensity of FANP2 continually dropped to more than 30% (**Figure 5.8**, **Figure 5.9C, D**) over the five hours of the experiment. Hence, compared with a molecular sensor of pH, such as FA, FANP2 is more sensitive, especially in the presence of a lower amount of bacteria as at the beginning of the experiment. This is probably due to the location of the sensing dyes in the nanoparticles. The local concentration of FA surrounding the nanoparticles is increased significantly compared to the free FA molecules. If the distance between the fluorophore and the bacterial cell influences its change in fluorescence, then a larger change in signal would result for each nanoparticle nearby a cell than for each individual fluorophore molecule.

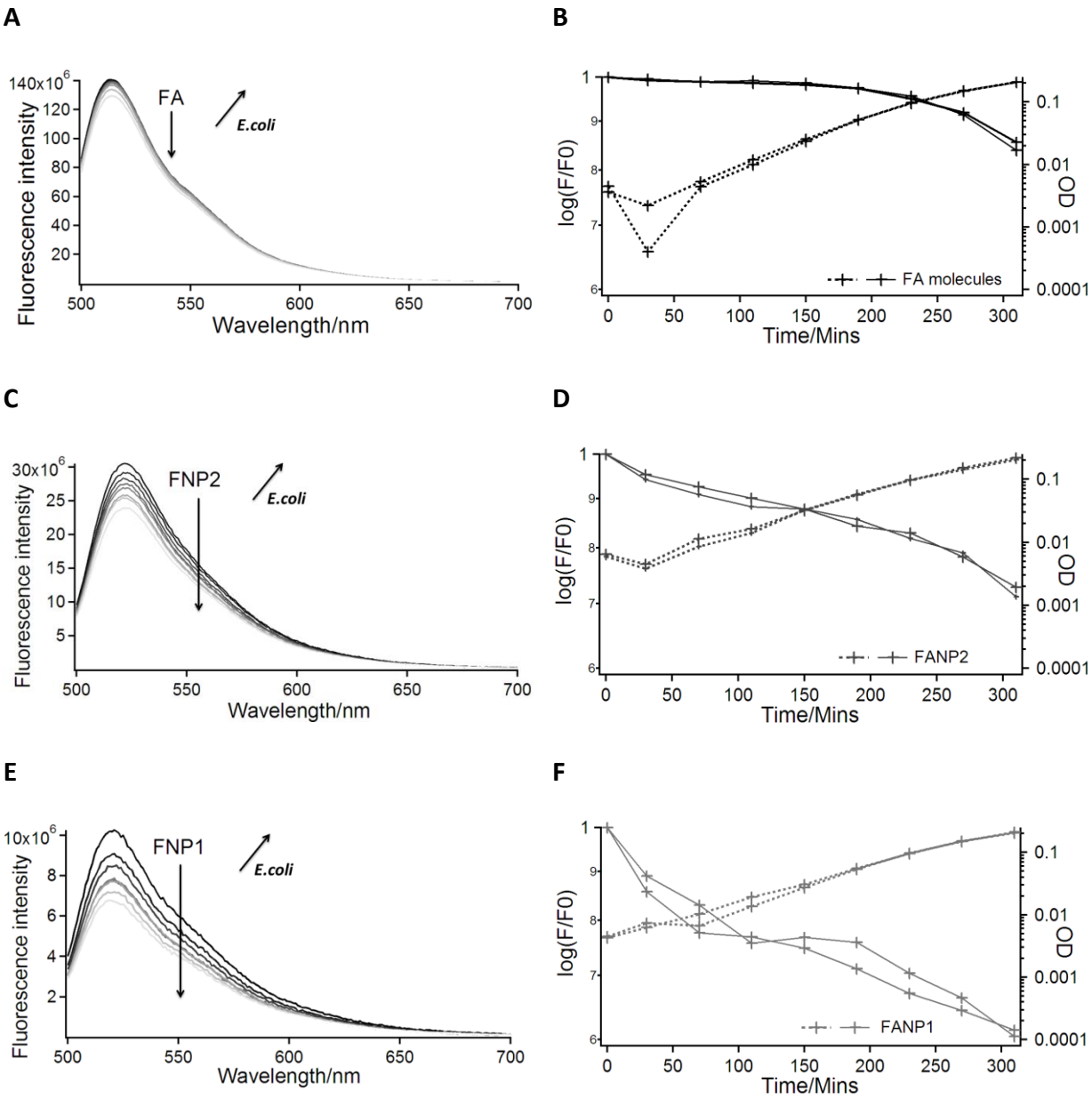



**Figure 5.9** Change in the fluorescence emission spectra of FA molecules (A), FANP1 (C) and FANP2 (E) with bacterial growth ($\lambda_{exc}$=495nm; Modified M9 Minimal Medium).Real-time bacterial growth curve and the decrease (%) of fluorescence intensity as a function of time for FA molecules (B), FANP1 (D) and FANP2 (F). The two lines represent the replicates within the experiment.

Furthermore, the FANP1 appeared to be even more sensitive than FANP2 in detecting *E.coli* bacteria. Indeed, during the first hour of bacterial growth, the fluorescence intensity of FANP1 continually decreased by almost 20% which is twice as much compared with FANP2 (**Figure 5.8**). Until 3 hours the fluorescence intensity of FANP1 decreased more than 30%, and at the end of the experiment it had decreased up to 40% (**Figure 5.8**, **Figure 5.9E, F**). The difference between the two FANPs is probably due to the different shell architecture of

FANP1 and FANP2**.** It is likely that the linear chains (FANP1 $PEO_{45}$-b-$PAA_{19}$) allow a greater accessibility to protons than the branched shell (FANP2 $P(PEOA_{0.5}$-co-$AA_{0.5})_{22}$).

As mentioned above, the growth of the cells was monitored using a spectrophotometer that reads the optical density (OD@600nm) of the samples every 30 minutes (**Figure 5.8**). From the time at which the bacteria started to grow until two hours of growth, it was found that this small amount of bacteria couldn't be measured accurately by a measurement of the change in optical density. In addition, there were large fluctuations in the signal in the first hour of growth, and as the bacterial number increased, the measurements of spectrophotometers became more reproducible. However, as shown in **Figure 5.8**, the fluorescence intensity measurements from the FANP1 and FANP2 particles are very reliable and reproducible from the very beginning until the end of the experiments. These results show that these pH-sensitive nanoparticles are not only more sensitive than a molecular sensor such as the FA molecules but also more sensitive than typical OD measurements.

## 5.5 High-throughput screening applications

### 5.5.1 Screening of cell growth in a 96 well plate

Since the FANPs can be used to measure the change in pH resulting from the metabolic activity of live bacteria, they can be used to discriminate whether the bacteria have died or have a decreased growth rate due to the fluorescence intensity change caused by metabolism. This approach can thus be more sensitive compared with typical OD meters and can be performed in complex media. We next tested the potential ability of FANPs for high-throughput screening of *E.coli* bacteria.

In order to measure the fluorescence evolution of FANPs when incubated with smaller volumes of bacteria, *E.coli* were incubated in a 96-well plate with different concentrations ($8.2x10^{-7}$M, $4.1x10^{-7}$M and $8.2x10^{-8}$M) of FANP1 or FANP2 and placed in a plate reader at 37°C in the dark overnight. A control with bacteria without nanoparticles was also prepared. The fluorescence intensity of each well was monitored every 6 minutes by using a F485/14 filter for excitation and a F535/40 filter for emission (**Figure 5.10**).

The fluorescence of FANPs was measured during the growth of *E.coli* for over ten hours. The fluorescence intensity of FANP1 decreased simultaneously with *E.coli* growth independently of the FANP1 concentration (**Figure 5.10A**). Comparison of the three different concentrations of FANP1 used shows that the response is independent of the amount of FANP1 present **(Figure 5.10B)**. Using FANP2 to measure the growth of *E.coli* gave very similar results as those obtained with FANP1 (**Figure 5.10C, D**). The correlation between the $OD_{600}$ and the fluorescence of FANPs is shown in **Figure 5.11**. One can see that the change in fluorescence of FANPs as a function of the growth of bacteria shows a good correlation with the OD ($r^2$=0.94 for FANP1 and 0.93 for FANP2) over 15 hours of continuous measurements which is a significantly improved correlation compared with a previous report using acridine orange [208].

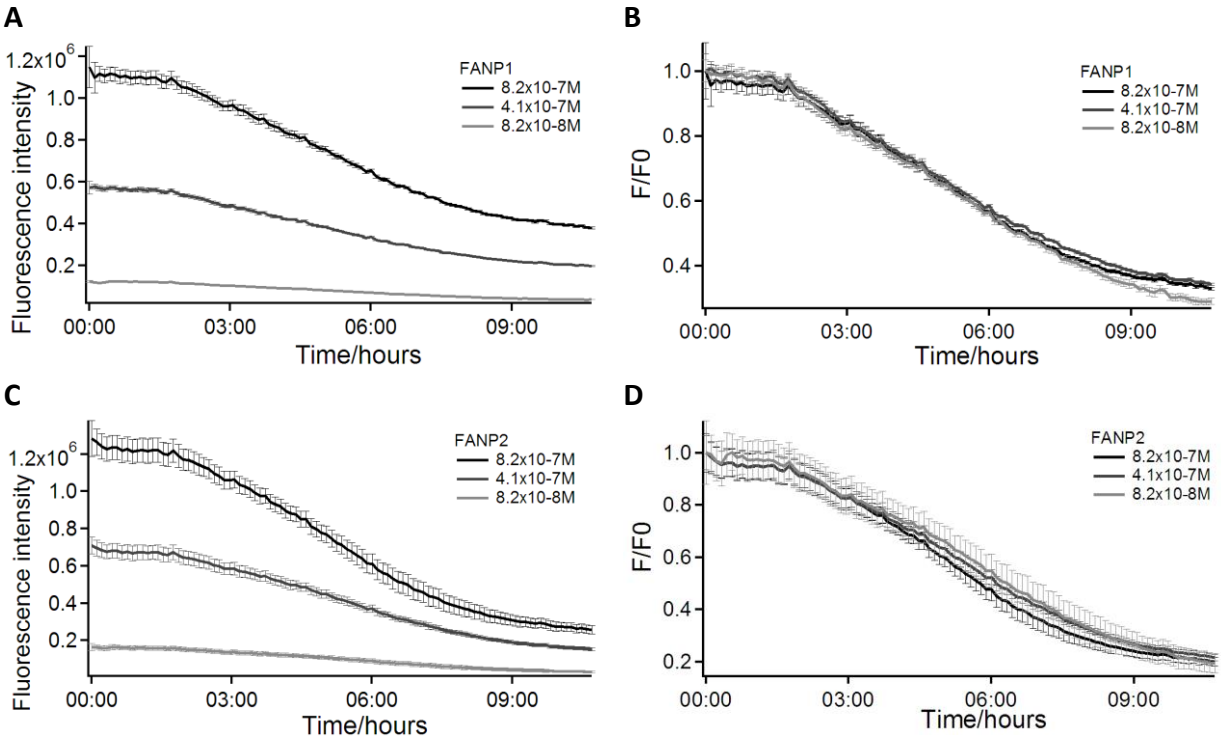



**Figure 5.10** Fluorescence evolution screening of FANP1 (A) and FANP2 (C) incubated with *E.coli*. The decrease (%) of fluorescence intensity as a function of time for three different concentrations of FANP1 (B) and FANP2 (D): $8.2x10^{-7}$M (black lines), $4.1x10^{-7}$M (dark grey lines) and $8.2x10^{-8}$M (light grey lines). Data were extracted from *E.coli* background fluorescence; the error bars indicate the difference between the three replicates in the experiment.

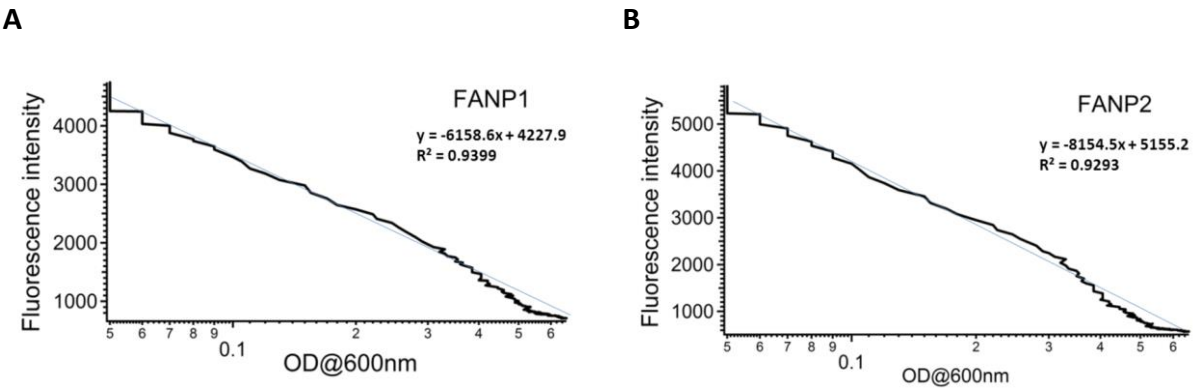



**Figure 5.11** Correlation between optical density and FANP1 (A) and FANP2 (B) for overnight incubation.

As a comparison the amount of FANP1 used in the cuvette experiment was the highest of the three used here, $8.2x10^{-7}$M.This shows that even after a ten-fold decrease in the concentration of FANP1 ($8.2x10^{-7}M \rightarrow 8.2x10^{-8}M$), one can still detect bacterial growth rapidly and accurately. Because of their stability and sensitivity these FANPs could be used as a novel indicator for screening of potential growth inhibition experiments.

### 5.5.2 High-throughput screening of bacterial growth inhibition by antibiotics

After demonstrating that FANPs can be used for measurement of *E.coli* bacteria growth in small volumes, we wanted to determine whether this approach could be used for high throughput experiments such as the detection of antibiotic resistance. In order to compare the results obtained by the change in OD with the change in fluorescence of FANPs ($8.2x10^{-8}$M) the effects of several common antibacterial drugs (Chloramphenicol, Kanamycin, and Ampicillin) on bacteria growth and metabolism were measured. The concentration of antibiotics used were 0.5, 1, 5, 10, 50 μg/mL, which cover the range of the known recommended concentrations of these antibiotics. The inhibitory effect of these drugs on the growth of *E.coli* as measured by the increase of the OD or the decrease in fluorescence of FANP1 is shown in **Figure 5.12.**

When increasing the concentration of antibiotics, the growth rate of *E.coli* bacteria decreases as measured by OD (**Figure 5.12A, C, E**). At the same time, the fluorescence intensity of FANP1 decreases when increasing the dose of the drugs (**Figure 5.12B, D, F**).

Moreover, from the growth curve, one can notice that after about ten hours of incubation bacterial growth, as measured by the OD, reached the stationary phase,

indicating that cell growth slowed down and that bacteria grew and died at the same rate, resulting in a constant number of bacteria. However, by measuring the OD it is not possible to measure the presence of bacterial growth once the population has reached stationary phase. On the other hand, the increase in the change in fluorescence at these later time points allows for a measurement of the amount of ongoing metabolism of *E.coli*. The same results were obtained for FANP2 (**Figure 5.13**). As anticipated, reducing the dose of antibiotics reduces its inhibitory effect, and the changes in cell metabolism can be measured reliably and accurately by using FANPs.

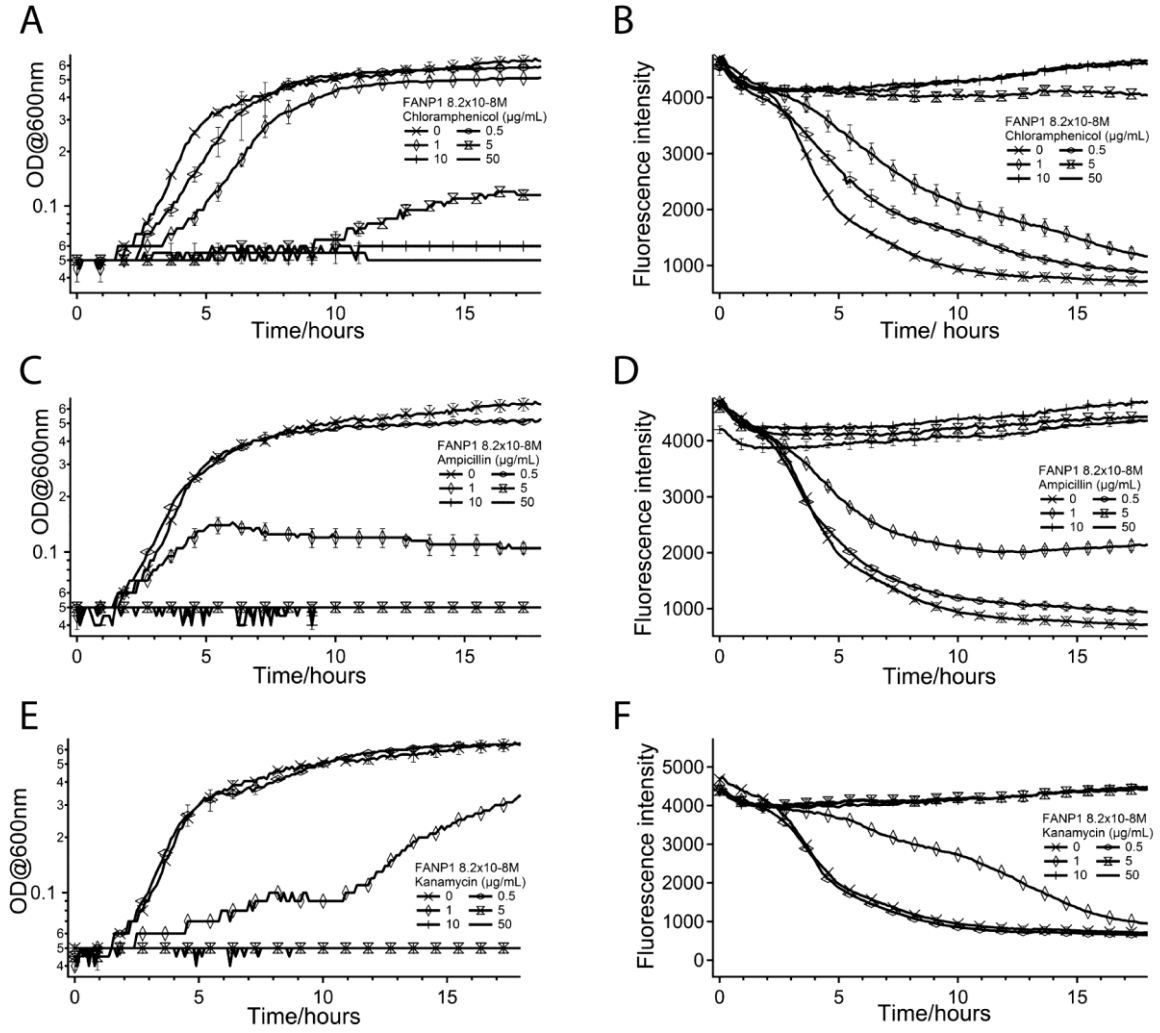



**Figure 5.12** The inhibitory effect of three antibiotics on the growth of bacteria: Chloramphenicol (A,B), Kanamycin (C,D), and Ampicillin (E,F) at different concentrations (0.5, 1, 5, 10, 50 μg/mL). The change in the growth of *E.coli* was measured by an increase of the OD (A, C, E) and by a decrease of fluorescence of FANP1 (B, D, F). The error bars indicate the difference between the three replicates in the experiment.

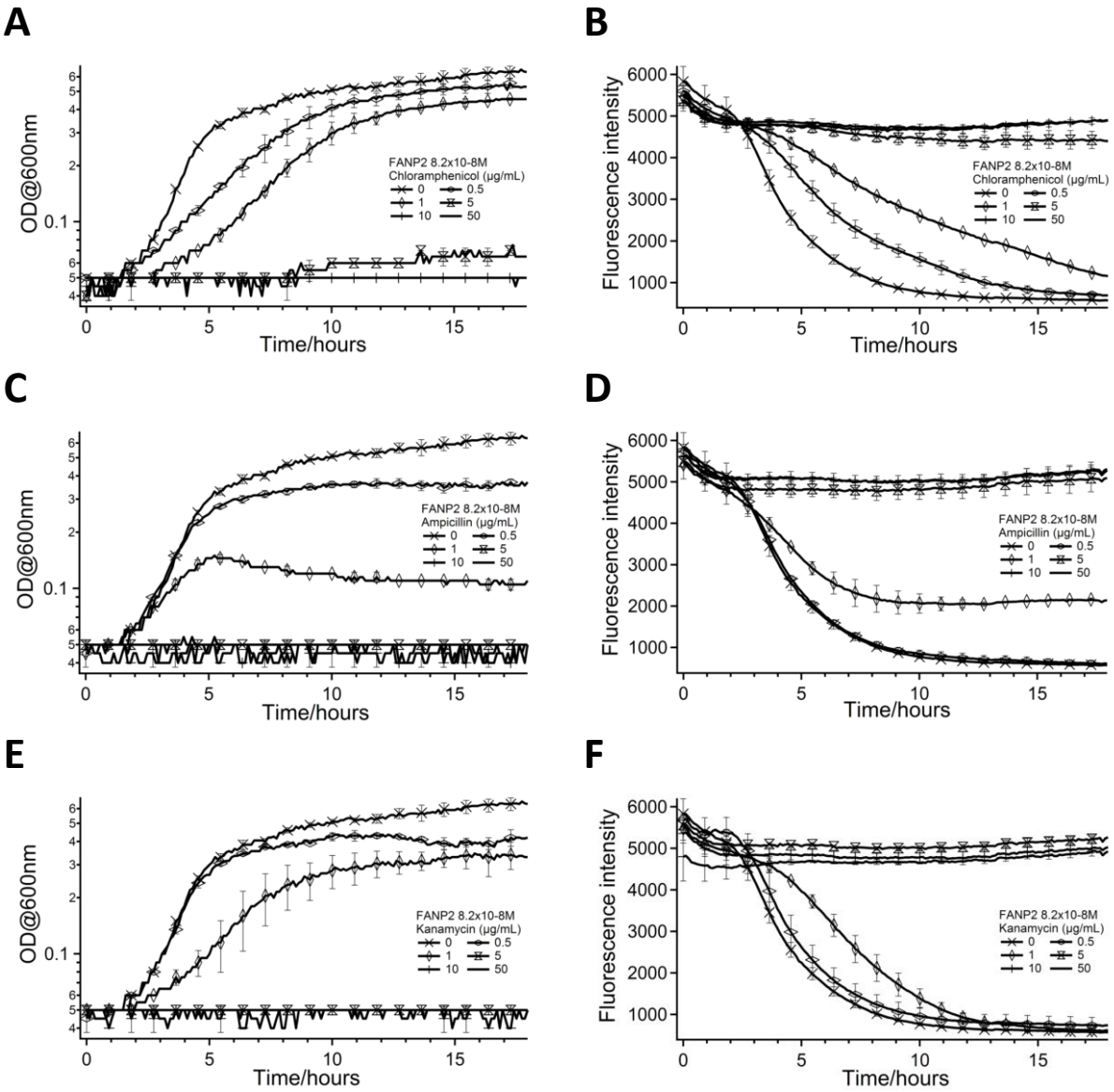



**Figure 5.13** The inhibitory effect of three antibiotics on the growth of bacteria: Chloramphenicol (A,B), Kanamycin (C,D), and Ampicillin (E,F) at different concentrations (0.5, 1, 5, 10, 50 μg/mL). The change in the growth of *E.coli* was measured by an increase of the OD (A, C, E) and by a decrease of fluorescence of FANP2 (B, D, F). The error bars indicate the difference between the three replicates in the experiment.

## 5.6 Imaging of *E.coli* growth

FANP1 and FANP2 were added to the growth medium with an initial concentration of *E.coli* of 3-6x$10^5$ CFU/mL (OD=0.003-0.006) inside a cuvette (**Figure 5.14A a0, c0**). After an overnight incubation, the fluorescence intensity of the cuvettes with bacteria decreased significantly (**Figure 5.14A a1, c1**) and the decrease could be easily seen by eye with the help of a lamp (exc@470nm). However, the fluorescence intensity of the cuvettes without bacteria remains unchanged (**Figure 5.14A b0, b1, d0, d1**).

In order to test whether these FANPs could be used to monitor bacterial growth on a solid support, they were embedded in agar with growth medium, as used traditionally to follow the formation of bacterial colonies.

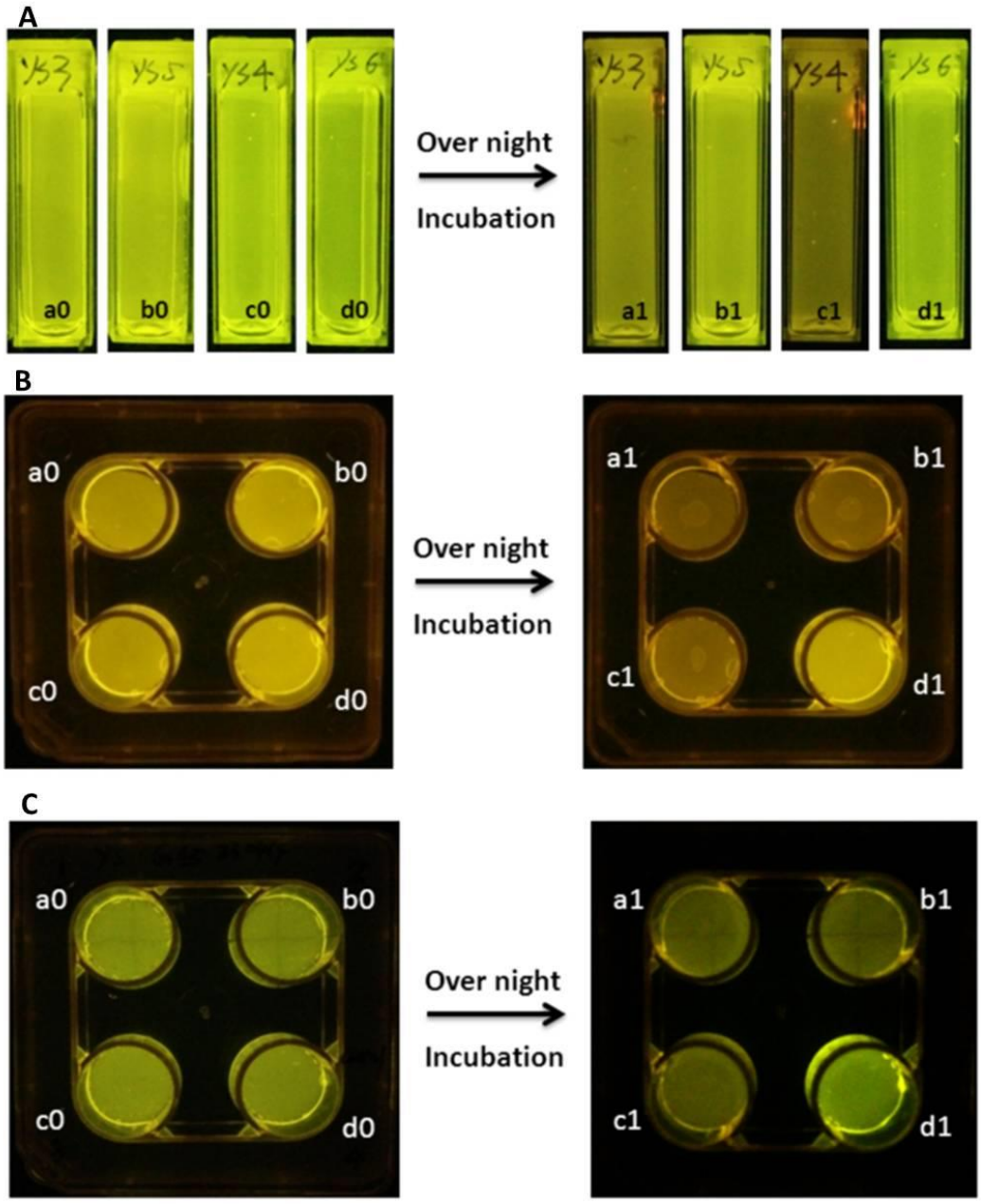



**Figure 5.14** A: a0, c0: FANP1 and FANP2 in growth medium with an initial concentration of *E.coli* of $3x10^5$CFU/ml (OD=0.003). b0 and d0: FANP1 and FANP2 in growth medium. a1, b1, c1, d1 are fluorescence images of a0, b0, c0, d0 after one night incubation (37°C). B: Fluorescence images of bacterial growth on FANP2 agarose (a0, b0, c0), compared to fluorescence images of FANP2 agarose alone (d0). a1, b1, c1, d1 are fluorescence images of a0, b0, c0, d0 after one night incubation (37°C). C: Fluorescence images of bacterial growth on FANP1 agarose (a0, b0, c0), fluorescence images of FANP1 agarose alone (d0). a1, b1, c1, d1 are fluorescence images of a0, b0, c0, d0 after one night incubation (37°C).

As shown in **Figure 5.14B, C**, the pH-sensitive cell culture plates initially display a homogeneous yellow-green fluorescence, indicating a starting pH value of 6.8. After an overnight growth of bacteria it can be seen that significant acidification of the whole agarose layer has occurred. Even if the initial localizations of bacterial solutions are different, the protons produced by the bacteria during growth have caused a global influence on the particles in the agarose as the fluorescence intensity of the whole surface is strongly reduced. This result indicates that these particles could be used to screen for bacteria that grow selectively on solid media.

## 5.7 Conclusion

The novel pH-sensitive nanoparticles described herein have distinct features that make them suitable for the development of biosensors including brightness, stability in growth medium, non-toxicity, high water solubility, high sensitivity, and ease of bioconjugation and incorporation into a biocompatible matrix. They can rapidly and accurately detect bacterial growth by detecting the change of pH resulting from cellular metabolism. Due to the brightness of these nanoparticles, they could be used to develop new systems for quantitative biosensor applications for microfluidic devices. One of the important advantages of this approach is that a change in pH can be easily monitored either by a simple change in fluorescence at a specific wavelength or even by eye for a qualitative result in either a liquid or solid support. These FNAPs can be easily synthesized with low cost and can be used in any laboratory without additional expensive instruments or operators. Moreover, these particles allow for continuous monitoring for long time scale experiments and can be used to monitor a large number of samples for high-throughput screening applications. For example they can be used to measure the metabolic activities of bacteria as an indicator of their susceptibility to antibacterial drugs, as shown here, or for the screening and discovery of novel growth inhibitors.

# Chapter 6 General conclusion and perspectives

The main aim of my PhD research project was to study fluorescent nanomaterials for bioimaging and biosensing on *E.coli* bacteria.

Nine different fluorescent nanomaterials were synthesized, characterized and used as fluorescent agents for biological experiments with *E.coli* bacteria: Fluorescent nanoparticles ($FNP^-$, $FNP^+$, $FNP\text{-}PEG^+$), Fluorescent polymer chains ($GFPC^-$, $GFPC^0$, $RFPC^-$, $RFPC^+$) and fluorescent pH-sensitive nanoparticles (FANP1 and FNAP2). All these fluorescent nanomaterials have been proved to be nontoxic to *E.coli* bacteria.

The negatively fluorescent nanoparticles $FNP^-$ have a core-shell structure with around 3000 BODIPY fluorophores copolymerized in the core and hydrophilic polymer chains in the shell, the size of the particle is around 65nm. Thanks to the thousands of fluorophores inside the core, $FNP^-$ brightness was very high ($10^7\ M^{-1}.cm^{-1}$). It is approximately 1000 times brighter than traditional organic dyes such as BODIPY and Fluorescein. They are also very stable due to the fluorophores protection in the hydrophobic core. By coupling reactions with amine, two different positively charged fluorescent nanoparticles are obtained: $FNP^+$ and $FNP\text{-}PEG^+$. These fluorescent nanomaterials described in the manuscript have proved to be ideal tools for biolabeling and bioimaging applications in life science due to their high brightness, high photostability and rich functionalization ability.

In order to study the internal bioimaging of *E.coli* with FNPs, electroporation was performed to insert FNPs inside bacteria (**Figure 6.1A**). Bioimaging experiments indicated that *E.coli* bacteria interacted with fluorescent nanoparticles. Methylene blue was introduced to quench the fluorescence of particles outside the bacteria, the fluorescence of particles inside bacteria remained thus proving that particles are successfully inserted inside bacteria. However, very few bacteria survived after electroporation. This is a strong drawback for internal bioimaging application. New strategies were needed to apply the particles to bioimaging of *E.coli*. One was to use the particles for external bioimaging of *E.coli*. On the other hand, if these FNPs bind selectively to dead bacterial cells they could be used to measure the toxicity of potential antibiotic molecules using a small number of cells for drug screening application.

Thanks to the poly acrylic acid groups all around the particle, biological molecules (e.g. biotin, antibody…) could be conjugated on the surface of the particles (**Figure 6.1B**). In order to study the external bioimaging of *E.coli* with FNPs, a "sandwich system" was created to target the bacterial membrane. *E.coli* was targeted with an antibody conjugated with biotin. After conjugating the biotin to nanoparticles and then with a streptavidin, I used this particle based "sandwich system" ($FNP^-$ -biotin-streptavidin-biotin-antibody-bacteria) to target the *E.coli*'s outer membrane. In the "sandwich system", three agents are needed to link the $FNP^-$ to the antibody which can target the bacteria. Even if it was shown by fluorescence and SEM images that the "sandwich system" was successfully obtained, the targeting efficiency on bacteria was not high enough for further application. In order to simplify this approach, I attempted to directly graft the anti-*E.coli* antibody to the surface of fluorescent nanoparticles but the characterization of the reaction is still underway. I applied the "nanoparticle-antibody" system to label the bacterial membrane, after a preliminary test, the particles conjugated with antibody could label bacterial outer membrane.

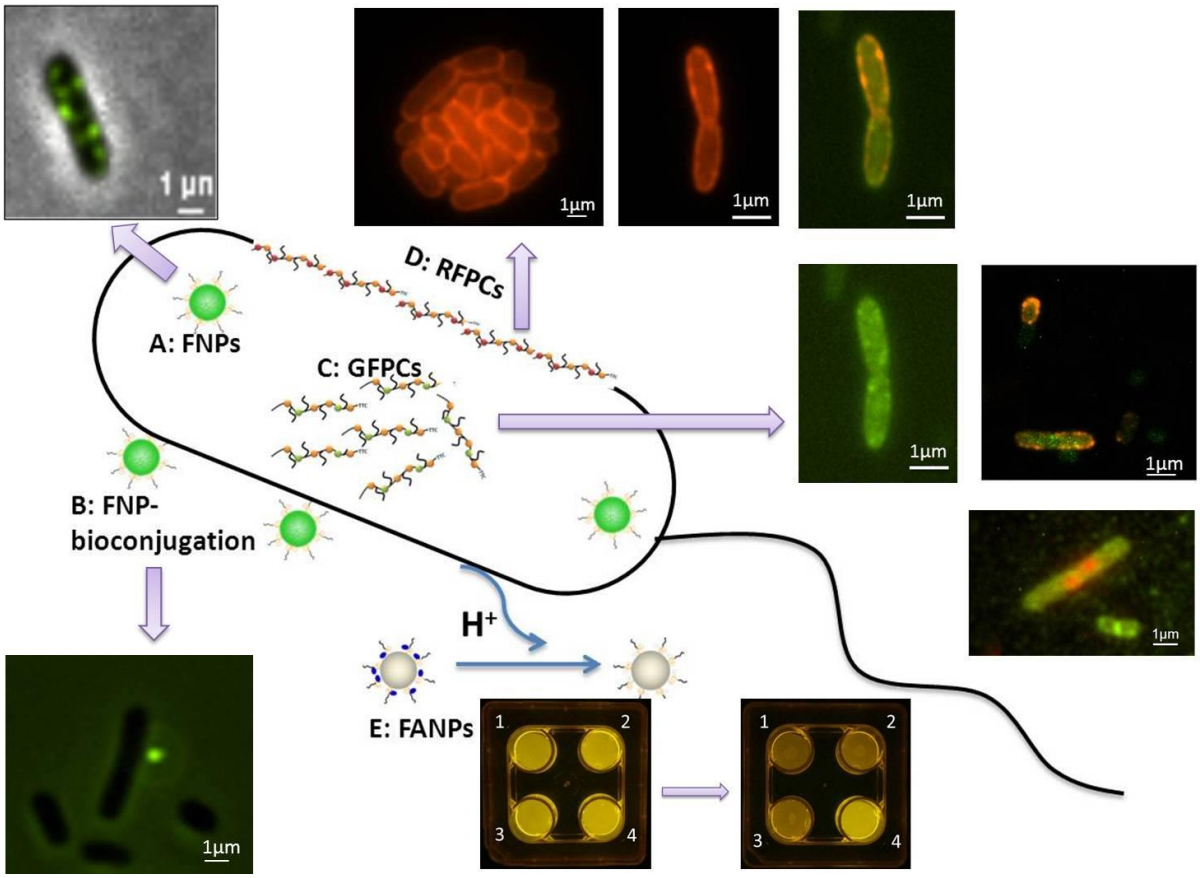



**Figure 6.1** Fluorescent nanomaterials for internal and external bioimaging and biosensing application on *E.coli* bacteria. (A) FNPs: Fluorescent nanoparticles for internal bioimaging of *E.coli*. (B) FNP-

bioconjugation with biotin or antibody to label bacterial membrane. (C) GFPCs: Green fluorescent polymer chains for internal bioimaging of *E.coli* and multi-color imaging with DRAQ 5 or PKH26 dye, (D) RFPCs: Red fluorescent polymer chains for labeling bacterial membrane and multi-color imaging with $GFPC^-$. (E) FANPs: pH-sensitive fluorescent nanoparticles for rapid detection of *E.coli* growth.

Fluorescent nanoparticles with a size of 65nm proved to be too big and they could only be internalized in bacteria by electroporation. Smaller fluorescent nanomaterial: fluorescent polymer chains (4-6nm) were thus synthesized and investigated for bioimaging on *E.coli* bacteria.

Green fluorescent polymer chains (GFPCs) could easily enter inside bacteria by simple incubation (**Figure 6.1C**). Particularly, flow cytometry experiments showed that $GFPC^-$ could label all the bacteria. I also developed a multi-color application of $GFPC^-$. DRAQ5 was introduced to label bacterial DNA while at the same time the cytoplasm of bacteria was labelled by $GFPC^-$. It was found that $GFPC^-$ could only label the bacterial cytoplasm but not the DNA. Another dye PKH26 was also introduced to label bacterial membrane while $GFPC^-$ was used for labelling the cytoplasm.

Red fluorescent polymer chains (RFPCs) could label the bacterial membrane easily by standard incubation (**Figure 6.1D**). $GFPC^-$ and $RFPC^+$ were compatible with each other and they could be used for bacteria internal and external bioimaging at the same time. Compared with the commercial membrane dye PKH26, RFPCs have shown significant advantages: we can use at least 100 times less RFPCs material to label the same amount of bacteria.

The designed FPCs series are highly water-soluble, biocompatible, stable and bright. With different multi-color image tests, FPCs have shown good compatibility with different types of commercial dyes. Moreover, they are very easy and cheap to synthesize and can be easily used to either internal (cytoplasm) or external (membrane) bioimaging applications of bacteria.

After these bioimaging studies, two highly water-soluble, biocompatible, stable and bright fluoresceinamine based pH-sensitive nanoparticles (FANPs) were investigated for biosensing application on *E.coli* bacteria (**Figure 6.1E**). They could rapidly and accurately detect bacterial growth by signalling the change of pH resulting from cellular metabolism. One of the important advantages of this approach is that a change in pH can be easily

monitored either by a simple change in fluorescence or even by eye for a qualitative result in either a liquid or solid support. These FNAPs can be easily synthesized with low cost and can be used in any laboratory without additional expensive instruments or operators. Moreover, these particles allow for continuous monitoring for long time scale experiments and can be used to monitor a large number of samples for high-throughput screening applications. For example we used them to measure the metabolic activities of bacteria as an indicator of their susceptibility to antibacterial drugs.

Various potential approaches may need to be investigated in the future. Eukaryotic cells are much bigger compared with bacteria, FNPs may be internalized by cells through the process of endocytosis. Due to their high brightness and high photostability, FNPs can be useful tools for single-particle tracking experiments inside eukaryotic cells to understand dynamics in cells[209].

FNPs based "Sandwich system" and "Nanoparticle-antibody" system can be used to study specific membrane protein dynamics[210] on bacteria or eukaryotic cells in the future. For example, by changing the general anti-*E.coli* antibody to the specific antibody for membrane protein which control the growth of flagella, nanoparticles can label particularly on this membrane protein and may allow tracking the growth dynamics of flagella[211].

Besides bioimaging application, in the future, $GFPC^-$ can also be used to distinguish and quantify live and dead bacteria with a combination of propidium iodide (PI) by flow cytometry. $GFPC^-$ can label all bacteria while PI can label only dead cells, the viability is measured according to the proportion of bound strains by $GFPC^-$ and PI[200]. RFPCs have shown great potential for membrane labelling, in the future, they can be investigated for labeling of the membrane of eukaryotic cells, and study the cells' division by microscopy.

FANPs also possess great potential for various approaches, they can be used to develop new systems for quantitative biosensor applications for microfluidic devices or for the screening and discovery of novel growth inhibitors. These particles could also be used to study the change in metabolism in different biological systems such as during the formation of biofilms [212], in the event of skin infections [213] or even to detect the presence of tumour cells during surgery due to their acidic environment [214].

# Chapter 7 Experimental methods and materials

## 7.1 Materials

Acrylic acid (99%, Sigma-Aldrich, AA), poly(ethylene oxide) methyl ether acrylate (Mn=480 g/mol, Sigma-Aldrich, APEG), 4,4'-azobis(4-cyanopentanoic acid) (Sigma-Aldrich, ACPA), 2-methyl-2-[(dodecylsulfanylthiocarbonyl)sulfanyl] propanoic acid (> 97%, Strem, TTCA), 2-(dimethylamino)ethyl acrylate (98%, Sigma-Aldrich, DMAEA), 1-ethyl-3-(3-dimethylaminopropyl) carbodiimide hydrochloride (>98%, Fluka, EDC.HCl), ethylenediamine (>99%, Sigma-Aldrich), Poly(ethylene glycol) diamine (Sigma-Aldrich), Fluoresceinamine, isomer I (Sigma-Aldrich, FA), ethanolamine (>99%, Sigma-Aldrich, EtA), citric acid (99.8%, Carlo Erba), sodium phosphate dibasic dihydrate (>99.5%, Sigma-Aldrich), paraformaldehyde (Sigma-Aldrich, PFA), Poly(ethylene glycol) 2-aminoethyl ether biotin(average Mn 2300 (n~45), Sigma-Aldrich), Anti- *E.coli* antibody ab13627(IgG, abcam), Anti- *E.coli* antibody (Biotin) ab20640 (IgG, abcam), Anti-rabbit IgG (H+L), F(ab')2 Fragment (Alexa Fluor® 488 Conjugate) #4412 (Cell Signaling Technology), Streptavidin (Sigma-Aldrich), Formaldehyde (Sigma-Aldrich, 36.5-38%) were used as received. Chloramphenicol, kanamycin, and ampicillin antibiotics were obtained from Sigma-Aldrich and used as received.

2,2'-Azobis(2-methylpropionitrile) (AIBN, Sigma, 98%) was recrystallized from chloroform and few drops of petroleum ether. Styrene (Sigma Aldrich, ≥99%) and Dichloromethane (97%, Fluka, DCM) were distilled under reduced pressure. Distilled water was used for nanoparticles synthesis, the pH of water was adjusted with aqueous sodium hydroxide solution (1M) to a value comprised between 12 and 12.5. Solvents (Carlo Erba) were of synthetic grade and purified according to standard procedures. Silica gel 60A ˚ (70–200mm porosity) was bought from SDS. Deionized water (15MΩ.cm at 20°C) was prepared with a Milli-Q system (Millipore).

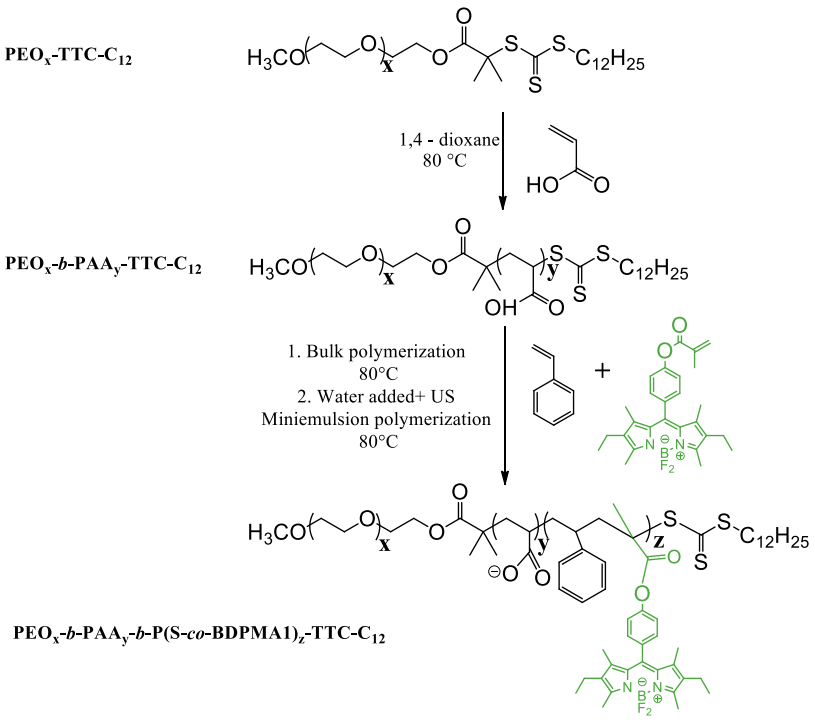
## 7.2 Synthesis of fluorescent nanomaterials

### 7.2.1 Synthesis of fluorescent nanoparticles (FNPs)

BODIPY derivative: BODIPY methacrylate-1 (BDPMA1), and PEO-*b*-PAA-TTC-$C_{12}$ macroRAFT agents were synthesized as described elsewhere[27]. Reversible addition-fragmentation chain transfer (RAFT) polymerization[215] of styrene and BDPMA1 is performed

in the presence of poly(ethylene oxide)-*b*-poly(acrylic acid), $PEO_{45}$-*b*-$PAA_{10}$-TTC-$C_{12}$ (PEO: Polyethylene glycol**,** PAA: Polyacrylic Acid, TTC: Trithiocarbonate), copolymers as macroRAFT agent in a one-pot phase inversion process. In a septum-sealed flask, PEO-*b*-PAA macroRAFT ($3.9x10^{-5}$ mol, 137 mg) is dissolved with a mixture of styrene ($6.45x10^{-3}$ mol, 671 mg), AIBN (Azobisisobutyronitrile) (2.0 mg, $1.24x10^{-5}$ mol) and BDPMA1 ($6.68x10^{-5}$ mol, 31 mg). The mixture is purged with argon for 30 min in an ice bath, and then placed in an oil bath thermostated at 80°C to initiate polymerization. After 70 min, the reaction is stopped by immersion of the flask in iced water (**Scheme 7.1**).

To the cold organic mixture, 5mL of basic water (pH=12.5) is added. An ultrasonic horn (Bandelinelectronics, SonoplusHD2200) is then placed in the biphasic mixture cooled down in an ice bath and powered at 130 W for 10 min. After the miniemulsion formation, the pH decreased to 11. The miniemulsion is purged with argon for 30 min in an ice bath, and then placed in an oil bath thermostated at 80°C to re-initiate polymerization.




**Scheme 7.1** Synthetic pathway for fluorescent nanoparticles ($FNP^-$).

We obtained fluorescent nanoparticles $PEO_{45}$-*b*-PAA-*b*-P(S-*co*-BODIPY)-TTC-$C_{12}$ with about 1750 chains, and 1.7 BODIPY per chain. The molar mass of the $FNP^-$ (negatively charged fluorescent nanoparticle) is $3x10^7$ g/mol[27].

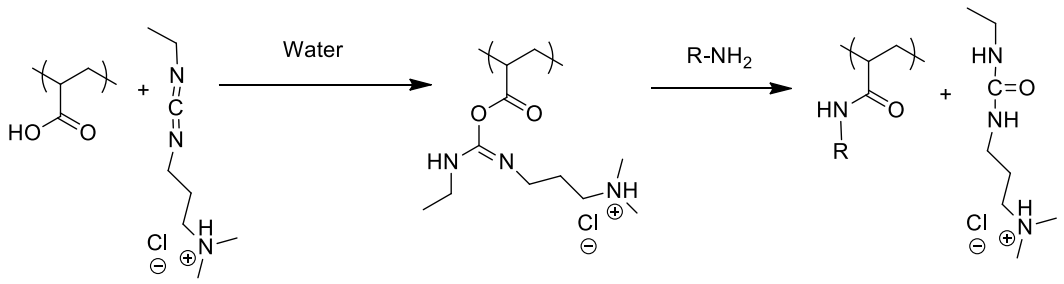
**Conversion of $FNP^-$ to $FNP^+$ and FNP-$PEG^+$ (Scheme 7.2)**

***Coupling Reaction 1*** **($FNP^+$)**

Ethylenediamine (10.8 mg, 179.4 µmol) and fluorescent nanoparticle ($FNP^-$) (2.58 mg, 35.9 µmol) are dissolved in distilled water (4 mL). A mixture of EDC.HCl {1-ethyl-3-(3-dimethylaminopropyl) carbodiimide hydrochloride } (27 mg, 143.5 µmol) in water is added to the previous solution which was subsequently stirred at 4°C for 24h and then dialyzed against water (pH=5-6) to remove the excess ethylenediamine. The water (1L) surrounding the dialysis tube was changed once a day during the process for one week.

Coupling Reaction 2 (FNP-$PEG^+$)

Poly(ethylene glycol) diamine (39.5 mg, 179.4 µmol) and fluorescent nanoparticle ($FNP^-$) (2.58 mg, 35.9 µmol) were dissolved in distilled water (4 mL). A mixture of EDC.HCl {1-ethyl-3-(3-dimethylaminopropyl) carbodiimide hydrochloride } (27 mg, 143.5 µmol) in water is added to the previous solution which was subsequently stirred at 4°C for 24h and then dialyzed against water (pH=5-6) to remove the excess of poly(ethylene glycol) diamine. The water (1L) surrounding the dialysis tube was changed once a day during the process for one week.

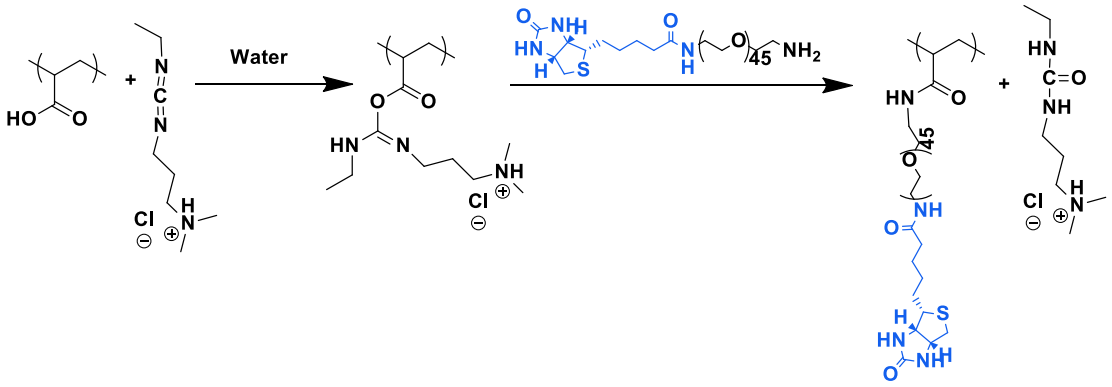



**Scheme 7.2** Synthetic pathway to get positively charged FNP (R refers to Ethylenediamine or Poly(ethylene glycol)diamine).

## 7.2.2 Conjugation of biotin on $FNP^-$

Fluorescent nanoparticle ($FNP^-$) (2.19 mg, 30.3 µmol) was dissolved in distilled water (4 mL). The total number of acrylic acid units present on the surface of the particles was taken as 1 equiv. Poly(ethylene glycol) 2-aminoethyl ether biotin (69.9 mg, 30.3 µmol) was diluted in 0.5 mL ethanol and then the solution was added into the particle suspension and mixed up to four degree (4°C). About 10 minutes later, a mixture of EDC.HCl {1-ethyl-3-(3-

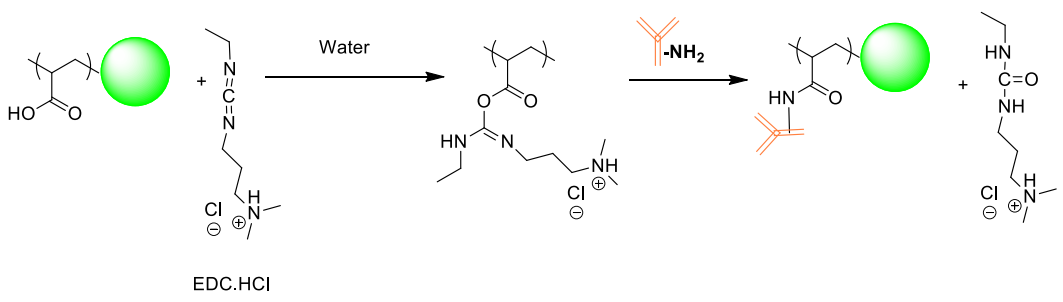
dimethylaminopropyl) carbodiimide hydrochloride } (23.2 mg, 121.5 µmol) in water was added in the previous solution and was left to stir at 4°C for 24h and then transferred into a cellulose ester dialysis membrane (MWCO: 12-14kDa, Spectrapor) and dialyzed against water to remove the excess of biotin. The water (1L) surrounding the dialysis tube was changed once a day during the process for one week (Scheme 7.3).




**Scheme 7.3** Synthetic pathway for biotin conjugation to $FNP^-$.

### 7.2.3 Conjugation of antibody on $FNP^-$

Fluorescent nanoparticle ($FNP^-$) was dissolved in distilled water (2 mL). The total number of acrylic acid units present on the surface of the particles was taken as 1 equiv. a mixture 200µL of EDC.HCl {1-ethyl-3-(3-dimethylaminopropyl) carbodiimide hydrochloride} (4 equiv.) in PBS was added in the previous solution, left for 20mins. Anti- *E.coli* antibody ab13627 (IgG, abcam) (4 equiv.) was added in and mixed inside the solution. The reaction was left to stir at 4°C for 24h. And then 230µL glycine was added to quench the unreacted sites. The mixture was then transferred into a cellulose ester dialysis membrane (MWCO: 300kDa, Spectrapor) and dialyzed against water to remove excess particles for one night (**Scheme 7.4**).

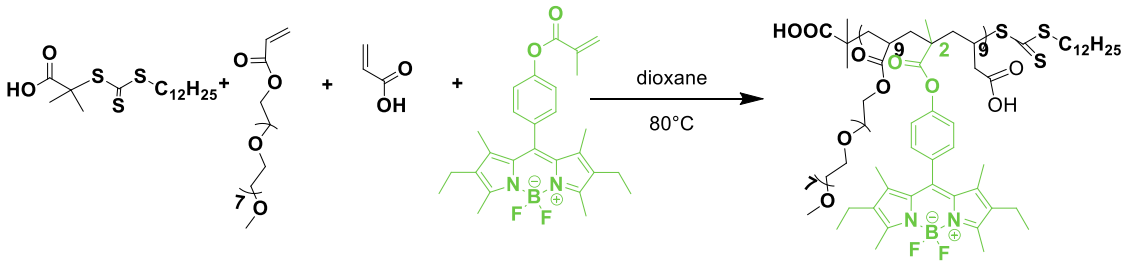



**Scheme 7.4** Synthetic pathway for antibody conjugation to $FNP^-$.

## 7.2.4 Synthesis of fluorescent polymer chains (FPCs)

### Synthesis of negative green fluorescent polymer chains ($GFPC^-$)

BODIPY derivate: BODIPY methacrylate-1 (BDPMA1) was synthesized as described elsewhere.[27] Green negative fluorescent polymer chain $P(AA_9\text{-}co\text{-}APEG_9\text{-}co\text{-}BDPMA1_2)_{20}$-TTC-$C_{12}$ was synthesized in 1.4-dioxane at 80°C under nitrogen atmosphere. APEG (0.88 mmol, 398 mg), AA (0.93 mmol, 67 mg), TTCA RAFT agent (0.1 mmol, 36.4 mg), DMF (0.54 mmol, 39.7 mg), BDPMA1 (0.24 mmol, 113 mg) were dissolved in 0.97 mL of 1,4-dioxane at room temperature. Then, 0.029 mL of a 0.3 M solution of ACPA in 1.4-dioxane was added. The mixture solution was then purged with nitrogen for 30 min in an ice bath. After this, to initiate the polymerization, the mixture was placed in an oil bath and heated to 80°C. The reaction lasted for 90 minutes and stopped by putting the flask in ice water (**Scheme 7.5**).

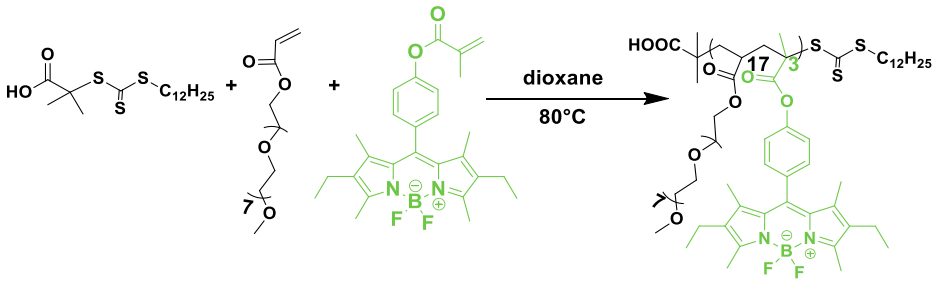



**Scheme 7.5** Synthetic pathway to get negative green fluorescent polymer chain ($GFPC^-$).

After precipitation in n-pentane, negatively charged green fluorescent polymer chains ($P(AA_9\text{-}co\text{-}APEG_9\text{-}co\text{-}BDPMA1_2)_{20}$-TTC-$C_{12}$) are obtained with 2 BODIPY fluorophores per chain.

### Synthesis of neutral green fluorescent polymer chain ($GFPC^0$)

Green neutral fluorescent polymer chain $P(APEG_{17}\text{-}co\text{-}BDPMA1_3)_{20}$-TTC-$C_{12}$ was synthesized in 1,4-dioxane at 80°C under nitrogen atmosphere. In a typical experiment, APEG (1.77 mmol, 802.2 mg), TTCA RAFT agent (0.11 mmol, 39.4 mg), DMF (0.88 mmol, 0.62 mg), BDPMA1 (0.3 mmol, 140.5 mg) were dissolved in 1.42 mL of 1,4-dioxane at room temperature. Then, 0.029 mL of a 0.3 M solution of ACPA in 1.4-dioxane was added. The mixture was purged with nitrogen for 30min in an ice bath, then placed in an oil bath thermostated at 80°C to initiate the polymerization. After 90 min, the reaction is stopped by immersion of the flask in iced water (**Scheme 7.6**).



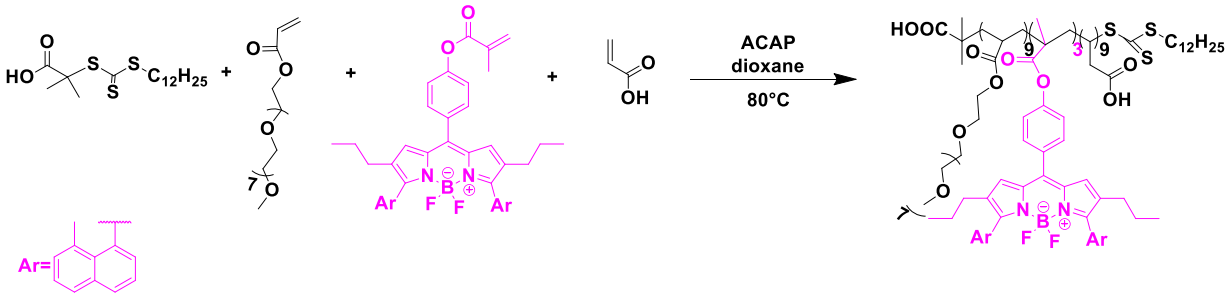

**Scheme 7.6** Synthetic pathway to get neutral green fluorescent polymer chain ($GFPC^0$)

After precipitation in n-pentane, we obtained neutral green fluorescent polymer $P(APEG_{17}\text{-}co\text{-}BDPMA1_3)_{20}\text{-}TTC\text{-}C_{12}$ with 3 BODIPY fluorophores per chain.

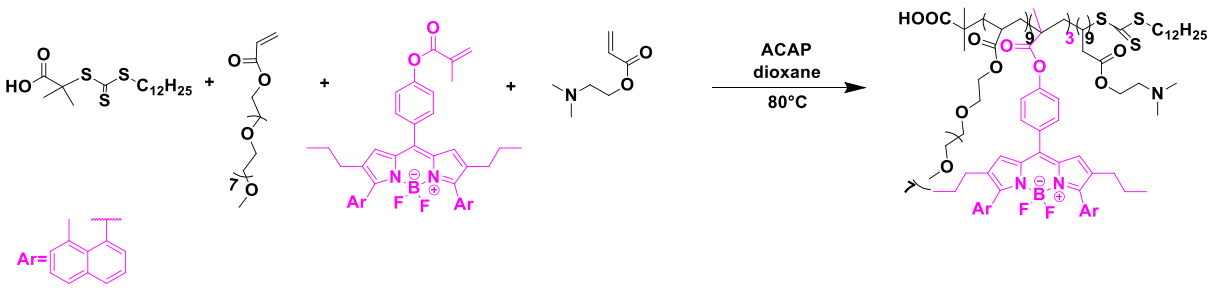
**Synthesis of red fluorescent polymer chains (RFPCs)**

The synthesis of BODIPY Methylnaphtalene-2 (BDPMA2) is described elsewhere[27]. Negative red fluorescent polymer chain is synthesized in 1.4-dioxane at 80°C under nitrogen atmosphere. APEG (9 equiv.), AA (9 equiv.), TTCA RAFT agent (1 equiv.), DMF (5 equiv.), BDPMA2 (3 equiv.) were dissolved in 1 mL of 1,4-dioxane at room temperature. Then, 0.03 mL of a 0.3 M solution of ACPA in 1.4-dioxane was added. The mixture solution was then purged with nitrogen for 30 min in an ice bath. After this, to initiate the polymerization, the mixture was placed in an oil bath and heated to 80°C. The reaction lasted for 90 minutes and stopped by putting the flask in ice water.

After precipitation in n-pentane, a negative red fluorescent polymer chain ($RFPC^-$) is obtained. For positive red fluorescent polymer chain ($RFPC^+$), 2-(Dimethylamino)ethyl acrylate (9 equiv., DMAEA) was used instead of acrylic acid. The synthesis processes of the two red fluorescent polymer chains are displayed in **Scheme 7.7** and **Scheme 7.8**.




**Scheme 7.7** Synthetic pathway for negative red fluorescent polymer chain ($RFPC^-$)




**Scheme 7.8** Synthetic pathway for positive red fluorescent polymer chain (RFPC$^-$)

### 7.2.5 Synthesis of fluorescent pH-sensitive nanoparticles (FANPs)

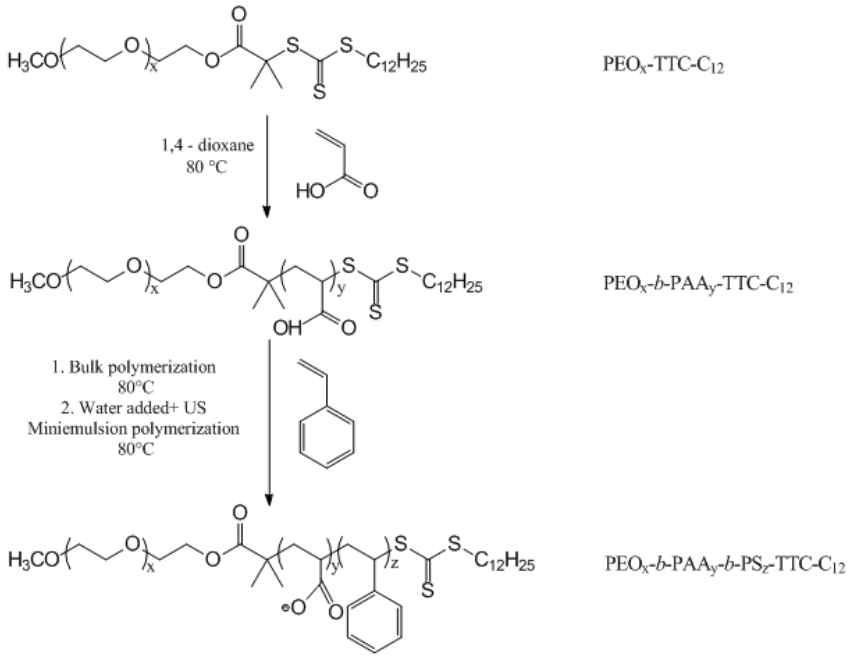
#### Synthesis of macroRAFT agents

The $PEO_{45}$-*b*-$PAA_{19}$-TTC macroRAFT agents were synthesized as described elsewhere [180]. The $P(PEOA_{0.5}$-*co*-$AA_{0.5})_{22}$-TTC macroRAFT agent with equal amounts of AA and PEOA was synthesized in 1,4-dioxane at 75°C under argon atmosphere according to Boisse et al.'s procedure [216]. In the experiment, the RAFT agent TTCA (0.29 g, 0.8 mmol), AA (720 mg, 10 mmol) and PEOA (4.54 g, 10 mmol) were dissolved at room temperature in a flask with 9.9 mL of 1,4-dioxane. 0.1 mL of ACPA solution in 1, 4-dioxane (0.5 M) was then added. The mixed solution was purged for 30 minutes with argon in an ice bath. After this, to initiate the polymerization, the mixture was placed in an oil bath and heated to 75°C. The reaction lasted for 80 minutes and stopped by putting the flask in ice water. The individual molar conversion of each monomer was determined by $^1$H NMR in $CDCl_3$ using DMF as an external standard. The conversion of both monomer was found to be 86%, thus the composition of this copolymer was found to be $P(AA_{0.5}$-*co*-$PEOA_{0.5})_{22}$-TTC. The copolymer was precipitated twice in cold diethyl ether in ice water and dried under vacuum at room temperature for 24h.

#### Synthesis of Polystyrene Nanoparticles (PSNPs)

RAFT polymerization of styrene was performed in the presence of $PEO_{45}$-*b*-$PAA_{19}$-TTC macroRAFT agents in a one-pot phase inversion process similar to what was reported recently [180]. RAFT polymerization of styrene in the presence of $P(PEOA_{0.5}$-*co*-$AA_{0.5})_{22}$-TTC copolymers as macroRAFT agent was performed by the same procedure. In a typical experiment (**Scheme7.9**), P(PEOA-*co*-AA)-TTC macroRAFT agent (197mg, $3.2 \times 10^{-5}$mol), styrene (650mg,$6.3 \times 10^{-3}$mol) and AIBN (2mg, $1.2 \times 10^{-5}$mol) were dissolved in a flask. The mixed solution was then purged for 30 minutes with argon in an ice bath. After this, to initiate the polymerization, the mixture was placed in an oil bath and heated to 80°C. The

reaction lasted for 150 minutes and stopped by putting the flask in ice water. 5 mL of basic water (pH=12.5) were added into the mixture. This biphasic mixture was then placed in an ice bath and an ultrasonic horn (Bandelin electronics, Sonoplus HD 2200) was then placed inside and powered at 130W for 10 minutes. After ultrasonication, the miniemulsion was purged again for 30 minutes in an ice bath with argon. To re-initiate the polymerization, the mixture was placed in an oil bath and heated to 80°C. By this procedure two different PSNPs were obtained with a core-shell structure, while the shell of PSNP1 is $PEO_{45}$-*b*-$PAA_{19}$, the shell of PSNP2 is $P(PEOA_{0.5}$-*co*-$AA_{0.5})_{22}$. Both PSNP1 and PSNP2 have a polystyrene core.

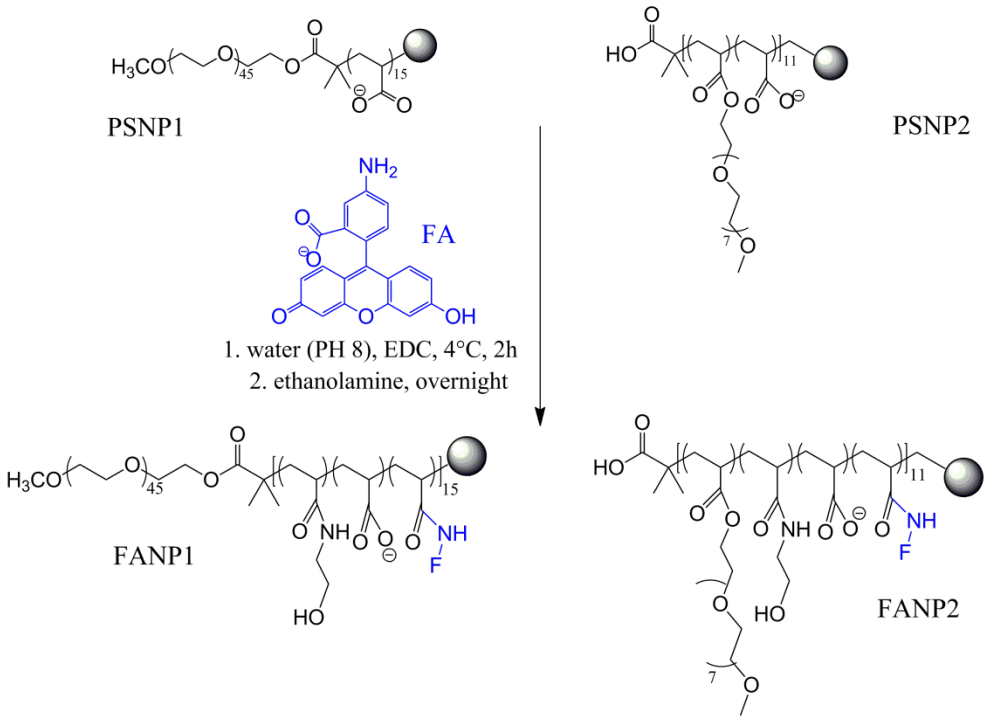



**Scheme7.9** Synthetic scheme employed for the synthesis of the PSNP1.

**Functionalization of PSNPs with fluoresceinamine (FA)**[27]

In a typical experiment, 0.3 mL of PSNPs (0.1 mg/mL) obtained above was diluted in 4 mL of distilled water in the dark. In parallel, depending on the number of the AA units, 0.5 (PSNP1) or 1 (PSNP2) equivalents of FA (3.35 or 6.7 mg) were dissolved in 0.4 mL ethanol and the solution was added to the PSNPs solution. The mixture was then stirred at 4°C. A solution of EDC (4 equiv., 15 mg) in water (1 mL) was then added to the previous mixture. After two hours, ethanolamine (2 equiv., 2.3 µL) was added in order to quench the reaction. The mixture was stirred at 4°C overnight in the dark. Finally, the solution was transferred

into a cellulose ester dialysis membrane (MWCO: 300 kDa, Spectrapor) and dialyzed against water in the dark for 7 days. Two different fluoresceinamine (FA) based fluorescent nanoparticles were thus obtained: FANP1 and FANP2 (**Scheme 7.10**).




**Scheme 7.10** Preparation of pH nanosensors (FANP1 and FANP2) from PSNP1 and PSNP2.

## 7.3 Characterization of fluorescent nanomaterials

### 7.3.1 Absorption and fluorescence spectroscopy

UV-visible spectra were measured on a Varian Cary 5000 (Palo Alto, CA USA) double beam spectrometer using 4.5mL BRAND Polymethacrylate (PMMA) Cuvette. Excitation and emission spectra were recorded on a SPEX SPEX Fluoromax-3 (Horiba Jobin-Yvon). A right-angle configuration was used. Optical density of the samples was checked to be less than 0.1 to avoid reabsorption artifacts. The relative fluorescence quantum yields $\Phi_F$ were determined by using Rhodamine 590 ($\Phi_F$ = 0.95 in ethanol) or Rhodamine 101 ($\Phi_F$ = 0.96 in ethanol) as a reference (error of 15%)[48,180].

### 7.3.2 Hydrodynamic diameter

The average hydrodynamic particle or polymer diameter (named $D_h$) was determined by dynamic light scattering (DLS) of the diluted aqueous dispersions at 20°C, with a 4 mW

He-Ne laser at 633 nm, using a Zetasizer Nano S90 from Malvern. All calculations were performed using the Nano DTS software.

### 7.3.3 Size exclusion chromatography (SEC)

The number-average molar mass $M_n$, weight-average molar mass Mw, and the molar mass distribution (polydispersity index $M_w/M_n$) were determined by size exclusion chromatography (SEC) using THF as an eluent at a flow rate of 1 mL.min$^{-1}$. For analytical purposes, the acidic functions of the block or statistical copolymers were turned into methyl esters. The copolymers were recovered by drying of the aqueous suspensions. After dissolution in a THF/$H_2O$ mixture and acidification of the medium with a 1 M HCl solution, they were methylated using an excess of trimethyl-silyldiazomethane. After filtration through 0.45 µm pore size membrane, polymers were analyzed at a concentration of 5 mg.mL$^{-1}$ in THF. The SEC apparatus is equipped with a sample delivery module (Viscotek GPCmax) and two columns thermostated at 40 °C (PLgel Mixed; 7.5 × 300 mm2; bead diameter, 5 µm). Detection was made with a differential refractive index detector (Viscotek VE 3580 RI detector) and an Ultraviolet−Visible (UV−vis) detector (Waters 486 tunable absorbance detector). The Viscotek OmniSEC software (v 4.6.2) was used for data analysis, and the relative $M_n$ and $M_w/M_n$ were calculated with a calibration curve based on polystyrene standards (from Polymer Laboratories).

### 7.3.4 Critical micelle concentration (CMC)

The critical micelle concentration (CMC) of GFPCs in water was determined at 20°C or in LB medium determined at 37°C by dynamic light scattering (DLS) using a commercial multi-angle Laser Light Scattering AVL CGS-3 (Compact Goniometer System) equipped with an AVL-5003 digital correlator and a He-Ne Laser (632 nm, 22 mW)[3]. Stock solutions of GFPCs (2mg/mL in deionized water, milli-Q grade) were prepared and filtered through a 0.45 µm membrane. Solutions of $GFPC^-$ and $GFPC^0$ of concentrations in the range of 0.01 to 2 mg/mL were prepared by dilution with water milli-Q. The scattered light intensity at 90° was collected for these different samples. By plotting the intensity of scattered light as a function of $GFPC^-$ or $GFPC^0$ concentration, the CMC was determined at the intersection of the straight lines.

### 7.3.5 Titration of $FNP^-$ or $GFPC^-$ with Methylene blue

Titration experiments were prepared to characterize the process of $FNP^-$ or $GFPC^-$ quenching with methylene blue. $FNP^-$ solution with an initial concentration of $5x10^{-4}$μM or $GFPC^-$ with an initial concentration of $4x10^{-3}$μM was placed inside a 4.5mL BRAND Polymethacrylate (PMMA) Cuvette. Absorption and emission spectra were measured. Methylene blue solutions (1eq, 5 eq, 10eq…) were added inside $FNP^-$ or $GFPC^-$ solution gradually, and emission spectra of $FNP^-$ or $GFPC^-$ after adding methylene blue were measured each time. When the decrease of fluorescence intensity of $FNP^-$ or $GFPC^-$ didn't change anymore, the process was supposed to reach its maximum and the titration was stopped.

### 7.3.6 Surface Plasmon Resonance (SPR) experiment

Streptavidin chips were prepared on a glass prism (SF 10 with a high refractive index: n 1.707987 at λ =830 nm) activated by Reactive Ion Etching (RIE) prior to the thermal evaporation of a 50 nm gold layer. First, a fresh gold layer was immersed in a solution containing 0.1 mM of 1-undecanethiol substituted with a hydroxyl-terminated tetra(ethylene glycol) (EG4-OH) diluted in ethanol over night at room temperature. Before streptavidin deposition, the prisms were thoroughly rinsed three times in pure ethanol for 20 min. The streptavidin solution was spotted on the freshly pre-treated prism surface at different concentrations (10 μM, 1 μM in phosphate buffer (0.4 M) at pH 7.4) and incubated for two hours. The prism was then directly inserted into the SPRi apparatus and the PBS buffer was immediately flowed across the surface at 25 μL/minutes. 1 nM $FNP^-$ solution was flowed across the SPRi surfaces containing the spotted streptavidin first. Different images before and after the injection were taken. Then, the surface was washed by PBS buffer. After washing, 1 nM $FNP^-$-Biotin solution was flowed across the SPRi surfaces containing the spotted streptavidin, different images before and after the injection were taken, followed by another washing process.

### 7.3.7 pH measurements

pH measurements were carried by using a glass electrode connected to a PHM210 Standard pH meter from Meterlab.

### 7.3.8 Photostability and reversibility assessment of FANPs

2.5mL of Modified M9 minimal growth medium were placed inside a 4.5mL BRAND Methacrylate (PMMA) Cuvette. Aliquots of either FANP1 or FANP2 solutions were added to reach a final concentration of $8.2x10^{-7}$M. Samples were incubated at either 37°C or at room temperature in the dark and the fluorescence emission spectrum ($\lambda_{exc}$=495nm) of each sample was monitored using a SPEX Fluoromax-3 (Horiba Jobin-Yvon) every 30 minutes. The experiments lasted for 4 hours.

The reversibility and dynamic behaviour of FANPs was investigated by alternating the pH of the modified M9 minimal growth medium between pH 4 and 8 several times inside the cuvette in the presence of FANPs by adding 1M NaOH or HCl alternatively.

An overnight experiment was also carried out to assess the photostability of FANPs. 150µL of the Modified M9 minimal growth medium were placed in each well of a 96 well Falcon Polystyrene Flat Bottom Plate. Different volumes (from 2 to 10 µL) of the stock FANP1 and FANP2 solutions were added into the solution to reach final FA concentrations of $8.2x10^{-7}$M, $4.1x10^{-7}$M and $8.2x10^{-8}$M. Each plate contained three repeats of the same concentration. One control with only the Modified M9 minimal growth medium was also prepared. 70 µL of mineral oil were added to each well in order to avoid evaporation. Samples were incubated in a plate reader (Perkin Elmer Victor3 1420 Multilabel Plate Counter) at 37°C in the dark. The fluorescence intensity of FANPs was measured every 6 minutes by using a F485/14 filter for excitation and a F535/40 filter for emission. The experiments lasted overnight for ten hours.

## 7.4 Toxicity assessments of fluorescent nanomaterials on *E.coli*

### 7.4.1 Bacteria growth medium

Luria broth (LB) medium is a nutritionally rich medium, which is primarily used for the growth of bacteria.

M9 Minimal Medium is a microbial growth medium used for the culture of *E. coli*. This buffered minimal microbial medium contains only salts, so it is traditionally supplemented with glucose, amino acids and vitamins as needed.

For pH-sensor experiments described in **Chapter 5**, I use a Modified M9 minimal medium with a lower concentration of phosphate salts in order to decrease the buffering capacity of the growth medium and thus obtain a more sensitive measure of bacterial growth from the response of the FANPs. The Modified M9 minimal medium contains 5.9mM $Na_2HPO_4 \cdot 2H_2O$, 4.4mM $KH_2PO_4$, 3.7mM $NH_4Cl$, 1.7mM NaCl, 2mM $MgSO_4$, 0.1mM $CaCl_2$, 19.6µM tryptophan, 20.6µM thymidine, 0.5% casamino acids, 22.2mM glucose.

### 7.4.2 Toxicity assessments of FNPs and FPCs on *E.coli*

Live *E.coli* bacterial cells (K-12 BW25113) were used for the following experiments. Bacterial cultures were prepared overnight from stock cultures inoculated in Luria Broth (LB) growth medium.

The overnight culture of bacteria was diluted 1:1000 in two different growth media: M9 or LB in order to check the growth medium influence. 150µL of bacterial solution were placed in each well of a 96 well Falcon Polystyrene Flat Bottom Plate. Different volumes of the FNPs or GFPCs or RFPCs solutions were added into the *E.coli* solution to reach final concentration of $6.6x10^{-3}$M (FNPs), $6.6x10^{-5}$M (GFPCs) or $2x10^{-10}$M (RFPCs). Each plate contained three repeats of the same concentration. One control with only bacteria and one blank with only M9 minimal growth medium or LB medium were also prepared. 70 µL of mineral oil were added to each well in order to avoid evaporation. Samples were incubated in a plate reader (Perkin Elmer Victor3 1420 Multilabel Plate Counter) at 37°C in the dark. The growth of the cells was monitored every nine minutes by reading the optical density (OD@600nm). The experiments lasted overnight.

## 7.5 Techniques to insert FNPs inside bacteria

### 7.5.1 Chemical treatment to introduce FNPs in *E.coli* Bacteria

1mL of LB growth medium with an initial concentration of $5x10^7$ CFU/mL (OD=0.5) of *E.coli* bacteria was placed inside a 2mL Eppendorf Safe-Lock Tube. Different volumes of $FNP^-$ solutions were added to this *E.coli* suspension to reach different final concentrations: $2.6x10^{-2}$µM, $3.9x10^{-2}$µM and $5.2x10^{-2}$µM. Di(ethylene glycol) is added to reach 5% of the total volume. Two repeats of the same concentration were carried out during the experiments. The samples were incubated at 37°C in the dark for one hour. After the

incubation, the cells were gently centrifuged at 4000rpm for 3 minutes at 4°C and washed with filtered PBS twice to remove free FNPs. The cells were then fixed by adding a fixing solution (4% PFA, 0.03% glutaraldehyde in 1x PBS) for 20 minutes. After the fixing process, cells were washed with PBS for three times and re-suspended in PBS before flow cytometry measurements and bioimaging experiments.

### 7.5.2 Electroporation to introduce FNPs in *E.coli* Bacteria

Electroporation is a mechanical method used to introduce molecules into a host cell through the cell membrane. In this procedure, a large electric pulse temporarily disturbs the phospholipid bilayer, allowing molecules like DNA to pass into the cell. Electrocompetent cells are prepared by incubation using 10 % glycerol cold medium. Cells are resuspended in GYT (10 % glycerol, 0.125 % yeast extract, 0.25 % tryptone) cold medium.

An electroporator (Eppendorf, E2510) is used in our experiments. To a Bio-Rad 0.4 cm electrode gap cuvette, we add 50µL electrocompetent cells ($8x10^7$ bacteria/µL) mixed with different volumes of FNPs to reach different final concentrations of $2.7x10^{-4}$µM, $1.4x10^{-3}$ µM, $2.7x10^{-3}$ µM, $1.4x10^{-2}$ µM, $2.7x10^{-2}$ µM and $5.2x10^{-2}$ µM. This mixture was placed on ice for 10 minutes before electroporation at the specified voltage (15kV/cm). Immediately after electroporation, 1 mL SOC media (Super Optimal broth with Catabolite repression, a nutrient-rich bacterial growth medium) was added. The cells were then incubated at 37°C for one hour. After the incubation, the cells were gently centrifuged at 4000rpm for 3 minutes at 4°C and washed with filtered PBS twice to remove free FNPs. The cells were then fixed by adding a fixing solution (4% PFA, 0.03% glutaraldehyde in 1x PBS) for 15 minutes. After the fixing process, cells were washed with PBS three times and re-suspended in PBS before flow cytometry measurements and bioimaging experiments.

## 7.6 Techniques of "Sandwich system" and "Nanoparticle-antibody system" formation

### 7.6.1 Process of "sandwich system" formation

Live *E.coli* bacterial cells (K-12 BW25113) were used for the following experiments. Bacterial cultures were prepared overnight from stock cultures inoculated in Luria Broth (LB) growth medium. 1mL of LB growth medium with an initial concentration of $5x10^7$ CFU/mL (OD=0.5) of *E.coli* bacteria was placed inside a 2mL Eppendorf Safe-Lock Tube. The cells were

gently centrifuged at 4000rpm for 3 minutes at 4°C and washed with 1mL filtered PBS once and concentrated in 90 µL PBS. 10µL primary antibody (0.4mg/mL) were added into bacterial solution and mixed up at room temperature for two hours incubation. Then the mixture was washed by 400 µL PBS twice and re-suspended in 20 µL PBS. 1 µL streptavidin (0.1 mg/mL) was added to the previous mixture and mixed up at room temperature for 30 minutes, and then washed by 400 µL PBS, twice, and re-suspended in 10 µL PBS. At last, 5 µL $FNP^{-}$-biotin (36 nM) were added to the mixture and mixed up at room temperature for 30 minutes, and then washed by 400 µL PBS twice and then re-suspended in 100 µL PBS before bioimaging experiments.

### 7.6.2 Secondary fluorescent antibody labelling

Anti-Rabbit IgG (H+L) $F(ab')_2$ Fragment was conjugated to Alexa Fluor® 488 fluorescent dye under optimal conditions. 100 µL of LB growth medium with an initial concentration of $5x10^7$ CFU/mL (OD=0.5) of *E.coli* bacteria was placed inside a 1.5 mL Eppendorf Safe-Lock Tube. The cells were gently centrifuged at 4000rpm for 3 minutes at 4°C and washed with 400 µL filtered PBS once and concentrated in 9 µL PBS. 1 µL primary antibody (0.4mg/mL) was added into bacterial solution and mixed up at room temperature for two hours incubation. After, the mixture was washed by 400 µL PBS twice and re-suspended in 9 µL PBS. 1 µL secondary antibody (0.2mg/mL) was added into the solution and mixed up at room temperature for one hour incubation. The mixture was then washed by 400 µL PBS and re-suspended in 10 µL PBS before bioimaging experiments.

### 7.6.3 Process of "Nanoparticle-antibody system" formation

Live *E.coli* bacterial cells (K-12 BW25113) were used for the following experiments. Bacterial cultures were prepared overnight from stock cultures inoculated in Luria Broth (LB) growth medium. 25µL of M9 medium with an initial concentration of $1x10^6$ CFU/mL (OD=0.4) of *E.coli* bacteria was placed inside a 0.5mL Eppendorf Safe-Lock Tube. The cells were mixed with FNP-antibody ($6.6x10^{-3}$µM) gently and incubated at room temperature (shaking for one hour). After incubation, bacteria were centrifuged at 4000rpm for 3 minutes at 4°C and washed with 400µL filtered PBS Tween 20 (a wash buffer in immunolabeling techniques. Tween 20 is added to promote more effective washings, resulting in decreased non-specific background staining) once and suspended in 20 µL before bioimaging experiments.

## 7.7 Incubation to introduce FPCs into *E.coli* bacteria

### 7.7.1 Incubation to introduce GFPCs into *E.coli* bacteria

1mL of LB growth medium with an initial concentration of $5x10^7$ CFU/mL (OD=0.5) of *E.coli* bacteria was placed inside a 2mL Eppendorf Safe-Lock Tube. Different volumes of $GFPC^-$ and $GFPC^0$ solutions were added to this *E.coli* suspension to reach different final concentrations of $6.6x10^{-4}$M, $6.6x10^{-5}$M, $6.6x10^{-6}$M. Two repeats of the same concentration were carried out during the experiments. The concentration of GFPCs (0.002-0.3mg/mL) in all samples is below the CMC of GFPCs at 37°C (0.4-0.5mg/mL). GFPCs are not likely to form micelles when incubated with *E.coli* bacteria.

The samples were incubated at 37°C in the dark for one hour. After the incubation, the cells were centrifuged at 4000rpm for 3 minutes at 4°C and washed with filtered PBS twice to remove free GFPCs. The cells were then fixed by adding a fixing solution (4% PFA, 0.03% glutaraldehyde in 1x PBS) for 15 minutes. After the fixing process, cells were washed with PBS for three times and re-suspended in PBS before flow cytometry measurements and bioimaging experiments.

### 7.7.2 Incubation to introduce RFPCs into *E.coli* bacteria

1mL of M9 growth medium with an initial concentration of $5x10^7$ CFU/mL (OD=0.5) of *E.coli* bacteria was placed inside a 2mL Eppendorf Safe-Lock Tube. Different volumes of $RFPC^+$ and $RFPC^-$ solutions were added to this *E.coli* suspension to reach a final concentration of $2x10^{-10}$M. Two repeats of the same concentration were carried out during the experiments.

The samples were incubated at 37°C in the dark for one hour. After the incubation, the cells were gently centrifuged at 4000rpm for 3 minutes at 4°C and washed with filtered PBS twice to remove free RFPCs. The cells were then fixed by adding a fixing solution (4% PFA, 0.03% glutaraldehyde in 1x PBS) for 15 minutes. After the fixing process, cells were washed with PBS for three times and re-suspended in PBS before bioimaging experiments.

## 7.8 Characterization of fluorescent nanomaterials interaction with *E.coli* by flow cytometry

Accurate measurement of live, dead, total bacteria and fluorescent cells percentage is obtained by Flow Cytometry (BD, FACS Calibur, **Figure 7.1A**). Flow cytometry is an analytical technology used for counting and sorting of mesoscopic objects suspended in a fluid. The percentage of bacteria labeled with fluorescent nano-objects can thus be quantitatively measured.

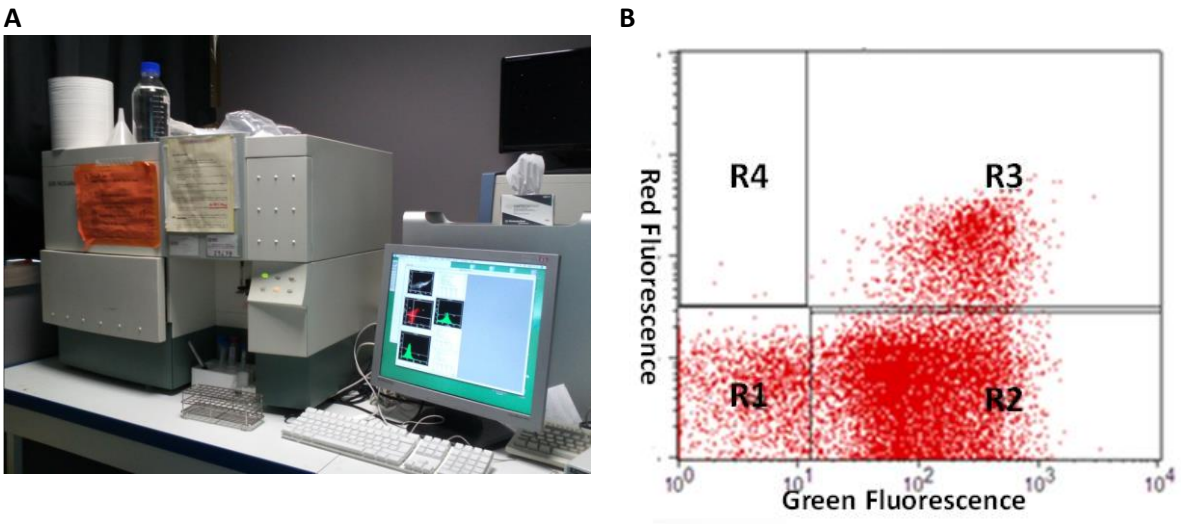



**Figure 7.1** Flow Cytometry (BD, FACS Calibur) (A), analysis of flow cytometry (B) X axis: green fluorescence, Y axis: red fluorescence. R1 refers to live non-fluorescent cells percentage, R2 refers to live green fluorescent cells percentage, R3 refers to dead red-green fluorescent cells percentage and R4 refers to dead red fluorescent cells percentage.

Live cells have intact membranes and are impermeable to dyes such as propidium iodide (PI), which only leaks into dead cells with compromised membranes. In this way, we could measure the percentage of live cells in each sample, and assess the toxicity of nano-objects on *E.coli*[217]. Before flow cytometry, propidium iodide (PI, 10µL, $1.3x10^{-2}$ mg/mL) was added into each sample. PI emits in the red (317nm) once it is bound to the DNA inside the bacteria. FNPs or GFPCs emit in the green (548nm), the emission signal will be measured if they remain inside or attached to the membrane of the bacteria, otherwise they are lost during the washing steps. Analysis of the cells by flow cytometry is shown in **Figure 7.1**. R1 refers to live non-fluorescent cells percentage, R2 refers to live green fluorescent cells percentage, R3 refers to dead red-green fluorescent cells percentage and R4 refers to dead red fluorescent cells percentage.

## 7.9 Techniques for rapid detection of *Escherichia coli* growth by fluorescent pH-sensitive nanoparticles (FANPs)

### 7.9.1 Screening of bacterial growth in a 96 well plate

Live *E.coli* bacterial cells (K-12, BW25113) were used for the following experiments. Bacterial cultures were prepared overnight from stock cultures inoculated in Luria Broth (LB) growth medium.

The overnight culture of bacteria was diluted 1:1000 in the Modified M9 minimal growth medium. 150µL of this bacterial solution were placed in each well of a 96 well Falcon Polystyrene Flat Bottom Plate. Different volumes (from 2 to 10 µL) of the stock FANP1 and FANP2 solutions were added into the *E.coli* solution to reach final concentrations of $8.2x10^{-7}$M, $4.1x10^{-7}$M and $8.2x10^{-8}$M. Each plate contained three repeats of the same concentration. One control with only bacteria and one blank with only the Modified M9 minimal growth medium were also prepared. 70 µL of mineral oil were added to each well in order to avoid evaporation. Samples were incubated in a plate reader (Perkin Elmer Victor3 1420 Multilabel Plate Counter) at 37°C in the dark. The growth of the cells was monitored every 6 minutes by reading the optical density (OD@600nm). Fluorescence was measured using a F485/14 filter for excitation and a F535/40 filter for emission. The experiments lasted overnight for ten hours.

### 7.9.2 Real-Time detection of *E.coli*

2.5mL of Modified M9 minimal growth medium with an initial concentration of $2x10^7$ CFU/mL (OD=0.2) or $3\text{-}6x10^5$ CFU/mL (OD=0.003-0.006) of *E.coli* bacteria were placed inside a 4.5mL BRAND Methacrylate (PMMA) Cuvette. Different volumes of FA (fluoresceinamine) solution, or FANP1 or FANP2 suspensions were added to this *E.coli* suspension to reach a final concentration of $8.2x10^{-7}$M. Two repeats of the same concentration were carried out during each of the experiments.

The samples were incubated at 37°C in the dark. Every 30 minutes the growth of the cells was monitored using a spectrophotometer, Varian Cary 5000 (Palo Alto, CA USA) that reads the optical density (OD@600nm) of the samples compared to a blank of Modified M9

minimal medium. The pH of the samples was measured using a glass electrode. Emission and excitation spectra of the samples were measured on a SPEX Fluoromax-3 (Horiba Jobin-Yvon).

### 7.9.3 High-through put screening of bacterial growth inhibition by antibiotics

The assay is performed in a 96 well Falcon Polystyrene Flat Bottom Plate as described above. 150µL of a bacterial solution (1:1000 dilution of an overnight culture) were placed in each well. FANP1 and FANP2 solutions were added into the *E.coli* solution to reach final concentrations of $8.2x10^{-8}$M. Three different antibiotics (Chloramphenicol, Kanamycin, and Ampicillin) were added into the bacterial solution to reach an increasing concentrations of 0.5, 1, 5, 10, 50 µg/mL, respectively. Each plate contained two repeats of the same concentration. Controls without antibiotics and one blank with only the Modified M9 minimal growth medium were also prepared.

### 7.9.4 Preparation of pH sensitive agarose culture plates

Agarose (2% final) was dissolved in 5mL of water and heated at approximately 75°C. Once the mixture became transparent and cooled down to around 45°C, 5 ml of a 2X solution of the modified M9 minimal medium and different volumes of either FANP1 or FANP2 solutions were added to reach a final concentration of $8.2x10^{-7}$M. Stirring for 2 minutes yielded a homogeneous mixture which was poured into each of the 1cm wells of a Nunc 4 well cell culture plate to form am agarose layer upon cooling to room temperature. *E.coli* bacterial solutions with an initial concentration of $1\text{-}2x10^{4}$ CFU/mL were added on different positions of the culture plates. The samples were incubated at 37°C in the dark overnight.

### 7.9.5 Imaging of *E.coli* growth

Fluorescence images of the samples in the cuvettes and in the culture plates were taken by a smartphone (Google Nexus 5) by putting samples on a Safe Imager™ 2.0 Blue Light Transilluminator (exc@470nm).

## 7.10 Bioimaging of fluorescent nanomaterials interaction with *E.coli* bacteria

### 7.10.1 Fluorescence microscopy

Images of fluorescent nanomaterials with the *E.coli* bacteria are taken by epifluorescence microscopy (Nikon inverted microscope ECLIPSE TI-E **Figure 7.2A**) with a motorized perfect focus system (PFS).

**A** **B**

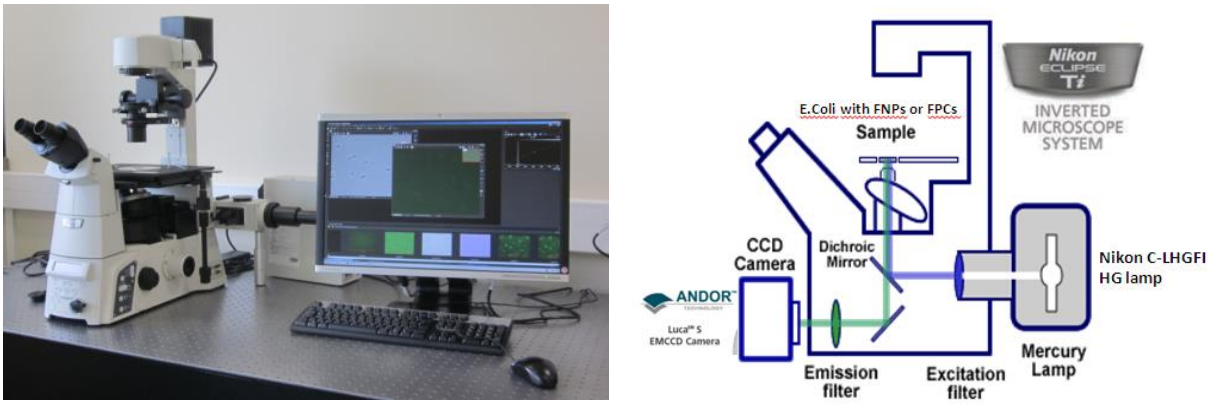
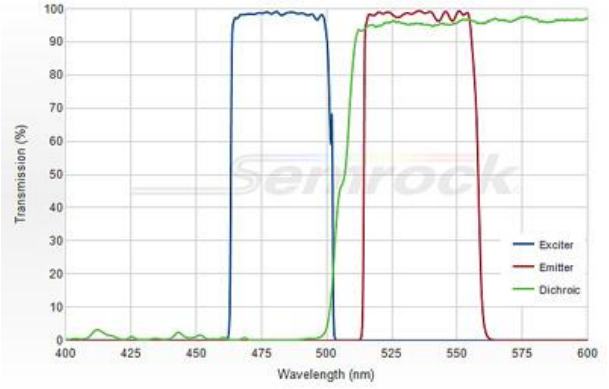



**Figure 7.2** Nikon inverted microscope ECLIPSE TI-E (A), Scheme of Nikon epifluorescence microscope (B)

The scheme of the Nikon Epifluorescence microscope (C-HGFI Intense light Nikon) is shown in **Figure 7.2B**. The resolution of the microscope is about 450 nm at the wavelength of 528 nm. FITC-3540C BrightLine single-band filter (**Figure 7.3A**) is used in this microscope. It provides both high brightness and signal-to-noise ratio. It is also ideal for fluorophores that have narrow, more closely spaced excitation and emission peaks, like BODIPY. *E.coli* cells with FNPs or GFPCs are illuminated with light of a wavelength (482 nm) which excites FNPs or GFPCs. TRITC-B BrightLine single-band filter (**Figure 7.3B**) is also used for RFPCs. *E.coli* cells with RFPCs are illuminated with light of a wavelength (543 nm) which excites RFPCs. The fluorescent light is then imaged through a microscope objective with an emCCD camera. Objectives 60X (CFI S Plan Fluor ELWD, NA 0.7) and 100X (CFI Plan Apo VC, NA 1.4, Nikon 50 TYPE NF IMMERISION OIL) are both used in this research. During the experiment, I take intensity images of the samples. Firstly, the focus is made on the bacteria with white light and the phase contrast image is recorded. Secondly, I turn on the mercury lamp and choose the right filter for the fluorescence image. We can also overlap the phase contrast and

fluorescence images together to measure clearly fluorescent nanomaterials interacting with the *E.coli* bacteria.

**A**
**FITC-3540C**




**B**
**TRITC-B**

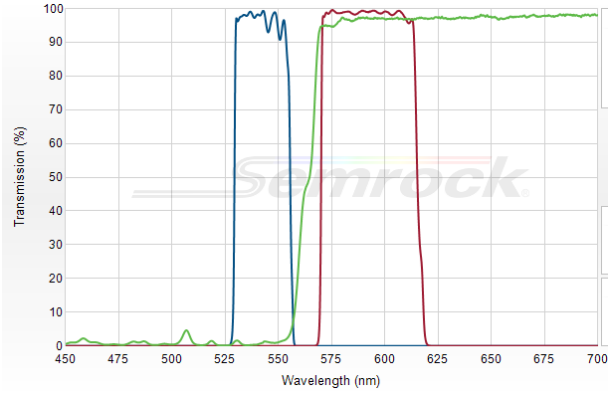



**Figure 7.3** FITC-3540C BrightLine single-band filter (A), TRITC-B BrightLine single-band filter (B).

### 7.10.2 Usage of methylene blue for bioimaging experiments

2 µL *E.coli* with FNP$^-$ or GFPC$^-$ samples was added inside a 0.5 mL Eppendorf Safe-Lock Tube, then 2 µL methylene blue with an initial concentration of 32 µM was added into the tube to reach a final concentration of 16 µM. The solution was quickly mixed before microscopy experiments.

### 7.10.3 Usage of DRAQ 5 for labelling the DNA of *E.coli* bacteria

DRAQ5 (1:1000 dilution) with an initial concentration of 5mM was added at the same time with GFPC$^-$ to *E.coli* suspension in M9 medium. The samples were incubated at 37°C in the dark for one hour. After the incubation, the cells were gently centrifuged at 4000rpm for 3 minutes at 4°C and washed with filtered PBS twice to remove free GFPCs and DRAQ5. The cells were then fixed by adding a fixing solution (4% PFA, 0.03% glutaraldehyde in 1x PBS) for 15 minutes. After the fixing process, cells were washed with PBS for three times and re-suspended in PBS before bioimaging experiments.

### 7.10.4 Usage of PKH26 for labelling the membrane of *E.coli* bacteria

The following procedure uses a 500 µL final staining volume containing final concentration of $2x10^{-6}$ M of PKH26 and $1x10^8$cells/mL. After introducing GFPC$^-$ into *E.coli* bacteria, samples were washed twice by PBS and re-suspended in 250 µL diluent C (an aqueous solution designed to maintain cell viability) in order to further perform membrane

labelling. 1 µL PKH26 with an initial concentration of 1mM was added into 250 µL diluent C, and then the bacterial solution was quickly transferred in to PKH26 dilution and mixed at room temperature for 5 minutes. The staining process is stopped by adding an equal volume of 1% BSA and incubate for 1 minute to allow binding of the dye in excess. Finally, the samples were washed three times by filtered PBS and re-suspended in PBS before bioimaging experiments.

### 7.10.5 Main preparation pathways for SEM

SEM images were recorded at the MICALIS laboratory (UMR 1319) by Alexis Canette (campus AgroParisTech de Massy, France). Fresh bacterial samples were fixed by 2.5% glutaraldehyde for one hour at room temperature and then washed by CdS buffer three times. Then, fixed cells were dehydrated by substitution of water in the cells step by step with ethanol at different concentrations (70%, 90% and 100%), each concentration was repeated twice and each substitution lasted 10 minutes. After the substitution, a critical point dryer was used to replace ethanol in an ethanol dehydrated specimen with liquid carbon dioxide. Then the liquid carbon dioxide is heated so that at a certain temperature and sample chamber pressure (the critical point) the carbon dioxide passes from the liquid state to the dry gaseous state with little or no damage due to surface tension. Finally, a thin heavy metal platinum layer is applied to the specimen surface by coating in order to increase contrast.

## 7.11 Equations

**BODIPY methacrylate-1 (BDPMA1) conversion**[180]

BDPMA1 conversion was determined by SEC, UV-vis. detection (λ = 528 nm, abs. max of BDPMA1) comparing the integration of the monomer (BDPMA1) and copolymer (P(AA-*co*-APEG-*co*-BDPMA)-TTC-$C_{12}$ or P(APEG-*co*-BDPMA)-TTC-$C_{12}$ traces. To do so, we assumed that

$\varepsilon^{528}_{monomer} \approx \varepsilon^{528}_{polymer}$(73000 L.mol$^{-1}$.cm$^{-1}$)[27]. This assumption appears acceptable since the photophysical properties of BODIPY chromophores are known to be weakly affected by their environment. Hence BDPMA1 conversion was determined as:

$$y = \frac{S_{PBDPMA1}}{S_{PBDPMA1} + S_{BDPMA1}} \qquad \textbf{Equation 7.1}$$

Where,

y: BDPMA1 conversion

$S_{PBDPMA}$: integration of the UV-vis. signal corresponding to the polymerized BDPMA1 (PBDPMA1)

$S_{BDPMA}$: integration of the UV-vis. signal corresponding to the BDPMA1 monomer (MW = 464 g/mol)

**Theoretical number-average molar mass ($M_{nth}$)**[180]

$$\boldsymbol{M_{nth} = M_{nTTCA} + \frac{1}{n_{TCCA}}(x \times m_A + y \times m_{BDPMA1})} \qquad \textbf{Equation 7.2}$$

Where,

$M_{nth}$: theoretical number-average molar mass

$M_{nTCCA}$: number-average molar mass of the chain transfer agent (TCCA, macroRAFT agent)

$n_{TCCA}$: mole of TCCA

x: APEG and AA conversion determined by NMR $^1H$ in $CDCl_3$.

y: BDPMA1 conversion determined by SEC (UV vis. detection)

$m_A$: mass of APEG and AA used in the polymerization

$m_{BDPMA}$: mass of BDPMA1 used in the polymerization

**Stern-Volmer equation**[23]**:**

$$\boldsymbol{\frac{F_0}{F} = 1 + K_D[Q]} \qquad \textbf{Equation 7.3}$$

Where,

$F_0$: Fluorescence intensity of $FNP^-$ or $GFPC^-$ in the absence of quencher methylene blue

F: Fluorescence intensities of $FNP^-$ or $GFPC^-$ in the presence of quencher methylene blue

$K_D$: Stern-Volmer quenching constant

Q: The concentration of quencher methylene blue

Quenching data are usually presented as plots of F0/F versus [Q]. This is because F0/F is expected to be linearly dependent upon the concentration of quencher. A plot of F0/F versus [Q] yields an intercept of one on the y-axis and a slope equal to $K_D$. Intuitively, it is useful to note that $K_D^{-1}$ is the quencher concentration at which $F_0/F$= 2 or 50% of the intensity is quenched.

**Modified Stern-Volmer equation[23]:**

$$\frac{F_0}{\Delta F} = \frac{1}{f_a K_a [Q]} + \frac{1}{f_a}$$ **Equation 7.4**

Where,

$F_0$: Fluorescence intensity of $FNP^-$ or $GFPC^-$ in the absence of quencher methylene blue

$\Delta F$: The difference between fluorescence intensities of $FNP^-$ or $GFPC^-$ in the absence and presence of quencher methylene blue ($F_0$-F).

$f_a$: The fraction of the initial fluorescence of $FNP^-$ or $GFPC^-$ that is accessible to quencher methylene blue.

$K_a$: The Stern-Volmer quenching constant of the accessible fraction.

[Q] : the concentration of quencher methylene blue.

This modified form of the Stern-Volmer equation allows $f_a$ and $K_a$ to be determined graphically. A plot of $F_0/\Delta F$ versus 1/[Q] yields $f_a^{-1}$ as the intercept and $(f_a K_a)^{-1}$ as the slope. A y-intercept of $f_a^{-1}$ may be understood intuitively. The intercept represents the extrapolation to infinite quencher concentration (1/[Q] = 0). The value of $F_0/(F_0 - F)$ at this quencher concentration represents the reciprocal of the fluorescence that was quenched. At high quencher concentration only the inaccessible residues will be fluorescent.

**Brightness[27]**

Brightness is the total efficiency of absorption and fluorescence emission of a fluorophore. Brightness of a dye depends on two properties: molar extinction coefficient at the excitation wavelength ε(λ) and fluorescence quantum efficiency, $\Phi_F$[26].

The brightness (B) of a fluorophore is proportional to the molar extinction coefficient at the excitation wavelength ε(λ) and quantum yield ($\Phi_F$), as indicated in the following relationship[26]:

$$B = \varepsilon(\lambda) \times \Phi_F$$

For fluorescent nanomaterials (FNPs or GFPCs), the brightness is defined as[27]:

$$B = N \times \varepsilon(\lambda) \times \Phi_F \qquad \textbf{Equation 7.5}$$

Where,

N: Number of fluorophores contained inside the FNPs or GFPCs

ε(λ): molar extinction coefficient of the fluorophore at the excitation wavelength,

we assumed that $\varepsilon^{528}_{monomer} \approx \varepsilon^{528}_{polymer}$ (73000 L.mol$^{-1}$.cm$^{-1}$)[27]. This assumption appears acceptable since the photophysical properties of BODIPY chromophores are known to be weakly affected by their environment.

$\Phi_F$: fluorescence quantum yield of the FNPs or GFPCs.

# References


1. Kumar, M., Mommer, M. S. & Sourjik, V. Mobility of Cytoplasmic, Membrane, and DNA-Binding Proteins in Escherichia coli. *Biophys. J.* **98,** 552–559 (2010).

2. Ando, T. & Skolnick, J. Crowding and hydrodynamic interactions likely dominate in vivo macromolecular motion. *Proc. Natl. Acad. Sci.* **107,** 18457–18462 (2010).

3. Nenninger, A., Mastroianni, G. & Mullineaux, C. W. Size Dependence of Protein Diffusion in the Cytoplasm of Escherichia coli. *J. Bacteriol.* **192,** 4535–4540 (2010).

4. Whitman, W. B., Coleman, D. C. & Wiebe, W. J. Prokaryotes: The unseen majority. *Proc. Natl. Acad. Sci.* **95,** 6578–6583 (1998).

5. Fredrickson, J. K. *et al.* Geomicrobiology of High-Level Nuclear Waste-Contaminated Vadose Sediments at the Hanford Site, Washington State. *Appl. Environ. Microbiol.* **70,** 4230–4241 (2004).

6. Lusby, P. E., Coombes, A. L. & Wilkinson, J. M. Bactericidal Activity of Different Honeys against Pathogenic Bacteria. *Arch. Med. Res.* **36,** 464–467 (2005).

7. Finegold, S. M. & Jousimies-Somer, H. Recently Described Clinically Important Anaerobic Bacteria: Medical Aspects. *Clin. Infect. Dis.* **25,** S88–S93 (1997).

8. Unc, A. & Goss, M. J. Transport of bacteria from manure and protection of water resources. *Appl. Soil Ecol.* **25,** 1–18 (2004).

9. McKeon, D. M., Calabrese, J. P. & Bissonnette, G. K. Antibiotic resistant gram-negative bacteria in rural groundwater supplies. *Water Res.* **29,** 1902–1908 (1995).

10. Leroy, F. & De Vuyst, L. Lactic acid bacteria as functional starter cultures for the food fermentation industry. *Trends Food Sci. Technol.* **15,** 67–78 (2004).

11. Gram, L. *et al.* Food spoilage—interactions between food spoilage bacteria. *Int. J. Food Microbiol.* **78,** 79–97 (2002).

12. Leyer, G. J., Wang, L. L. & Johnson, E. A. Acid adaptation of Escherichia coli O157:H7 increases survival in acidic foods. *Appl. Environ. Microbiol.* **61,** 3752–3755 (1995).

13. Radke, S. M. & Alocilja, E. C. A high density microelectrode array biosensor for detection of E. coli O157:H7. *Biosens. Bioelectron.* **20,** 1662–1667 (2005).

14. Su, C. & Brandt, L. J. Escherichia coli O157: H7 Infection in Humans. *Ann. Intern. Med.* **123,** 698–707 (1995).

15. Barker, L. M. *et al.* Multiple pH measurement during storage may detect bacterially contaminated platelet concentrates. *Transfusion (Paris)* **50,** 2731–2737 (2010).

16. Palavecino, E. L., Yomtovian, R. A. & Jacobs, M. R. Detecting bacterial contamination in platelet products. *Clin. Lab.* **52,** 443–456 (2006).

17. Washington, J. A. in *Medical Microbiology* (ed. Baron, S.) (University of Texas Medical Branch at Galveston, 1996).

18. Farris, L. *et al.* in *Principles of Bacterial Detection: Biosensors, Recognition Receptors and Microsystems* (eds. Zourob, M., Elwary, S. & Turner, A.) 213–230 (Springer New York, 2008).

19. Ko, S., Gunasekaran, S. & Yu, J. Self-indicating nanobiosensor for detection of 2,4-dinitrophenol. *Food Control* **21,** 155–161 (2010).

20. Wang, Y., Ye, Z. & Ying, Y. New Trends in Impedimetric Biosensors for the Detection of Foodborne Pathogenic Bacteria. *Sensors* **12,** 3449–3471 (2012).

21. http://science.howstuffworks.com/life/evolution/evolution2.htm.

22. Valeur, B. in *Molecular Fluorescence* (Wiley-VCH Verlag GmbH, 2001).

23. Lakowicz, Joseph R. *Principles of Fluorescence Spectroscopy*. (Springer US, 2006).

24. https://commons.wikimedia.org/wiki/File:Stokes_shift.png.

25. in *Handbook of Fluorescence Spectra of Aromatic Molecules (Second Edition)* (ed. Berlman, I. B.) iii (Academic Press, 1971).

26. Braslavsky, S. E. Glossary of terms used in photochemistry, 3rd edition (IUPAC Recommendations 2006). *Pure Appl. Chem.* **79,** (2007).

27. Grazon, C. *Élaboration de nanoparticules fluorescentes à base de BODIPY par polymérisation RAFT en miniémulsion : synthèse, caractérisation et fonctionnalisation de surface*. (Cachan, Ecole normale supérieure, 2012).

28. Demchenko, Alexander P. *Introduction to Fluorescence Sensing*. (Springer Netherlands, 2009).

29. Carrascosa, L. G., Moreno, M., Álvarez, M. & Lechuga, L. M. Nanomechanical biosensors: a new sensing tool. *TrAC Trends Anal. Chem.* **25,** 196–206 (2006).

30. Palecek, E., Fojta, M. & Jelen, F. New approaches in the development of DNA sensors: hybridization and electrochemical detection of DNA and RNA at two different surfaces. *Bioelectrochemistry Amst. Neth.* **56,** 85–90 (2002).

31. Warsinke, A., Benkert, A. & Scheller, F. W. Electrochemical immunoassays. *Fresenius J. Anal. Chem.* **366,** 622–634 (2000).

32. Baird, C. L. & Myszka, D. G. Current and emerging commercial optical biosensors. *J. Mol. Recognit. JMR* **14,** 261–268 (2001).

33. Homola, J. Present and future of surface plasmon resonance biosensors. *Anal. Bioanal. Chem.* **377,** 528–539 (2003).

34. Reimer, L. *Transmission Electron Microscopy: Physics of Image Formation and Microanalysis*. (Springer, 2013).

35. Principles and techniques of scanning electron microscopy: Biological applications, Volume 6. *Cell* **17,** 235–236 (1979).

36. Wang, F., Tan, W. B., Zhang, Y., Fan, X. & Wang, M. Luminescent nanomaterials for biological labelling. *Nanotechnology* **17,** R1 (2006).

37. http://www.sciencesetavenir.fr/fondamental/20120504.OBS4671/h5n1-quatre-mutations-qui-rendent-un-virus-aviaire-contagieux-entre-mammiferes.html.

38. http://www.wisegeek.com/what-are-gram-negative-bacteria.htm.

39. http://www.nature.com/scitable/topicpage/beyond-prokaryotes-and-eukaryotes-planctomycetes-and-cell-14158971.

40. http://www.biotechrabbit.com/antibody-production-services-and-oem/monoclonal-antibodies.html.

41. https://www.lifetechnologies.com/order/catalog/product/F1906.

42. Martin, M. M. & Lindqvist, L. The pH dependence of fluorescein fluorescence. *J. Lumin.* **10,** 381–390 (1975).

43. Twining, S. S. Fluorescein isothiocyanate-labeled casein assay for proteolytic enzymes. *Anal. Biochem.* **143,** 30–34 (1984).

44. Kutyavin, I. V. *et al.* 3′-Minor groove binder-DNA probes increase sequence specificity at PCR extension temperatures. *Nucleic Acids Res.* **28,** 655–661 (2000).

45. Rusinova, E., Tretyachenko-Ladokhina, V., Vele, O. E., Senear, D. F. & Alexander Ross, J. B. Alexa and Oregon Green dyes as fluorescence anisotropy probes for measuring protein–protein and protein–nucleic acid interactions. *Anal. Biochem.* **308,** 18–25 (2002).

46. Mottram, L. F., Boonyarattanakalin, S., Kovel, R. E. & Peterson, B. R. The Pennsylvania Green Fluorophore: A Hybrid of Oregon Green and Tokyo Green for the Construction of Hydrophobic and pH-Insensitive Molecular Probes. *Org. Lett.* **8,** 581–584 (2006).

47. Xu, Z., Rollins, A., Alcala, R. & Marchant, R. E. A novel fiber-optic pH sensor incorporating carboxy SNAFL-2 and fluorescent wavelength-ratiometric detection. *J. Biomed. Mater. Res.* **39,** 9–15 (1998).

48. Kubin, R. F. & Fletcher, A. N. Fluorescence quantum yields of some rhodamine dyes. *J. Lumin.* **27,** 455–462 (1982).

49. Johnson, L. V., Walsh, M. L. & Chen, L. B. Localization of mitochondria in living cells with rhodamine 123. *Proc. Natl. Acad. Sci. U. S. A.* **77,** 990–994 (1980).

50. https://www.lifetechnologies.com/order/catalog/product/R302.

51. Haugland, R. P. *Handbook of Fluorescent Probes & Research Chemicals: Deutsche Mark Version*. (Molecular Probes Inc, 1996).

52. Panchuk-Voloshina, N. *et al.* Alexa Dyes, a Series of New Fluorescent Dyes that Yield Exceptionally Bright, Photostable Conjugates. *J. Histochem. Cytochem.* **47,** 1179–1188 (1999).

53. The Molecular Probes® Handbook. 11th edition, lifetechnologies.

54. Loudet, A. & Burgess, K. BODIPY dyes and their derivatives: syntheses and spectroscopic properties. *Chem. Rev.* **107,** 4891–4932 (2007).

55. Karolin, J., Johansson, L. B.-A., Strandberg, L. & Ny, T. Fluorescence and Absorption Spectroscopic Properties of Dipyrrometheneboron Difluoride (BODIPY) Derivatives in Liquids, Lipid Membranes, and Proteins. *J. Am. Chem. Soc.* **116,** 7801–7806 (1994).

56. Ulrich, G., Ziessel, R. & Harriman, A. The chemistry of fluorescent bodipy dyes: versatility unsurpassed. *Angew. Chem. Int. Ed Engl.* **47,** 1184–1201 (2008).

57. Meng, Q. *et al.* Design and synthesis of a photocleavable fluorescent nucleotide 3'-O-allyl-dGTP-PC-Bodipy-FL-510 as a reversible terminator for DNA sequencing by synthesis. *J. Org. Chem.* **71,** 3248–3252 (2006).

58. Schade, S. Z., Jolley, M. E., Sarauer, B. J. & Simonson, L. G. BODIPY–α-Casein, a pH-Independent Protein Substrate for Protease Assays Using Fluorescence Polarization. *Anal. Biochem.* **243,** 1–7 (1996).

59. McCalla, T. M. Cation Adsorption by Bacteria 1. *J. Bacteriol.* **40,** 23–32 (1940).

60. Smith, P. J., Wiltshire, M. & Errington, R. J. DRAQ5 labeling of nuclear DNA in live and fixed cells. *Curr. Protoc. Cytom. Editor. Board J Paul Robinson Manag. Ed. Al* **Chapter 7,** Unit 7.25 (2004).

61. http://www.ebi.ac.uk/chebi/searchId.do?chebiId=CHEBI:52036.

62. Rochelle A. Diamond, Susan Demaggio,*In Living Color*. (Springer Berlin Heidelberg, 2000).

63. Ford, J. W., Welling, T. H., Stanley, J. C. & Messina, L. M. PKH26 and 125I-PKH95: characterization and efficacy as labels for in vitro and in vivo endothelial cell localization and tracking. *J. Surg. Res.* **62,** 23–28 (1996).

64. https://www.lifetechnologies.com/order/catalog/product/P3566.

65. Chudakov, D. M., Matz, M. V., Lukyanov, S. & Lukyanov, K. A. Fluorescent Proteins and Their Applications in Imaging Living Cells and Tissues. *Physiol. Rev.* **90,** 1103–1163 (2010).

66. Tsien, R. Y. The Green Fluorescent Protein. *Annu. Rev. Biochem.* **67,** 509–544 (1998).

67. Shaner, N. C. *et al.* Improved monomeric red, orange and yellow fluorescent proteins derived from Discosoma sp. red fluorescent protein. *Nat. Biotechnol.* **22,** 1567–1572 (2004).

68. Day, R. N. & Davidson, M. W. The fluorescent protein palette: tools for cellular imaging. *Chem. Soc. Rev.* **38,** 2887–2921 (2009).

69. Miyawaki, A., Nagai, T. & Mizuno, H. Mechanisms of protein fluorophore formation and engineering. *Curr. Opin. Chem. Biol.* **7,** 557–562 (2003).

70. Chalfie, M. GFP: Lighting up life. *Proc. Natl. Acad. Sci.* **106,** 10073–10080 (2009).

71. Mérola, F. *et al.* Newly engineered cyan fluorescent proteins with enhanced performances for live cell FRET imaging. *Biotechnol. J.* **9,** 180–191 (2014).

72. Erard, M. *et al.* Minimum set of mutations needed to optimize cyan fluorescent proteins for live cell imaging. *Mol. Biosyst.* **9,** 258–267 (2013).

73. Andersen, J. B. *et al.* New Unstable Variants of Green Fluorescent Protein for Studies of Transient Gene Expression in Bacteria. *Appl. Environ. Microbiol.* **64,** 2240–2246 (1998).

74. Chudakov, D. M., Lukyanov, S. & Lukyanov, K. A. Fluorescent proteins as a toolkit for in vivo imaging. *Trends Biotechnol.* **23,** 605–613 (2005).

75. Vintersten, K. *et al.* Mouse in red: Red fluorescent protein expression in mouse ES cells, embryos, and adult animals. *genesis* **40,** 241–246 (2004).

76. Llopis, J., McCaffery, J. M., Miyawaki, A., Farquhar, M. G. & Tsien, R. Y. Measurement of cytosolic, mitochondrial, and Golgi pH in single living cells with green fluorescent proteins. *Proc. Natl. Acad. Sci.* **95,** 6803–6808 (1998).

77. Westermann, B. & Neupert, W. Mitochondria-targeted green fluorescent proteins: convenient tools for the study of organelle biogenesis in Saccharomyces cerevisiae. *Yeast* **16,** 1421–1427 (2000).

78. Miroux, B. & Walker, J. E. Over-production of Proteins inEscherichia coli: Mutant Hosts that Allow Synthesis of some Membrane Proteins and Globular Proteins at High Levels. *J. Mol. Biol.* **260,** 289–298 (1996).

79. Geoffroy, M.-C. *et al.* Use of Green Fluorescent Protein To Tag Lactic Acid Bacterium Strains under Development as Live Vaccine Vectors. *Appl. Environ. Microbiol.* **66,** 383–391 (2000).

80. Tombolini, R., Unge, A., Davey, M. E., Bruijn, F. J. de & Jansson, J. K. Flow cytometric and microscopic analysis of GFP-tagged Pseudomonas fluorescens bacteria. *FEMS Microbiol. Ecol.* **22,** 17–28 (1997).

81. Roy, M. *et al.* Estimation of Minimum Doses for Optimized Quantum Dot Contrast-Enhanced Vascular Imaging In Vivo. *Small* **8,** 1780–1792 (2012).

82. Michael R. Warnement, I. D. T. Fluorescent Imaging Applications of Quantum Dot Probes. *Curr. Nanosci.* **3,** 273–284 (2007).

83. So, M.-K., Xu, C., Loening, A. M., Gambhir, S. S. & Rao, J. Self-illuminating quantum dot conjugates for in vivo imaging. *Nat. Biotechnol.* **24,** 339–343 (2006).

84. Wu, X. *et al.* Constructing NIR silica–cyanine hybrid nanocomposite for bioimaging in vivo: a breakthrough in photo-stability and bright fluorescence with large Stokes shift. *Chem. Sci.* **4,** 1221–1228 (2013).

85. He, X., Wang, Y., Wang, K., Chen, M. & Chen, S. Fluorescence Resonance Energy Transfer Mediated Large Stokes Shifting Near-Infrared Fluorescent Silica Nanoparticles for in Vivo Small-Animal Imaging. *Anal. Chem.* **84,** 9056–9064 (2012).

86. Jing liang Li, B. T. A review of optical imaging and therapy using nanosized graphene and graphene oxide. *Biomaterials* **34,** 9519–9534 (2013).

87. Liu, Q., Guo, B., Rao, Z., Zhang, B. & Gong, J. R. Strong Two-Photon-Induced Fluorescence from Photostable, Biocompatible Nitrogen-Doped Graphene Quantum Dots for Cellular and Deep-Tissue Imaging. *Nano Lett.* **13,** 2436–2441 (2013).

88. Demchenko, A. P. & Dekaliuk, M. O. Novel fluorescent carbonic nanomaterials for sensing and imaging. *Methods Appl. Fluoresc.* **1,** 042001 (2013).

89. Yu, J., Choi, S., Richards, C. I., Antoku, Y. & Dickson, R. M. Live Cell Surface Labeling with Fluorescent Ag Nanocluster Conjugates†. *Photochem. Photobiol.* **84,** 1435–1439 (2008).

90. Fischer, I., Petkau-Milroy, K., Dorland, Y. L., Schenning, A. P. H. J. & Brunsveld, L. Self-Assembled Fluorescent Organic Nanoparticles for Live-Cell Imaging. *Chem. – Eur. J.* **19,** 16646–16650 (2013).

91. Howes, P., Green, M., Levitt, J., Suhling, K. & Hughes, M. Phospholipid Encapsulated Semiconducting Polymer Nanoparticles: Their Use in Cell Imaging and Protein Attachment. *J. Am. Chem. Soc.* **132,** 3989–3996 (2010).

92. Ding, D. *et al.* Bright Far-Red/Near-Infrared Conjugated Polymer Nanoparticles for In Vivo Bioimaging. *Small* **9,** 3093–3102 (2013).

93. Pecher, J., Huber, J., Winterhalder, M., Zumbusch, A. & Mecking, S. Tailor-Made Conjugated Polymer Nanoparticles for Multicolor and Multiphoton Cell Imaging. *Biomacromolecules* **11,** 2776–2780 (2010).

94. Thielbeer, F., Chankeshwara, S. V. & Bradley, M. Polymerizable Fluorescein Derivatives: Synthesis of Fluorescent Particles and Their Cellular Uptake. *Biomacromolecules* **12,** 4386–4391 (2011).

95. Kim, Y. *et al.* Single Step Reconstitution of Multifunctional High-Density Lipoprotein-Derived Nanomaterials Using Microfluidics. *ACS Nano* **7,** 9975–9983 (2013).

96. Reul, R. *et al.* Near infrared labeling of PLGA for in vivo imaging of nanoparticles. *Polym. Chem.* **3,** 694–702 (2012).

97. Zhou, S. *et al.* Fluorescent dextran-based nanogels: efficient imaging nanoprobes for adipose-derived stem cells. *Polym. Chem.* **4,** 4103–4112 (2013).

98. Yao, J., Yang, M. & Duan, Y. Chemistry, Biology, and Medicine of Fluorescent Nanomaterials and Related Systems: New Insights into Biosensing, Bioimaging, Genomics, Diagnostics, and Therapy. *Chem. Rev.* **114,** 6130–6178 (2014).

99. Pinaud, F. *et al.* Advances in fluorescence imaging with quantum dot bio-probes. *Biomaterials* **27,** 1679–1687 (2006).

100. Smith, A. M., Duan, H., Mohs, A. M. & Nie, S. Bioconjugated quantum dots for in vivo molecular and cellular imaging. *Adv. Drug Deliv. Rev.* **60,** 1226–1240 (2008).

101. Rizvi, S. B., Ghaderi, S., Keshtgar, M. & Seifalian, A. M. Semiconductor quantum dots as fluorescent probes for in vitro and in vivo bio-molecular and cellular imaging. *Nano Rev.* **1,** (2010).

102. Alivisatos, A. P. Semiconductor Clusters, Nanocrystals, and Quantum Dots. *Science* **271,** 933–937 (1996).

103. Burda, C., Chen, X., Narayanan, R. & El-Sayed, M. A. Chemistry and properties of nanocrystals of different shapes. *Chem. Rev.* **105,** 1025–1102 (2005).

104. Editorial board. *Curr. Opin. Biotechnol.* **16,** i (2005).

105. Vasudevan, D., Gaddam, R. R., Trinchi, A. & Cole, I. Core–shell quantum dots: Properties and applications. *J. Alloys Compd.* **636,** 395–404 (2015).

106. Gao, X., Cui, Y., Levenson, R. M., Chung, L. W. K. & Nie, S. In vivo cancer targeting and imaging with semiconductor quantum dots. *Nat. Biotechnol.* **22,** 969–976 (2004).

107. Jaiswal, J. K., Mattoussi, H., Mauro, J. M. & Simon, S. M. Long-term multiple color imaging of live cells using quantum dot bioconjugates. *Nat. Biotechnol.* **21,** 47–51 (2003).

108. Qian, J. *et al.* Imaging pancreatic cancer using surface-functionalized quantum dots. *J. Phys. Chem. B* **111,** 6969–6972 (2007).

109. Wegner, K. D. & Hildebrandt, N. Quantum dots: bright and versatile in vitro and in vivo fluorescence imaging biosensors. *Chem. Soc. Rev.* (2015). doi:10.1039/C4CS00532E

110. Kim, S. *et al.* Near-infrared fluorescent type II quantum dots for sentinel lymph node mapping. *Nat. Biotechnol.* **22,** 93–97 (2004).

111. Chen, F. & Gerion, D. Fluorescent CdSe/ZnS Nanocrystal−Peptide Conjugates for Long-term, Nontoxic Imaging and Nuclear Targeting in Living Cells. *Nano Lett.* **4,** 1827–1832 (2004).

112. Bruchez, M., Moronne, M., Gin, P., Weiss, S. & Alivisatos, A. P. Semiconductor nanocrystals as fluorescent biological labels. *Science* **281,** 2013–2016 (1998).

113. Jin, Z. & Hildebrandt, N. Semiconductor quantum dots for in vitro diagnostics and cellular imaging. *Trends Biotechnol.* **30,** 394–403 (2012).

114. Geißler, D. *et al.* Lanthanides and Quantum Dots as Förster Resonance Energy Transfer Agents for Diagnostics and Cellular Imaging. *Inorg. Chem.* **53,** 1824–1838 (2014).

115. Michalet, X. *et al.* Quantum dots for live cells, in vivo imaging, and diagnostics. *Science* **307,** 538–544 (2005).

116. Medintz, I. L., Uyeda, H. T., Goldman, E. R. & Mattoussi, H. Quantum dot bioconjugates for imaging, labelling and sensing. *Nat. Mater.* **4,** 435–446 (2005).

117. Frasco, M. F. & Chaniotakis, N. Bioconjugated quantum dots as fluorescent probes for bioanalytical applications. *Anal. Bioanal. Chem.* **396,** 229–240 (2009).

118. Kloepfer, J. A. *et al.* Quantum Dots as Strain- and Metabolism-Specific Microbiological Labels. *Appl. Environ. Microbiol.* **69,** 4205–4213 (2003).

119. Xue, X., Pan, J., Xie, H., Wang, J. & Zhang, S. Fluorescence detection of total count of Escherichia coli and Staphylococcus aureus on water-soluble CdSe quantum dots coupled with bacteria. *Talanta* **77,** 1808–1813 (2009).

120. Wu, S.-M. *et al.* Quantum-Dot-Labeled DNA Probes for Fluorescence In Situ Hybridization (FISH) in the Microorganism Escherichia coli. *ChemPhysChem* **7,** 1062–1067 (2006).

121. Sulatha Dwarakanath, J. G. B. Quantum dot-antibody and aptamer conjugates shift fluorescence upon binding bacteria. *Biochem. Biophys. Res. Commun.* **325,** 739–43 (2004).

122. Gunsolus, I. L. *et al.* Facile method to stain the bacterial cell surface for super-resolution fluorescence microscopy. *Analyst* **139,** 3174–3178 (2014).

123. Ow, H. *et al.* Bright and Stable Core−Shell Fluorescent Silica Nanoparticles. *Nano Lett.* **5,** 113–117 (2005).

124. Santra, S., Zhang, P., Wang, K., Tapec, R. & Tan, W. Conjugation of biomolecules with luminophore-doped silica nanoparticles for photostable biomarkers. *Anal. Chem.* **73,** 4988–4993 (2001).

125. Santra, S., Wang, K., Tapec, R. & Tan, W. Development of novel dye-doped silica nanoparticles for biomarker application. *J. Biomed. Opt.* **6,** 160–166 (2001).

126. Zhao, X., Tapec-Dytioco, R. & Tan, W. Ultrasensitive DNA detection using highly fluorescent bioconjugated nanoparticles. *J. Am. Chem. Soc.* **125,** 11474–11475 (2003).

127. Zhao, X., Bagwe, R. P. & Tan, W. Development of Organic-Dye-Doped Silica Nanoparticles in a Reverse Microemulsion. *Adv. Mater.* **16,** 173–176 (2004).

128. Zhou, X. & Zhou, J. Improving the signal sensitivity and photostability of DNA hybridizations on microarrays by using dye-doped core-shell silica nanoparticles. *Anal. Chem.* **76,** 5302–5312 (2004).

129. Ha, S.-W., Camalier, C. E., Jr, G. R. B. & Lee, J.-K. New method to prepare very stable and biocompatible fluorescent silica nanoparticles. *Chem. Commun.* 2881–2883 (2009).

130. Qhobosheane, M., Santra, S., Zhang, P. & Tan, W. Biochemically functionalized silica nanoparticles. *Analyst* **126,** 1274–1278 (2001).

131. Christian Argyo, V. W. Multifunctional Mesoporous Silica Nanoparticles as a Universal Platform for Drug Delivery. *Chem. Mater.* **26,** (2013).

132. Grifantini, R. *et al.* Previously unrecognized vaccine candidates against group B meningococcus identified by DNA microarrays. *Nat. Biotechnol.* **20,** 914–921 (2002).

133. Yang, H.-H. *et al.* Nanometer fluorescent hybrid silica particle as ultrasensitive and photostable biological labels. *The Analyst* **128,** 462–466 (2003).

134. He, X. *et al.* A novel fluorescent label based on organic dye-doped silica nanoparticles for HepG liver cancer cell recognition. *J. Nanosci. Nanotechnol.* **4,** 585–589 (2004).

135. Wang, L. & Tan, W. Multicolor FRET silica nanoparticles by single wavelength excitation. *Nano Lett.* **6,** 84–88 (2006).

136. Zhao, W., Wang, L. & Tan, W. in *Bio-Applications of Nanoparticles* (ed. Chan, W. C. W.) 129–135 (Springer New York, 2007).

137. Wang, L., Zhao, W., O'Donoghu, M. B. & Tan, W. Fluorescent Nanoparticles for Multiplexed Bacteria Monitoring. *Bioconjug. Chem.* **18,** 297–301 (2007).

138. Tran, H. N. *et al.* Dye-doped silica-based nanoparticles for bioapplications. *Adv. Nat. Sci. Nanosci. Nanotechnol.* **4,** 043001 (2013).

139. Zhao, X. *et al.* A rapid bioassay for single bacterial cell quantitation using bioconjugated nanoparticles. *Proc. Natl. Acad. Sci. U. S. A.* **101,** 15027–15032 (2004).

140. Qin, D., He, X., Wang, K. & Tan, W. Using fluorescent nanoparticles and SYBR Green I based two-color flow cytometry to determine Mycobacterium tuberculosis avoiding false positives. *Biosens. Bioelectron.* **24,** 626–631 (2008).

141. Burns, A., Ow, H. & Wiesner, U. Fluorescent core–shell silica nanoparticles: towards 'Lab on a Particle' architectures for nanobiotechnology. *Chem. Soc. Rev.* **35,** 1028–1042 (2006).

142. Zhong, W. Nanomaterials in fluorescence-based biosensing. *Anal. Bioanal. Chem.* **394,** 47–59 (2009).

143. Cho, E. C., Glaus, C., Chen, J., Welch, M. J. & Xia, Y. Inorganic nanoparticle-based contrast agents for molecular imaging. *Trends Mol. Med.* **16,** 561–573 (2010).

144. Swierczewska, M., Lee, S. & Chen, X. Inorganic nanoparticles for multimodal molecular imaging. *Mol. Imaging* **10,** 3–16 (2011).

145. Tantra, R. & Knight, A. Cellular uptake and intracellular fate of engineered nanoparticles: A review on the application of imaging techniques. *Nanotoxicology* **5,** 381–392 (2010).

146. Tang, L. & Cheng, J. Nonporous silica nanoparticles for nanomedicine application. *Nano Today* **8,** 290–312 (2013).

147. Benya, R., Quintana, J. & Brundage, B. Adverse reactions to indocyanine green: A case report and a review of the literature. *Cathet. Cardiovasc. Diagn.* **17,** 231–233 (1989).

148. Liechty, W. B., Kryscio, D. R., Slaughter, B. V. & Peppas, N. A. Polymers for Drug Delivery Systems. *Annu. Rev. Chem. Biomol. Eng.* **1,** 149–173 (2010).

149. Kievit, F. M. & Zhang, M. Cancer Nanotheranostics: Improving Imaging and Therapy by Targeted Delivery Across Biological Barriers. *Adv. Mater.* **23,** H217–H247 (2011).

150. Taylor, J. R., Fang, M. M. & Nie, S. Probing specific sequences on single DNA molecules with bioconjugated fluorescent nanoparticles. *Anal. Chem.* **72,** 1979–1986 (2000).

151. Conde, J. *et al.* Revisiting 30 years of biofunctionalization and surface chemistry of inorganic nanoparticles for nanomedicine. *Chem. Eng.* **2,** 48 (2014).

152. Landfester, K. Polyreactions in Miniemulsions. *Macromol. Rapid Commun.* **22,** 896–936 (2001).

153. Landfester, K. The Generation of Nanoparticles in Miniemulsions. *Adv. Mater.* **13,** 765–768 (2001).

154. Sarrazin, P., Chaussy, D., Vurth, L., Stephan, O. & Beneventi, D. Surfactant (TTAB) Role in the Preparation of 2,7-Poly(9,9-dialkylfluorene-co-fluorenone) Nanoparticles by Miniemulsion. *Langmuir* **25,** 6745–6752 (2009).

155. Tuncel, D. & Demir, H. V. Conjugated polymer nanoparticles. *Nanoscale* **2,** 484–494 (2010).

156. Kurokawa, N., Yoshikawa, H., Hirota, N., Hyodo, K. & Masuhara, H. Size-Dependent Spectroscopic Properties and Thermochromic Behavior in Poly(substituted thiophene) Nanoparticles. *ChemPhysChem* **5,** 1609–1615 (2004).

157. Szymanski, C. *et al.* Single Molecule Nanoparticles of the Conjugated Polymer MEH−PPV, Preparation and Characterization by Near-Field Scanning Optical Microscopy. *J. Phys. Chem. B* **109,** 8543–8546 (2005).

158. Su, J. *et al.* Synthesis and photochromic property of nanoparticles with spiropyran moieties via one-step miniemulsion polymerization. *Polym. Bull.* **61,** 425–434 (2008).

159. Chen, J. *et al.* Synthesis and characterization of novel reversible photoswitchable fluorescent polymeric nanoparticles via one-step miniemulsion polymerization. *J. Phys. Chem. B* **115,** 3354–3362 (2011).

160. Li, K. & Liu, B. Polymer-encapsulated organic nanoparticles for fluorescence and photoacoustic imaging. *Chem. Soc. Rev.* **43,** 6570–6597 (2014).

161. Gluz, E., Grinberg, I., Corem-Salkmon, E., Mizrahi, D. & Margel, S. Engineering of new crosslinked near-infrared fluorescent polyethylene glycol bisphosphonate nanoparticles for bone targeting. *J. Polym. Sci. Part Polym. Chem.* **51,** 4282–4291 (2013).

162. Moon, J. H., McDaniel, W., MacLean, P. & Hancock, L. F. Live-Cell-Permeable Poly(p-phenylene ethynylene). *Angew. Chem. Int. Ed.* **46,** 8223–8225 (2007).

163. Feng, X. *et al.* A Convenient Preparation of Multi-Spectral Microparticles by Bacteria-Mediated Assemblies of Conjugated Polymer Nanoparticles for Cell Imaging and Barcoding. *Adv. Mater.* **24,** 637–641 (2012).

164. Moogooee, M., Ramezanzadeh, H., Jasoori, S., Omidi, Y. & Davaran, S. Synthesis and in vitro studies of cross-linked hydrogel nanoparticles containing amoxicillin. *J. Pharm. Sci.* **100,** 1057–1066 (2011).

165. Pinto-Alphandary, H., Andremont, A. & Couvreur, P. Targeted delivery of antibiotics using liposomes and nanoparticles: research and applications. *Int. J. Antimicrob. Agents* **13,** 155–168 (2000).

166. Zhu, C., Yang, Q., Lv, F., Liu, L. & Wang, S. Conjugated Polymer-Coated Bacteria for Multimodal Intracellular and Extracellular Anticancer Activity. *Adv. Mater.* **25,** 1203–1208 (2013).

167. Radovic-Moreno, A. F. *et al.* Surface Charge-Switching Polymeric Nanoparticles for Bacterial Cell Wall-Targeted Delivery of Antibiotics. *ACS Nano* **6,** 4279–4287 (2012).

168. Pulkkinen, M. *et al.* Three-step tumor targeting of paclitaxel using biotinylated PLA-PEG nanoparticles and avidin–biotin technology: Formulation development and in vitro anticancer activity. *Eur. J. Pharm. Biopharm.* **70,** 66–74 (2008).

169. Yang, J. *et al.* Antibody conjugated magnetic PLGA nanoparticles for diagnosis and treatment of breast cancer. *J. Mater. Chem.* **17,** 2695–2699 (2007).

170. Fujita, Y. & Taguchi, H. Current status of multiple antigen-presenting peptide vaccine systems: Application of organic and inorganic nanoparticles. *Chem. Cent. J.* **5,** 48 (2011).

171. Fernandes, R., Zuniga, M., Sassine, F. R., Karakoy, M. & Gracias, D. H. Enabling Cargo-Carrying Bacteria via Surface Attachment and Triggered Release. *Small* **7,** 588–592 (2011).

172. Emmanuelle Imbert-Laurenceau, M.-C. B. Surface modification of polystyrene particles for specific antibody adsorption. *Polymer* 1277–1285 (2005).

173. R van Erp, Y. E. M. L. Characterization of monoclonal antibodies physically adsorbed onto polystyrene latex particles. *J. Immunol. Methods* **152,** 191–9 (1992).

174. Akin, D. *et al.* Bacteria-mediated delivery of nanoparticles and cargo into cells. *Nat. Nanotechnol.* **2,** 441–449 (2007).

175. Bhawana Thakur, C. A. A. Polyaniline nanoparticle based colorimetric sensor for monitoring bacterial growth. *Sens. Actuators B Chem.* **207,** (2015).

176. Wang, X., Meier, R. J. & Wolfbeis, O. S. Fluorescent pH-Sensitive Nanoparticles in an Agarose Matrix for Imaging of Bacterial Growth and Metabolism. *Angew. Chem. Int. Ed.* **52,** 406–409 (2013).

177. Munkholm, C., Parkinson, D. R. & Walt, D. R. Intramolecular fluorescence self-quenching of fluoresceinamine. *J. Am. Chem. Soc.* **112,** 2608–2612 (1990).

178. Resch-Genger, U., Grabolle, M., Cavaliere-Jaricot, S., Nitschke, R. & Nann, T. Quantum dots versus organic dyes as fluorescent labels. *Nat. Methods* **5,** 763–775 (2008).

179. Shaner, N. C., Steinbach, P. A. & Tsien, R. Y. A guide to choosing fluorescent proteins. *Nat. Methods* **2,** 905–909 (2005).

180. Grazon, C., Rieger, J., Méallet-Renault, R., Clavier, G. & Charleux, B. One-Pot Synthesis of Pegylated Fluorescent Nanoparticles by RAFT Miniemulsion Polymerization Using a Phase Inversion Process. *Macromol. Rapid Commun.* **32,** 699–705 (2011).

181. Vu, T. T. *et al.* Understanding the Spectroscopic Properties and Aggregation Process of a New Emitting Boron Dipyrromethene (BODIPY). *J. Phys. Chem. C* **117,** 5373–5385 (2013).

182. Grazon, C., Rieger, J., Charleux, B., Clavier, G. & Méallet-Renault, R. Ultrabright BODIPY-Tagged Polystyrene Nanoparticles: Study of Concentration Effect on Photophysical Properties. *J. Phys. Chem. C* **118,** 13945–13952 (2014).

183. Luo, P. G. & Stutzenberger, F. J. Nanotechnology in the detection and control of microorganisms. *Adv. Appl. Microbiol.* **63,** 145–181 (2008).

184. William Godfrey, R. A. Bacterial Detection and Live/Dead Discrimination by Flow Cytometry. *BD Biosci. San Jose CA* (2002).

185. Cassler, M. R., Grimwade, J. E., McGarry, K. C., Mott, R. T. & Leonard, A. C. Drunken-cell footprints: nuclease treatment of ethanol-permeabilized bacteria reveals an initiation-like nucleoprotein complex in stationary phase replication origins. *Nucleic Acids Res.* **27,** 4570–4576 (1999).

186. Mirrett, S., Lauer, B. A., Miller, G. A. & Reller, L. B. Comparison of acridine orange, methylene blue, and Gram stains for blood cultures. *J. Clin. Microbiol.* **15,** 562–566 (1982).

187. Thomas, J. T. Phloxine-methylene blue staining of formalin-fixed tissue. *Stain Technol.* **28,** 311–312 (1953).

188. Radfar, A. *et al.* Synchronous culture of Plasmodium falciparum at high parasitemia levels. *Nat. Protoc.* **4,** 1899–1915 (2009).

189. Introduction to Electron Microscopy, Andres Kaech. University of Zurich. Center for Microscopy and Image Analysis.

190. Neish, C. S., Martin, I. L., Henderson, R. M. & Edwardson, J. M. Direct visualization of ligand-protein interactions using atomic force microscopy. *Br. J. Pharmacol.* **135,** 1943–1950 (2002).

191. Kuzuya, A., Numajiri, K., Kimura, M. & Komiyama, M. Single-molecule accommodation of streptavidin in nanometer-scale wells formed in DNA nanostructures. *Nucleic Acids Symp. Ser. 2004* 681–682 (2008).

192. Barbillon, G. *et al.* How nanoparticles encapsulating fluorophores allow a double detection of biomolecules by localized surface plasmon resonance and luminescence. *Nanotechnology* **19,** 035705 (2008).

193. Reth, M. Matching cellular dimensions with molecular sizes. *Nat. Immunol.* **14,** 765–767 (2013).

194. Willig, K. I., Rizzoli, S. O., Westphal, V., Jahn, R. & Hell, S. W. STED microscopy reveals that synaptotagmin remains clustered after synaptic vesicle exocytosis. *Nature* **440,** 935–939 (2006).

195. Green, N. M. Avidin. *Adv. Protein Chem.* **29,** 85–133 (1975).

196. Alexa Fluor® 488 dye. at <http://www.lifetechnologies.com/fr/fr/home/life-science/cell-analysis/fluorophores/alexa-fluor-488.html>

197. µ-Slide VI 0.4, I. http://ibidi.com/xtproducts/en/ibidi-Labware/Flow-Chambers/m-Slide-VI-0.4.

198. King, D. J. *Applications And Engineering Of Monoclonal Antibodies*. (CRC Press, 1998).

199. Alves, C. S. *et al.* Escherichia coli cell surface perturbation and disruption induced by antimicrobial peptides BP100 and pepR. *J. Biol. Chem.* **285,** 27536–27544 (2010).

200. Lehtinen, J., Nuutila, J. & Lilius, E.-M. Green fluorescent protein-propidium iodide (GFP-PI) based assay for flow cytometric measurement of bacterial viability. *Cytom. Part J. Int. Soc. Anal. Cytol.* **60,** 165–172 (2004).

201. Sjöback, R., Nygren, J. & Kubista, M. Absorption and fluorescence properties of fluorescein. *Spectrochim. Acta. A. Mol. Biomol. Spectrosc.* **51,** L7–L21 (1995).

202. Montalbetti, C. A. G. N. & Falque, V. Amide bond formation and peptide coupling. *Tetrahedron* **61,** 10827–10852 (2005).

203. Grazon, C., Rieger, J., Méallet-Renault, R., Charleux, B. & Clavier, G. Ultrabright Fluorescent Polymeric Nanoparticles Made from a New Family of BODIPY Monomers. *Macromolecules* **46,** 5167–5176 (2013).

204. Carvell, M., Robb, I. D. & Small, P. W. The influence of labelling mechanisms on the fluorescence behaviour of polymers bearing fluorescein labels. *Polymer* **39,** 393–398 (1998).

205. Duong, H. D., Sohn, O.-J., Lam, H. T. & Rhee, J. I. An optical pH sensor with extended detection range based on fluoresceinamine covalently bound to sol–gel support. *Microchem. J.* **84,** 50–55 (2006).

206. Badugu, R., Kostov, Y., Rao, G. & Tolosa, L. Development and application of an excitation ratiometric optical pH sensor for bioprocess monitoring. *Biotechnol. Prog.* **24,** 1393–1401 (2008).

207. Wang, F. *et al.* Development of luminescent pH sensor films for monitoring bacterial growth through tissue. *Adv. Healthc. Mater.* **3,** 197–204 (2014).

208. Pak, D. *et al.* Acridine orange as an alternative to optical density to study growth kinetics of Lactobacillus bulgaricus ATCC 7517. *J. Environ. Sci. Health B* **48,** 512–515 (2013).

209. Levi, V. & Gratton, E. Chromatin dynamics during interphase explored by single-particle tracking. *Chromosome Res. Int. J. Mol. Supramol. Evol. Asp. Chromosome Biol.* **16,** 439–449 (2008).

210. Saxton, M. J. & Jacobson, K. SINGLE-PARTICLE TRACKING:Applications to Membrane Dynamics. *Annu. Rev. Biophys. Biomol. Struct.* **26,** 373–399 (1997).

211. Suzuki, H., Yonekura, K. & Namba, K. Structure of the Rotor of the Bacterial Flagellar Motor Revealed by Electron Cryomicroscopy and Single-particle Image Analysis. *J. Mol. Biol.* **337,** 105–113 (2004).

212. Vroom, J. M. *et al.* Depth Penetration and Detection of pH Gradients in Biofilms by Two-Photon Excitation Microscopy. *Appl. Environ. Microbiol.* **65,** 3502–3511 (1999).

213. Valdés, P. A. *et al.* Quantitative, spectrally-resolved intraoperative fluorescence imaging. *Sci. Rep.* **2,** (2012).

214. Pellegrini, P. *et al.* Acidic extracellular pH neutralizes the autophagy-inhibiting activity of chloroquine. *Autophagy* **10,** 562–571 (2014).

215. Schork, F. J. *et al.* in *Polymer Particles* (ed. Okubo, M.) 129–255 (Springer Berlin Heidelberg, 2005).

216. Boissé, S. *et al.* Amphiphilic block copolymer nano-fibers via RAFT-mediated polymerization in aqueous dispersed system. *Chem. Commun.* **46,** 1950 (2010).

217. Brayner, R. *et al.* Toxicological Impact Studies Based on Escherichia coli Bacteria in Ultrafine ZnO Nanoparticles Colloidal Medium. *Nano Lett.* **6,** 866–870 (2006).

# Acknowledgements

My time at PPSM and LBPA has been impactful, formative, and an extraordinary experience that I will remember with gratitude throughout my life. I must express my great appreciation to these who accompanied me during my PhD study.

My deepest gratitude goes first and foremost to my supervisors: Pr. Rachel Méallet-Renault, Dr. Bianca Sclavi, and Dr. Gilles Clavier for giving me the opportunity to do this research in ENS-Cachan. Words are simply not enough for expressing gratitude towards them. They are the one who are always available for research questions, and always ready to give advice and to help in overcoming difficulties either in the study or in life during my staying in France. They inspired me to do my best in performing experiments, preparing talks and writing report, also offer me many opportunities to participate in conferences and summer school. It is their intellectual support, encouragement, enthusiasm, and intelligent guidance, which made this dissertation possible.

I want to express my warm and sincere thanks to Dr. Chloé Grazon, who helps me to get familiar with the lab, taught me hand by hand during experiments. I would not have completed my research without her encouragement and sound advice. I am very grateful to Jean-Frédéric Audibert, who was very experienced in microscope and he provides great assistant for my microscopy experiments, thanks to his useful discussion, patience and inspiration. I would like to express my great thanks to my dear be loved friend, Dr. Elisa Brambilla, who not only helped me a lot in biological experiments but also always warmhearted to help me out of any difficulties during my stay in Cachan.

I would like to extend my gratitude to my committee: Pr. Niko Hildebrandt, Dr. Marie Erard and Dr. Romain Briandet for taking the time to read my dissertation and give me useful advice to improve my dissertation.

I warmly thank to all the teachers during my master and PhD study, thank you for teaching me systemic science knowledge, you guide me on the way to science.

I would like to acknowledge Dr. Fabien Miomandre, Dr. Malcolm Buckle, Dr. Eric Deprez, Dr. Isabelle Leray, Prof. Keitaro Nakatani, Prof. Pierre Audebert, Prof. Robert Pansu, Prof. Joanne Xie, Dr. Clemence Allain, Dr. Valerie Genot, Prof. Anne Debarre, Dr. Carine Julien, Dr. Guillaume Laurent, Dr. Remi Metivier, and Dr. Claude Nogues who helped me during my whole stay in Cachan. Thank you for your helpful suggestions and constant encouragement.

I would like to thank all the past and present members of the PPSM and LBPA: Andrée Husson, Christian Jean-Baptiste, Jacky Fromont, Arnaud Brosseau, Stéphanne Maisonnneuve, Laurent Galmiche, Ni Ha Nguyen, Laura Nodin, Meriem Stamboul, Claire Déo, Corentin Pavageau, Charlotte Rémy, Marine Louis, Paul Rouschmeyer, Clarisse Tourbillon, Jérémy Bell, Jérémy Malinge, Hervé Leh, Marie-Christine Bouger, Gladys Mbemba, Marine Baudin… I appreciate your warm help and kind assistance. I am deeply grateful for every colleague, you guys have always been so nice to me, and my work would not have been possible finished without the collaboration, help, and support of all of you.

I also want to thank all my dear beloved friends I met in France during the past five years: Jia Su, Qing Zhou, Yayang Tian, Qing Zhang, Yanhua Yu, Yinbin Ruan, Yuanyuan Liao, Na Chen, Yuan Li, Sha Li, Lve Huang, Xiaoju Ni, Feifei Liang, Xiaoqian Xu, Tiantian He, Wei Song, Marta Gordel, Aleksandra Delplanque, Akiko Hatakeyama, Claudia Irene Trainito, Gaïa Grassini, and Rawand Masoud… You guys have lighten my life and made my stay in France so wonderful.

I want to express my great thanks to my boyfriend, Xiao, who is always there for me. I cannot imagine how life will be without you. Finally, my greatest love and support is my family. I would like to thank my parents for their continuous support and encouragement.